FABRICATION AND CHARACTERISATION OF NOVEL ULTRASOUND TRANSDUCERS

By

Yun Jiang

A thesis submitted to The University of Birmingham

for the degree of

DOCTOR OF PHILOSOPHY

School of Metallurgy and Materials

College of Engineering and Physical Sciences

The University of Birmingham

April 2013

Abstract

1-3 connectivity piezoceramic-polymer composites that can operate above 30 MHz are in demand to improve spatial resolution for biomedical ultrasound imaging applications. However, increasing the operational frequency of these materials is extremely challenging as ultrafine dimensions are required in conventional composite designs. An innovative randomised composite design has been previously reported to relax overall dimensional restrictions and to eliminate spurious resonance modes. However, realisation of such a design presents a significant challenge to conventional fabrication techniques.

In this work, a novel moulding approach based on a combination of gel casting and soft lithography techniques has been developed for producing random composites. A maximum green strength of 38 MPa has been obtained in the gel-cast green bodies. Irregular-shaped ceramic segments with feature sizes varying from 2 to 50 μm and aspect ratios up 70 have been achieved. Random piezocomposites with operational frequencies up to 100 MHz and thickness coupling factors over 0.5 have been fabricated and demonstrated. Two complete transducers working at 30 MHz and 70 MHz incorporating the random composites have been produced and characterised. Results from the transducers demonstrated their functional performance and showed the potential of the novel random piezocomposites for high frequency ultrasound applications.

Acknowledgements

Firstly, my sincere thanks go to my supervisor Prof. Tim Button for his valuable insight, patient guidance and continuous encouragement throughout this work.

I would also like to thank all of the members of the Functional Materials Group at the University of Birmingham. In particular, I want to thank Dr. Susana M. Olhero, Dr. Luipremixs Garcia-Gancedo, Dr. Florent Dauchy and Dr. Hana Hughes for their contributions to the composite development. Special thanks go to Mr. Carl Meggs for his technical assistance and proof-reading of this thesis.

I should also thank Dr. Tim Jackson for the provision of the clean room facilities in the School of Electronic, Electrical and Computer Engineering and Dr. Maolong Ke and Donna Holdom for their generous help in the clean room.

I am also indebted to Prof. Sandy Cochran, Dr. Christine Démoré and Mr. Srikanta Sharma from the University of Dundee, Dr. Robert Ssekitoleko from the University of Strathclyde, for their help in characterising the random composites and transducers, as well as Prof. Tom Stevenson and Dr. Camelia Dunare from the University of Edinburgh for their contributions to the development of the silicon master moulds. Dr. Christine Démoré also designed the random patterns and helped me in the modelling work presented in this thesis. The stimulating discussions with her greatly increased my understanding of composite designs and ultrasound imaging.

This thesis would not have been possible without the support and encouragement from my family and friends. Finally, I would like to express my deepest gratitude to my parents for their love.

Contents

INDEX OF FIGURES

INDEX OF TABLES

NOMENCLATURE AND ACRONYMS

A	Area (m^2)
A_a	Arrhenius pre-exponential factor
a	Correlation length (m)
C	Capacitance (F)
C_L	Low-frequency capacitance (F)
C_H	High-frequency capacitance (F)
C_s	Solution concentration
c_{mn}	Elastic stiffness constant (N/m^2)
c_{mn}^E	Elastic stiffness constant at constant electric field (N/m^2)
c_{mn}^D	Elastic stiffness constant at constant electric displacement (N/m^2)
D_i	Electric displacement (C/m^2)
D_M	Diameter of master mould (m)
D_d	Diameter of dried sample (m)
d_{Iij}, $d_{iIJ,}$ d_{Im}	Piezoelectric charge constant (C/N)
E_I	Electric field (V/m)
E_α	Activation energy (J/mol)
$e_{Im,}$ e_{in}	Piezoelectric stress constant (C/m^2)
F	Focal length (m)
f	Frequency (Hz)
f_r	Resonant frequency (Hz)
f_a	Anti-resonant frequency (Hz)
f_t	Fundamental thickness resonant frequency (Hz)
f_{l1}	Resonant frequency of the first spurious mode (Hz)
f_{l2}	Resonant frequency of the second spurious mode (Hz)
$G(s)$	Gaussian distribution
G'	Elastic modulus (Pa)
G''	Loss modulus (Pa)
I_a	Acoustic intensity (W/m^2)
K	Compressibility (N/m^2)
K_c	Overall calibration constant
K_r	Reaction rate
k_{eff}	Effective electromechanical coupling factor
k_t	Electromechanical coupling factor, thickness-extensional mode
k_p	Electromechanical coupling factor, planar-extensional mode
k_{33}	Electromechanical coupling factor, length-extensional mode
L	Linear shrinkage

l	Span (m)
$P(s)$	Random phase component in Gaussian distribution
P_c	Capillary pressure
P_f	Fracture load (N)
Q_m	Mechanical quality factor
R	Resistance (Ω)
R_g	Gas constant
R_L	Lateral resolution (m)
R_A	Axial resolution (m)
S_{ij}, S_n	Strain
s	Spatial frequency domain matrix
s_{ijIJ}	Elastic compliance constant (m^2/N)
s^E_{ijIJ}	Elastic compliance constant at constant electric field (m^2/N)
$T_{IJ,}$ T_m	Mechanical stress (N/m^2)
h	Thickness (m)
T_K	Absolute temperature (K)
t_p	Pulse duration (s)
t_{exp}	Exposure time (s)
t_{dev}	Development time (s)
t_g	Gelation time (s)
V	Volume percentage
v	Sound velocity (m/s)
W_d	Dry weight (N)
W_w	Wet weight (N)
w	Width (m)
X	Reactance (Ω)
X_C	Capacitive reactance (Ω)
x	Distance (m), spacing (m)
Z_a	Acoustic impedance (Rayl)
Z_e	Electrical impedance (Ω)
α	Attenuation coefficient (dB/mm)
ε_{iI}	Permittivity (F/m)
ε_0	Vacuum permittivity (F/m)
ε_r	Relative permittivity
ε^T	Permittivity at constant stress
ε^s	Permittivity at constant strain
ρ	Density (kg/m^3)
λ	Wavelength length (m)

η	Viscosity (Pa·s)
ω	Spin speed (rpm)
$\Gamma(s)$	Randomised spatial frequency distribution
σ	Surface tension $(\mathrm{N/m})$
σ_f	flexural stress (Pa)
θ	Phase (°)
θ_c	Contact angle (°)
θ_i	Incident angle (°)
θ_r	Reflection angle (°)
θ_t	Refracted angle (°)

AC	Alternating current
AM	Acrylamide
APS	Ammonium persulfate
CT	Computed Tomography
DC	Direct current
DMSO	Dimethyl sulfoxide
DSC	Differential scanning calorimetry
EDGDE	Ethylene glycol diglycidyl ether
FEM	Finite element modelling
FFT	Fourier Transformation
GPGE	Glycerol polyglycidyl ether
HFUS	High frequency ultrasound
LNO	Lithium niobate
LIGA	Lithographie, Galvanoformung and Abformung
MAM	Methacrylamide
MEMS	Micro-electrical-mechanical systems
MRI	Magnetic resonance imaging
MBAM	Methylene bisacrylamide
MPB	Morphotropic phase boundary
NVP	N-vinylpyrrolidone
PMMA	Poly(methyl methacrylate)
PMN-PT	Lead magnesium niobate and lead titanate
PZN-PT	Lead zirconate niobate and lead titanate
PVDF	Polyvinylidene fluoride
PZT	Lead zirconate titanate
PDMS	Poly(dimethylsiloxane)
SEM	Scanning electron microscopy

SPGE	Sorbitol polyglycidyl ether
SPL	Spatial pulse length
SSA	Specific surface area
TEMED	Tetramethylethylenediamine
TGA	Thermogravimetric analysis
VPP	Viscous polymer processing
µ-EDM	Micro-electro-discharge machining

CHAPTER 1 INTRODUCTION

High frequency (>30 MHz) ultrasound (HFUS) transducers have been under considerable on-going research, aiming to benefit a vast range of biomedical imaging applications through their micro-scale resolution. The preferred active materials in HFUS transducers are 1-3 piezocomposites because of their advantageous properties, such as enhanced electromechanical coupling and acoustic matching to tissue, when compared to monolithic piezoceramics. However, as smaller dimensions are required for increasing operating frequency, whilst avoiding the interference of lateral resonances, the fabrication of such composites using conventional dicing techniques becomes increasingly difficult.

To overcome the challenge in the development of HFUS transducers, a novel piezocomposite design has been proposed and reported to relax the overall fine-scale restrictions imposed on a high frequency composite by employing a distribution of ceramic geometries, dimensions and separations [1]. Finite element analysis of these composites has suggested their particular advantage in suppressing undesirable spurious resonance modes whilst maintaining high functional performance.

This work aims to develop practical fabrication methods for the realisation of the piezocomposites with such novel randomised design. Micro-moulding is selected as an alternative approach to the conventional dice-and-fill technique. By combining gel casting for the ceramic slurry preparation and soft lithography for the micro-mould fabrication, ultra-fine features as well as variable shapes of ceramic segments have been fabricated.

The thesis is divided into 10 chapters of which the introduction is the first. The literature review consists of three sections separately presented in chapters 2, 3, & 4 respectively. In the first section, the fundamentals of medical ultrasound imaging are introduced, followed by a review of the techniques and methods for the fabrication of 1-3 piezocomposites. From this review, a micro-moulding route based on gel casting of ceramics was selected. The techniques for producing the high-aspect-ratio moulds of adequate thickness to be used in this fabrication route are presented in the third section. Chapter 5 outlines the aims and objects of this project, and Chapter 6 details the experimental methods and procedures that have been used. Chapters 7 and 8 focus on the development of an optimised gel-casting slurry system and appropriate micro-sized moulds, respectively, which are the two essential factors of the micro-moulding route. Chapter 9 details the fabrication and characterisation of the piezocomposites and transducers produced using these optimised procedures. Finally, Chapter 10 summaries the conclusions from this work as well as suggestions for further work.

Reference:

[1] C. E. M. Demore, *et al.*, "1-3 piezocomposite design optimised for high frequency kerfless transducer arrays," in *Ultrasonics Symposium (IUS), 2009 IEEE International*, 2009, pp. 1-4.

CHAPTER 2 MEDICAL ULTRASOUND IMAGING

2.1 Medical imaging modalities

The last few decades have witnessed a significant development of medical imaging technologies. The image quality has been continuously improved and also a range of new modalities has been introduced, which enables excellent diagnosis and monitoring of diseases for both clinical and research purposes. Among the various imaging modalities available, conventional X-ray, X-ray computed tomography (CT), ultrasound, magnetic resonance imaging (MRI) and nuclear medicine are most commonly used. Table 2-1 shows a comparison of the main characteristics of these techniques.

Table 2-1 Comparison of common medical imaging modalities [1-3].

	Conventional X-ray	**CT**	**MRI**	**Nuclear Medicine**	**Ultrasound**
What is imaged	Tissue absorption of X-ray	Tissue absorption of X-ray	Biochemistry	Distribution of radiotracer	Mechanical properties
Typical spatial resolution	~ 1 mm	~ 1 mm	~ 1 mm	5-10 mm	0.3-3 mm
Safety	Low-level ionising radiation	High-level ionising radiation	Hazards arising from strong magnetic fields	High-level ionising radiation	Generally safe. Possible thermal effect and cavitation.
Real-time	Yes	No	No	No	Yes
2D/3D	2D	2D/3D	2D/3D	2D	2D/3D
Examination time	Short	Medium	Long	Long	Medium
Relative capital cost	Low	Fairly high	High	Fairly high	Medium
Relative cost per scan	Low	Medium	High	Medium to High	Low
Portability	Good	Poor	Poor	Poor	Excellent

As seen from the table, each modality has its own strengths and limitations and no single modality can provide all the desirable characteristics. For example, traditional X-ray is fairly straightforward and relatively low in cost. It has been most frequently used in chest imaging but has difficulties in differentiating soft tissues. CT is particularly effective in showing different types of tissues including lung, bone and soft tissues but always comes with high levels of ionising radiation. MRI is one of the best techniques for imaging soft tissues without the use of ionising radiation and it is especially useful in brain imaging. However, it is usually more expensive, particularly in respective of capital costs, and may take longer time to perform than other modalities. Nuclear medicine can specifically provide metabolic function information of organs, rather than the structural imaging provided by the diagnostic methods, but it needs very long preparation times of up to several days.

In comparison, ultrasound imaging is somewhat unique in the sense that it can provide images of comparable or better resolution as other imaging modalities at a relatively low cost while being non-invasive, capable of real-time operation, and highly portable [1]. As a mature technology existing for more than sixty years, medical ultrasound has been developed for almost a full range of clinical applications including obstetrics, cardiology, abdominal, vascular and surgery imaging with demonstrated accuracy and efficacy [4], and it now accounts for approximately one in four of all the hospital imaging procedures [5]. It is well-known that ultrasound is routinely used for monitoring foetuses during pregnancy. A typical example of an obstetric ultrasound image is shown in Figure 2-1. In addition to imaging the appearance of internal structures, ultrasound can also be used to measure functional changes such as blood flow and organ motion owing to its real-time imaging capability.

Figure 2-1 Example of medical ultrasound for baby scan [6].

2.2 High frequency medical ultrasound

For each particular clinical application, medical ultrasound is operated at a specific frequency range to offer the required resolution and penetration depth depending on the tissue to be imaged. For abdominal obstetrical and cardiological applications, lower frequencies ranging from 2-5 MHz are adopted, for pediatric and peripheral vascular imaging, frequencies of 5-7.5 MHz are utilised, and for intravascular, intracardiac and opthalmic examinations, higher frequencies from 10-30 MHz are employed [7]. Table 2-2 summarises the resolutions and depths of ultrasound imaging for various medical applications. In this thesis, HFUS is referred to ultrasound operating at frequencies over 30 MHz. Higher frequencies are of interest as there are still a number of small and near-surface structures that cannot be revealed at the resolution levels shown in the table.

Table 2-2 Summary of the resolutions and depths of ultrasound imaging for various medical applications [1].

Application	Resolution (mm)	Depth (cm)
Cardiology	2-3	2-16
obstetrics/gynaecology	2-3	2-20
Intravascular	0.3	<1
Intracardiac	0.5	1-5
General imaging	2-3	2-20
Vascular/small parts	0.3	1-5

The resolution of an ultrasonic image is principally dependent on the wavelength. The shorter the wavelength, the higher the resultant resolution i.e the smaller the object that can be resolved. The wavelength length λ is related to the frequency, *f*, and the propagation ultrasound velocity in the tissue, *v*, given by:

$$\lambda = \frac{v}{f} \qquad \textbf{Equation 2-1}$$

This equation suggests that higher frequency ultrasound leads to an improved resolution, enabling smaller objects to be imaged and hence more information for clinical diagnostics to be obtained. Figure 2-2 gives a visual comparison of intravascular ultrasound images obtained from a 30 MHz and 50 MHz ultrasound scan, showing that significantly enhanced resolution is achieved by increasing the frequency.

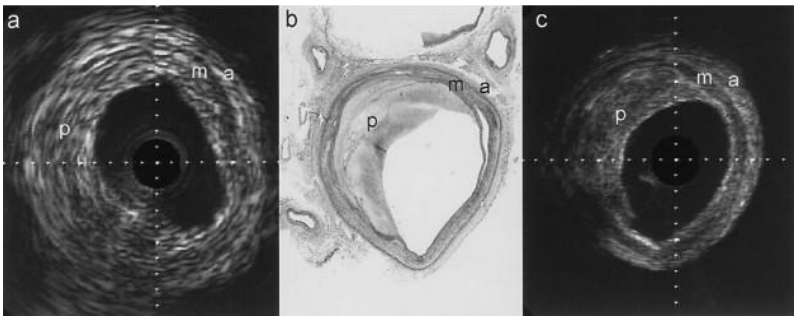

Figure 2-2 (a) 30-MHz and (c) 50-MHz intravascular ultrasound images; (b) corresponding histology of a stenosed femoral artery *ex vivo*. At 50 MHz, the clarity of the plaque and vessel structure are significantly improved compared with the image obtained from 30 MHz [8].

Ultrasound propagation velocity varies with the transmission medium and in soft tissues it has an average value of 1540 m/s. By substituting this value into Equation 2-1, it can be seen that the frequency range of 2-5 MHz conventionally used for baby scans has a wavelength ranging from 308 to 770 μm. By increasing the operation frequency to over 30 MHz, the wavelength is decreased to less than 50 μm. However, the improvement of the resolution comes at the expense of penetration depth owing to the increased attenuation of high frequency ultrasound during propagation. As shown in Table 2-2, resolution values below 1 mm are all associated with imaging depths below 5 cm. For a HFUS transducer operating at 30-50 MHz, the penetration depth is on the order of 10 mm [9]. The shallow penetration depth along with the improved resolution brought by HFUS make it particularly useful for specific medical imaging applications that involve fine and superficial structures, such as ophthalmology, dermatology and small animal imaging [10-12]. For example, higher than 50 MHz medical ultrasound can efficiently image anterior segments of the eye, diagnose glaucoma and ocular tumours and also aid refractive surgery [13].

2.3 Basics of ultrasound imaging

2.3.1 Pulse-echo operation

Ultrasound imaging is based on the principle of pulse-echo. Figure 2-3 schematically depicts the techniques used to form an ultrasound image. The process involves the use of a piezoelectric transducer for the production and detection of ultrasound waves. With the excitation of a voltage pulse, the transducer generates a short ultrasound pulse that travels into the tissues of the body. During propagation, the sound pulse is reflected back at the interfaces of tissues where acoustic mismatch exists, giving rise to the generation of echoes. The reflected sound waves are received and converted to

electrical pulses by the transducer. The elapsed time between the transmitted pulse and the returned echo can be used to calculate the distance between the transducer and the object where the reflection has occurred, which makes it possible to determine the tissue geometry.

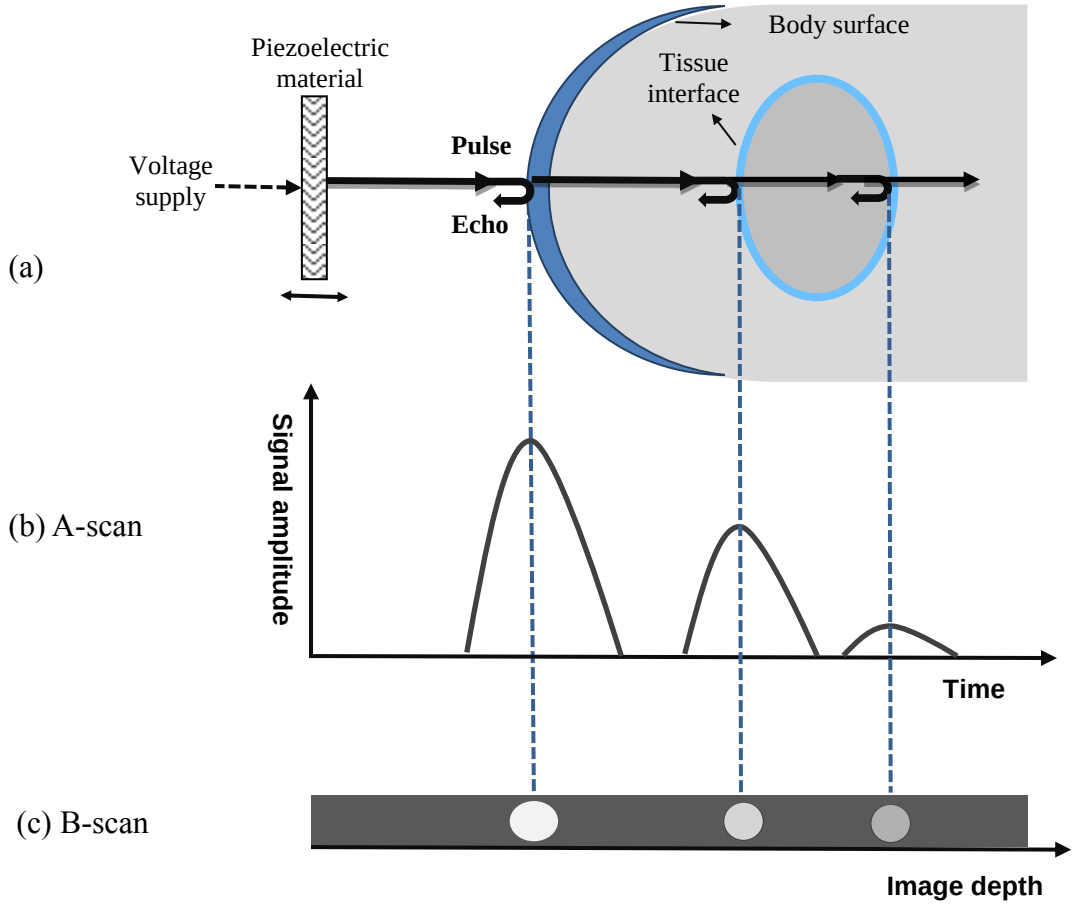

Figure 2-3 Schematic diagram of the basic ultrasound imaging technique. (a) Principle of pulse-echo. A piezoelectric transducer is excited by a voltage signal and transmits an ultrasound pulse into the human body, which is reflected back at tissue boundaries as acoustic echoes to be detected by the transducer. (b) A-scan mode. The reflected echoes are converted to electrical pulses that are plotted as a function of time. (c) B-scan mode. The same reflected pulses are converted into grey-scale spots with different brightness.

In ultrasound imaging, the earliest and simplest scanning form is called an amplitude scan or A-scan, from which other imaging methods are derived. A-scan is a one-dimensional measurement in which ultrasound pulses are transmitted along one direction. As shown in Figure 2-3(b), the amplitudes of the echoes reflected at the

interfaces are plotted on the Y-axis as a function of the travelling time recorded on the X-axis. A-scan is not found on most of the medical imaging systems but it is widely adopted in non-destructive testing such as rail inspection to detect flaws in the metal. Brightness scan or B-scan is currently the standard method to display diagnostic images. It is a two-dimensional presentation of ultrasound by sending down a series of pulses and recording echoes reflected back from the imaging area rather than from individual points as in an A-scan, i.e. it is a series of A-scans. The amplitudes are displayed in terms of varying brightness such that strong reflections appear as bright dots while weak echoes appear dark on the image as seen in Figure 2-3(c). Different shades of grey yield the information on the differentiation of tissues.

2.3.2 Ultrasound waves

Ultrasound is used to describe sound waves with a frequency that exceeds 20 kHz, above the audible range of human hearing. Like all sound waves, ultrasound in the form of a pressure wave transports energy and propagates through various media by different means [14]. During the propagation, a molecule in the medium is forced to oscillate around its equilibrium state, transmitting the oscillation to a neighbouring molecule and resulting in alternating compression and rarefaction in the medium. Longitudinal (or compression) and transverse (or shear) waves are two basic types of waves as illustrated in Figure 2-4. In a longitudinal wave, the particle displacement is along the direction of propagation while in a transverse wave, the motion of the particle is perpendicular to the direction of propagation. The wave velocity in a certain medium is related to the density ρ of the medium and the compressibility K given by Equation 2-2.

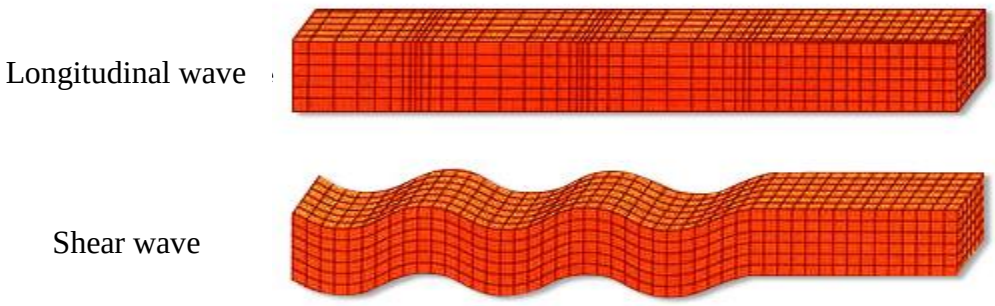

Figure 2-4 Longitudinal wave and shear wave propagating in a bulk solid [15].

$$v = \frac{1}{\sqrt{\rho K}} \qquad \textbf{Equation 2-2}$$

In the soft tissues, the shear wave can only travel at low velocity, varying from a few to hundreds of meters per second, and is heavily attenuated even at low kHz frequencies [16, 17]. This is because the soft tissues are similar to viscous liquids [18] and liquids do not support shear stress. Thus, ultrasound waves propagate in tissues as longitudinal waves and the wave velocity is faster in relatively denser and stiffer media such as bones and slower in more compressible material like soft tissues according to Equation 2-2.

Apart from the two basic types, there are other categories of waves: surface and plate waves, arising from coupling between longitudinal and shear waves under certain boundary conditions. Surface waves, also known as Rayleigh waves, propagate on the surface of a material, slower than transverse or longitudinal waves in the same material [19, 20]. Plate waves such as Lamb waves have particle displacement both in the direction of wave propagation and normal to the plate, but only exist in thin plate-like structures [21, 22]. The velocity of a Lamb wave is related to the frequency and

the thickness of the plate. In medical ultrasound imaging, the interaction of longitudinal waves with tissues is used to produce ultrasound images and the possible presence of Lamb waves in the transducer would degrade the image quality. This issue and possible solutions are further addressed in Chapter 3.

2.3.3 Interaction of ultrasound with tissues

As a beam of ultrasound is transmitted into the human body, it can interact with tissues in various modes including reflection, refraction, scattering, attenuation etc., in which the reflection and refraction of ultrasound waves form the basis of ultrasonic imaging. Reflection occurs when ultrasound waves travelling in one medium meet an interface with a second medium with different acoustic impedance. Analogous to electrical impedance (see Section 3.1.5), which is employed to describe the opposition of an electric component to the flow of current through it, acoustic impedance is used to describe the opposition of a medium to the passage of ultrasound. The characteristic acoustic impedance Z_a of a given medium is a product of the material density ρ and the velocity of sound v in the medium given by the following expression:

$$Z_a = \rho \cdot v \qquad \textbf{Equation 2-3}$$

It is usually expressed in MRayl (10^6 kg/m^{2}s). Table 2-3 provides some examples of the density, compressibility, sound velocity and acoustic impedance of different propagation media. The acoustic impedance values of most soft tissues are similar. Organs filled with air such as the lung have the lowest impedance and dense tissues like bones have much higher impedance values. The greater the difference in acoustic impedance between the two media, the greater the amount of energy reflected back.

For example, the acoustic impedance values of gallstones differ dramatically from soft tissues, resulting in strong reflections or echoes, enabling them to be diagnosed.

Table 2-3 Acoustic properties of various media [23].

	ρ (kg/m^3)	K (10^{-12} m^2/N)	c (m/s)	Z_a (Mrayl)
Fat	950	508	1440	1.37
Blood	1025	396	1570	1.61
Muscles	1070	353-393	1542-1626	1.65-1.74
Bones	1380-1810	25-100	2700-4100	3.75-7.4
Air (0 ℃)	1.2	8x10^6	330	0.0004
Water (25 ℃)	988	452	1497	1.48

Due to the similarity of soft tissues in terms of the acoustic properties, only a small portion of the ultrasound is reflected at such interfaces whereas the majority is transmitted, allowing imaging of deeper structures [24]. As illustrated in Figure 2-5, when an incident beam travels from medium 1, with propagation velocity of v_1, to medium 2 with velocity of v_2, part of the beam is reflected and the remainder is refracted into the second medium. Thus the wave continues propagating but in a new direction.

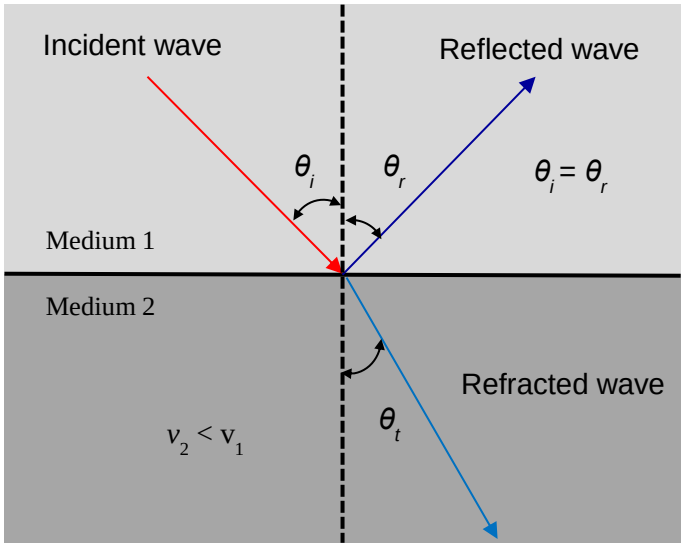

Figure 2-5 Schematic diagram showing the reflection and refraction of ultrasound at the interface of two materials.

The angle of the reflected wave θ_r equals the angle of the incident wave θ_i in respect to the interface normal. The relationship between the incident angle θ_i and the refraction angle θ_t follows Snell's law in optics given by the following equation:

$$\frac{\sin\theta_i}{\sin\theta_t} = \frac{v_1}{v_2} \qquad \textbf{Equation 2-4}$$

The result of the reflection and refraction processes is that the ultrasonic wave is attenuated. These are not the only mechanisms of the attenuation of ultrasound. Other interactions between ultrasound and tissues such as absorption and scattering also lead to the attenuation of ultrasound energy. The absorption of ultrasound refers to the conversion of acoustic energy to heat, which is mainly due to frictional forces arising in molecules during wave transmission [24]. Scattering mainly happens when the ultrasound wave encounters tissue structures with dimensions much smaller than the wavelength. The overall attenuation of acoustic energy depends on three factors: the distance travelled, the tissue type and the operating frequency of the transducer [25]. With the increase of the depth of penetration, the attenuation is increased exponentially [26] given by the following expression:.

$$I_a = I_0 e^{-\alpha x} \qquad \textbf{Equation 2-5}$$

where I_a is the intensity of the ultrasound wave at distance x, I_0 is the initial intensity and α is the attenuation coefficient. Figure 2-6 shows the dependence of α on the tissue type and the operating frequency of ultrasound. It can be seen that α increases approximately linearly with frequency in the range 20-100 MHz for all tissue types, although the actual frequency-dependence varies. This explains why the choice of frequency for a particular application depends on the properties of the targeted tissue

(see Table 2-2), and why higher frequency ultrasound of interest in this thesis is more suitable for imaging near-surface structures.

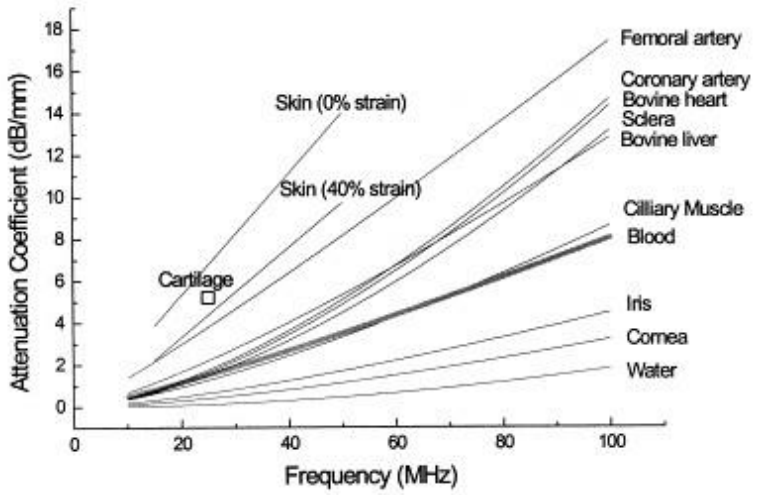

Figure 2-6 Attenuation coefficient of different tissue types as a function of frequency [8].

2.4 Ultrasound transducers

The overall performance of a medical ultrasound imaging system mainly relies on the characteristics of the adopted ultrasonic transducer, which produces and receives sound waves based on the conversion of electricity to mechanical ultrasound waves and vice versa. Ultrasonic transducers fall into two basic types in terms of construction: single-element and arrays. As the names imply, the former consists of a single active element, which is mechanically steered to form B-scan images. In comparison, the latter is made up of multiple small active elements, allowing electronic steering that provides higher frame rate and dynamic focusing, resulting in improved image quality. The focus of this thesis is high frequency single element transducers as the first step in the validation and implementation of the piezocomposites with novel random design. For the illustration of the roles of

constitutive materials in a transducer, the simpler configuration of a single element transducer is analysed, followed by a section describing the properties of transducers.

2.4.1 Basic transducer construction

A basic transducer consists of an active element, matching layer, backing layer, a metal housing and electrical connectors as shown in Figure 2-7. All of them are specifically discussed in the following paragraphs.

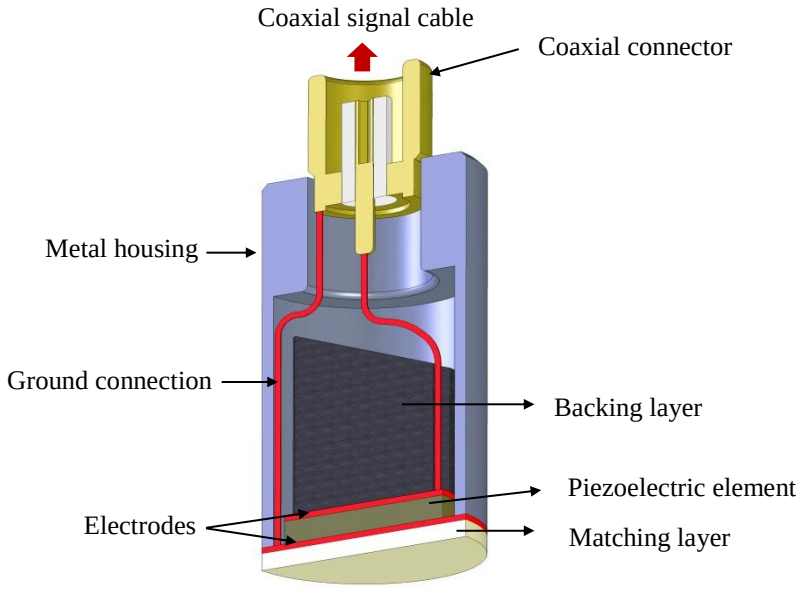

Figure 2-7 Schematic of a cross section of a typical single element transducer (adapted from [27]).

The metallic housing provides the necessary support to protect the components inside and insulate them from the outside environment electrically and acoustically. The housing is also often used as the part of the electrical circuit, facilitating the electrical connection (ground) between the front electrode on the composite and the coaxial outer cable. Electrical connectors are used to link the electric signals between other ultrasound instrumentation and the transducer.

Active material, typically a piezoceramic, is the actual ultrasound generator and receiver and thus is considered to be the heart of a transducer. A thin film of sputtered chrome-gold or fired-silver is attached to each side of the element as electrodes. The dimensions and properties of the active material play a vital role in the performance of the transducer, which are discussed in detail in Chapter 3.

A matching layer is applied between the active material and the testing medium. The thickness of the layer is typically around a quarter wavelength ($\lambda/4$) at a given operating frequency to maximise the acoustic energy transmission occurring at face of the transducer [28]. The acoustic impedance of the matching layer should be in between that of the active material and the propagation medium so that the acoustic impedance mismatch at the interface can be reduced and the efficiency of acoustic energy transfer from the active element to the medium and vice versa can be improved. For further improvement of the performance, sometimes multiple matching layers with graded acoustic impedance are used [29]. Detailed design principles of the matching layer can be found in [30, 31]. In addition to that, coupling materials such as acoustic gels are often applied in ultrasound imaging to minimise the acoustic mismatch between the transducer and the patient.

A thick layer is mounted on the inner face of the active material as the backing. It is usually made of an epoxy loaded with small particles, typically tungsten powders. Firstly, it serves as a mechanical support for the thin layer of active element. Secondly, it is designed to attenuate the backward radiating pulses, stopping reflections from the electrical connections or from the rear of the backing layer passing into the active element to avoid false signals. Also, the backing provides damping for the active element, preventing internal reverberation (continued vibration after excitation)

within the piezoelectric element. Damping limits the number of pulse cycles, which improves the axial resolution (see Section 2.4.2.2). If the acoustic impedance of the backing is identical to that of the active element, it would eliminate such reverberation but would be at the cost of sensitivity because most of ultrasound energy would be transferred to the backing. Thus, a trade-off between efficient damping and optimal sensitivity must be made in choosing the acoustic impedance of the backing according the requirements for each application. More detailed information regarding the design and characteristics of backing layers are found in [27].

For the purpose of focusing, the active element is geometrically curved or a lens is incorporated as illustrated in Figure 2-8. Lenses are usually made of polystyrene or epoxy resin with a velocity different than that of the targeted tissue but with an acoustic impedance matched to it [20, 32]. It is generally considered that the transducer with a curved piezoelectric element provides better performance as the use of an acoustic lens may lead to uneven losses of the ultrasound energy as a result of varied travelling path length [33]. Therefore, in this thesis, focusing was achieved by curving the active layer.

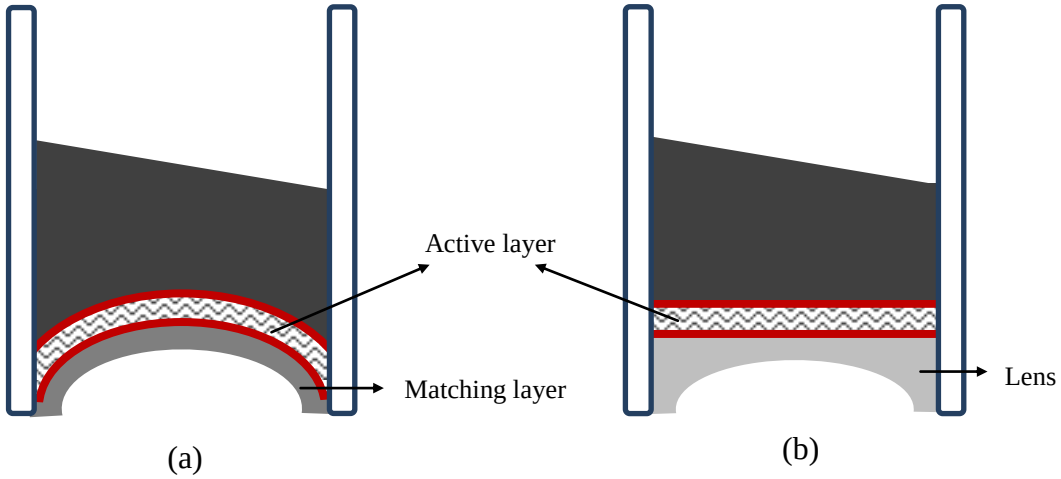

Figure 2-8 Two approaches commonly used for focusing a transducer: (a) curving the active piezoelectric material and (b) incorporating a focused lens.

2.4.2 Transducer properties

2.4.2.1 Beam profile

Transducer beam or transducer field represents a collection of ultrasound waves travelling longitudinally from the transducer surface to the propagation medium. The geometry of the beam for a focused transducer, as shown in Figure 2-9, exhibits three distinct parts: near field, focal zone and far field. In the near field, the generated ultrasound waves travel perpendicular to the concave surface and converge towards a focal point in the focal zone and then diverge in the far field. The focal zone is usually defined as the region over which the intensity is half of the maximum (-3 dB) [34], and the focal point is at the centre of the focal zone. The focal length is defined as the distance between the transducer and the focal point.

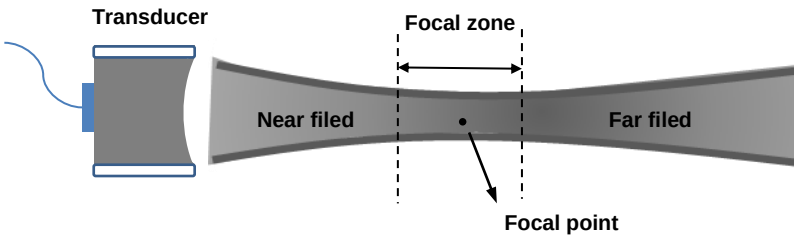

Figure 2-9 Beam shape of a focused transducer.

2.4.2.2 Axial resolution

The quality of ultrasound images mainly depends on the spatial resolution, axial and lateral. The axial resolution refers to the ability to resolve two discrete structures along the central axis of the ultrasound beam as illustrated in Figure 2-10. The axial resolution R_A is primarily determined by the spatial pulse length (SPL) of the pulse transmitted from the transducer [35]. A pulse typically consists of 2-3 cycles [20, 36] and each cycle has the same wavelength but the amplitude attenuates with imaging depth. The axial resolution is limited by one half of the SPL [20, 35]. Two reflectors with distances closer than ½ SPL cannot be resolved on the screen as the echo signals reflected from the two objects are overlapped. A better axial resolution requires a shorter pulse. SPL can either be shortened by applying efficient damping with the use of a properly designed backing layer to reduce the number of cycles or by increasing the frequency of the transducer to decrease the wavelength. Figure 2-10 schematically shows that a high frequency transducer with a shorter transmitter pulse has better axial resolution than a low frequency one with a longer pulse.

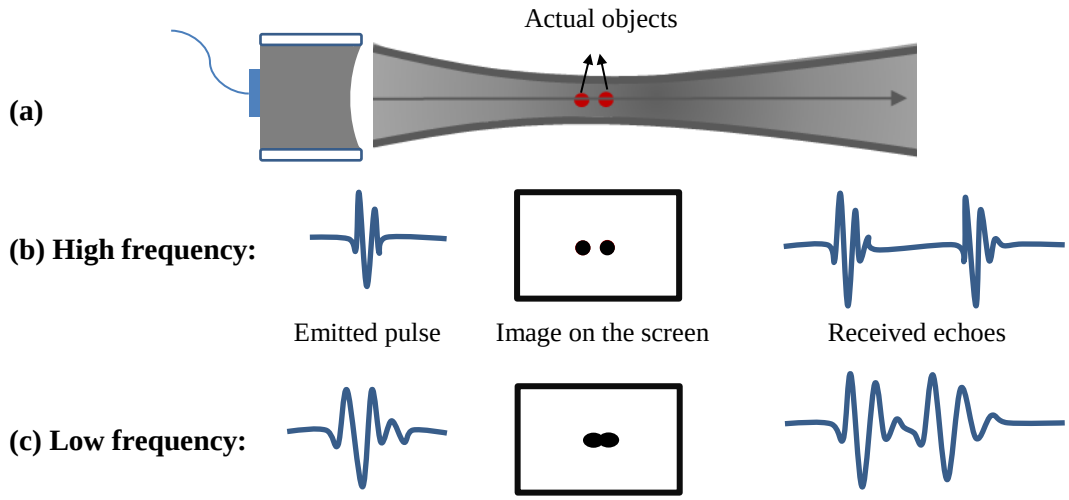

Figure 2-10 Schematic illustration of (a) axial resolution, (b) two resolved objects from a high frequency transducer which results in a short emitted pulse and two differentiated echoes and (c) unresolved objects from a low frequency transducer which results in a long emitted pulse and two overlapped echoes.

R_A can be given by the following equation:

$$R_A = \frac{1}{2} v t_p \qquad \textbf{Equation 2-6}$$

where v is the sound velocity in the tissue and t_p is the pulse duration, for which the time taken for the pulse to decrease to half of its maximum (-6 dB width is typically used) [20].

2.4.2.3 Lateral resolution

Lateral resolution (R_L) refers to the ability to resolve two discrete structures in a plane perpendicular to the sound wave. It is determined by the beam width and the narrower the beam width gives the better lateral resolution. Hence, the lateral resolution is the finest in the focal zone where the beam width is close to the narrowest (see Figure 2-9). Lateral resolution is also dependent on the frequency of the transducer because a higher frequency transducer with shorter wavelength gives a narrower beam width

than the one with the same transducer diameter but operating at lower frequency at its focal length, schematically illustrated in Figure 2-11.

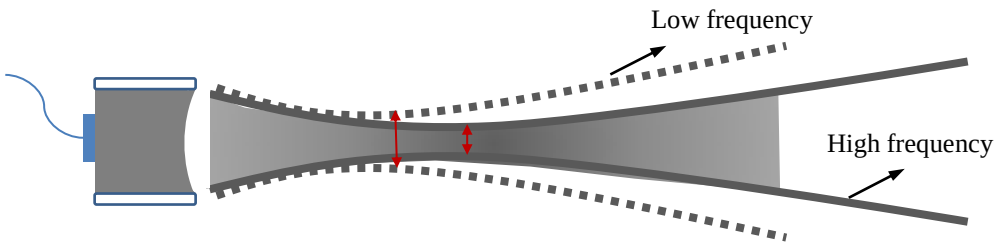

Figure 2-11 Schematic illustration of the beam shapes for high and low frequency transducers, showing the high frequency transducer has narrower beam width at its focal length compared with that of the low frequency one.

R_L of a focused transducer is given by the following expression:

$$R_L = \lambda \frac{Focal\ length}{Aperture\ diameter} \qquad \textbf{Equation 2-7}$$

The lateral resolution can be improved by increasing the frequency, reducing the focal distance or increasing the transducer aperture.

2.5 Summary

This chapter covered the background and theory behind medical ultrasound imaging. The need for high frequency ultrasound to improve the imaging resolution was addressed. The basic principles of ultrasound imaging and the interactions between ultrasound waves and tissues were described. The construction of the single-element ultrasound transducer was illustrated and the function of each constituent part was explained, along with a discussion of the properties of ultrasound transducers.

2.6 References

[1] K. Iniewski, *Medical imaging*: Wiley Online Library, 2009.

[2] T. Szabo, *Diagnostic Ultrasound Imaging: Inside Out: Inside Out*: Academic Press, 2004.

[3] (Last accessed: 2013/02/28). Table of comparison of medical imaging techniques. Available: http://www.voxelera.co.uk/downloads/tablepart1_jan2006.pdf.

[4] S. M. Bierig and A. Jones, "Accuracy and cost comparison of ultrasound versus alternative imaging modalities, including CT, MR, PET, and angiography," *Journal of Diagnostic Medical Sonography*, vol. 25, pp. 138-144, 2009.

[5] "Front Matter," in *Physical Principles of Medical Ultrasonics*, ed: John Wiley & Sons, Ltd, 2005, pp. i-xv.

[6] (Last accessed 2013/02/28). *Prenatal Testing—Ultrasound*. Available: http://www.genetics.edu.au/Information/Genetics-Fact-Sheets/FS17A.pdf

[7] T. R. Gururaja, "Piezoelectric transducers for medical ultrasonic imaging," in *Applications of Ferroelectrics, 1992. ISAF '92., Proceedings of the Eighth IEEE International Symposium on*, 1992, pp. 259-265.

[8] F. S. Foster, *et al.*, "Advances in ultrasound biomicroscopy," *Ultrasound in Medicine & Biology*, vol. 26, pp. 1-27, 2000.

[9] F. Kiessling and B. J. Pichler, *Small Animal Imaging: Basics and Practical Guide*: Springer, 2011.

[10] C. Passmann and H. Ermert, "A 100-MHz ultrasound imaging system for dermatologic and ophthalmologic diagnostics," *Ultrasonics, Ferroelectrics and Frequency Control, IEEE Transactions on*, vol. 43, pp. 545-552, 1996.

[11] G. Lockwood, *et al.*, "Beyond 30 MHz [applications of high-frequency ultrasound imaging]," *Engineering in Medicine and Biology Magazine, IEEE*, vol. 15, pp. 60-71, 1996.

[12] D. H. Turnbull, "In utero ultrasound backscatter microscopy of early stage mouse embryos," *Computerized medical imaging and graphics*, vol. 23, pp. 25-31, 1999.

[13] C. J. Pavlin and F. S. Foster, *Ultrasound biomicroscopy of the eye*: Springer-Verlag, 1995.

[14] M. Hennerici and D. Neuerburg-Heusler, *Vascular diagnosis with ultrasound: clinical reference with case studies* vol. 1: Thieme, 2005.

[15] (Last accessed 2013/03/02). *Earthquake waves*. Available: http://elearning.stkc.go.th/lms/html/earth_science/LOcanada5/503/1_en.htm

[16] M. Fink, *et al.*, *Imaging of complex media with acoustic and seismic waves* vol. 82: Springer, 2002.

[17] S. N. Gurbatov, *et al.*, *Nonlinear random waves and turbulence in nondispersive media: waves, rays, particles*: Manchester University Press, 1991.

[18] R. Mantke and U. Peitz, *Surgical Ultrasound: An Interdisciplinary Approach for Surgeons, Internists, and Ultrasound Technicians*: TIS, 2007.

[19] A. L. Fetter and J. D. Walecka, *Theoretical mechanics of particles and continua*: Dover Publications, 2003.

[20] C. E. M. Démoré, "Design of Ultrasound Transducer Arrays for Medical Imaging," PhD, Queen's University, 2006.

[21] M. J. Crocker, *Handbook of acoustics*: Wiley-Interscience, 1998.

[22] Z. Su and L. Ye, *Identification of Damage Using Lamb Waves: From Fundamentals to Applications*: Springer, 2009.

[23] B. Angelsen, *Ultrasound imaging: Waves, signals, and signal processing*: Emantec, 2000.

[24] T. G. Nyland and J. S. Mattoon, *Small animal diagnostic ultrasound*: WB Saunders Company, 2002.

[25] S. A. Grant and D. B. Auyong, *Ultrasound guided regional anesthesia*: Oxford University Press, 2012.

[26] T. D. Rossing, *Springer handbook of acoustics*: Springer Verlag, 2007.

[27] R. A. Webster, "Passive Materials for High Frequency Piezocomposite Ultrasonic Transducers," PhD, University of Birmingham, 2009.

[28] A. A. Vives, *Piezoelectric transducers and applications*: Springer, 2008.

[29] J. H. Goll and B. A. Auld, "Multilayer Impedance Matching Schemes for Broadbanding of Water Loaded Piezoelectric Transducers and High Q Electric Resonators," *Sonics and Ultrasonics, IEEE Transactions on*, vol. 22, pp. 52-53, 1975.

[30] R. S. Cobbold, *Foundations of biomedical ultrasound*: Oxford University Press on Demand, 2007.

[31] J. Zhu, *Optimization of Matching Layer Design for Medical Ultrasonic Transducer*: ProQuest, 2008.

[32] S. K. Bhargava, *Principles and practice of ultrasonography*: Alpha Science International Limited, 2003.

[33] D. MacLennan, "Fundamental Characterisation and Early Functional Testing of Micromoulded Piezocomposites " PhD, University of Strathclyde 2009.

[34] H. Lee, *et al.*, "Design of Focused Ultrasound Array for Non-Invasive Transesophageal Cardiac Ablation," *Open Medical Devices Journal,* vol. 2, pp. 51-60, 2010.

[35] J. Machi and E. D. Staren, *Ultrasound for surgeons*: Lippincott Williams & Wilkins, 2004.

[36] T.A.Whittingham, "Transducers and beam forming in medical ultrasonic imaging," *Insight-Non-Destructive Testing and Condition Monitoring,* vol. 41, pp. 8-12, 1999.

CHAPTER 3 1-3 PIEZOCOMPOSITES - PRINCIPLES, DESIGN CONSIDERATIONS AND FABRICATION ROUTES

The heart of an ultrasound transducer is the active piezoelectric element, used for both transmitting and receiving acoustic signals. The properties of the piezoelectric element determine the ultimate performance of a transducer including the working frequency, the beam shape, and the resolution etc. This chapter aims to provide a general review of the fundamentals of piezoelectric effects and the available piezoelectric materials, with emphasis on the principles and characteristics of 1-3 piezocomposites as well as the novel design and fabrication routes of these materials.

3.1 Fundamentals of piezoelectricity

3.1.1 Piezoelectric effect

The word piezoelectricity is derived from a Greek word piezein, meaning to press or squeeze [1]. The name was proposed by W.G.Hankel in 1881 after the piezoelectric phenomenon was firstly discovered in quartz by the brothers Pierre and Jacques Curie in 1880 [2]. Piezoelectricity represents the reversible interaction between electrical and mechanical characteristics in some crystalline materials. If a stress is applied on a thin piezoelectric plate, a charge difference would be generated across the plate. This is known as the direct piezoelectric effect, which is the basis of sensors for measuring strain, forces, pressure and vibration etc. Conversely, if the plate is subjected to an electric field, a strain or stress is produced in response, resulting in dimensional changes. This is the reverse or indirect piezoelectric effect, which is the driving force for the development of actuators to generate mechanical motion from electrical energy, for example in micro-positioning systems.

In ultrasound transducer applications, both direct and indirect effects are exploited. When applying a short burst of electricity, the piezoelectric material undergoes mechanical deformation, producing ultrasound waves to propagate in the tissue structures. During reception, the reflected ultrasound echoes result in mechanical vibrations of the piezoelectric material, which then generate electrical pulses. It is worth noting that the amplitudes of the echoes are orders of magnitude lower than the transmitted pulses, hence the active material needs to be extremely sensitive.

3.1.2 Crystal structure and piezoelectricity

From the molecular or atomic point of view, piezoelectricity originates from an asymmetric charge distribution, which only exists in a structure without a centre of symmetry. According to the crystallographic symmetry, all the crystals can be classified into 32 point groups, 20 of which have no centre of symmetry and exhibit piezoelectric behaviour. When the centre of the positive charges does not coincide with that of the negative charges, a net dipole moment is developed in the unit cell within a crystal. Ten among the piezoelectric class only develop a dipole when subjected to an external stress along certain directions, whereas others have a permanent net dipole in the unit cells. These polar materials display spontaneous polarisation as a function of temperature, the property of which is called pyroelectricity (pyro means fire in Greek). With increasing temperature, the polarisation decreases and at a particular temperature known as the Curie temperature, the polarisation vanishes. In some pyroelectric materials, the polarisation can be permanently retained and the magnitude and direction of the polarisation can be altered by an external electric field, i.e. ferroelectric behaviour. Piezoelectric materials commonly used in ultrasound transducers are ferroelectric. Figure 3-1 gives the tree-

like hierarchy for the classification of the crystals according to centrosymmetry and polar properties.

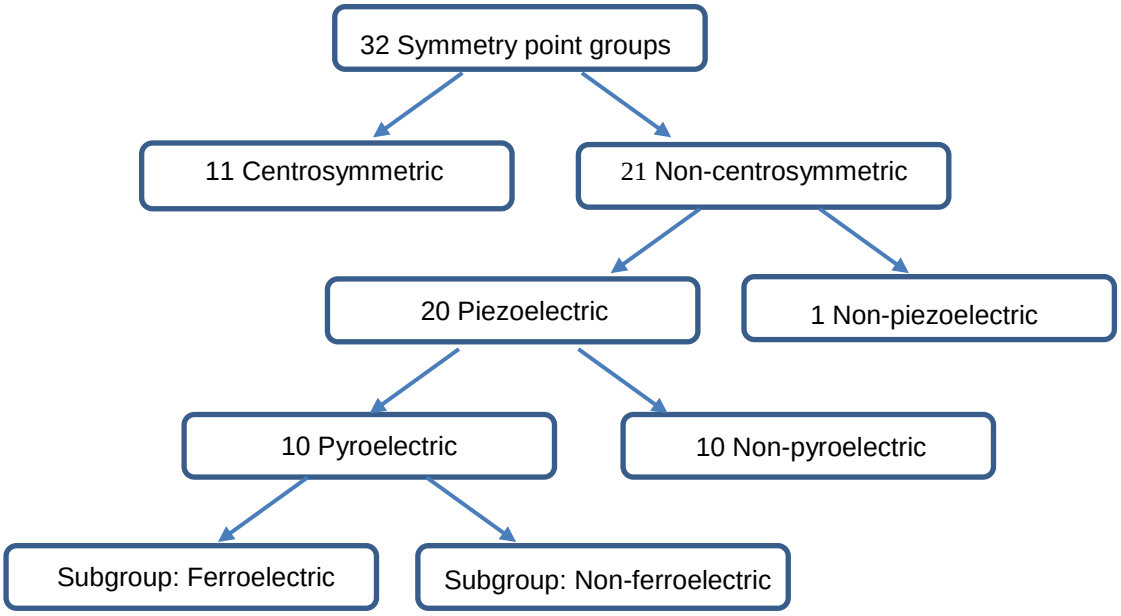

Figure 3-1 Crystallographic classification showing the symmetry hierarchy for piezoelectricity (adapted from [3]).

Perovskite ceramics, named after the mineral calcium titanate ($CaTiO_3$) [4], are of great importance in the family of ferroelectric materials. They have the general chemical formula of ABO_3, where A and B generally represent divalent and tetravalent metal ions, respectively, and examples of such materials are lead zirconate titanate, $PbZrO_3$, barium titanate, $BaTiO_3$, potassium niobate, $KNbO_3$ etc. The perovskite structure is highly versatile, such that can be distorted as a function of temperature, resulting in the change of piezoelectric properties. The most common piezoelectric material used in medical imaging transducers is Lead Zirconate Titanate ($PbZr_xTi_{1-x}O_3$) perovskite ceramic. Figure 3-2 shows the crystallographic structures of PZT for three phases. Above the Curie temperature, PZT exhibits cubic symmetry with no piezoelectricity as the charges in the unit cell cancel each other, giving a zero

net dipole. While below the Curie point, the lattice structure becomes distorted along <100> or <111> directions. In the resultant tetragonal and rhombohedral unit cells, Ti and Zr atoms are slightly off-centre and therefore net dipoles are developed in the directions indicated by the arrows.

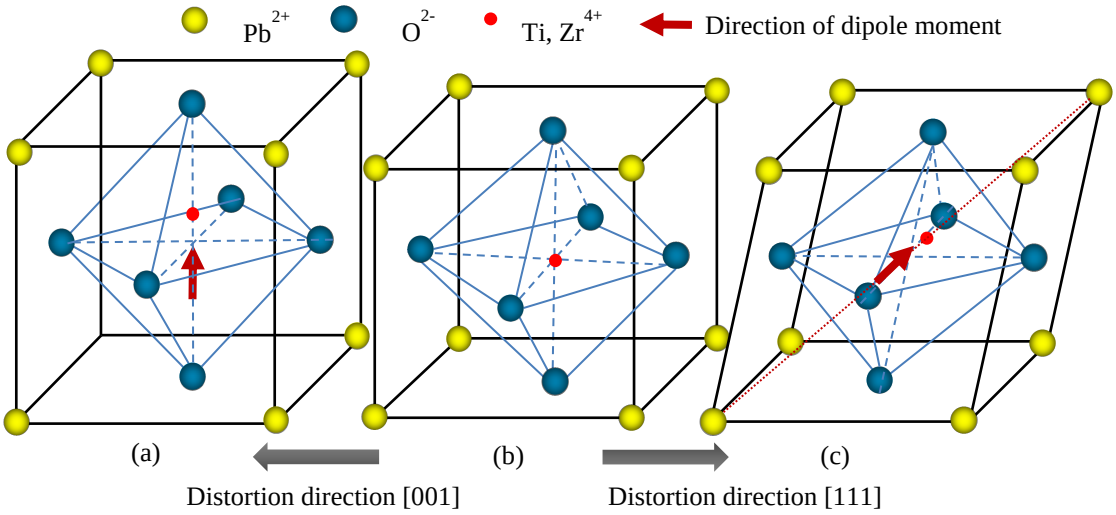

Figure 3-2 Crystallographic structures of the Lead Zirconate Titanate ceramic: (a) tetragonal, (b) cubic and (c) rhombohedral phases. The arrows show the directions of the dipoles developed in the unit cells.

For PZT, the Curie temperature can be tuned by changing the composition, more specifically, the mole ratio of Zr and Ti, i.e. the x value in the general formula, as seen in the phase diagram of the lead zirconate – lead titanate system shown in Figure 3-3. It is interesting to notice that the transition boundary between the tetragonal and rhombohedral phases, known as the morphotropic phase boundary (MPB), is nearly independent of temperature. PZT ceramics show best piezoelectric properties for compositions near the MPB (x=0.52 at room temperature) due to the coexistence of the two ferroelectric phases in this region [5].

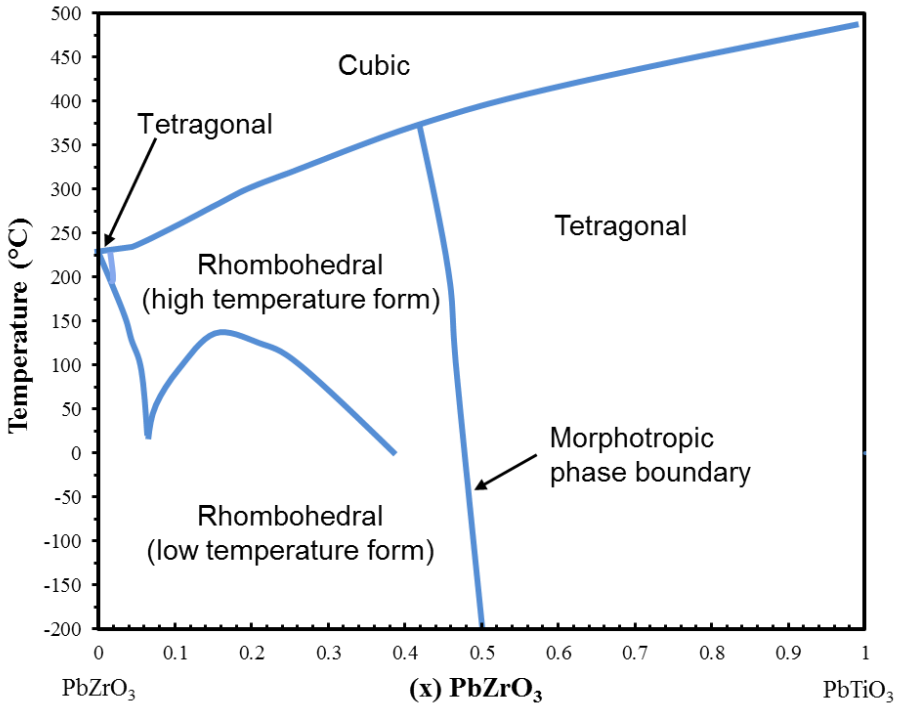

Figure 3-3 Phase diagram of lead zirconate titanate (PZT) (adapted from [6]).

3.1.3 Domains and poling

On the microscopic scale, every unit cell in a piezoelectric material has a certain polarisation direction. A group of unit cells with the same electric dipole orientation is called a domain. Ferroelectric ceramics are mainly in the polycrystalline form, consisting of small crystals or grains. Each of the grains contains single or multiple domains depending on the size and shape of the grain. Figure 3-4 shows SEM (scanning electron microscope) images of domains in tetragonal and rhombohedral PZT as two examples. The two structures exhibit distinct domain features, with significantly higher density of domains observed in the tetragonal PZT, which is due to the higher lattice distortion in this particular structure [7]. Detailed analysis of domains in the crystals can be found in numerous literature reports [8-10].

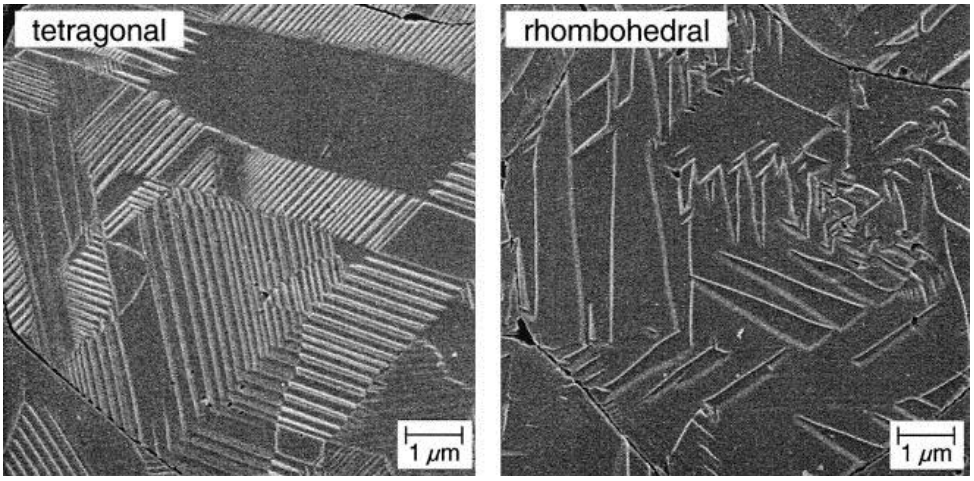

Figure 3-4 SEM micrographs showing domain configurations of tetragonal and rhombohedral PZT [7].

On the macroscopic scale, ferroelectric ceramics exhibit no piezoelectricity in the natural state due to the random distribution of their domains. Polarisation from the individual grains or domains cancel each other out, producing a net zero dipole in the whole material. In order to make the ceramics piezoelectrically active, domains are permanently aligned in a preferred direction by a process called poling. The commonly used poling technology relies on the simultaneous application of heat and high DC (direct current) electric field. During poling, the piezoceramic is heated up to an elevated temperature below the Curie point. For PZT, poling is usually performed at 110-150 ºC. As the temperature increases, the mobility of domain walls increases. With the simultaneous application of electric field, typically 1-3 kV/mm for PZT, the randomly oriented domains are compelled to align towards the direction of the applied external field. After removal of the applied field, this alignment is nearly locked in place, producing a net dipole in the poling direction. A simple schematic illustration of the poling process is shown in Figure 3-5.

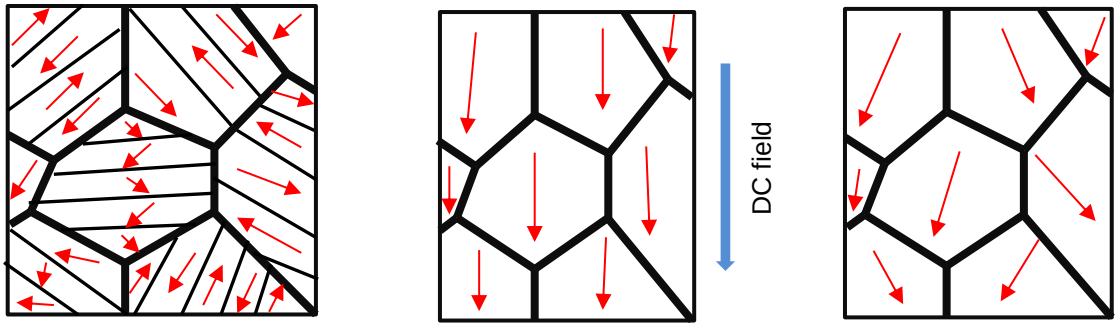

(a) Before poling (b) During poling (c) After poling

Figure 3-5 Schematic representation of the poling process (adapted from [11]). (a) Before poling, domains in the grains are randomly oriented, (b) during poling, domains are forced to align in the direction of the DC field, and (c) after poling, the alignment is retained.

The number of aligned dipoles depends on a variety of factors, such as poling field, temperature, poling direction, and the time held at the voltage, which can be optimised according to specific requirements. However, poling cannot switch all the domains, as some domains cannot be reoriented and some domains will switch back after the removal of the poling field [12]. For tetragonal PZT, domain switching is more difficult than that for the rhombohedral form, i.e. more difficult to be poled [13].

Caution must be taken when handling poled samples, as depoling may occur at high temperatures beyond the Curie point or under the application of external stress or field, causing the degradation or even total loss of piezoelectric properties.

3.1.4 Constitutive equations and related material parameters

After poling, the piezoelectricity is anisotropic in the piezoelectric ceramics. Directional notations are given to various parameters used for describing piezoelectric behaviour along different directions. The designation of the axes is displayed in Figure 3-6, where the poling direction is marked as 3 (z), axes 1 (x), 2 (y) are perpendicular with axis 3 (z). Numbers 4, 5 and 6 represent the shear directions about

axes 1, 2 and 3 respectively. Based on the defined coordinate system, the piezoelectric effect can be described in terms of a series of parameters and equations.

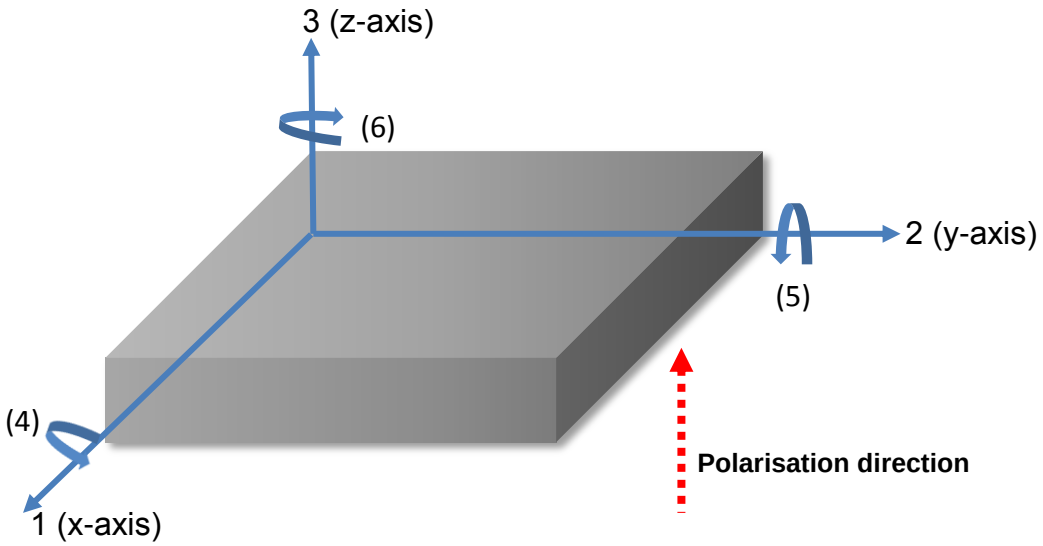

Figure 3-6 Coordinate axis for a thin piezoelectric plate poled along the thickness direction.

When subjected to low electric fields or small external stresses, piezoelectric materials are considered to exhibit a linear coupling between mechanical and electrical properties, referred as the classical linear theory of piezoelectricity [14, 15]. Non-linear theory of piezoelectricity has also been modelled and experimentally proved by a number of research studies under certain conditions such as high electric fields [16, 17]. Such conditions are not involved in this work, thus only linear coupling is discussed in the thesis. The notations and equations used here are based on the most commonly used IEEE standard of piezoelectricity [18].

For an unstressed dielectric medium, the electric displacement D is related to the electric field E by:

$$D = \varepsilon E \qquad \textbf{Equation 3-1}$$

where ε is the permittivity of the material. When placed in zero electric field, the strain S and the stress T of an elastic medium are governed by Hooke's law as follows:

$$S = sT \qquad \textbf{Equation 3-2}$$

where s is the compliance of the material.

For a piezoelectric material, the electrical and mechanical equations are combined together to describe the linear coupling relationship：

$$S_{ij} = s_{ijIJ}^{E} T_{IJ} + d_{Iij} E_I \qquad \textbf{Equation 3-3}$$

$$D_i = d_{iIJ} T_{IJ} + \varepsilon_{iI}^{T} E_I \qquad \textbf{Equation 3-4}$$

where i, j, I and J =1, 2 or 3 and d_{Iij} ,d_{iIJ} are the piezoelectric charge constants (C/N). The superscripts T and E denote that the ε_{iI} and the s_{ijIJ} are measured under conditions of constant stress and constant electric field, respectively. The pair of equations is the preferred strain-charge form of constitutive equations on piezoelectricity.

For convenience of writing, the tensors in the form of matrix arrays, a simplification of notation used in crystallography is introduced. According to the conversion shown in Table 3-1 [19], the tensor notations are reduced by replacing dual indices *ij* or *IJ* by single indices *m* or *n*.

Table 3-1 Conversion between tensor and reduced matrix notation.

Tensor notation (*ij* or *IJ)*	11	22	33	23, 32	13, 31	12, 21
Reduced matrix notation (*m* or *n)*	1	2	3	4	5	6

In this way, for example, fully denoted d_{Iij} with a 3x3x3 matrix is simplified to d_{Im} (I=1~3 and m=1~6) with a 3x6 matrix, in which the first subscript I designates the direction of the electric field while m refers to the direction of mechanic stress or

strain related to the defined coordinate system shown in Figure 3-6. For example, d_{33} relating to the change of dimension in the poling direction is known as the longitudinal piezoelectric constant and d_{31} corresponding to the displacement developed in the 1 direction perpendicular to the poling direction is called as the transverse piezoelectric constant.

The independent number of components in the matrix of each tensor can be reduced considering the symmetry relations in the material. For a piezoelectric polycrystalline ceramic material such as PZT, the poling process causes it to become anisotropic but with transversely isotropic symmetry i.e. symmetric in direction 1 and 2. Therefore, all the dielectric, elastic and piezoelectric properties relating to the 1 and 2 directions are the same and most of the coefficients in the matrix become zero by using the high degree of symmetry. The complete matrix form of Equation 3.3 and Equation 3.4 for PZT is shown as follows:

$$\begin{bmatrix} S_1 \\ S_2 \\ S_3 \\ S_4 \\ S_5 \\ S_6 \\ \hdashline D_1 \\ D_2 \\ D_3 \end{bmatrix} = \left[\begin{array}{cccccc:ccc} s_{11}^E & s_{12}^E & s_{13}^E & 0 & 0 & 0 & 0 & 0 & d_{31} \\ s_{12}^E & s_{11}^E & s_{13}^E & 0 & 0 & 0 & 0 & 0 & d_{31} \\ s_{13}^E & s_{13}^E & s_{33}^E & 0 & 0 & 0 & 0 & 0 & d_{33} \\ 0 & 0 & 0 & s_{44}^E & 0 & 0 & 0 & d_{15} & 0 \\ 0 & 0 & 0 & 0 & s_{44}^E & 0 & d_{15} & 0 & 0 \\ 0 & 0 & 0 & 0 & 0 & s_{66}^E & 0 & 0 & 0 \\ \hdashline 0 & 0 & 0 & 0 & d_{15} & 0 & \varepsilon_{11}^T & 0 & 0 \\ 0 & 0 & 0 & d_{15} & 0 & 0 & 0 & \varepsilon_{11}^T & 0 \\ d_{31} & d_{31} & d_{33} & 0 & 0 & 0 & 0 & 0 & \varepsilon_{33}^T \end{array}\right] \begin{bmatrix} T_1 \\ T_2 \\ T_3 \\ T_4 \\ T_5 \\ T_6 \\ \hdashline E_1 \\ E_2 \\ E_3 \end{bmatrix} \quad \textbf{Equation 3-5}$$

Similar to the strain-charge form, constitutive equations can also be written in the stress-charge form using the reduced notation:

$$T_m = c_{mn}^E S_n - e_{Im} E_I \quad \textbf{Equation 3-6}$$

$$D_i = e_{in} S_n + \varepsilon_{il}^S E_I$$ **Equation 3-7**

where c is the elastic constant of the material and e is the piezoelectric stress constant. ε^S is related to ε^T by the following expression:

$$\varepsilon^S = \varepsilon^T (1 - k^2)$$ **Equation 3-8**

where k is one of the most important piezoelectric parameters, known as the electromechanical coupling coefficient. It can be expressed as a measure of energy conversion efficiency by:

$$k^2 = \frac{stored\ converted\ energy}{stored\ input\ energy}$$ **Equation 3-9**

The subscripts for k are used to indicate the vibration mode of interest in the same way as explained for d_{Im}, hence the commonly used term, longitudinal coupling factor k_{33}. Specially, for a plate or a disc, the planar coupling factor k_p is used for the simultaneous vibrations in both the 1 and 2 direction and the thickness coupling factor k_t is used for thickness vibrations when the lateral dimensions are much larger than the thickness.

In the forms of the constitutive equations listed above, the loss of energy is assumed to be negligible. In fact, for a piezoelectric material placed in an alternating electric field, the dissipation of electromechanical energy, known as dielectric loss, is inherent. In the typical piezoelectric ceramic case, the domain wall motions significantly contribute to this phenomenon [20, 21]. The dielectric loss can be expressed by considering the permittivity in a complex form [22]:

$$\varepsilon = \varepsilon' - j\varepsilon''$$ **Equation 3-10**

where ε' is the real part of the permittivity and ε'' is the imaginary part. The dielectric loss factor *tan* δ is defined by the ratio of ε'' and ε' as:

$$\tan\delta = \frac{\varepsilon''}{\varepsilon'} \qquad \textbf{Equation 3-11}$$

Similarly, a complex elastic stiffness c is introduced to describe the mechanical loss as:

$$c = c' - jc'' \qquad \textbf{Equation 3-12}$$

where c' is the real part of the stiffness and c'' is the imaginary part. The mechanical quality factor Q_m is given by the ratio of c' and c'' as:

$$Q_m = \frac{c'}{c''} \qquad \textbf{Equation 3-13}$$

It is generally observed that for a piezoelectric material driven off-resonance, the heat generation is primarily caused by the dielectric loss; whilst when driven at the resonance frequency, the mechanical loss mainly accounts for the heating [21].

3.1.5 Electrical impedance

Electrical impedance, Z_e, a measure of the opposition to AC (alternating current), is another key property for piezoelectric materials. It is a complex quantity where the real part is the resistance R (the opposition to DC) and the imaginary part is the reactance X (the opposition to the change of voltage and current). Z_e of a material is described by the magnitude of Z_e, $|Z_e|$, and phase, θ as follows [23]:

$$|Z_e| = \sqrt{R^2 + X^2} \qquad \textbf{Equation 3-14}$$

$$\theta = \arctan\frac{R}{X} \qquad \textbf{Equation 3-15}$$

The reactance here is a combination of inductive and capacitive reactance. For transducer applications, the electrically insulating piezoelectric substrate with electrodes on both major surfaces can be considered as a parallel capacitor, and the capacitive reactance X_C of it is the major concern for the calculation of the electrical impedance [24, 25]. X_C can be given by the following expression:

$$X_C = \frac{1}{2\pi fC} \qquad \textbf{Equation 3-16}$$

where C is the capacitance. For a plate-like capacitor, C is defined by:

$$C = \frac{A\varepsilon}{h} = \frac{A\varepsilon_0\varepsilon_r}{h} \qquad \textbf{Equation 3-17}$$

Where A is the active electrode area, h is the thickness of the plate, and ε_0 and ε_r are the permittivity of the space and relative permittivity (also called dielectric constant), respectively. Based on the above discussion and equations, it can be identified that the electrical impedance for a given piezoelectric substrate in a transducer is a function of the driving frequency and the relative permittivity of the material.

Figure 3-7 shows electrical impedance and phase plot versus frequency for a piezoelectric ceramic vibrating along the thickness direction in air with no damping layer attached. The abrupt change of electrical impedance at resonant frequencies, where the vibration of the material approaches its maximum, is a distinguishing characteristic of piezoelectric materials compared with other capacitors. The frequencies corresponding to the minimum and maximum values of $|Z_e|$ on the plot are referred to as resonant (or electrical resonant) frequency, f_r, and anti-resonant (or mechanical resonant) frequency, f_a, respectively. Accordingly, the phase angle abruptly rises to a maximum value close to 90° between the resonance and anti-

resonance where the electrical equivalent is inductive [26]. While at frequencies below f_r or higher than f_a, the piezoelectric material behaves like a capacitor with the phase angle of -90°. The electrical impedance spectra can be used to identify the vibration mode of the piezoelectric element, and the presence of any unwanted modes occurring near the frequency of interest suggests that the sensitivity and bandwidth of the transducer may be compromised [27].

Most of the important material parameters discussed in Section 3.1.4, can be calculated based the electrical impedance spectra according to MacLennan [28], providing only the thickness resonance mode is considered. The relations for the calculations which were used in this work for characterisation purposes are listed in the Appendix I.

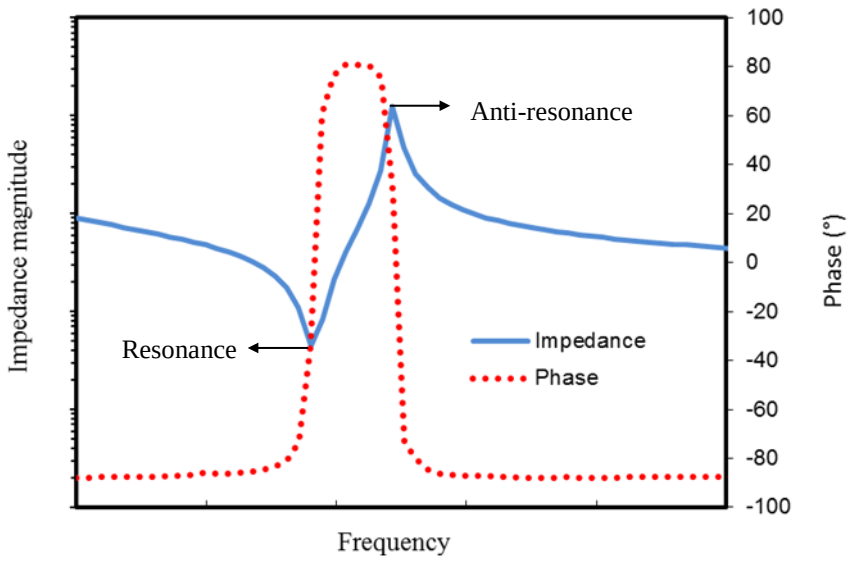

Figure 3-7 Electric impedance magnitude and phase diagram as a function of frequency for a poled piezoelectric ceramic. The impedance is plotted on the logarithmic scale.

3.2 Piezoelectric materials for high frequency ultrasound

3.2.1 Specific requirements

For optimum performance of ultrasonic transducers, the requirement of the active piezoelectric elements is a complex combination of elastic, dielectric and piezoelectric properties. Among those, there are several crucial factors that need to be taken into account primarily in choosing the active material, summarised from [3, 29, 30]:

1) In order to efficiently convert the electrical energy to acoustic energy and vice versa, the effective electromechanical coupling coefficient k_{eff} should be high, ideally close to 1;
2) In order to minimise energy loss during the propagation of ultrasound, the acoustic impedance Z_a should to be as close as possible to that of human tissue (~1.5 MRayl for soft tissues), as explained in Chapter 2. The less the

mismatch in Z_a, the higher the intensity of transmitting wave, hence the stronger signal;

3) For electrical signal transmission, the permittivity of the material is desired to be large so that the electrical impedance can be matched with the imaging instrumentation circuitry.
4) Both mechanical and dielectric losses should be small to achieve good sensitivity.
5) The piezoelectric material needs to be machinable with a relatively low cost, and ideally should also be mechanically flexible to facilitate the production of focused transducers without the need for lenses.

Table 3-2 gives a comparison of the key properties of different types of piezoelectric materials used for ultrasound imaging applications. The desirable characteristics and drawbacks of these materials are further discussed in the following sections.

Table 3-2 Comparison of material properties of piezocoelectric materials for medical ultrasound transducers.

Material type	PZT-based ceramic	Piezopolymer	Single crystal	1-3 composite
Representative example	PZT-5H	PVDF	PMN-33%PT	30 vol% PZT-5H/epoxy
k_t	0.50	0.15	0.58	0.66
k_{33}	0.75	N/A	0.94	N/A
Z (MRayl)	34	3.92	36.9	12
$\varepsilon^s_{33}/\varepsilon_0$ (Clamped)	1470	5	797	428.5
Q_m	65	13	50	N/A
$tan\ \delta$	0.02	0.25	0.0036	N/A
Flexibility	Poor	Excellent	Poor	Good
Cost & Ease of fabrication	Excellent	Excellent	Poor	Medium
References	[31]	[32]	[33, 34]	[28]

3.2.2 PZT-based piezoelectric ceramics

Among the many available piezoelectric materials, PZT-based piezoceramics are the most commonly used materials in medical imaging transducers. Their popularity comes from their superb properties such as a high electromechanical coupling coefficient, a high dielectric constant and a moderate dielectric loss. By doping PZT with other elements such as Nb, La and Nd, piezoelectric and dielectric properties can be adjusted for specific applications [35-37]. Among various available compositions, PZT-5H type with high k_{33} and ε_r is the mainstay for ultrasound transducers [38].

Nevertheless, PZT-based ceramics possess acoustic impedances over 30 MRayl, making it difficult to achieve a good acoustic impedance match, which has to be compensated by applying one or multiple matching layers. Additionally, due to their

brittle nature, they cannot be easily formed into focused geometries. Another disadvantage lies in that PZT contains lead, which has recently caused serious environmental concerns.

3.2.3 Piezoelectric polymers

Since the exceptional piezoelectric properties of polyvinylidene fluoride (PVDF) discovered by Kawai in 1969 [39], there have been continuous investigations into the use of polymers for ultrasound transducers [40, 41] . PVDF was the first widely used and also the most popular piezoelectric polymer. This kind of material offers several notable advantages for application in ultrasound transducers. Besides being inexpensive, as a polymer, it is inherently flexible and can be easily formed into a variety of shapes to suit different requirements of transducer design. Moreover, it has a low acoustic impedance which is much more matched to human tissue compared with ceramics and therefore no matching layers are required. However, the electromechanical coupling coefficient of PVDF is significantly lower than those of ceramics and composites as seen in Table 3-2, resulting in much poorer overall sensitivity. In addition, the low dielectric constant and high dielectric loss of PVDF also limits its application in transducers.

3.2.4 Piezoelectric single crystals

Although single crystal piezoelectric materials have been known since the discovery of piezoelectricity in quartz and Rochelle salt, they have had very limited use in ultrasound transducers as they were found to have much lower piezoelectric activity than PZT [42]. The recent advances in developing relaxor-based ferroelectric single crystals with excellent piezoelectric properties have attracted renewed interest in these materials [42, 43].

A few examples of these materials are lead magnesium niobate and lead titanate (PMN-PT) and lead zirconate niobate and lead titanate (PZN-PT). Like PZT, they have perovskite structures and their piezoelectric properties reach peak values near MPBs due to the existence of multiple phases [44].

Compared with traditionally used PZT, the main advantages of these single crystal materials are their giant-piezoelectric characteristics, including large electromechanical coupling factors, especially k_{33} values > 0.9, and high piezoelectric constants, which offer improvements in both sensitivity and bandwidth [45, 46]. Recently, a PMN-PT single element transducer that works at frequencies up to 44 MHz has been reported [47]. However, due to difficulties in the crystal growth process, they suffer from small yield and thus high cost [34]. Also, they are brittle and have difficulties in being curved for focused transducer designs and being cut into small elements for arrays. Additionally, their high acoustic impedance, close to that of PZT, is not desirable for tissue imaging.

Other single crystals based on lead-free materials such as lithium niobate (LNO) also exhibit high coupling coefficients, though lower than those of PMN-PT and PZN-PT, but comparable with PZT. LNO has been used for high frequency transducers operating in the 50-100 MHz range [48] but its low dielectric constant and high acoustic impedance creates problems in electrical and acoustic matching.

3.2.5 Piezoelectric composites

As discussed above, several inherent limitations in the single phase piezoelectric materials, either ceramics, single crystals or polymers, restrict their extensive use and growth potential in ultrasonic imaging applications. Piezoelectric composites or

piezocomposites are designed to combine two different materials, typically a piezoelectrically active ceramic and a passive non-piezoelectric polymer, thereby taking the advantages of desirable properties in both phases. Since their concept was developed by Newnham in 1970s [49], piezocomposites have become widely used in commercial medical ultrasound imaging transducers [50].

Connectivity of a piezoelectric composite is of great importance as it determines the manner in which the constituent materials couple with each other and hence governs the overall electromechanical properties. The geometry arrangement of the two component phases within a composite is generally denoted by X-Y, where X and Y are the connectivity of the ceramic and polymer respectively and each phase can be self-connected or continuous in zero, one, two or three dimensions. There are ten connectivity pattern types: 0-0, 0-1, 0-2, 0-3, 1-1, 1-2, 1-3, 2-2, 2-3, 3-3. In particular, 1-3 piezocomposites shown in Figure 3-8 consisting of one-dimensionally connected piezoelectric ceramic pillars surrounded by a three-dimensionally continuous polymer matrix is the prevalent form for constructing ultrasound transducers.

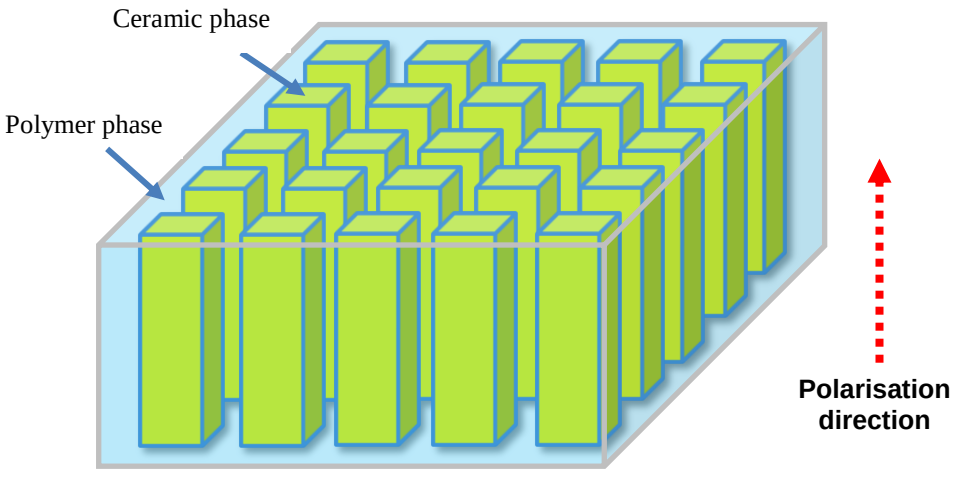

Figure 3-8 Schematic illustration of a typical 1-3 piezocomposite consisting of regularly arranged active piezoelectric pillars embedded in a polymer matrix.

1-3 Piezocomposites offer a number of distinctive benefits for medical ultrasound applications. In contrast to conventional piezoceramics, piezocomposites provide an enhanced coupling factor as the higher k_{33} of the piezoelectric pillars is utilised and a reduction of unwanted resonance modes as the lateral vibrations are suppressed by the polymer matrix. Moreover, they have low acoustic impedance due to the existence of the polymer phase, allowing better acoustic matching to tissues. The improved piezoelectric and acoustic properties lead to an increase in sensitivity and bandwidth. Also, such piezocomposites are much more flexible than the single-phase piezoelectric ceramics and therefore can be curved for different focusing geometries. A further advantage is that by adjusting the selection of constituent materials, composite configurations and the design parameters such as the volume fraction and the shape of the piezoelectric pillars, the overall properties of piezocomposites can be tailored over a wide range to meet specific requirements for different applications. The main drawback of piezocomposites lies in the relatively high manufacturing cost and complexity, especially when ultra-fine spatial scales of piezoelectric pillars are required to produce materials for high frequency applications over 30 MHz.

Of all the piezoelectric materials available, piezocomposites achieve the best compromise between energy conversion efficiency and acoustic impedance. Due to their excellent tailorable properties, piezocomposites have now replaced monolithic piezoelectric materials and become dominant in many medical ultrasound transducer applications including single element and arrays.

3.3 Design considerations of 1-3 piezocomposites

For a particular application, all the merits of a 1-3 piezocomposite might not be achieved simultaneously. In order to maximise its performance, the compositions and

geometric dimensions of a piezocomposite need to be appropriately designed for the target performance. Each of the key property requirements discussed in Section 3.2.1 appears to be individual but actually correlates with each other, forming an intricate network. The following steps give a clear picture that shows how design choices are made in a sequence, summarised from the work reported by Smith et al. [51] and Clipsham [52]:

1) Choose the constituent materials and adjust their proportions to optimise the effective properties of the composite;
2) Define the thickness of the piezocomposite, according to the target operating frequency and the velocity of sound in the composite;
3) Choose the height-to-width aspect ratio and calculate the width of piezoceramic pillar and the inter-pillar spacing (kerf);
4) For a more targeted specification, finite element modelling (FEM) methods such as PZFlex [53] are used. Further adjustments on the volume fractions and spatial scale are made according to the results such as the electrical impedance obtained from FEM.

3.3.1 Effective properties and volume percentage

In the design of piezocomposites, the composite material can be considered as a homogeneous medium with new effective properties. The overall performance of the transducer can be then predicted from the calculation of effective properties of the piezocomposite active material. The most commonly used model for designing 1-3 piezocomposites was proposed by Smith et al. [54].

As an illustration of this model, it is useful to consider an example. Assume a piezocomposite is composed of a routinely used PZT-5H type ceramic (TRS 610,

TRS Technologies, USA) and Epofix epoxy resin (Struers, Solihull, UK) [55], the combination of which has been proven to be capable of achieving desirable properties [56, 57]. The detailed calculation process based on the model as well as the relative parameters of the two constituents is shown in the Appendix II. The calculated effective thickness coupling coefficient ($\overline{k_t}$) and acoustic impedance of the piezocomposite ($\overline{Z_a}$) are plotted against the volume percentage of PZT (V_c) as shown in Figure 3-9. It can be seen that the variation of $\overline{k_t}$ is very small over a wide range of the volume percentage of PZT except for the two extremes when V_c is less than 20% or higher than 80%. At the lower end, the large amount of elastic loading stiffens the ceramic pillars, resulting in reduced values of $\overline{k_t}$. While at the higher end, the pillars are laterally clamped by the epoxy matrix, causing the decrease of $\overline{k_t}$ [54]. The acoustic impedance of the piezocomposite increases nearly linearly with the volume percentage of PZT. Decreasing the ceramic volume percentage lowers the acoustic impedance but possibly at the expense of a reduction in the electromechanical coupling factor. Therefore, a trade-off between high $\overline{k_t}$ and low $\overline{Z_a}$ has to be achieved. For the combination of the TRS 610 ceramic and the Epofix filler, it can be roughly determined from Figure 3-9 that the ceramic volume percentage is desired to be in the range of 30%-50% to achieve a good acoustic match without losing sensitivity.

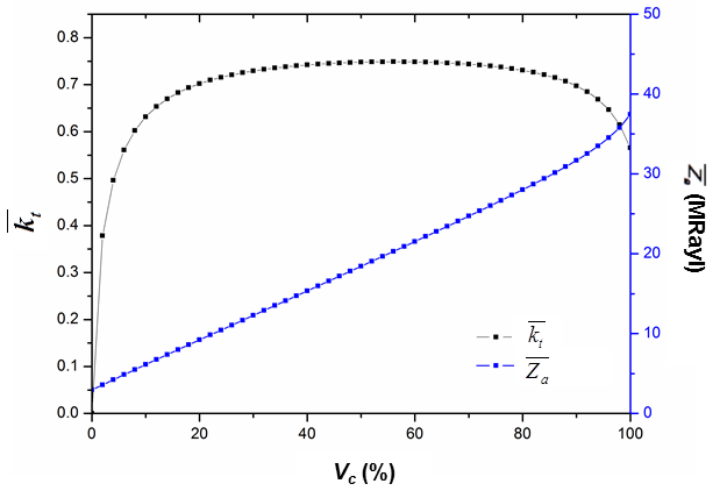

Figure 3-9 Effective thickness coupling coefficient $\overline{k_t}$ and effective specific acoustic impedance $\overline{Z_a}$ of the piezocomposite made up of TRS 610 ceramic and Epofix epoxy resin versus the volume percentage of the ceramic phase (V_c).

3.3.2 Spatial scale and resonance modes

The spatial scale of the piezocomposite plays a vital role in the performance of the transducer as it is closely associated with the resonances generated in the composite. The thickness resonance of the composite is of significant interest in this study as it is exploited for transmitting and receiving ultrasound waves. As discussed in Chapter 2, an ultrasound wave travelling across the active element is partially reflected back and reverberates internally in the thickness direction from one face to the other and then back to the starting point. The thickness resonance occurs when the reflected wave, finishing a round trip, is exactly in phase with the original wave cycle and adds constructively to it, resulting in increased amplitude and prolonged vibrations [58]. The condition of the thickness resonance is firstly met when the thickness of the piezoelectric element, h, is equal to a half-wavelength of the ultrasound wave, $\lambda/2$. The fundamental thickness mode frequency, f_t, that corresponds to half of the wavelength thickness can then be determined by substituting $\lambda=2h$ into Equation 2-1 and rearranging to give:

$$h = \frac{v}{2 f_t}$$ **Equation 3-18**

where v is the longitudinal velocity of sound in the piezoelectric material. For a piezocomposite, when the volume percentage (V) of the ceramic phase is determined, the longitudinal velocity of it can be approximately estimated from the following expression, known as the rule of mixtures:

$$v_{comp} = v_c V_c + v_p V_p$$ **Equation 3-19**

where the subscripts *comp*, *c* and *p* denote the composite, ceramic and the polymer. Using v_c to be ~4000 m/s, v_p to be ~2000 m/s and V_c to be 50%, v_{comp} is calculated to be 3000 m/s [59].

For the most efficient electromechanical conversion, ultrasound transducers are preferably driven at the fundamental thickness resonance frequency, which in turn defines the thickness of the piezoelectric element. By substituting the calculated v_{comp} value and the targeting frequency into Equation 3-18, the required thickness of the composite is obtained. Using v_{comp} value of 3000 m/s, a composite thinner than 50 μm is required for frequencies over 30 MHz.

Following the determination of the thickness, or the pillar height, the required pillar width can be then calculated based on the aspect ratio (pillar height to pillar width). Investigations have been carried out specifically on the effect of the pillar aspect ratio on the performance of the piezocomposite with various pillar shapes [60, 61]. The results all show a similar trend in that the reduction of the pillar aspect ratio leads to the deterioration of the fundamental thickness mode coupling. For a piezocomposite with a given ceramic volume percentage, it is found that the lower the pillar aspect ratio, the more strongly the coupled lateral modes and thus the more difficult to detect

a reliable thickness resonance [61]. In practice, it is generally considered that an aspect ratio greater than 2 is necessary for a piezocomposite to produce the correct pulse response, and an aspect ratio greater than 5 is preferred to maximise electromechanical conversion efficiency [62].

For a periodically arranged pillar pattern, such as square or hexagonal packed pillars, the inter-pillar spacing or kerf can be calculated from the determined ceramic percentage and pillar width. It is essential to make sure the obtained kerf value to be 'sufficiently fine' to keep away from the interference of any spurious resonances. These spurious resonances are caused by laterally propagating Lamb waves (described in Section 2.3.2) being resonantly reflected in the periodic array of pillars [63-65]. If these resonances are in the vicinity of the thickness mode resonance of a piezocomposite, they would cause significant degradation of its performance by severely distorting the desired 'piston-like' vibrations.

Gururaja et.al studied the propagation of the lamb waves in piezocomposites and confirmed the existence of two spurious modes [65]. A square array of square pillars is used here for illustration as shown in Figure 3-10. For either of the modes, the resonance frequency (f_{l1} and f_{l2}) is inversely proportional to the inter-pillar spacing [66] as defined in Equation 3-20 and 3-21.

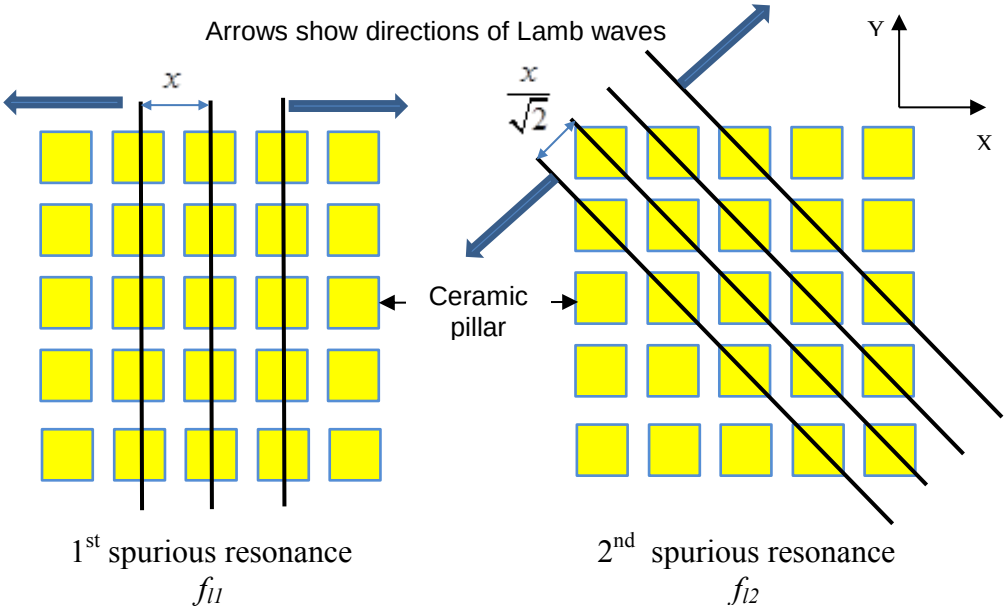

Figure 3-10 Schematic illustration of the generation of spurious resonances on the surface of a piezocomposite consisting of square ceramic pillars (adapted from [66]).

$$f_{l1} = \frac{v_{phase}}{x} \qquad \textbf{Equation 3-20}$$

$$f_{l1} = \frac{\sqrt{2}v_{phase}}{x} \qquad \textbf{Equation 3-21}$$

where v_{phase} is the phase velocity of lamb waves, which is typically 800-1500 m/s for 1-3 piezocomposites [67]. In order to obtain a broadband frequency response around the thickness mode resonance, the lowest lateral resonance is generally expected to be more than twice the thickness resonance [50], i.e. $f_{l1} > 2f_t$, which drives the spacing of the pillars to be much smaller than the thickness of the pillars. In fact, the kerf is the smallest dimension in the piezocomposite.

Table 3-3 gives the calculated dimensions and aspect ratios of a 1-3 piezocomposite with square packed square pillars having a 50% volume percentage. It can be seen that as frequency increases, all the dimensions of the piezocomposite dramatically decrease. In particular, for a relatively low pillar aspect ratio of 3, piezocomposites

operating at over 30 MHz requires a very fine kerf of <7 μm, which actually poses the greatest challenge in the fabrication process. It must be noted that although the finished composite requires an aspect ratio >2, during the initial stages of manufacture considerably larger aspect ratios need to be achieved in order to allow sufficient tolerances for the subsequent process steps as discussed further in Section 4.1.

Table 3-3 The dimensions and aspect ratios of a piezocomposite with a 50% ceramic volume percentage for different frequency applications. The calculations are based on square pillars with square configuration and a composite longitudinal velocity of 3000 m/s.

Frequency	Thickness (μm)	Pillar width (μm)	Kerf (μm)	Pillar aspect ratio	Kerf aspect ratio
10 MHz	150	50	21	3	7
30 MHz	50	17	7	3	7
50 MHz	30	10	4	3	7.5

3.3.3 Novel random piezocomposite design

With increasing operating frequency, the difficulty in fabricating fine-scale piezocomposites increases, especially the challenge to obtain very small pillar and kerf dimensions. Therefore, alternative solutions to the suppression of the spurious resonances have been developed, for example by employing triangular pillars [68]. Yin et al. [69] and Yang et al. [70] have also suggested that the highest level of geometrical complexity would suppress the lateral modes to the greatest degree. However, only semi-randomised pillar designs with a combination of simple geometries have been fabricated and reported and the lateral resonances of the resulting piezocomposites still existed, though with reduced effect on the thickness mode [70].

Recently, a novel randomised piezocomposite design employing a distribution of ceramic geometries, dimensions and separations has been proposed by Démoré et al.

[71]. Finite element analysis of these composites has suggested that they are capable of spreading any spurious modes over a broad frequency range, hence effectively eliminating the influence of lateral resonances whilst maintaining high functional performance. Another advantage of this composite design is that the irregularly shaped ceramic structures are less likely to tilt or fall over during fabrication due to the improved structural stability of the ceramic segments.

The novel pattern of random distributed ceramic for the piezocomposite was generated using an algorithm based on a correlation length, adapted from [72]. As shown in Equation 3-22 and 3-23, a randomised spatial frequency distribution Γ is given by a modified Gaussian distribution *G(s)* with a correlation length *a* and a random phase component *P(s)*.

$$G(s) = s^2 e^{-\pi^2 a^2 s^2} \qquad \textbf{Equation 3-22}$$

$$\Gamma(s) = G(s)\cos(P(s)) + G(s)\sin(P(s)) \qquad \textbf{Equation 3-23}$$

where *s* represents spatial frequency domain matrix, which is determined by the designed composite size and the spatial resolution required in the pattern. The random phase component provides a random number for each spatial frequency value. A spatial domain distribution is generated from the real part of the inverse Fourier transform of Γ. A binary pattern is obtained by applying a threshold value to the distribution. The nominal feature size of the composite is controlled by the input correlation length, *a*, and the ceramic volume fraction is controlled by the applied threshold value. A flow chart illustrating the pattern design process is presented in Appendix IV.

Figure 3-11 depicts a binary pattern with a ceramic volume percentage of 40 vol% and Figure 3-12 shows the impedance spectra of this pattern with a thickness of 40 µm calculated by PZFlex as reported in [71], with no evident spurious modes present. The features required for this design for implementation at over 30 MHz are ~2-50 µm. At the commencement of the work reported in this thesis, no attempts to fabricate such a complex composite design had been reported.

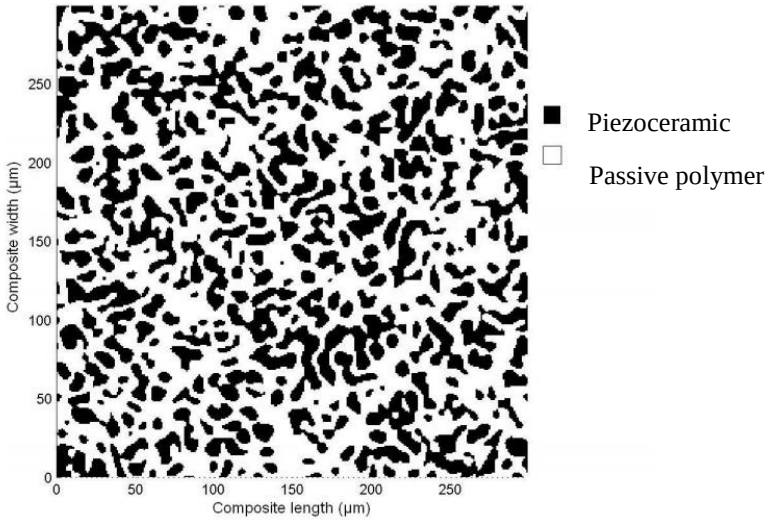

Figure 3-11 Randomised composite pattern with 40 vol% piezoceramic [71].

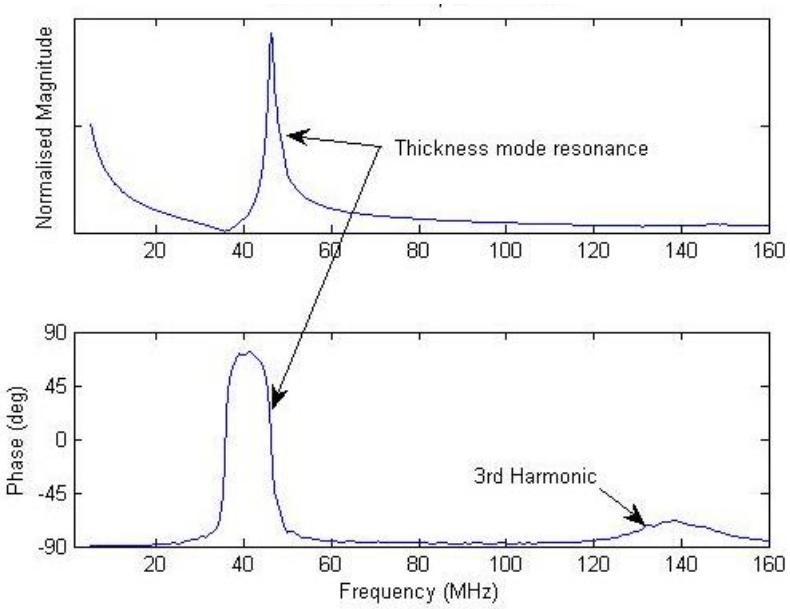

Figure 3-12 Calculated electrical impedance spectra for the randomised composite with the pattern design shown in Figure 3-11 and the thickness of 40 µm [71].

3.4 Fabrication routes for 1-3 piezocomposites

With traditional 1-3 piezocomposite designs of periodically arranged and regularly-shaped pillars, ultrafine spatial scales of ceramic pillars are desired as illustrated in Table 3-3 with pillar widths <17 μm and kerf values <7 μm to push the ultrasound operating frequency to over 30 MHz for the improvement of imaging resolution. With the novel random design discussed above, these ultrafine-scale restrictions are relaxed as relatively large ceramic segments with lateral dimensions of ~30-50 μm are allowed to be in the design but micro-sized ceramic segments with lateral dimensions down to a couple of microns are required, in addition to the requirements of various geometries and separations, which significantly challenge the fabrication methods of 1-3 piezocomposites.

Manufacturing of a piezocomposite involves a number of steps. Typically, it starts from producing a so called bristle-block structure consisting of tall and thin ceramic pillars upstanding from a ceramic block as depicted in Figure 3-13, followed by infiltrating the bristle block with a polymer matrix and lapping the resultant intermediate composite to a required thickness.

A rich variety of fabrication routes have been developed with the main differences lying in the methods for the production of the bristle-block structure. Their processing characteristics, current capabilities, along with advantages and limitations are discussed below.

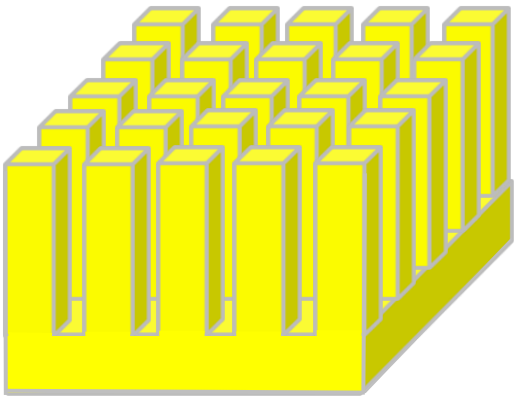

Figure 3-13 Schematic representation of a bristle-block structure.

3.4.1 Dice and fill

The dice and fill technique is now predominately used for 1-3 piezocomposites fabrication in the manufacturing industry due to its simplicity [73]. In this approach, a dense sintered ceramic block with the desired properties is chosen as the starting material. A series of parallel grooves are cut into it by means of a precision dicing saw, followed by a second set of parallel cuts made in the perpendicular direction to give a bristle-block structure. The main stages in this technique are illustrated in Figure 3-14. In addition to the production of commonly used square pillars, the dice and fill method has also been used to produce triangle [68] and hexagonal pillars [74] by making three sets of grooves into the ceramic block.

The dice and fill technique is sufficient for fabricating piezocomposites operating up to 20 MHz [68], however, for higher frequency applications, it becomes significantly difficult due to several limitations. First, the smallest kerf achieved from this method is limited to the width of the saw blade at around 15 μm [75] and dicing using such thin blades suffers from high tooling cost as well as long processing time. Second, it is challenging to make the pillar width smaller than 100 μm, considering the brittleness of the ceramic pillar and the size of the defects (~50 μm) in conventionally

pressed ceramic blocks [59, 75], resulting in unacceptable manufacturing yields. To achieve finer spatial scales, alternative dicing methods have been developed such as laser [76] and ultrasonic machining [77]. However, they are rather time-consuming and inevitably encounter the problem of cross-section tapering [73, 75]. The other disadvantage of the dice and fill technique is that only straight channels can be produced and thus pillar shapes are limited to simple geometries.

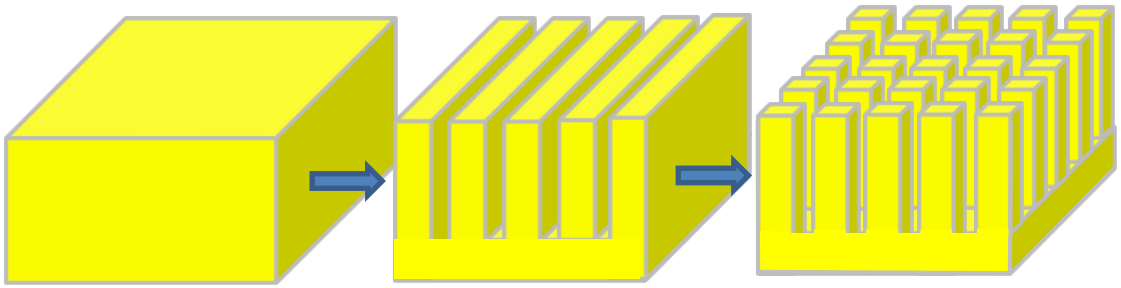

(a) Ceramic block (b) Cuts in 1st direction (c) Cuts in 2nd direction

Figure 3-14 Schematic illustration of the method to create the bristle-block structure in the industry standard dice-and-fill route, where a set of parallel grooves were cut into a ceramic block, followed by a second set of cuts in a perpendicular direction.

3.4.2 Injection moulding

Injection moulding, well-known for its advances in the plastics industry for the production of complex-shaped components, is employed as a commercial alternative method to dice and fill for 1-3 piezocomposite fabrication. In this process, a piezoceramic powder is thoroughly mixed with a polymer binder to produce a thermoplastic mixture that can be liquidised at elevated temperatures and pushed into a cold mould with required shaped cavities under high pressure. After cooling, the moulded structure is released from the mould and then heated for binder removal and sintering. Such a process would allow the piezocomposites to have more complex ceramic geometries than those made from dice and fill.

However, for the fabrication of fine-scale piezocomposites, demoulding is challenging for the pillars with pitch sizes smaller than 50 μm [62] and the need for a metal mould with a small cavity size leads to long production cycle and high manufacturing cost. Other disadvantages of injection moulding include the facts that ceramic pillars made by this method are severely tapered and generally show a low volume fraction [78, 79].

3.4.3 Lost mould techniques

In comparison to injection moulding, lost mould routes utilise sacrificial moulds made from a selection of materials, and combine versatile mould filling techniques, such as casting ceramic slurry and embossing ceramic dough, without being limited by expensive injection systems and metal moulds. Figure 3-15 depicts the three important stages of the lost mould technique for the fabrication of the bristle-block structure - mould filling, drying and mould removal. A wide range of shapes and dimensions of ceramic components can be produced by these techniques, dependent on the mould being used; however, each mould can only be used once, requiring moulds to be of relatively low-cost.

Since the pioneering work of Siemens Corp. [80], the lost mould technique has been under continuous development. Different combinations of mould materials, mould filling and mould removal techniques have given rise to the development of a variety of lost mould routes as summarised in Table 3-4. Among them, viscous polymer processing (VPP), combined with a chemical dissolution technique for mould removal, has been shown to have the ability to produce fine ceramic segments with kerf sizes down to 4 μm, as seen in Figure 3-16, and shows more promise than other routes. This technique has been investigated for the realisation of novel random patterns but

the ceramic scale was limited by the ability to produce a mould of the desired shape [71].

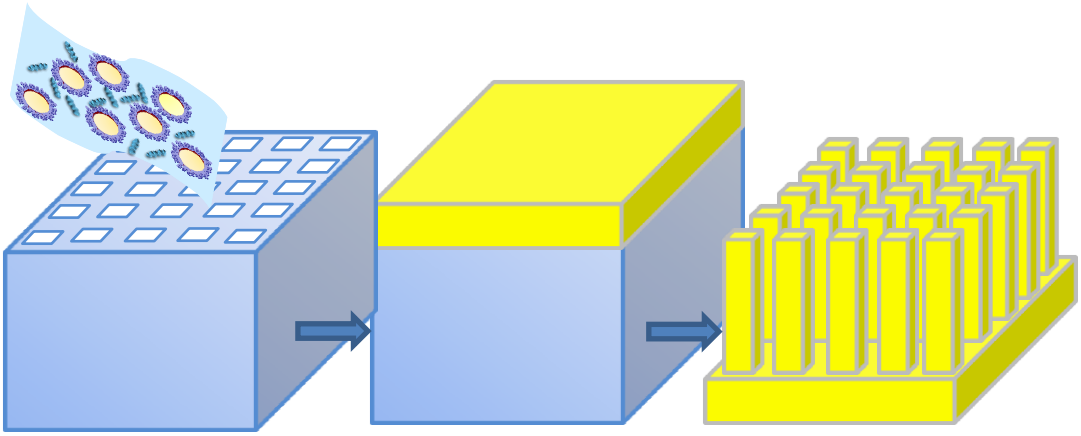

(a) Fill the mould with a ceramic/binder system

(b) After drying

(c) After removal of the mould

Figure 3-15 Schematic illustration of the lost mould technique for the production of a bristle-block structure. (a) Fill the mould with ceramic powder and binder(s); (b) After drying, a green-state ceramic stock is formed on the mould surface; (c) the resulting structure after the removal of the mould and sintering.

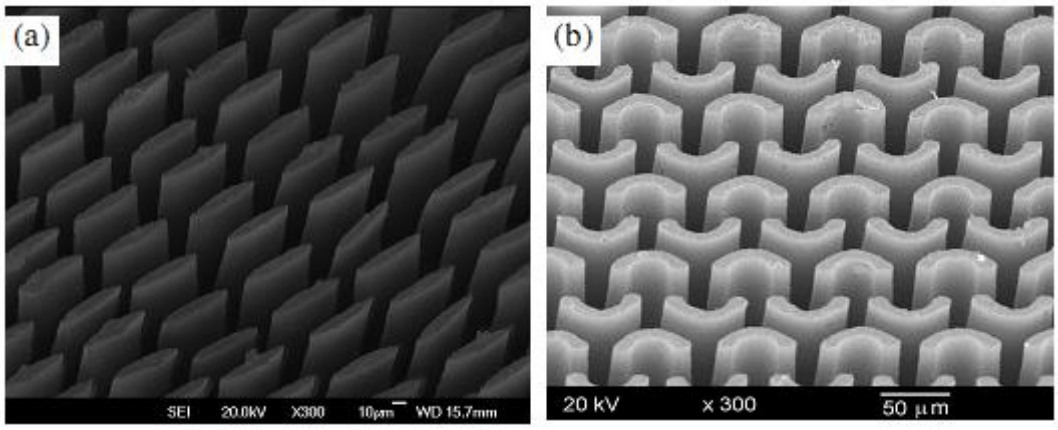

Figure 3-16 Green-state PZT structures: (a) ellipses and (b) arcs fabricated by viscous polymer processing (VPP) combined with lost polymer moulds [71].

Table 3-4 Characteristics and capabilities of current lost mould techniques.

Processing characteristics			Resulting piezocermic segments					Comments	Ref.
Mould material	Mould filling	Mould lost technique	Shape	Width (μm)	Height (μm)	Kerf (μm)	Aspect ratio		
Polymer	Casting PZT slurry	Burnout	Hexagonal	50	400	50	8	pillars < 20 μm distorted by the viscous flow of polymer mould during burnout	[81-83]
Polymer	Injecting PZT slurry	Plasma etching mould before sintering	Square circular	25	60-180	-	2.5-7	Low aspect ratio, slow process and high cost.	[82, 84]
Silicon	Casting PZT slurry	Plasma etching mould after sintering	Square	7	90	12	~12	Possible chemical reaction between PZT and Si occurred during sintering; High cost.	[82]
Polymer	Embossing PZT viscous polymer dough	Chemical dissolution	Hexagonal square circular	10-50	50-850	7-100	2-10	High viscosity system, high moulding pressure, limited by the strength of the mould at small sizes.	[62, 71, 85-87]
			Ellipse Arc	**≥8**	100	**≥4**	**~12**		

3.4.4 Soft-moulding route

Soft moulding shares the basic idea of micro-replication with lost mould techniques but is a more cost-effective process as it utilises a reusable soft polymer mould that is not destroyed during the demoulding process. The core stages in soft moulding are similar to those depicted in Figure 3-15 and the mould filling generally involves casting ceramic slurry, and the mould removing step specifically refers to peeling off of the soft polymer mould.

The soft elastomeric mould used in this route is replicated from a master mould with the desired bristle-block structure. The master mould can be fabricated using a range of microsystem techniques such as micromachining, photolithography, e-beam writing, chemical or plasma etching. An elastomer is poured against the master, hardened and peeled off to yield a soft mould. Among various candidates, the most commonly used elastomer is poly(dimethylsiloxane) (PDMS) which allows the replication of master structures down to nanometer accuracy due to its excellent flexibility [88]. PDMS has a low interfacial energy and excellent chemical stability which minimises adherence to the master moulds and reaction with molecules or polymers from the materials being moulded [89]. The optical transparency of the PDMS mould is also particularly useful as it allows observation of the moulded material by eye or under a microscope.

The master mould can also be reused to produce numerous soft moulds and each soft mould can be used to transfer the pattern many times without deterioration, which results in a highly scalable and economic process. The actual usage life of the master and soft moulds depends on a variety of factors including the geometry, the dimension and the aspect ratio of the desired structure, and the operator's skill. Finer scales and

the higher aspect ratio of the ceramic structures generally make the demoulding process more difficult. To maintain the integrity of fine-scale ceramic segments, high green strength is a key advantage.

Stake et al. in 1998 initially introduced the soft moulding process for the fabrication of piezocomposites and reported successful manufacture of 1-3 composites with variable pillar shape, size and arrangement [90-92]. However, their relatively coarse scale with lateral dimensions of pillars in the range of 48-145 μm, aspect ratio ~5 and kerfs over 36 μm made these composites unsuitable for high frequency applications.

In 2011, Olhero et al. reported using a gel casting approach for the soft moulding of PZT pillar structures [93]. They used the sintered VPP-processed bristle blocks with ellipsoidal and semi-circle shaped pillars as shown in Figure 3-16 as the master moulds. The green-state ceramic structures with lateral features smaller than 8 μm and aspect ratios over 10 were successfully demoulded from the PDMS moulds without defects, as shown in Figure 3-17, by taking advantage of the newly developed gel casting system. The soft-moulding process combined with the gel casting technique has been shown to be well-suited for 1-3 piezocomposites fabrication and opened up new possibilities for fabricating pillar arrays with variable configuration and geometry, high aspect ratios and fine-scale features at the micron level.

The capabilities of all of the soft-moulding and lost mould techniques are primarily dependent on two factors, one being the structure of the mould, the other being the ability of the ceramic/binder system to survive the demoulding process. A variety of methods for the fabrication of thick and high-aspect-ratio moulds are reviewed in

Chapter 4 and the gel casting system as a promising ceramic/binder candidate is discussed in the following section.

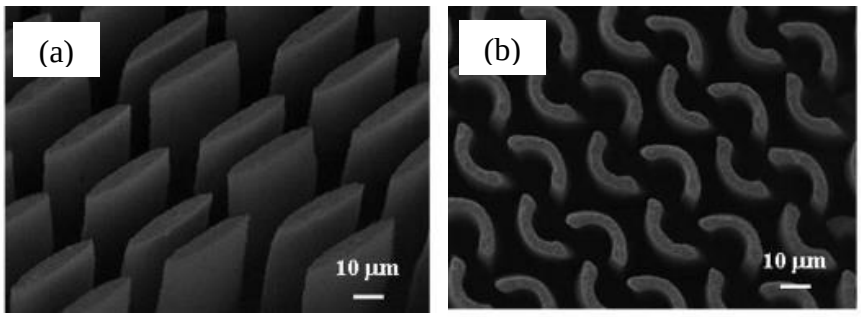

Figure 3-17 Green-state PZT structures: (a) ellipses and (b) arcs fabricated by the soft moulding route combined with a novel gel casting system, employing the sintered structures as shown in Figure 3-16 as the master moulds [93].

3.5 Gel casting technique

Wet or colloidal processing has been proved to be one of the most promising approaches for manufacturing ceramic bodies with high quality and improved reliability [94]. The core feature of colloidal processing lies in the solidification of well-dispersed suspensions into dense and homogeneous green bodies. In previous decades, different colloidal consolidation techniques have been investigated, among which, gel casting has drawn the continuous attention of scientists and technologists.

Gel casting is an attractive near net-shape technique to fabricate complex-shaped, homogeneous ceramic bodies. The principle gel casting process was originally developed in Oak Ridge National Laboratory (Oak Ridge, USA) by Omatete and Janney during the 1980s and is based on a synthetic idea originated from conventional ceramics and from polymer chemistry [95, 96]. The most common gel casting process involves dispersing ceramic powders in a solution containing a monomer, crosslinker, initiator and catalyst to form a castable slurry with high solids loading, which is subsequently poured into an appropriately designed mould and rapidly solidified in-

situ to form a green body with the shape of the mould. The gelled part is removed from the mould after gelation and then dried under controlled conditions to remove the solvent, followed by binder removal and sintering stages as applicable to other ceramic processing routes. Both organic and aqueous dispersing media can be used for gel casting, but the aqueous system is preferred.

3.5.1 Advantages of gel casting

Gel casting is capable of producing ceramic parts with complex shapes similar to those widely produced by injection moulding. Compared with injection moulding, gel casting does not require expensive moulds; a large range of mould materials like metal, glass, and polymer can be used [97]. Moreover, a separate binder removal step is not required due to the small amounts of organic binder used in gel casting. In contrast with slip casting and pressure casting used for the production of larger-size parts beyond the capability of injection moulding, gel casting provides a quicker moulding process, higher as-formed and dried green strengths, and much more homogenous properties [97, 98].

3.5.2 Mechanisms for gel casting

The heart of the gel casting process is the irreversible formation of a gel, which allows particles to retain their dispersed state and gives significant strength to the gelled green body. The permanently bonded gel can be formed based on a number of different mechanisms such as polymerisation, coordination chemistry, and biopolymer chemistry, giving rise to the development of various gel casting systems.

3.5.2.1 Free radical polymerisation

The original gel casting system proposed by ORNL scientists was based on the free radical polymerisation of acrylamide (AM) monomer and methylene bisacrylamide (MBAM) crosslinker [97]. The polymerisation can be initiated by ammonium persulfate (APS) and accelerated by tetramethylethylenediamine (TEMED).The chain forming process in this system is presented in Figure 3-18. With the addition of free radicals, AM monomers are crosslinked by MBAM resulting in long polymer chains with a series of branches.

As the AM monomers used in the initial work are neurotoxins, alternative monomers have been developed such as Methacrylamide (MAM) and n-vinyl pyrrolidone (NVP) [94, 95]. In general, the strength of the formed gel increases with the total monomer concentration in the solution and the ratio of crosslinker to monomer. However, the concentration that can be used is limited by the solubility of the monomer and the crosslinker in water. For the commonly used MBAM crosslinker, the solubility in water at room temperature is as low as 2 wt% [97], resulting in limited green strength of the gel cast bodies. The other disadvantage associated with the monomer-crosslinker system when carried out in air, is the surface exfoliation problem due to the inhibition of oxygen [99, 100]. This problem can be suppressed under a nitrogen atmosphere but at the expense of a higher cost of production [100].

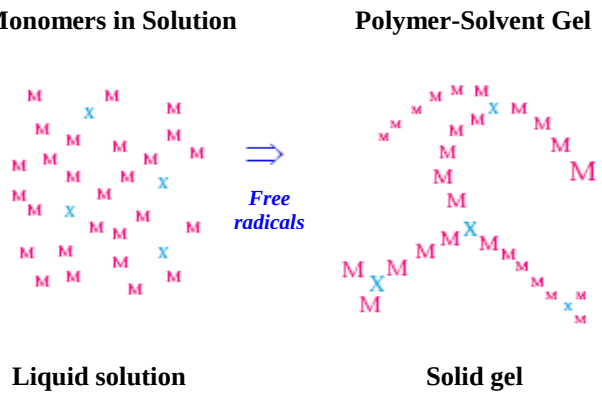

Figure 3-18 Schematic illustration of free radical polymerisation [97]. M represents the chain building monomer and X stands for the chain branching monomer. After adding free radicals, polymerisation occurs, resulting in long chains formed by the M and X monomers.

3.5.2.2 Coordination chemistry

Continuous efforts have been made to develop low toxicity/non-toxic gel casting systems and one of the novel strategies is based on the coordination chemistry of metal ions. Xie et al. [101-103] reported using calcium ions to crosslink sodium alginate in aqueous alumina suspensions. In this gel casting process, upon heating, free calcium ions were released and coordinated to the hydroxyl and carboxyl groups contained in the alginate molecules, leading to the formation of a network structure known as an 'egg box' model as depicted in Figure 3-19. Alumina particles were enclosed in the network and green bodies were formed. However, the inadequate green strength (8 MPa) [101] of the gelled ceramic parts made by this process discouraged the use of sodium alginate-calcium system for most applications.

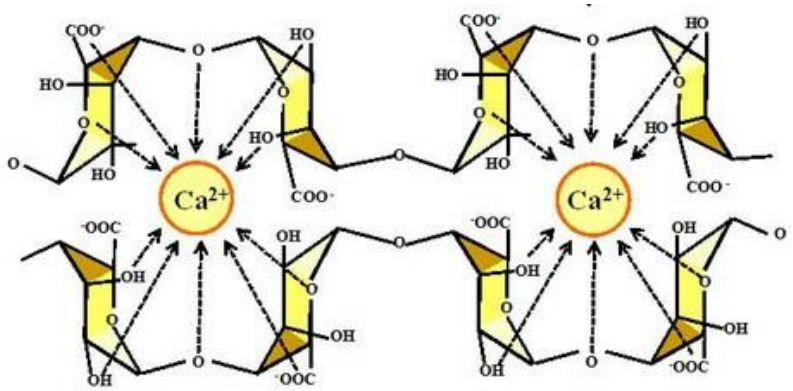

Figure 3-19 Schematic illustrations of the "egg-box" model for alginate gelation with calcium ions in which free calcium ions are coordinated to the hydroxyl and carboxyl groups contained in the alginate molecules [104].

3.5.2.3 *Biopolymer chemistry*

Gelation of harmless biopolymers has also been explored for gel casting. Lyckefldt et al. [105] reported the use of proteins as gelling agents. These systems are based on the mechanism that the chain conformation of some types of globular proteins such as egg white powder and whey protein concentrate can be altered by heating or cooling [105]. When heated up to a certain temperature, the chains of these proteins are unfolded and become tangled to form a three dimensional network that can solidify a ceramic suspension in situ to form a ceramic green body. However, the foam stabilising ability of globular proteins limits their use for gel casting of dense ceramics.

Other biopolymers such as agar, agarose and gelatine can be dissolved in hot water and gel when cooled down thus they have also been applied as consolidators in gel casting processes [106-108]. However, several drawbacks including difficult process control and high cost are found in the processes using these polymers.

3.5.2.4 Ring-opening polymerisation

One of the most recent developments of gel casting systems involves the use of water soluble epoxies and amine hardeners. Inspired by a self-hardening slip-casting method reported by Takeshita and Kurita [109], Mao et al. [110] introduced an epoxy resin, sorbitol polyglycidyl ether (SPGE) as a gelling agent for the gel casting of alumina. However, the high viscosity (5 Pa·s) and low water solubility (~9.5 wt%) of SPGE [111] necessitated the search for more suitable resins that could be compatible with the aqueous media, ceramic powder and dispersant.

Various epoxy resins have been applied to the consolidation of alumina bulk ceramics and ethylene glycol diglycidyl ether (EGDGE) and glycerol polyglycidyl ether (GPGE) have emerged to be excellent alternatives to SPGE [111] due to their ability to form high-strength dried gel cast bodies. Based on previous work reported, Olhero et al. [93] managed to gel cast PZT pillars, as described in Section 3.4.4, incorporating EGDGE as a gelling agent, and a very high green strength of 35.21 ± 0.39 MPa was achieved, making this system an attractive option for producing fine-scale and complex-shaped ceramic structures.

These novel epoxy-amine gel casting systems are based on a ring-opening polymerisation mechanism. In contrast to the free-radical polymerisation, the ring-opening polymerisation can be carried out in an air atmosphere; also, due to its auto-catalytic nature [112], the epoxy-amine curing process can occur without the need for additional initiators and catalysts. The generally accepted epoxy-amine curing scheme is depicted in Figure 3-20 showing three main reactions. Initial reaction between epoxy and amine species takes place via the addition of primary amines to the epoxy groups, yielding secondary amines which in turn are able to react with the remaining

epoxy groups to produce tertiary amines. The hydroxyl groups generated in the second reaction continuously react with epoxy groups, facilitating the formation of a three dimensional network. It can be seen that one active hydrogen atom is possible to link with one epoxy group, from which the theoretical concentration relationship between the epoxy and the amine hardener can be determined.

(1) Primary amine-epoxy addition

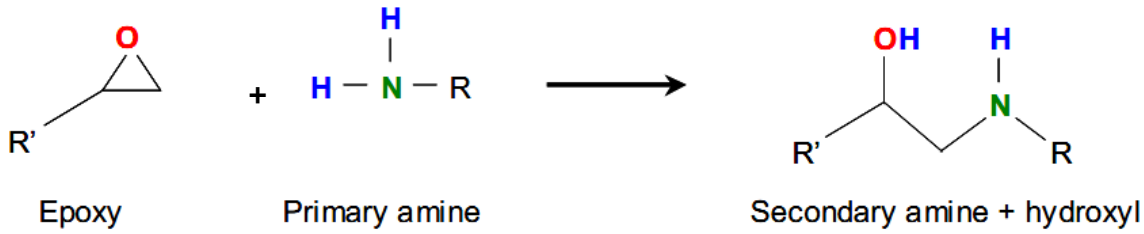

(2) Secondary amine-epoxy addition

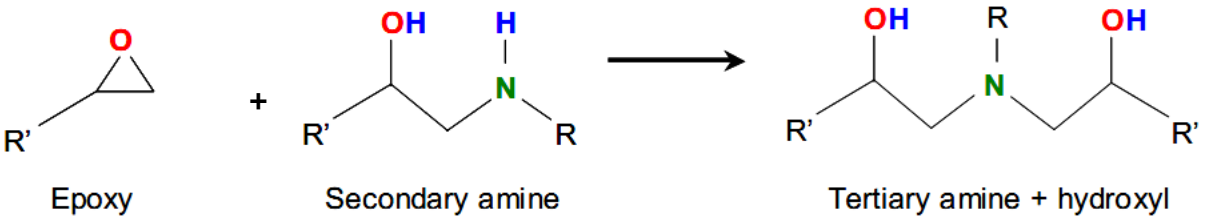

(3) Hydroxyl – epoxy addition (etherification)

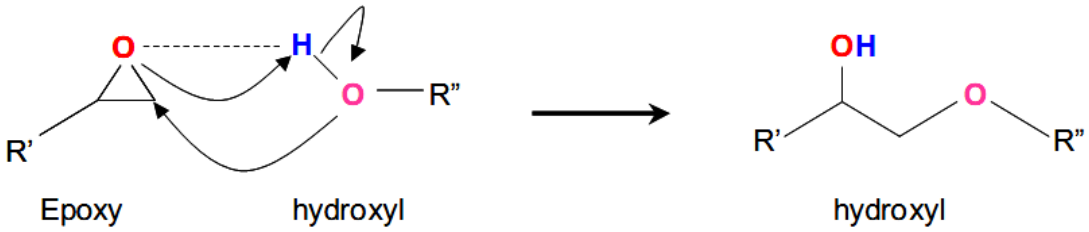

Figure 3-20 Reaction mechanism of epoxy-amine ring-opening polymerisation (adapted from [113]).

3.6 Summary

This chapter provided the background information required for the study on the fabrication and characterisation of novel 1-3 piezocomposite. Fundamental knowledge of piezoelectricity was introduced to lay the groundwork for understanding the principles and properties of piezocomposites. An overview of the piezoelectric materials used for ultrasound transducers was given and the advantages of 1-3 piezocomposites over piezoelectric ceramics and polymers were discussed. To maximise the performance of piezcomposites for HFUS application, trade-offs in composite design were described, in which the importance of fine-scale requirements for high frequency operation was addressed. Considering the difficulty in producing extremely fine kerf dimensions in regular composites, a random composite design as an alternative was introduced, including the strategy for the generation of the random pattern and the modelling results on the random composite. To select the method for the production of the random composite, a range of fabrication routes were reviewed, amongst which the lost-mould and soft-moulding strategies were identified to be more promising than the others. Based on the discussion of the current limitations in these micro-moulding techniques, the requirements for a suitable mould and a compatible ceramic/binder system were highlighted. An epoxy-amine gel-casting system previously reported for moulding of PZT pillars was selected for ceramic processing and the mechanisms and advantages of this system were discussed by comparing it with other gel-casting systems.

3.7 References

[1] V. Gibbs, *et al.*, *Ultrasound Physics and Technology: How, Why and When*: Churchill Livingstone, 2009.

[2] G. Gautschi, *Piezoelectric sensorics: Force, strain, pressure, acceleration and acoustic emission sensors, materials and amplifiers*: Springer, 2006.

[3] A. Safari and E. K. Akdogan, *Piezoelectric and acoustic materials for transducer applications*: Springer, 2008.

[4] M. De Graef and M. E. McHenry, *Structure of materials: an introduction to crystallography, diffraction and symmetry*: Cambridge University Press, 2007.

[5] G. W. Taylor, *et al.*, *Piezoelectricity*: Gordon and Breach, 1985.

[6] A. Bouzid, *et al.*, "PZT phase diagram determination by measurement of elastic moduli," *Journal of the European Ceramic Society,* vol. 25, pp. 3213-3221, 2005.

[7] M. J. Hoffmann, *et al.*, "Correlation between microstructure, strain behavior, and acoustic emission of soft PZT ceramics," *Acta Materialia,* vol. 49, pp. 1301-1310, 2001.

[8] A. K. Tagantsev, *et al.*, *Domains in ferroic crystals and thin films*: Springer, 2010.

[9] D. Damjanovic and M. Demartin, "Contribution of the irreversible displacement of domain walls to the piezoelectric effect in barium titanate and lead zirconate titanate ceramics," *Journal of Physics: Condensed Matter,* vol. 9, p. 4943, 1999.

[10] G. Arlt, "The role of domain walls on the dielectric, elastic and piezoelectric properties of ferroelectric ceramics," *Ferroelectrics,* vol. 76, pp. 451-458, 1987.

[11] Y. Xu and X. Yuhuan, *Ferroelectric materials and their applications*: North-Holland Amsterdam ets, 1991.

[12] D. Damjanovic, "Ferroelectric, dielectric and piezoelectric properties of ferroelectric thin films and ceramics," *Reports on Progress in Physics,* vol. 61, p. 1267, 1999.

[13] F. X. Li and R. K. N. D. Rajapakse, "A constrained domain-switching model for polycrystalline ferroelectric ceramics. Part I: Model formulation and application to tetragonal materials," *Acta Materialia,* vol. 55, pp. 6472-6480, 2007.

[14] "Linear Theory of Piezoelectricity," *Sonics and Ultrasonics, IEEE Transactions on,* vol. 31, pp. 10-13, 1984.

[15] H. F. Tiersten, "Linear Piezoelectric Plate Vibrations- Elements of the Linear Theory of Piezoelectricity and the Vibrations of Piezoelectric Plates(Linear piezoelectric plate vibrations, Elements of linear theory of piezoelectricity and vibrations of piezoelectric plates, covering differential equations, boundary conditions, etc)," 1969.

[16] A. Dal Corso, *et al.*, "Nonlinear piezoelectricity in CdTe," *Physical Review B,* vol. 47, p. 16252, 1993.

[17] V. Birman, "Physically nonlinear behavior of piezoelectric actuators subject to high electric fields," DTIC Document2005.

[18] "IEEE Standard on Piezoelectricity," *ANSI/IEEE Std 176-1987,* p. 0_1, 1988.

[19] C. Z. Rosen and B. V. Hiremath, *Piezoelectricity* vol. 5: Amer Inst of Physics, 1992.

[20] G. Arlt and H. Dederichs, "Complex elastic, dielectric and piezoelectric constants by domain wall damping in ferroelectric ceramics," *Ferroelectrics,* vol. 29, pp. 47-50, 1980/08/01 1980.

[21] K. Uchino and S. Hirose, "Loss mechanisms in piezoelectrics: how to measure different losses separately," *Ultrasonics, Ferroelectrics and Frequency Control, IEEE Transactions on,* vol. 48, pp. 307-321, 2001.

[22] M. R. Srinivasan, *Physics For Engineers*: New Age International Limited, 1996.

[23] H. J. Pain and R. T. Beyer, "The physics of vibrations and waves," *The Journal of the Acoustical Society of America,* vol. 94, pp. 3529-3529, 1993.

[24] T. J. Clipsham, "The replication of micron scale pillar arrays for medical ultrasound applications," 2010.

[25] M. Analoui, *et al.*, *Medical Imaging: Principles and Practices*: CRC PressI Llc, 2012.

[26] J. L. Pons, *Emerging actuator technologies: a micromechatronic approach*: Wiley, 2005.

[27] C. E. M. Démoré, "Design of Ultrasound Transducer Arrays for Medical Imaging," PhD, Queen's University, 2006.

[28] D. MacLennan, "Fundamental Characterisation and Early Functional Testing of Micromoulded Piezocomposites " PhD, University of Strathclyde 2009.

[29] D. Waller, *et al.*, "Requirements of piezoelectric materials for medical ultrasound transducers," in *Applications of Ferroelectrics, 1996. ISAF '96., Proceedings of the Tenth IEEE International Symposium on*, 1996, pp. 565-568 vol.2.

[30] W. A. Smith, *et al.*, "Design of piezocomposites for ultrasonic transducers," *Ferroelectrics,* vol. 91, pp. 155-162, 1989.

[31] H. Jaffe and D. A. Berlincourt, "Piezoelectric transducer materials," *Proceedings of the IEEE,* vol. 53, pp. 1372-1386, 1965.

[32] L. F. Brown, *et al.*, "Ferroelectric nylon materials and their feasibility for ultrasound transducers," *Ultrasonics, Ferroelectrics and Frequency Control, IEEE Transactions on,* vol. 44, pp. 1049-1059, 1997.

[33] Z. Qifa, *et al.*, "PMN-PT single crystal, high-frequency ultrasonic needle transducers for pulsed-wave Doppler application," *Ultrasonics, Ferroelectrics and Frequency Control, IEEE Transactions on,* vol. 54, pp. 668-675, 2007.

[34] S.-E. E. Park and W. Hackenberger, "High performance single crystal piezoelectrics: applications and issues," *Current Opinion in Solid State and Materials Science,* vol. 6, pp. 11-18, 2002.

[35] L. Pdungsap, *et al.*, "Optimized conditions for fabrication of La-dopant in PZT ceramics," *Sensors and Actuators A: Physical,* vol. 122, pp. 250-256, 2005.

[36] B. Lee and E. Lee, "Effects of complex doping on microstructural and electrical properties of PZT ceramics," *Journal of Electroceramics,* vol. 17, pp. 597-602, 2006.

[37] T. Haccart, *et al.*, "Substitution of Nb doping on the structural, microstructural and electrical properties in PZT films," *Thin Solid Films,* vol. 423, pp. 235-242, 2003.

[38] T. R. Shrout, "Innovations in piezoelectric materials for ultrasound transducers," in *Applications of Ferroelectrics, 2008. ISAF 2008. 17th IEEE International Symposium on the*, 2008, pp. 1-4.

[39] E. Fukada, "History and recent progress in piezoelectric polymers," *Ultrasonics, Ferroelectrics and Frequency Control, IEEE Transactions on,* vol. 47, pp. 1277-1290, 2000.

[40] F. S. Foster, *et al.*, "A history of medical and biological imaging with polyvinylidene fluoride (PVDF) transducers," *Ultrasonics, Ferroelectrics and Frequency Control, IEEE Transactions on,* vol. 47, pp. 1363-1371, 2000.

[41] M. D. Sherar and F. S. Foster, "The design and fabrication of high frequency poly(vinylidene fluoride) transducers," *Ultrasonic Imaging,* vol. 11, pp. 75-94, 1989.

[42] C. G. Oakley and M. J. Zipparo, "Single crystal piezoelectrics: a revolutionary development for transducers," in *Ultrasonics Symposium, 2000 IEEE*, 2000, pp. 1157-1167 vol.2.

[43] P. W. Rehrig, *et al.*, "Status of piezoelectric single crystal growth for medical transducer applications," in *Ultrasonics, 2003 IEEE Symposium on,* 2003, pp. 766-769 Vol.1.

[44] P. Seung-Eek and T. R. Shrout, "Characteristics of relaxor-based piezoelectric single crystals for ultrasonic transducers," *Ultrasonics, Ferroelectrics and Frequency Control, IEEE Transactions on,* vol. 44, pp. 1140-1147, 1997.

[45] S. Michau, *et al.*, "Single crystal-based phased array for transoesophagial ultrasound probe," in *Ultrasonics Symposium, 2002. Proceedings. 2002 IEEE*, 2002, pp. 1269-1272 vol.2.

[46] T. R. Gururaja, *et al.*, "Single crystal transducers for medical imaging applications," in *Ultrasonics Symposium, 1999. Proceedings. 1999 IEEE*, 1999, pp. 969-972 vol.2.

[47] Z. Qifa, *et al.*, "PMN-PT single crystal, high-frequency ultrasonic needle transducers for pulsed-wave Doppler application," *Ultrasonics, Ferroelectrics and Frequency Control, IEEE Transactions on,* vol. 54, pp. 668-675, 2007.

[48] J. M. Cannata, *et al.*, "Design of focused single element (50-100 MHz) transducers using lithium niobate," in *Ultrasonics Symposium, 2000 IEEE*, 2000, pp. 1129-1133 vol.2.

[49] R. E. Newnham, *et al.*, "Connectivity and piezoelectric-pyroelectric composites," *Materials Research Bulletin,* vol. 13, pp. 525-536, 1978.

[50] W. A. Smith, "The role of piezocomposites in ultrasonic transducers," in *Ultrasonics Symposium, 1989. Proceedings., IEEE 1989*, 1989, pp. 755-766 vol.2.

[51] W. A. Smith, *et al.*, "Design of piezocomposites for ultrasonic transducers," *Ferroelectrics,* vol. 91:1, pp. 155-162, 1989.

[52] T. J. CLIPSHAM, "The Replication of Micron Scale Pillar Arrays For Medical Ultrasound Applications," PhD Thesis, University of Birmingham, 2010.

[53] (Last accessed 2013/04/07). *The manufacturer of PZFlex.* Available: http://www.pzflex.com/

[54] W. A. Smith and B. A. Auld, "Modeling 1-3 composite piezoelectrics: thickness-mode oscillations," *Ultrasonics, Ferroelectrics and Frequency Control, IEEE Transactions on,* vol. 38, pp. 40-47, 1991.

[55] A. L. Bernassau, *et al.*, "Characterisation of an epoxy filler for piezocomposite material compatible with microfabrication processes," in *Ultrasonics Symposium, 2008. IUS 2008. IEEE*, 2008, pp. 62-65.

[56] D. MacLennan, *et al.*, "Fundamental performance characterisation of high frequency piezocomposites made with net-shape viscous polymer processing for medical ultrasound transducers," in *Ultrasonics Symposium, 2008. IUS 2008. IEEE,* 2008, pp. 58-61.

[57] D. MacLennan, *et al.*, "2F-6 Properties and Application-Oriented Performance of High Frequency Piezocomposite Ultrasonic Transducers," in *Ultrasonics Symposium, 2007. IEEE,* 2007, pp. 100-103.

[58] P. Hoskins and A. Thrush, *Diagnostic Ultrasound: Physics and Equipment*: Cambridge University Press, 2002.

[59] T. Clipsham and T. Button, "1-3 Piezocomposites realised from small feature size, high aspect ratio, hot embossed moulds. Part II: piezocomposite fabrication," *Microsystem Technologies,* vol. 16, pp. 1983-1988, 2010.

[60] J. A. Hossack and G. Hayward, "Finite-element analysis of 1-3 composite transducers," *Ultrasonics, Ferroelectrics and Frequency Control, IEEE Transactions on,* vol. 38, pp. 618-629, 1991.

[61] G. Hayward and J. Bennett, "Assessing the influence of pillar aspect ratio on the behavior of 1-3 connectivity composite transducers," *Ultrasonics, Ferroelectrics and Frequency Control, IEEE Transactions on,* vol. 43, pp. 98-108, 1996.

[62] A. Abrar, *et al.*, "1–3 connectivity piezoelectric ceramic–polymer composite transducers made with viscous polymer processing for high frequency ultrasound," *Ultrasonics,* vol. 42, pp. 479-484, 2004.

[63] B. A. Auld and Y. Wang, "Acoustic Wave Vibrations in Periodic Composite Plates," in *IEEE 1984 Ultrasonics Symposium*, 1984, pp. 528-532.

[64] D. Certon, *et al.*, "Theoretical and experimental investigations of lateral modes in 1-3 piezocomposites," *Ultrasonics, Ferroelectrics and Frequency Control, IEEE Transactions on,* vol. 44, pp. 643-651, 1997.

[65] T. R. Gururaja, *et al.*, "Piezoelectric Composite Materials for Ultrasonic Transducer Applications. Part I: Resonant Modes of Vibration of PZT Rod-Polymer Composites," *Sonics and Ultrasonics, IEEE Transactions on,* vol. 32, pp. 481-498, 1985.

[66] P. Reynolds, *et al.*, "Analysis of spurious resonances in single and multi-element piezocomposite ultrasonic transducers," in *Ultrasonics, 2003 IEEE Symposium on*, 2003, pp. 1650-1653 Vol.2.

[67] J. A. Brown, *et al.*, "Fabrication and performance of a 40-MHz linear array based on a 1-3 composite with geometric elevation focusing," *Ultrasonics, Ferroelectrics and Frequency Control, IEEE Transactions on,* vol. 54, pp. 1888-1894, 2007.

[68] Y. Jianhua, *et al.*, "Effect of triangular pillar geometry on high- frequency piezocomposite transducers," *Ultrasonics, Ferroelectrics and Frequency Control, IEEE Transactions on,* vol. 57, pp. 957-968, 2010.

[69] J. Yin, *et al.*, "Effect of triangular pillar geometry on high-frequency piezocomposite transducers," *Ultrasonics, Ferroelectrics and Frequency Control, IEEE Transactions on,* vol. 57, pp. 957-968, 2010.

[70] H.-C. Yang, *et al.*, "A Study of 1-3 Pseudo-Random Pillar Piezocomposites for Ultrasound Transducers."

[71] C. E. M. Demore, *et al.*, "1-3 piezocomposite design optimised for high frequency kerfless transducer arrays," in *Ultrasonics Symposium (IUS), 2009 IEEE International*, 2009, pp. 1-4.

[72] J. Bamber and R. Dickinson, "Ultrasonic B-scanning: a computer simulation," *Physics in medicine and biology,* vol. 25, p. 463, 2000.

[73] A. Safari, *et al.*, "Development of fine-scale piezoelectric composites for transducers," *Aiche Journal,* vol. 43, pp. 2849-2856, 1997.

[74] Y. Jianhua, *et al.*, "High frequency piezo-composite transducer with hexagonal pillars," in *Ultrasonics Symposium (IUS), 2009 IEEE International*, 2009, pp. 2750-2753.

[75] K. Lubitz, *et al.*, "Microstructuring technology," in *Ultrasonics Symposium, 1993. Proceedings., IEEE 1993*, 1993, pp. 515-524 vol.1.

[76] N. Farlow, *et al.*, "Micromachining of a piezocomposite transducer using a copper vapor laser," *Ieee Transactions on Ultrasonics Ferroelectrics and Frequency Control,* vol. 48, pp. 639-640, 2001.

[77] Y. Ohara, *et al.*, "Partially stabilized zirconia-polymer composites fabricated with an ultrasonic cutter," *Journal of Materials Science Letters,* vol. 12, pp. 1279-1282, 1993.

[78] L. J. Bowen, *et al.*, "Injection molded fine-scale piezoelectric composite transducers," in *Ultrasonics Symposium, 1993. Proceedings., IEEE 1993*, 1993, pp. 499-503.

[79] B. Pazol, *et al.*, "Ultrafine scale piezoelectric composite materials for high frequency ultrasonic imaging arrays," in *Ultrasonics Symposium, 1995. Proceedings., 1995 IEEE*, 1995, pp. 1263-1268.

[80] E. W. Becker, *et al.*, "Fabrication of microstructures with high aspect ratios and great structural heights by synchrotron radiation lithography, galvanoforming, and plastic moulding (LIGA process)," *Microelectronic Engineering*, vol. 4, pp. 35-56, 1986.

[81] U. Bast, *et al.*, "New technique for the production of piezoelectric composites with 1-3 connectivity," in *Ceramics Today- Tomorrow's Ceramics. Proc. 7 th Int. Meeting on Modern Ceramics Technologies(7 th CIMTEC- World Ceramics Congress). Part C Montecatini Terme, 24-30 June 1990*, 2005, pp. 2005-2015.

[82] S. Wang, *et al.*, "Lost silicon mold process for PZT microstructures," *Advanced Materials*, vol. 11, pp. 873-876, 1999.

[83] Y. Hirata, *et al.*, "Effects of aspect ratio of lead zirconate titanate on 1-3 piezoelectric composite properties," *Japanese journal of applied physics*, vol. 36, pp. 6062-6064, 1997.

[84] Y. Hirata, *et al.*, "Piezocomposite of fine PZT rods realized with synchrotron radiation lithography," in *Ultrasonics Symposium, 1997. Proceedings., 1997 IEEE*, 1997, pp. 877-881.

[85] S. Cochran, *et al.*, "Net-shape ceramic processing as a route to ultrafine scale 1-3 connectivity piezoelectric ceramic-polymer composite transducers," in *Ultrasonics Symposium, 2004 IEEE*, 2004, pp. 1682-1685.

[86] D. Zhang, *et al.*, "Piezoelectric 1–3 Composites for high frequency ultrasonic transducer applications," *Ferroelectrics*, vol. 304, pp. 201-205, 2004.

[87] B. Su, *et al.*, "Embossing of 3D ceramic microstructures," *Microsystem technologies*, vol. 8, pp. 359-362, 2002.

[88] A. Ruiz, *et al.*, "Large-area protein nano-arrays patterned by soft lithography," *Nanotechnology*, vol. 18, p. 505306, 2007.

[89] M. S. Kim, *et al.*, "Synthesis of monodisperse PS-co-PDMS microspheres by dispersion polymerization," *Materials Science and Engineering: C*, vol. 27, pp. 1247-1251, 2007.

[90] S. Starke, *et al.*, "Fine scale piezoelectric 1-3 composites: a new approach of cost effective fabrication," in *Applications of Ferroelectrics, 1998. ISAF 98. Proceedings of the Eleventh IEEE International Symposium on*, 1998, pp. 393-396.

[91] S. Gebhardt, *et al.*, "Fine scale 1-3 composites fabricated by the soft mold process: Preparation and modeling," *Ferroelectrics*, vol. 241, pp. 67-73, 2000/03/01 2000.

[92] S. Gebhardt, *et al.*, "Quasistatic and dynamic properties of 1–3 composites made by soft molding," *Journal of the European Ceramic Society,* vol. 23, pp. 153-159, 2003.

[93] S. M. Olhero, *et al.*, "Innovative fabrication of PZT pillar arrays by a colloidal approach," *Journal of the European Ceramic Society,* vol. 32, pp. 1067-1075, 2012.

[94] J. Yang, *et al.*, "Recent developments in gelcasting of ceramics," *Journal of the European Ceramic Society,* vol. 31, pp. 2569-2591, 2011.

[95] M. A. Janney, *et al.*, "Development of low-toxicity gelcasting systems," *Journal of the American Ceramic Society,* vol. 81, pp. 581-591, 1998.

[96] O. O. Omatete, *et al.*, "GELCASTING - A NEW CERAMIC FORMING PROCESS," *American Ceramic Society Bulletin,* vol. 70, pp. 1641-&, 1991.

[97] M. Janney, *et al.*, "Gelcasting," *The Handbook of Ceramic Engineering,* pp. 1-15, 1998.

[98] O. O. Omatete, *et al.*, "Gelcasting: from laboratory development toward industrial production," *Journal of the European Ceramic Society,* vol. 17, pp. 407-413, 1997.

[99] S. Liya, *et al.*, "Investigation of the influencing factors on surface exfoliation on Al2O3–ZrO2 green bodies prepared by gelcasting," *Materials Science and Engineering: A,* vol. 464, pp. 63-67, 2007.

[100] J.-S. Ha, "Effect of atmosphere type on gelcasting behavior of Al2O3 and evaluation of green strength," *Ceramics International,* vol. 26, pp. 251-254, 2000.

[101] Z.-p. Xie, *et al.*, "Ceramic forming based on gelation principle and process of sodium alginate," *Materials Letters,* vol. 57, pp. 1635-1641, 2003.

[102] Y. Jia, *et al.*, "New gel-casting process for alumina ceramics based on gelation of alginate," *Journal of the European Ceramic Society,* vol. 22, pp. 1911-1916, 2002.

[103] Z.-P. Xie, *et al.*, "A new gel casting of ceramics by reaction of sodium alginate and calcium iodate at increased temperatures," *Journal of materials science letters,* vol. 20, pp. 1255-1257, 2001.

[104] K. Kashima and M. Imai, "Advanced Membrane Material from Marine Biological Polymer and Sensitive Molecular-Size Recognition for Promising Separation Technology," 2012.

[105] O. Lyckfeldt, *et al.*, "Protein forming — a novel shaping technique for ceramics," *Journal of the European Ceramic Society,* vol. 20, pp. 2551-2559, 2000.

[106] E. Adolfsson, "Gelcasting of Zirconia Using Agarose," *Journal of the American Ceramic Society,* vol. 89, pp. 1897-1902, 2006.

[107] Y. Chen, *et al.*, "Alumina casting based on gelation of gelatine," *Journal of the European Ceramic Society,* vol. 19, pp. 271-275, 1999.

[108] I. Santacruz, *et al.*, "Gel casting of aqueous suspensions of BaTiO3 nanopowders," *Ceramics International*, vol. 35, pp. 321-326, 2009.

[109] M. Takeshita and S. Kurita, "Development of self-hardening slip casting," *Journal of the European Ceramic Society*, vol. 17, pp. 415-419, 1997.

[110] X. Mao, *et al.*, "Gelcasting of Alumina Using Epoxy Resin as a Gelling Agent," *Journal of the American Ceramic Society*, vol. 90, pp. 986-988, 2007.

[111] X. J. Mao, *et al.*, "Investigation of new epoxy resins for the gel casting of ceramics," *Journal of the American Ceramic Society*, vol. 91, pp. 1354-1356, 2008.

[112] J. Barton, "The application of differential scanning calorimetry (DSC) to the study of epoxy resin curing reactions Epoxy Resins and Composites I." vol. 72, ed: Springer Berlin / Heidelberg, 1985, pp. 111-154.

[113] R. S. Mahendran, "Characterisation of cross-linking and moisture ingress detection in an epoxy/amine resin using fibre-optical sensors," PhD thesis, University of Birmingham, 2010.

CHAPTER 4 FABRICATION OF MOULDS WITH MICRO-SCALE FEATURES

4.1 Design considerations of micro-moulds

The realisation of the innovative fine-scale random pattern introduced in Section 3.3.3 for implementation in high frequency ultrasound transducers poses a considerable challenge for current lost mould and soft moulding techniques. The major limitations in these techniques lie in the generally poor strength of the ceramic/binder system and the achievable geometries, dimensions and aspect ratios of the mould. In Chapter 3, a novel water-soluble gel casting system has been identified as a promising candidate for the mould filling. This chapter reviews current microfabrication methods for the mould fabrication, to enable a suitable technique to be selected.

The mould can either be a lost mould that can be easily stripped or a master mould for the replication of a soft mould. Both of the two scenarios are considered in this thesis. The lost mould should have the negative structure of the desired bristle-block hence it has the form of a series of cavities while the master mould should possess the same structure of the designed ceramic segments; therefore, it consists of high-aspect-ratio positive relief structures on its surface.

For high frequency operation the lateral features in the pattern vary from around 2-50 μm, which accordingly demand the associated mould to offer micro-scale resolution and the ability to give the variations in the shape, size and separation. The cavity depth of the lost mould or the height of the surface relief in the master mould was desired to be larger than the required composite thickness to compensate for inevitable losses during lapping. The larger the mould depth/height, the taller the

demoulded PZT segments and the higher the chance would be to achieve a piezocomposite of the desired thickness. According to Clipsham [1], a lost mould depth should ideally be over 100 μm for the fabrication of a 30 MHz piezocomposite (~50 μm thick), when considering shrinkages due to drying and sintering ceramic, and final planarisation of the composite. Moreover, the lost mould material should be easy to be removed without introducing any defects on the green-state ceramics. For the master mould, it is required to survive the peeling off process without breaking or damaging the PDMS. In addition, the side walls of the features should be as straight as possible. For convenience, the required lost mould and master mould with randomised features are referred as random moulds when detailed description is not necessary. In summary, the material for fabricating random moulds for high frequency piezocomposites should have the following characteristics:

1) high resolution to resolve fine features down to 2-3 μm;
2) cavity depth/ positive relief height over 100 μm i.e. aspect ratio over 50;
3) ease of demoulding;
4) straight side wall definition.

These requirements of the mould added to the complexity of the challenge to fabricate randomised piezocomposites.

Commonly used microfabrication techniques are reviewed including micromachining, UV based lithography, LIGA and etching. Their principles, advantages and disadvantages, along with the feasibilities for this application are discussed below.

4.2 Micro-electro-discharge machining (µ-EDM)

Micro-electro-discharge machining employs a series of electrical sparks to erode the material of the workpiece. The material is removed by melting and evaporation through heat induced by the electrical discharges. µ-EDM can only be used for machining conductive material such as metals and graphite. These materials cannot be used as the lost mould in this application as they are cannot be easily removed. Therefore, only positive relief structures are considered.

For the production of positive structures, wire µ-EDM is preferred to be used, in which sparks are produced along a wire and cutting is achieved as the wire feeds between two reels. Wire µ-EDM has demonstrated its capability to fabricate complex-shaped positive structures with high aspect ratios in a range of applications. In a specific example, a beryllium copper pillar array that has a structure similar to the master mould for producing regular piezocomposites, with a height of over 700 µm and an aspect ratio up to 33, has been produced by wire µ-EDM as shown in Figure 4-1 [2]. In fact, the aspect ratio that µ-EDM can possibly achieve goes up to 100 [3, 4]. However, as the smallest wire used in wire µ-EDM is limited to 20 µm [5], kerfs smaller than that are impossible to be produced, making this technique not suitable for HFUS applications.

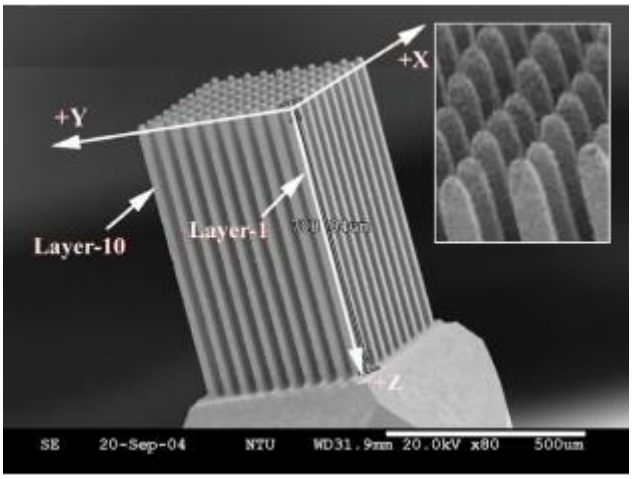

Figure 4-1 Beryllium copper pillar array with an aspect ratio up to 33 [2].

4.3 Laser machining

A laser beam utilises a highly focused coherent beam of light with high intensity to directly machine the material through ablation. The material can be removed by different mechanisms including melting, vaporization or chemical degradation [6]. In practice, this technique typically allows the fabrication of structures of ~10 μm with aspect ratios up to 10 [6-8]. With increasing the depth, the walls of the laser machined structures start to taper, attributed to the converging-diverging shape of the laser beam [9], and hence this limits the aspect ratio that can be achieved.

Continuous investigations have been carried out to increase the aspect ratio of the laser machined structures by reducing the beam divergence, improving the beam homogeneity and introducing a material with improved photon-ablation properties [8, 10, 11]. However, with the commonly used excimer lasers, the highest aspect ratio achieved is 30 and the lateral dimensions are still limited to the order of tens of microns [1, 8].

Zhang et al. reported using an ultra-fast laser with much higher energy than excimer lasers for the fabrication of PMMA (Poly(methyl methacrylate)) holes, which have structures closer to the lost mould used for the production of regular piezocomposites. Figure 4-2(a) shows a typical hole with a diameter of 40 μm and an aspect ratio slightly greater than 10. The same researchers also managed to achieve micro-strings with minimum lateral dimensions down to 2 μm and a depth greater than 10 mm, giving an aspect ratio over 5000, which is the greatest aspect ratio value in the reviewed structures. However, severe damage has been observed near the sample surface and along the depth as shown in Figure 4-2(b), showing very poor control of the precision for micro-scale features.

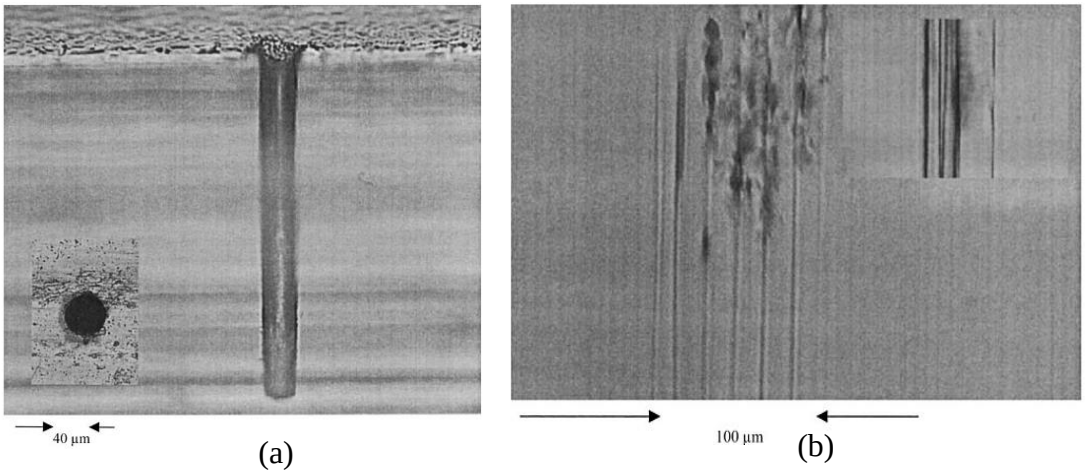

(a) (b)

Figure 4-2 (a) A hole of 40 μm diameter and an aspect ratio greater than 10 and (b) an array of micro-strings with the minimum diameter of 2 μm and a depth of 2 mm, produced in PMMA polymer using an ultrafast laser.

4.4 Photolithography

Photolithography or optical lithography is the most powerful and the most widely used method in microfabrication [12, 13], which has enabled the rapid development of the integrated circuit industry and brought about the revolution of modern microelectronics [14]. The word lithography derived its name from the Greek words lithos, meaning stones and graphia, meaning to write. The soft-moulding technique

mentioned in Section 3.4.4 is also a form of lithography but based on a non-photolithographic strategy.

In a photolithographic process, a light-sensitive polymer called photoresist is exposed to a light source through a patterned mask and subsequently developed in a chemical, thereby transferring the two-dimensional patterns on the mask to three-dimensional relief structures in the polymer. A series of steps are typically involved in this process: (1) spin coat a uniform layer of photoresist; (2) soft bake to evaporate the solvent and stabilise the resist film; (3) expose to transfer the desired pattern and (5) develop to remove the exposed area for the positive photoresist and unexposed part for the negative photoresist. All the processing stages are usually performed in a clean room, an enclosed area with a controlled level of pollutants and yellow lighting to prevent unwanted exposure.

Thick photoresists with positive/negative relief structures over 100 μm are of interest for the mould fabrication in this work. The capabilities of the process are dependent on a range of factors including the properties of the resist, the processing parameters and the capabilities of the equipment. Techniques and issues regarding thick photoresists are discussed below, followed by an overview of thick photoresists in the range of over 100 μm.

4.4.1 Spin coating

Spin coating is the standard method for depositing thin photoresist films in the photolithographic technology, involving the use of centrifugal force to spread liquid photoresist over a flat and clean substrate, usually a Si wafer. As illustrated in Figure 4-3, it consists of three phases [15]: dispensing the photoresist, acceleration of the

substrate and spinning at constant rate. The thinning behaviour is initially dominated by the outward flow of the fluid and subsequently dominated by the solvent evaporation [15, 16].

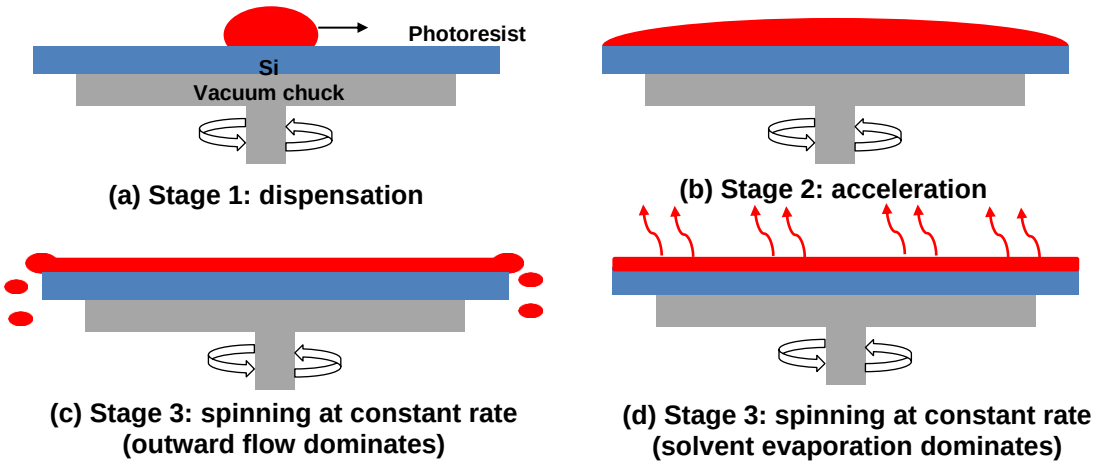

Figure 4-3 The standard process of spin coating.

The resulting thickness of the photoresist, h_p, is governed by the viscosity of the photoresist (η), the spin speed (ω) and the solution concentration (C_s), as expressed in the empirical equation shown below [15].

$$h_p = \frac{K_c C_s{}^{\beta} \eta^{\gamma}}{\omega^{\alpha}} \qquad \textbf{Equation 4-1}$$

where K_c is the overall calibration constant and the exponential factors β, γ and α are empirically determined.

To achieve film thicknesses over 100 µm, a very low spin speed is generally required. However, low spin speeds might increase the formation of an edge bead and decrease the homogeneity of the resist film. A commonly used strategy is to spin at a speed higher than required for a few seconds and then quickly ramp down to a lower

constant rate [17, 18]. A spin coating cycle suitable for producing a thick photoresist is depicted in Figure 4-4.

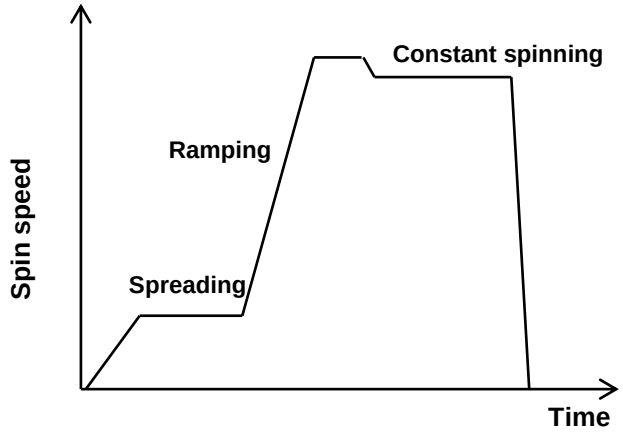

Figure 4-4 Spin coating cycle suggested for thick photoresists.

Double or multiple coating is used for some photoresists to increase the achievable thickness but a soft bake has to be carried in between the coatings, which increase the complexity of the process as well as the duration and cost.

Other methods for coating thick resist layers involves the use of modified or advanced coating tools or equipment such as a spin coater with a co-rotating cover, which creates a closed environment thereby avoiding the uncontrolled drying situation in a conventional open system [19, 20].

4.4.2 Soft bake

A photoresist consists of three components, a polymer matrix or resin, a solvent and a photoactive compound. Most of the residual solvent is driven out from the resulting resist film through a process known as soft bake. Soft baking reduces the solvent content from ~20-40 wt% to ~4-7 wt% by means of thermally activated solvent diffusion and evaporation [21, 22]. The main purposes of this step are to render stability of the resist film at room temperature as well as improve adhesion of the

resist to the substrate. Also, a baked film is less susceptible to particle contamination and less liable to stick to the photo mask [23].

With the increase of photoresist film thickness, longer bake times and/or higher temperatures are required, which might result in partial decomposition of the photoactive compound thus degrading the resist properties. A two-stage soft bake is usually adopted for thick photoresists, using an oven or a hot plate. However, the use of a convection oven for heating is often observed to encourage surface drying and skin formation and the use of a hot plate results in a temperature gradient across the film thickness with the bottom layer hotter than the top [24, 25]. A more uniform heating can be achieved from infrared radiation [24].

4.4.3 Exposure and development

The basic principle in photolithography is the change in solubility of the resist when subjected to light exposure, enabling the resist to be selectively removed in a developer [23]. In the case of a positive photoresist, UV light breaks the long-chain chemical bonds in the material, causing the exposed polymers to become more soluble in the developing solution. In contrast, for a negative photoresist, UV exposure results in cross linking of the polymers in the exposed region and thus reduced solubility in the developer. For certain types of photoresists, a post-exposure bake is required to finish off the chemical reactions initiated by UV light.

Contact, proximity and projection are the three primary exposure methods available, with different separations between the photo mask and the resist coated substrate [26]. In the laboratory environment, contact exposure is the commonly used mode. As the name implies, the mask is in direct contact with the resist layer with proper aligning

so that the desired mask patterns are transferred in a scale of 1:1 upon exposure. For a precise pattern transfer, the delivery of an optimum exposure dose is a critical requirement. Exposure dose is defined as the product of the intensity of the UV source, which is typically a mercury lamp, and the exposure time.

If the exposure dose is too low, i.e. underexposure, the UV induced chemical reaction would be incomplete, resulting in incomplete change of the resist solubility and thus only partial development of the pattern and, in the extreme case, a total loss of pattern [27]. In contrast, too high an exposure dose, i.e. overexposure, may cause the area outside of the pattern to be exposed, due to the accumulative influence of the possible reflection, scattering and diffraction of the UV light (detailed explanations can be found in [23]), and hence inaccurate pattern transfer.

In the final step, the exposed resist film is immersed in a developing solution to remove the soluble part. Development and exposure are strongly interrelated and it is the combined effects of both that determine the resulting pattern [28]. To a certain degree, overexposure can be compensated for by underdevelopment and vice versa [28]. In practical operation, an optimum result is obtained by the optimisation of a combination of exposure dose and development time.

For the processing of thick photoresists, there are several difficulties in the exposure stage. Firstly, underexposure of the base is a common issue [29]. Long exposure time is required for thick resists to make sure the base receives sufficient UV energy. In order to avoid overheating of the film surface by a high energy dose, exposure is usually conducted in multiple stages with short rest intervals [30]. Secondly, uneven surfaces are a particular problem for thick resist films over 100 μm [29], which can

lead to uneven contact with the mask during exposure. Additionally, with the contact mode, the mask and the resist film are liable to be damaged or contaminated. The presence of particles also causes uneven contact and any resulting defects on the mask may degrade the patterns, especially when small features are involved, thus reducing the overall resolution.

4.4.4 Thick photoresists for the fabrication of micro-moulds

In recent years, the demand for thick photoresists has been continuously rising for a number of applications including micro-electrical-mechanical systems (MEMS), bump bonding, wire interconnect and thin film heads [20, 31]. A series of thick photoresists with both negative and positive tones have been developed. Table 4-1 summarises some commonly used photoresists for >100 μm thick films, including the corresponding thicknesses and aspect ratios that have been reported, as well as their limitations. SEM images of several examples of thick photoresist micro-components are shown in Figure 4-5.

Up till now, an epoxy-based negative photoresist SU-8 is undoubtedly the most well-known material for producing thick and high-aspect-ratio structures. SU-8 films with thicknesses ranging from tens of microns up to 1.5 millimetres can be achieved by a single coating and even thicker films can be obtained by multiple coating [25, 32]. Ultra-high aspect ratios up to 100 have been reported by using SU-8 [33]. However, one of the main drawbacks of SU-8 for moulding applications is that it is extremely difficult to remove. A few methods such as high temperature burnout, bead blasting, plasma etching and wet removal have been developed for removing cross-linked SU-8 but they have compromised the integrity of micro metallic components [34]. This

means that it is impossible to use SU-8 as a lost mould in the HFUS application, but it is a promising candidate for being used as a master mould.

KMPR negative photoresist (MicroChem, USA), which can be more easily removed compared to SU 8, has been developed and adopted to produce thick micromoulds using a process similar to that used for fabricating SU 8 moulds [35, 36]. It is capable of providing thick films of several hundred microns by either single or multiple coating. Commercial resist strippers such as Remover PG (MicroChem, USA), have been shown capable of removing KMPR moulds, but mechanical agitation and heating are required, which may attack, distort or destroy the replicated structures, especially in the case of ultra-fine features. Other negative photoresists such as JSR THB-151N (JSR Micro, Japan), Diaplate 133 (HiTech Photopolymere, Switzerland) and BPR 100 (MicroChem, USA) are also being used for fabricating thick moulds over 100 μm [17]. However, they generally only achieve low aspect ratio structures and can be limited by the high viscosity of the initial solutions.

Compared with negative tone photoresists, positive photoresists have the main advantage of excellent strippability. Most of them can be completely removed in acetone without the use of a particular resist remover or strong agitation. AZ 9250 and AZ 4562 (AZ Electronic Materials, USA) are the two most widely used positive resists for producing thick resist microstructures. It is possible to produce thick films over 100 μm in a single coating but only with newly developed equipment [37]. By means of standard equipment, a multiple coating process, typically more than three times, is required to obtain layers over 50 μm [38, 39], which is rather time-consuming and thus increases cost.

Table 4-1 Comparison of commonly used thick photoresists in optical lithography.

	Negative photoresist					Positive photoresist	
	SU 8	**KMPR**	**JSR THB-151N**	**Diaplate 133**	**BPR 100**	**AZ 9260**	**AZ 4562**
Single coating thickness	up to 1.5 mm [32]	up to 400 µm [36]	over 50 µm [40]	up to 500 µm [41]	up to 150 µm [42]	up to 150 µm [43]	up to 100 µm [44]
Multiple coating thickness	up to 3 mm [25]	over 500 µm [45]	up to 150 µm [46]	N/A	up to 200 µm [42]	N/A	up to 200 µm [47]
Aspect ratio (Height to width)	up to 100 [33]	up to 18 [35]	2.6 [17]	~1 [41]	3 [48]	up to 20 [49]	up to 11 [50]
Limitation	Very difficult to strip [34]	Agitation and heat required for stripping [35]	Low aspect ratios yielded		Low aspect ratio and difficult to dispense [51]	Uneven coating surface for thick layers [39]	Multiple coating typically required for thick layers [38]

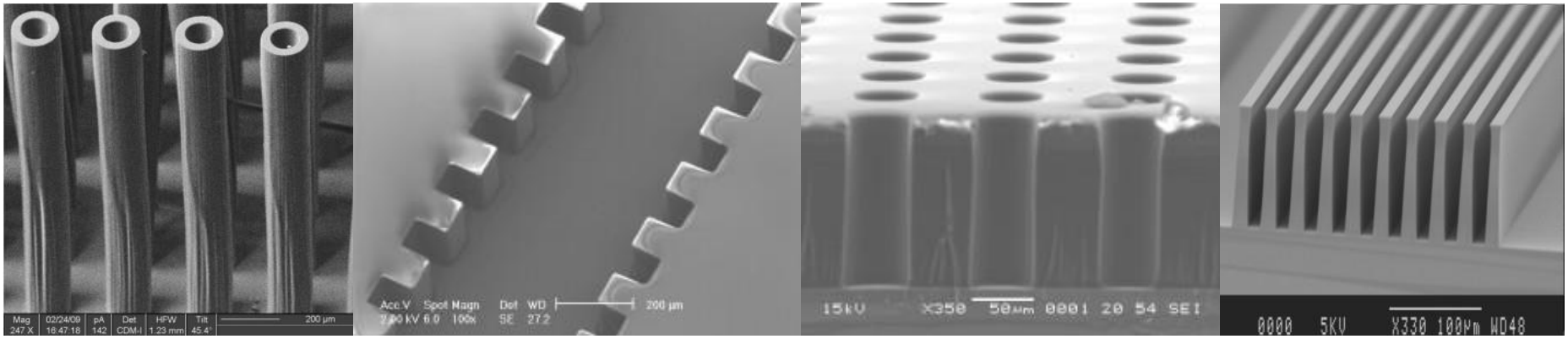

(a) SU 8: 1540 µm high hollow needles (b) KMPR: 180 µm thick micropiston mould (c) JSR THB-151N: 130 µm thick holes (d) AZ 9260: 100 µm thick layers

Figure 4-5 SEM images of examples of micro-components fabricated from thick photoresists: (a) SU 8 [52], (b) KMPR [35], (c) JSR THB-151N [17] and (d) AZ 9260[43].

4.5 LIGA

LIGA is the German acronym for Lithographie (lithography), Galvanoformung (electroforming) and Abformung (moulding), corresponding to the three major stages in this fabrication route. In this process, X-rays (usually produced by a Synchrotron) are used to pattern a thick photoresist (typically PMMA) that is then translated to the desired structures by electroplating. Although LIGA is regarded as the best process for producing thick structures (up to 500 μm) with high aspect ratios (easily over 100) [53], it suffers from low productivity and high cost. UV-LIGA involving optical lithography has been the preferred technology to conventional LIGA.

4.6 Bosch deep silicon etching

Deep etching of Si substrates is an essential process required in several advanced technologies such as MEMS and smart sensors. Nowadays, much of the silicon deep etching is accomplished by a patented method known as the Bosch process [54]. This process alternatively applies etch and passivation as illustrated in Figure 4-6, until a desired depth is reached. SF_6 and C_4F_8 are typically used as the etchant and passivation gas source, respectively [55, 56].

Before etching, the surface of a silicon substrate is patterned, typically using a photoresist, to have the area to be removed exposed. In the etching cycle, SF_6 produces a high density plasma to attack the exposed silicon, which lasts for 5-15 seconds [55]. The supply gas is then switched to C_4F_8 and a polymer protective film is deposited all over the silicon. It is followed by another etching step that removes the polymer layer on the bottom while the sidewalls are only slightly etched and therefore remain protected [28]. Repeated etching and passivation enables the silicon to be etched anisotropically.

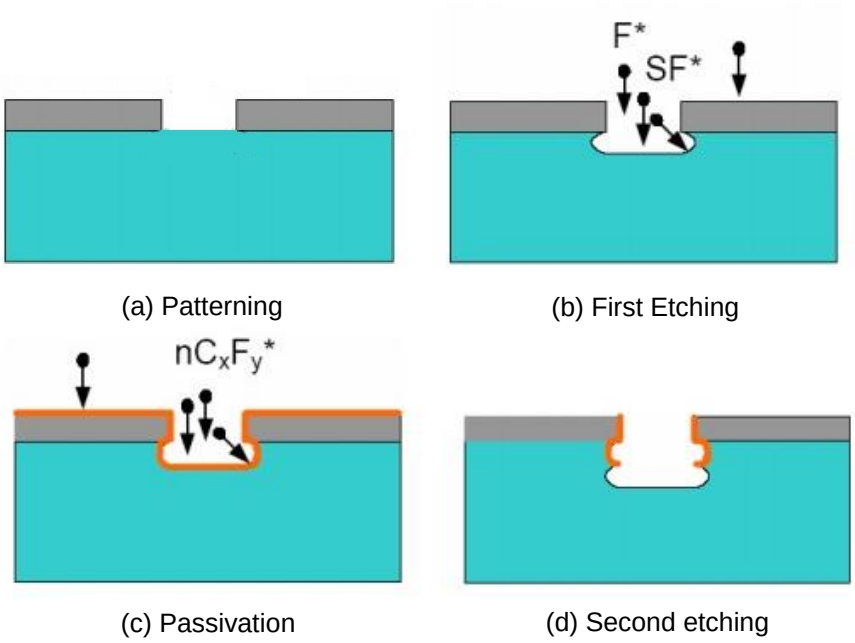

Figure 4-6 The stages in a standard Bosch process: (a) patterning of silicon substrate, (b) first etching step, (c) passivation step and (d) second etching step (adapted from [57]), in which SF_6 and C_4F_8 are typically used as the etchant gas and passivation source, respectively.

Examples of high-aspect-ratio structures fabricated by using this process are given in Figure 4-7. The Si nano-pillar array demonstrates that extremely fine lateral dimensions down to the nanoscale can be obtained. The 10 µm pillar array with a kerf of 5 µm and height of 220 µm is very close to the master mould structure required for high frequency regular piezocomposites. The fine trenches with depths up to ~300 µm demonstrate that a high-aspect-ratio up to ~100 is achievable. These characteristics make Bosch deep Si etching a promising technique for the mould fabrication in this study. However, considering Si cannot be easily removed by chemical dissolution or thermal burnout, it is not ideally suited for use as a lost mould.

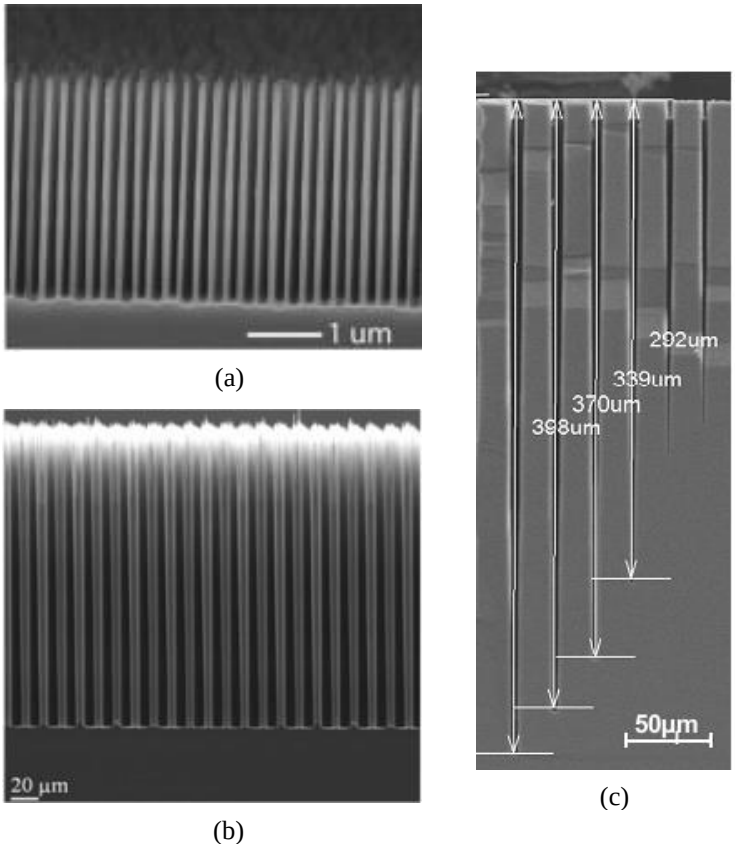

Figure 4-7 Examples of high-aspect-ratio structures fabricated by the Bosch process: (a) Si pillars with diameters of 80-95 nm and aspect ratios ~30 [58]; (b) 10 µm Si pillars with a height of 220 µm and kerf of 5 µm [59]; (c) Si trenches with a depth up to 308 µm and aspect ratios up to 97 [60].

One drawback of this technique is that the periodic etching/passivation in the Bosch process causes scalloping of the sidewalls in the obtained structures as shown in Figure 4-8. The presence of these scallops is apparently not desirable for it to be used in the soft moulding process. Such scallops can be reduced to be in the range of 50 nm by optimising the processing parameters such as the ratio of applied power to pressure, and the ratio of the etching to passivation step times [61]. Another possible method to improve the surface finish is to introduce a thin coating layer over the Si surface, covering these continuous scallops whilst still maintaining the desirable features. For example, Parylene deposition has been utilised to serve this purpose and proven to be effective in smoothing the sidewalls of etched Si structures [62, 63].

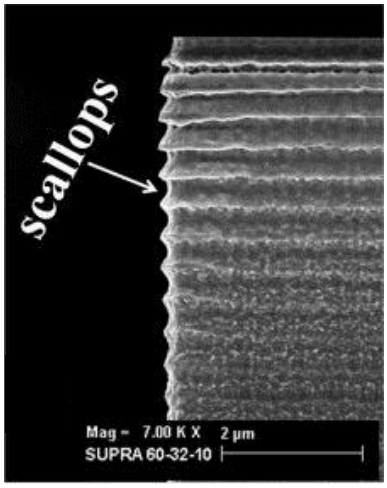

Figure 4-8 SEM image of a scalloped silicon side wall after standard Bosch etch [64].

4.7 Summary

Among the microfabrication techniques that have been reviewed, µ-EDM and laser machining are not suitable for producing micro-scale features, LIGA has the inherent drawback of high cost, while UV-lithography and Bosch deep etching silicon have shown to have good potential to meet the requirements for the mould fabrication, although no single structure reported to date possesses all the desirable features.

For the master mould, both UV-lithography of SU 8 and deep etching of Si are applicable, proven by the reviewed positive structures. The sidewall roughness of the etched Si requires further improvement by optimising the processing parameters and/or through conformal coating of a polymer film.

For the lost mould, UV-lithography is a much better choice than the Bosch process, considering the difficulty to etch Si away but still maintain the integrity of tall and thin ceramic segments. Of the currently available thick photoresists, negative resists are either difficult to remove or require mechanical agitation/heating to assist stripping; positive resists are easier to be stripped but typically require multiple spin coatings and hence is a more complicated process. Two new photoresists, negative-

tone AZ 125nXT and positive-tone AZ 40XT, originally designed for electroplating, were recommended by Microchemicals for this project. Both of them are claimed by the producer to have excellent strippabillity and to be able to produce thick films over 100 µm by standard single coating. Their possibilities for moulding ceramic micro-arrays have been investigated in this thesis.

4.8 References

[1] T. J. Clipsham, "The replication of micron scale pillar arrays for medical ultrasound applications," 2010.

[2] Y.-S. Liao, *et al.*, "Fabrication of high aspect ratio microstructure arrays by micro reverse wire-EDM," *Journal of Micromechanics and Microengineering*, vol. 15, p. 1547, 2005.

[3] K. Liu, *et al.*, "Process capabilities of Micro-EDM and its applications," *The International Journal of Advanced Manufacturing Technology*, vol. 47, pp. 11-19, 2010.

[4] K. Rajurkar, *et al.*, "Micro and nano machining by electro-physical and chemical processes," *CIRP Annals-Manufacturing Technology*, vol. 55, pp. 643-666, 2006.

[5] D. T. Pham, *et al.*, "Micro-EDM—recent developments and research issues," *Journal of Materials Processing Technology*, vol. 149, pp. 50-57, 2004.

[6] A. K. Dubey and V. Yadava, "Experimental study of Nd:YAG laser beam machining—An overview," *Journal of Materials Processing Technology*, vol. 195, pp. 15-26, 2008.

[7] J. Giboz, *et al.*, "Microinjection molding of thermoplastic polymers: a review," *Journal of micromechanics and microengineering*, vol. 17, p. R96, 2007.

[8] C.-R. Yang, *et al.*, "Photoablation characteristics of novel polyimides synthesized for high-aspect-ratio excimer laser LIGA process," *Journal of Micromechanics and Microengineering*, vol. 14, p. 480, 2004.

[9] A. K. Dubey and V. Yadava, "Laser beam machining—A review," *International Journal of Machine Tools and Manufacture*, vol. 48, pp. 609-628, 2008.

[10] L. Tunna, *et al.*, "Analysis of laser micro drilled holes through aluminium for micro-manufacturing applications," *Optics and Lasers in Engineering*, vol. 43, pp. 937-950, 2005.

[11] Y. Zhang, *et al.*, "High aspect-ratio micromachining of polymers with an ultrafast laser," *Applied surface science*, vol. 186, pp. 345-351, 2002.

[12] Y. Xia and G. M. Whitesides, "Soft lithography," *Annual review of materials science*, vol. 28, pp. 153-184, 1998.

[13] M. J. Madou, *Fundamentals of microfabrication: the science of miniaturization*: CRC, 2002.

[14] D. W. Kufe, *et al.*, "Holland-Frei cancer medicine," 2003.

[15] J. Derksen, *et al.*, "Extrusion-spin coating: an efficient photoresist coating process for wafers," in *Semiconductor Manufacturing Conference Proceedings, 1999 IEEE International Symposium on*, 1999, pp. 245-248.

[16] D. Bornside, *et al.*, "Spin coating: One‐dimensional model," *Journal of Applied Physics*, vol. 66, pp. 5185-5193, 1989.

[17] V. S. Rao, *et al.*, "A thick photoresist process for advanced wafer level packaging applications using JSR THB-151N negative tone UV photoresist," *Journal of Micromechanics and Microengineering*, vol. 16, p. 1841, 2006.

[18] (Last accessed 2013/02/14). *Spin Cating of Photoresists*. Available: http://www.microchemicals.com/technical_information/spin_coating_photoresist.pdf

[19] K. Cooper, *et al.*, "Conformal photoresist coatings for high aspect ratio features," *Proc. IWLPC, Sept*, 2007.

[20] B. Loechel, "Thick-layer resists for surface micromachining," *Journal of Micromechanics and Microengineering*, vol. 10, p. 108, 2000.

[21] E. Meng, *Biomedical microsystems*: CRC, 2010.

[22] M. Hennerici and D. Neuerburg-Heusler, *Vascular diagnosis with ultrasound: clinical reference with case studies* vol. 1: Thieme, 2005.

[23] C. Mack, *Fundamental principles of optical lithography: the science of microfabrication*: Wiley, 2011.

[24] M. Kubenz, *et al.*, "Effective baking of thick and ultra-thick photoresist layers by infrared radiation," *Microelectronic Engineering*, vol. 67, pp. 495-501, 2003.

[25] A. Del Campo and C. Greiner, "SU-8: a photoresist for high-aspect-ratio and 3D submicron lithography," *Journal of Micromechanics and Microengineering*, vol. 17, p. R81, 2007.

[26] B. Bhushan, *Springer handbook of nanotechnology*: Springer, 2004.

[27] M. Razeghi, *Fundamentals of solid state engineering*: Springer, 2009.

[28] S. Franssila, *Introduction to microfabrication*: Wiley, 2010.

[29] M. C. Peterman, *et al.*, "Building thick photoresist structures from the bottom up," *Journal of Micromechanics and Microengineering*, vol. 13, p. 380, 2003.

[30] M. J. Crocker, *Handbook of acoustics*: Wiley-Interscience, 1998.

[31] W. Flack, *et al.*, "The optimization and characterization of ultra-thick photoresist films," in *Advances in Resist Technology and Processing XV Proceedings*, 1998, pp. 1288-1303.

[32] C.-H. Lin, *et al.*, "A new fabrication process for ultra-thick microfluidic microstructures utilizing SU-8 photoresist," *Journal of Micromechanics and Microengineering*, vol. 12, p. 590, 2002.

[33] J. D. Williams and W. Wang, "Using megasonic development of SU-8 to yield ultra-high aspect ratio microstructures with UV lithography," *Microsystem technologies*, vol. 10, pp. 694-698, 2004.

[34] P. M. Dentinger, *et al.*, "Removal of SU-8 photoresist for thick film applications," *Microelectronic Engineering*, vol. 61, pp. 993-1000, 2002.

[35] C. Lee and K. Jiang, "Fabrication of thick electroforming micro mould using a KMPR negative tone photoresist," *Journal of Micromechanics and Microengineering*, vol. 18, p. 055032, 2008.

[36] Y.-M. Shin, *et al.*, "UV lithography and molding fabrication of ultrathick micrometallic structures using a KMPR photoresist," *Microelectromechanical Systems, Journal of*, vol. 19, pp. 683-689, 2010.

[37] Q. Wenmin, *et al.*, "UV-LIGA: a promising and low-cost variant for microsystem technology," in *Optoelectronic and Microelectronic Materials Devices, 1998. Proceedings. 1998 Conference on*, 1998, pp. 380-383.

[38] J. O'Brien, *et al.*, "Advanced photoresist technologies for microsystems," *Journal of Micromechanics and Microengineering*, vol. 11, p. 353, 2001.

[39] B. Todd, *et al.*, "Thick photoresist imaging using a three-wavelength exposure stepper," in *Symposium on Micromachining and Microfabrication*, 1999, pp. 330-344.

[40] H. Jung-Tang, *et al.*, "Using an Innovative Polishing Process to Fabricate Ultra-High Uniformity of Polymer Surface," in *Polymers and Adhesives in Microelectronics and Photonics, 2007. Polytronic 2007. 6th International Conference on*, 2007, pp. 213-216.

[41] P. Niedermann, *et al.*, "A novel thick photoresist for microsystem technology," *Microelectronic Engineering*, vol. 67, pp. 259-265, 2003.

[42] X. Wei, *et al.*, "Thick photoresists for electroforming metallic microcomponents," *Proceedings of the Institution of Mechanical Engineers, Part C: Journal of Mechanical Engineering Science*, vol. 222, pp. 37-42, 2008.

[43] V. Conédéra, *et al.*, "Potentialities of a new positive photoresist for the realization of thick moulds," *Journal of Micromechanics and Microengineering*, vol. 9, p. 173, 1999.

[44] W. Qu, *et al.*, "One-mask procedure for the fabrication of movable high-aspect-ratio 3D microstructures," *Journal of Micromechanics and Microengineering*, vol. 8, p. 279, 1999.

[45] J. R. Stanec, *et al.*, "Integrating micromachined circuits to submillimeter systems," in *Microwave Conference (EuMC), 2010 European*, 2010, pp. 53-56.

[46] H. Chung-Yi, *et al.*, "A thick photoresist process for open-channel sensing packaging applications by JSR THB-151N negative UV photoresist," in *Microsystems, Packaging, Assembly and Circuits Technology, 2007. IMPACT 2007. International*, 2007, pp. 288-291.

[47] B. Löchel, *et al.*, "Galvanoplated 3D structures for micro systems," *Microelectronic Engineering,* vol. 23, pp. 455-459, 1994.

[48] N. Basak, *et al.*, "Characterisation and application of BPR-100 thick photoresist," *Micro & Nano Letters, IET,* vol. 2, pp. 115-117, 2007.

[49] B.-T. Lee, *et al.*, "Fabrication of polymeric large-core waveguides for optical interconnects using a rubber molding process," *Photonics Technology Letters, IEEE,* vol. 12, pp. 62-64, 2000.

[50] S. Roth, *et al.*, "High aspect ratio UV photolithography for electroplated structures," *Journal of Micromechanics and Microengineering,* vol. 9, p. 105, 1999.

[51] S. Oh, "Thick single-layer positive photoresist mold and poly (dimethylsiloxane)(PDMS) dry etching for the fabrication of a glass–PDMS–glass microfluidic device," *Journal of Micromechanics and Microengineering,* vol. 18, p. 115025, 2008.

[52] B. P. Chaudhri, *et al.*, "A high aspect ratio SU-8 fabrication technique for hollow microneedles for transdermal drug delivery and blood extraction," *Journal of Micromechanics and Microengineering,* vol. 20, p. 064006, 2010.

[53] H.-K. Chang and Y.-K. Kim, "UV-LIGA process for high aspect ratio structure using stress barrier and C-shaped etch hole," *Sensors and Actuators A: Physical,* vol. 84, pp. 342-350, 2000.

[54] J. Donohue, *et al.*, "Recent Improvements in Deep Silicon Etching."

[55] N.-T. Nguyen and S. T. Wereley, *Fundamentals and applications of microfluidics*: Artech House Publishers, 2002.

[56] J. Burghartz, *Ultra-thin chip technology and applications*: Springer, 2010.

[57] H. Qu, "Development of DRIE CMOS-MEMS process and integrated accelerometers," PhD, University of Florida, 2006.

[58] K. J. Morton, *et al.*, "Wafer-scale patterning of sub-40 nm diameter and high aspect ratio (> 50: 1) silicon pillar arrays by nanoimprint and etching," *Nanotechnology,* vol. 19, p. 345301, 2008.

[59] Q. Cai, *et al.*, "Design, development and tests of high-performance silicon vapor chamber," *Journal of Micromechanics and Microengineering,* vol. 22, p. 035009, 2012.

[60] K. Owen, *et al.*, "High aspect ratio deep silicon etching," in *Micro Electro Mechanical Systems (MEMS), 2012 IEEE 25th International Conference on*, 2012, pp. 251-254.

[61] B. Wu, *et al.*, "High aspect ratio silicon etch: A review," *Journal of applied physics,* vol. 108, pp. 051101-051101-20, 2010.

[62] A. Andrei, *et al.*, "A response surface model predicting the in vivo insertion behavior of micromachined neural implants," *Journal of neural engineering,* vol. 9, p. 016005, 2011.

[63] H.-S. Noha, *et al.*, "Parylene micromolding, a rapid and low-cost fabrication method for parylene microchannel," *Sensors and Actuators B: Chemical*, vol. 102, pp. 78-85, 2004.

[64] M. Nowack, *et al.*, "Micro arc welding for electrode gap reduction of high aspect ratio microstructures," *Sensors and Actuators A: Physical*, vol. 188, pp. 495-502, 2012.

CHAPTER 5 AIMS AND OBJECTIVES

1-3 piezcomposites have become the active material of choice for commercial ultrasound transducers due to their high energy conversion efficiency, favourable acoustic impedance and flexibility. The need for improved imaging resolution for a range of applications in medical ultrasound calls for high frequency transducers, which requires the piezocomposites to be fabricated with smaller and smaller feature sizes. With conventionally used regular composite patterns, it becomes increasingly challenging to produce fine kerfs for frequencies over 30 MHz, and therefore the interference of spurious modes are almost unavoidable. The innovative random composite design is of interest in this project as it relaxes the overall fine-scale restrictions imposed on the high frequency piezocomposites whilst having the potential to completely eliminate undesired spurious resonances.

The physical realisation of such random composites is the primary goal of this research programme. The review of the relevant literature presented in the preceding chapters has enabled the following strategy to achieve this goal to be proposed.

Fabrication methods for piezocomposites, micro-moulding techniques including lost-mould (or hard-moulding) and soft-moulding routes have been identified to be promising candidates. However, the capabilities of these routes are currently limited by two factors: the strength of the ceramic/binder system and the structure of the mould. Therefore, the developments of a high strength ceramic/binder system and a suitable random mould fabrication technique for this particular application are two initial targets of paramount importance.

A gel-casting system based on water-soluble epoxy has been selected for the preparation of the PZT slurry. It is necessary to undertake further optimisation on constituent ratios and processing parameters in order to gain PZT components with sufficiently high green strength to maintain the desired structure through the subsequent fabrication steps.

Among various techniques for the mould fabrication, deep etching of Si and UV lithography of SU 8 have been selected as the fabrication routes for master moulds used in soft (indirect) moulding of random ceramic segments; UV lithography of two newly developed AZ photoresists has been proposed for the production of lost moulds required in hard (direct) moulding. Due to a lack of the equipment for Si etching within the School of Metallurgy and Materials, Birmingham, investigations into the Si master moulds will be carried out by a collaborator in the University of Edinburgh. The feasibility of the mould fabrication techniques will determine the selection of the moulding routes to be used.

Once the desired random negative mould structure is achieved, demoulding tests can be carried out using the gel-cast ceramics. Further modification of the gel casting slurry system and/or the demoulding conditions may be required at this stage to maintain the integrity of the demoulded ceramic segments. Successfully demoulded segments will allow the fabrication and evaluation of novel random piezocomposites. Finally, high frequency transducers can be constructed using the random composites as the active materials and the performance of these novel transducers can be assessed.

The key objectives in this project are:

1) Optimise the water-soluble epoxy-based gel casting system, considering all the processing stages from the preparation of premixed solution to sintering;
2) Evaluate the feasibility of UV lithography and deep silicon etching for the realisation of random negative structures ready for gel casting;
3) Study the compatibility between the gel casting system and the demoulding techniques, leading to the production of the randomised ceramic segments;
4) Fabricate and characterise 1-3 piezocomposites with the novel random design;
5) Construct and characterise high frequency transducers incorporating random composites.

CHAPTER 6 RESEARCH METHODOLOGY

6.1 Process procedures

6.1.1 Mould fabrication

6.1.1.1 Fabrication of photoresist moulds

All the photoresist moulds, also referred to as hard moulds in this research, were produced by traditional photolithography methods as illustrated in Figure 6-1. Novel thick photoresists AZ 125nXT and AZ 40XT provided by MicroChemicals GmbH in Germany and traditional thick photoresist SU 8-50 from Chestech Ltd. in the UK were used as the starting materials. 4-inch single crystal (<100>) silicon wafers (Compart Technology Ltd, UK) with one side polished, with the reversed etched, were employed as substrates. The processing parameters for each photoresist are listed and discussed in detail in Chapter 8.

Prior to spin coating, a hot plate (model 1000-1, Electronic Microsystems Ltd, UK) used for baking, was calibrated before use and set to the desired temperature. A Si wafer with the polished surface facing upward was placed and carefully centred on the vacuum chuck of a spin coater (Headway Research Inc., USA). The spin speed and the timer were adjusted to the required values. The photoresist with a controlled volume was then poured on the central area of the wafer surface. To ensure complete coverage of the wafer, the photoresist was poured onto the wafer to cover approximately 1/4 of the surface area. The spin coater was turned on and stopped automatically after the set spin cycle had been completed. The wafer, now uniformly coated with the photoresist was carefully transferred to the pre-heated hot plate.

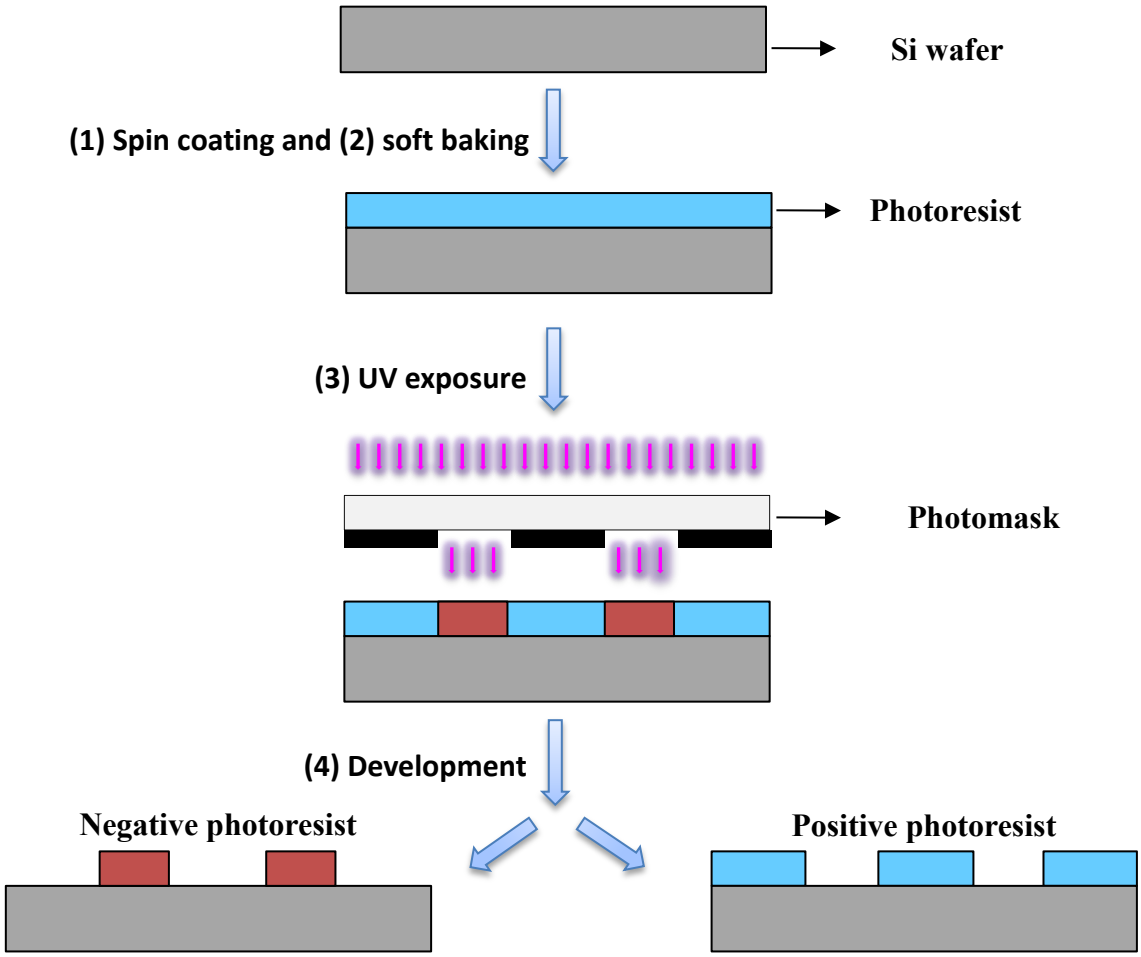

Figure 6-1 Schematic illustration of the photolithographic process.

Following coating and baking, the wafer was cut into rectangular sections, typically with dimensions of 2x3 cm, using a diamond pen along the [100] crystalline direction. A contact mask aligner (model MJB 3, Karl Suss, Germany) with a mercury lamp was employed to expose the photoresist coating through openings in a chromium-coated quartz photomask (Qudos technology, UK). The average output UV intensity was 4.58-4.88 mW/cm^2 during the experiments. A series of 4-inch photomasks with regular and randomised patterns (2x2 mm) were designed for the photoresist mould fabrication. Optical images of individual regular and random patterns are presented in Chapter 8.

A post-exposure bake is required for the AZ 40XT and SU 8-50 photoresists to thermally drive the chemical reactions but is not necessary for AZ 125nXT as it crosslinks at room temperature after/during exposure. Development was performed by submerging the sample in a suitable developer, which was AZ 816MIF (MicroChemicals, Germany) for the AZ photoresists and EC solvent (Chestech Ltd., UK) for SU 8-50, and agitating for the required period. The developed wafer was then rinsed with distilled water and dried most commonly using an N_2 gun. In the case where high-aspect-ratio positive structures were involved, the samples were dried in air without using the N_2 gun.

6.1.1.2 Fabrication of Si moulds

Si master moulds with randomised segments on the surface were fabricated by deep dry etching of Si at the University of Edinburgh. A schematic representation of the main processing steps is depicted in Figure 6-2. 3-inch single crystal (<100>) silicon wafers (Compart Technology Ltd, UK) with both sides polished were used as the starting material. All gases involved in the dry etching were from BOC industrial gases in the UK and the chemicals used for wet etching were from Rohm and Hass in the UK.

In this process, multi-layer structures were added to the Si wafer and etched sequentially in order to transfer the pattern onto to the Si. Firstly, the Si wafer was oxidized at 1100 ºC, resulting in the formation of thin silicon dioxide films of 1.5 μm on both sides. A 0.5 μm thick layer of pure Al was sputtered on the top surface of the wafer. Megaposit SPR 660-1 positive photoresist designed for processing features as small as 0.35 μm was spin coated on top of the Al coated sample and subsequently exposed under the UV energy of 60 mJ/cm^2 and then developed in A26 developer,

giving the desired randomised patterns with thicknesses of ~0.7 µm. Inductively coupled plasma involving Cl_2 and Ar gas mixture was used to etch the exposed Al. An O_2 plasma was applied to remove the remaining photoresist, followed by dry etching of the underlying oxide in CHF_3 and Ar gases, exposing the Si underneath. After etching the remaining Al in Aletch solution, the wafer was cleaned in Piranha solution and subsequently in an O_2 plasma. A low frequency (10 kHz) Bosch programme had been optimised to deep etch the Si by performing etching in SF_6 for 9.5 s and passivation in a C_4F_8 and O_2 mixture for 4.5 s. The oxide was removed in buffered HF (4:1) and the Si wafer with the desired structures was conformally coated with a 100 nm thick layer of Parylene.

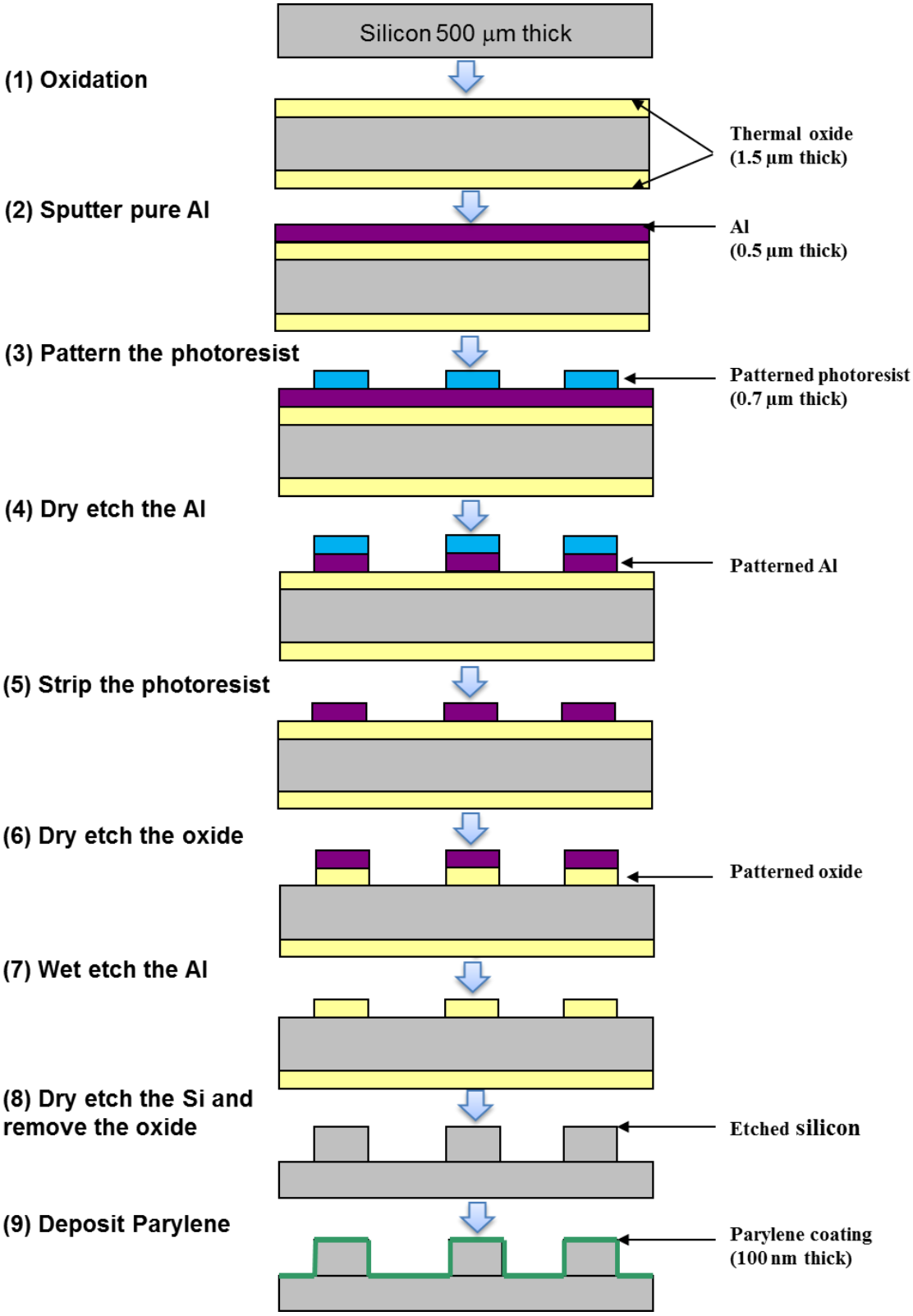

Figure 6-2 Schematic diagram of the main processing steps to fabricate Si master moulds with high-aspect-ratio randomised segments on the surface.

The design of the photomask used in deep etching is shown in Figure 6-3. The reason to design a mask with most of its area covered with desired features for etching is to improve manufacturing yield and also to decrease grass-like residues during etching as found from the practical experience of the researchers at the University of Edinburgh. Figure 6-4 gives a detailed illustration of the dimensions of an individual random pattern and the gaps in between features on the mask. The randomised patterns with the same overall size of 2x2 mm are separated by 100 µm gaps in the Y direction and 2 mm gaps in the X direction. The red lines on Figure 6-4 give an indication of the dicing channels on the resulting etched Si wafer. Each unit diced Si master mould would have a 2x2 mm square of randomised segments and a 2x2 mm square of bare silicon without any features on to be used as a handle for using tweezers. Figure 6-5 shows a 3D drawing of a unit diced Si master mould.

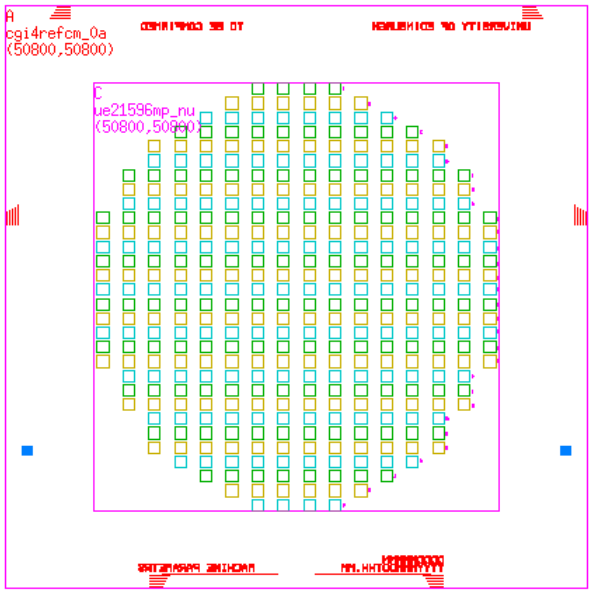

Figure 6-3 Design of 4-inch photomask with randomised patterns (2x2 mm) used for the etching of Si. The area inside of the square is the randomised features designed for etching.

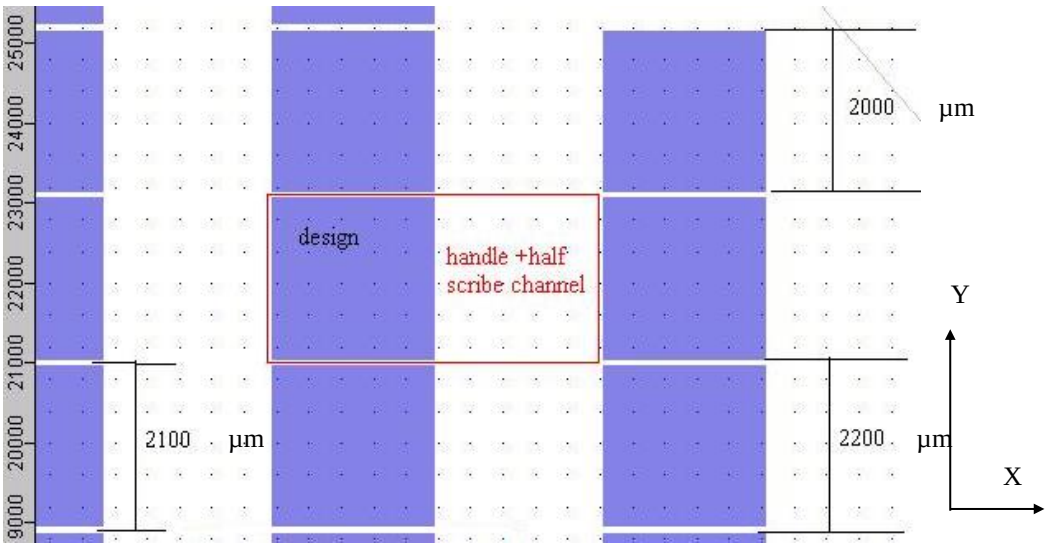

Figure 6-4 Schematic illustration of the dimensions of the patterns and the gaps in between as well as the designed dicing channels as marked in red.

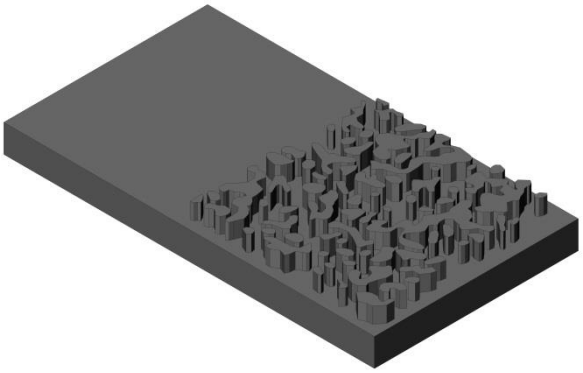

Figure 6-5 Schematic representation of a Si master mould after dicing. Note: the random pillars scale is larger and density lower in the schematic shown here for illustrative purposes only.

6.1.1.3 Fabrication of soft moulds

PDMS (Polydimethylsiloxane) as introduced in Section 3.4.4 was used for the fabrication of the elastomeric soft moulds in this project. A Schematic illustration of the fabrication procedures is shown in Figure 6-6. Firstly, the master mould was positioned at the centre of a petri dish with the target structures facing upwards. A range of master moulds was used for the replication of the soft moulds, including die pressed green-state Al_2O_3 discs, aluminium bars, etched Si with randomised structures

and other metal/polymer formers. Secondly, a 10:1 weight ratio mixture of PDMS-Sylgard Silicone Elastomer 184 and Sylgard Curing Agent (Dow Corning Corporation Limited, UK) was mixed thoroughly by hand in a beaker and then de-aired under vacuum until most of air bubbles had disappeared. The mixture was subsequently poured onto the master template and the whole assembly was transferred into a vacuum desiccator to get rid of any residual air bubbles. The degassing steps usually took approximately 10-30 min, varying with the amount of the mixture used. The PDMS then was cured at 65 °C for 4 h and the resulting rigid PDMS was carefully peeled off from the master, giving the soft mould with the negative of the desired structures.

When replicating from a Si master with high-aspect-ratio and randomised segments on its surface, according to the experience of the author, it was crucial to fix the assembly in place by sticking the bottom of the Si master to a substrate such as a glass slide before peeling.

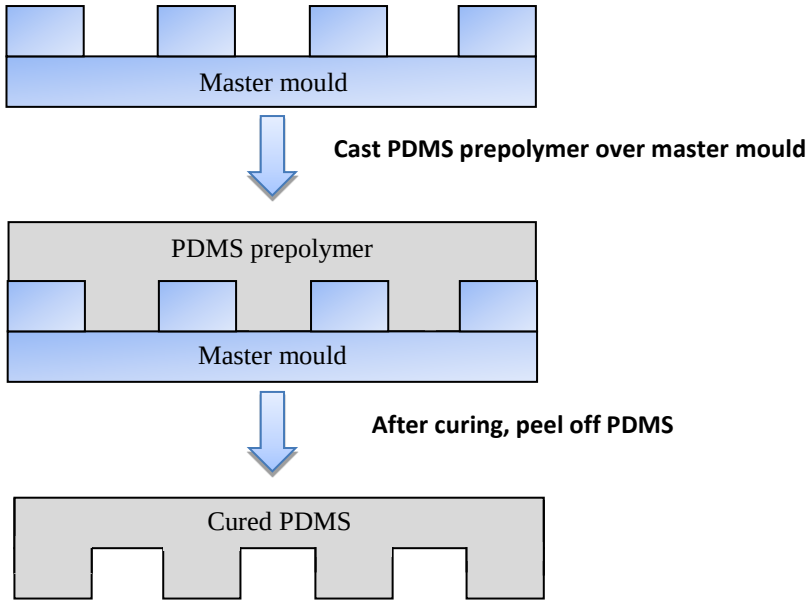

Figure 6-6 Outline of the procedures for fabricating PDMS soft moulds replicated from a master mould with relief structures on the surface.

6.1.2 Fabrication process of bulk ceramics by gel casting

6.1.2.1 Vibro-milling of PZT powder

A commercial PZT powder (TRS 610C, TRS Technologies, USA) with a density of 7.95 g/cm^3 [1] was used as the raw material for this study. Vibro-milling of the powder was introduced to break down any hard agglomerates. This process is schematically shown in Figure 6-7. In a typical batch, a few drops of the dispersant, ammonium polyacrylate (Dispex A40, Allied Colloids, Bradford, UK) and 250 g PZT powder was added to 300 ml of distilled water and the resulting suspension was vibro-milled with zirconia balls in a polythene bottle for 24 hours, followed by a freeze-drying stage for 2 days in a freeze drier (Labconco Corp., Kansas City, USA).

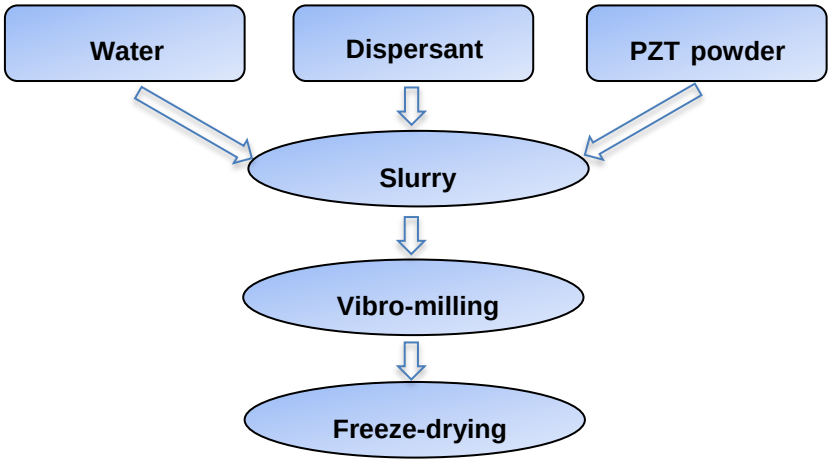

Figure 6-7 Flow chart of the vibro-milling process of the commercial PZT powder.

6.1.2.2 Preparation of gel casting PZT suspensions

The raw materials involved for the preparation of gel casting PZT suspensions with their functions, suppliers as well as important characteristics are listed in Table 6-1.

Table 6-1 Raw materials used for the preparation of gel casting PZT suspensions.

Material	Function	Product & Supplier	Details
Vibro-milled PZT	Powder	-	Mean particle size: 1.1 μm
Distilled water	Solvent	-	Resistivity at 25 ºC: 17 MΩ·cm
Ammonium polyacrylate (NH_4PAA)	Dispersant	Dispex A40, Allied Colloids, UK	Concentration: 37.6 wt.%
Ethylene glycol diglycidyl ether (EGDGE)	Epoxy Monomer	EX-810, Nagase ChemteX Corporation, Japan	Epoxy equivalent weight: 113 g/mol; Water solubility: 100%
Bis(3-aminopropyl)amine	Cross-linker	Sigma-Aldrich, Germany	Molecular weight: 131.22 g/mol

For consolidation of the slurry, EGDGE and Bis(3-aminopropyl)amine were employed as the epoxy resin and hardener, respectively, the chemical structures of which are shown in Figure 6-8. The amount of EGDGE used in this research is expressed as a weight percentage of the premix solution prepared by dissolving

EGDGE in the distilled water. The addition of the hardener is expressed as the number of moles per equivalent weight of epoxy in the premix solution, i.e. mol/eq [2].

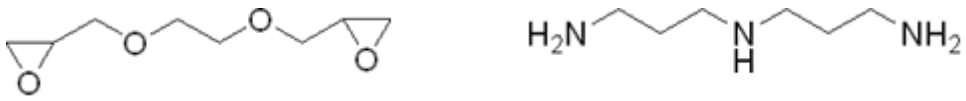

(a) EGDGE (b) Bis(3-aminopropyl)amine

Figure 6-8 Chemical structure for the (a) epoxide resin: $C_8H_{14}O_4$, EGDGE; (b) hardener: $C_6H_{17}N_3$, Bis(3-aminopropyl)amine.

For dispersion of the powder, Dispex A40 was used throughout this study. The amount of the dispersant is described by a dry weight of the PZT powder basis, equivalent to the wt. /wt. basis of the powder. The quantity of the PZT powder is represented by the solid volume fraction of the suspension, i.e. vol% solids loading. The solids loading was kept as 45 vol% in this thesis, a value which was selected based on previous work [3]. Table 6-2 shows an example of gel casting composition in terms of the actual amount and weight percentage of each material and in terms of how it was defined in this work.

Table 6-2 An example of gel casting composition.

	PZT	Dispex A40	Distilled water	EGDGE	Bis(3-aminopropyl)amine
Actual amount (g)	50.430	0.500	4.200	2.800	0.647
Actual wt% in the suspension	86.1 wt%	0.9 wt%	7.2 wt%	4.8 wt%	1.0 wt%
Define in this thesis	45 vol%	1 wt%	N/A	40 wt%	0.2 mol/eq

The amount of each constituent material was calculated according to the designed values. All reagents were weighed to ± 0.001 g and a typical batch size was 60 g. All the suspensions were prepared at room temperature. The preparation procedures of the

gel casting slurry are detailed as follows. Distilled water was added to a 60 ml plastic bottle (Azlon, UK), followed by adding appropriate amounts of epoxy and dispersant. The bottle was then sealed and put on a magnetic stirrer plate in order to obtain thorough mixing. The solution was continuously stirred on the magnetic stirrer for 20 minutes. Half of the required amount of PZT powder was gradually added into the solution, which took around 15 minutes to complete. The slurry mixture was ball-milled with 25 g of zirconia balls, of 4.8 mm diameter for 2 hours before loading more powder. Staged addition of the ceramic powder is demanded in the gel casting process in order to achieve a well-mixed slurry with high solids loading and low viscosity [4, 5]. In this work, additions of PZT powder followed a pattern of 1/2, 1/4, 1/8, 1/8 of the required amount as suggested in [4]. The powder addition and ball-milling regimes describing the amount of the powder added in each step, as well as the milling periods between the addition stages are depicted in Figure 6-9. A relatively low ball-milling speed of 70 rpm was applied to effectively incorporate the powder into the slurry and limit the amount of air bubbles generated during mixing.

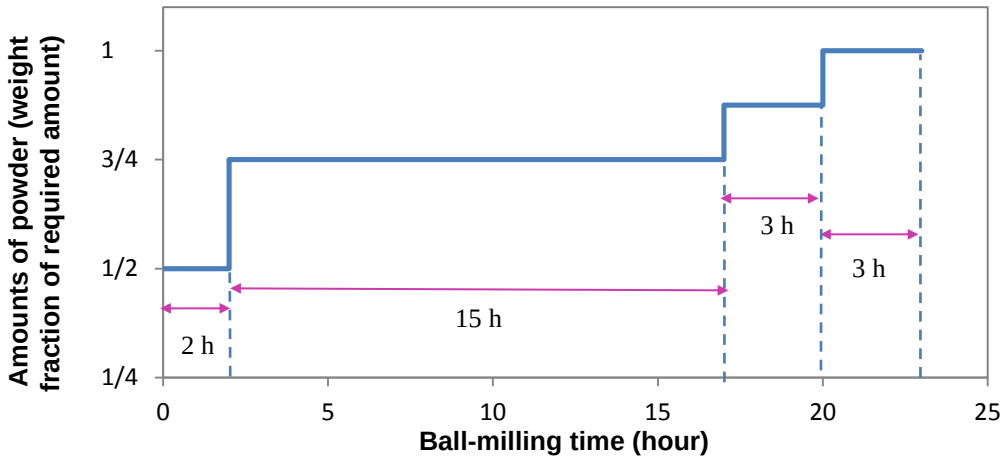

Figure 6-9 Schematic diagram of ball-milling and powder addition regime for all the gel casting suspensions.

6.1.2.3 De-airing, casting and drying

The ball-milled slurry was transferred into a beaker and the appropriate amount of Bis(3-aminopropyl)amine was added into the slurry and gently mixed using a spatula for 2-3 minutes. The air bubbles introduced during mixing was reduced by degassing the slurry in a vacuum chamber for 2-3 minutes. The mixture was then slowly cast into PDMS moulds replicated from die pressed ceramic discs and/or aluminium bars and vacuumed for 1-2 minutes. The aim of vacuuming the suspension at this stage was not only to remove the trapped air bubbles, but also to aid the suspension to fully fill the mould cavities, in a process known as vacuum casting. Long vacuum times were not desirable for the slurries with high solids loadings involved in this work because extensive vacuum times can result in removal of the solvents [4], thereby increasing the viscosity as observed and reported in [6]. The time for casting and de-airing was strictly controlled in practise, ensuring the processing time in total did not exceed the induction time of the cross-linking reaction in the presence of ceramic particles (see Section 7.4.3).

Staged drying was applied to the gel casting suspensions to prevent the formation of cracks in the green compacts as a result of inhomogeneous drying. The slurry was initially dried at room temperature for 24 hours and then at 40 ºC in an oven for 24 hours. After carefully peeling off the PDMS moulds, the green bodies were moved to an oven with the temperature increased from 40 ºC to 100 ºC at the rate of 1 ºC/min, and then held at 100 ºC for 2 hours. The samples, now fully dried were ready for characterisation and sintering.

6.1.2.4 Burnout and sintering

Burnout of the organic components and sintering of PZT was carried out in a muffle furnace (Lenton furnace, UK) with a single heating cycle. It is well-known that the lead oxide component in PZT is highly volatile at temperatures above 800 ºC [7] and the loss of lead can affect the resultant chemical composition as well as its functional properties [8], which is of particular concern in sintering PZT. A commonly used means to counter the evaporation of lead is to use a PbO rich sintering atmosphere. In this work, such an atmosphere was created by using lead (II, III) oxide (Sigma-Aldrich, Germany) and doped ZrO_2 sands (Ferro Corporation, USA). The green-state specimens were put in a rectangular alumina crucible and buried in the ZrO_2 sand as illustrated in Figure 6-10. The PZT sample was first placed on a flat bed of sand consisting of a layer of coarse particles at the bottom and a layer of finer particles on the top, they were then encapsulated with another thin layer of fine ZrO_2 sand. The alumina crucible was covered with an alumina lid.

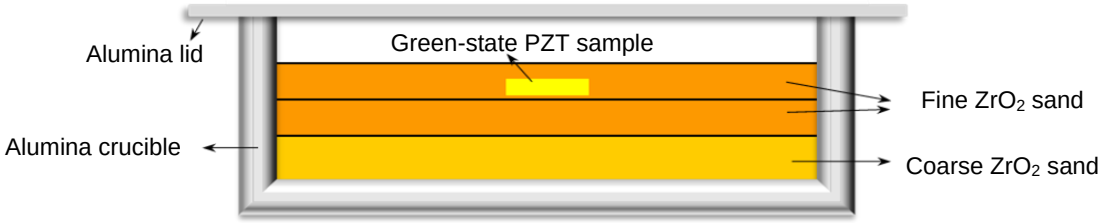

Figure 6-10 Schematic illustration of the arrangement of lead oxide doped ZrO_2 sand and the specimen in the alumina crucible for the burnout and sintering of bulk PZT samples.

The thermal regime for the burnout and sintering is schematically shown in Figure 6-11. Samples were heated at a slow temperature ramp rate of 1 ºC/min from 40 ºC to 500 ºC and dwelled for two hours to burn out the polymer, followed by a 5 ºC/min ramp to the sintering temperature of 1200 ºC. After one hour dwelling at 1200 ºC, the

samples were cooled down to 40 ºC at a ramp rate of 5 ºC/min. The ramp and temperature for the removal of the organics were designed based on the results of thermal analysis (see Section 7.5) and the temperature for sintering was selected as it was routinely used for PZT [3, 9].

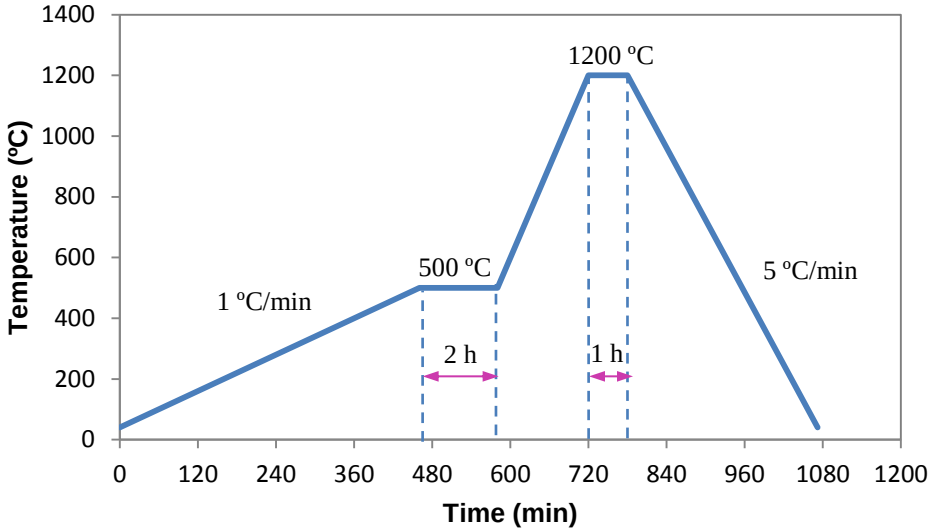

Figure 6-11 The thermal regime for the burnout of the organics and sintering for the green-state gel-cast PZT samples.

6.1.2.5 Summary

The flow chart of the gel casting process is presented in Figure 6-12, showing the raw materials and key processing stages involved from the slurry preparation to the final sintering.

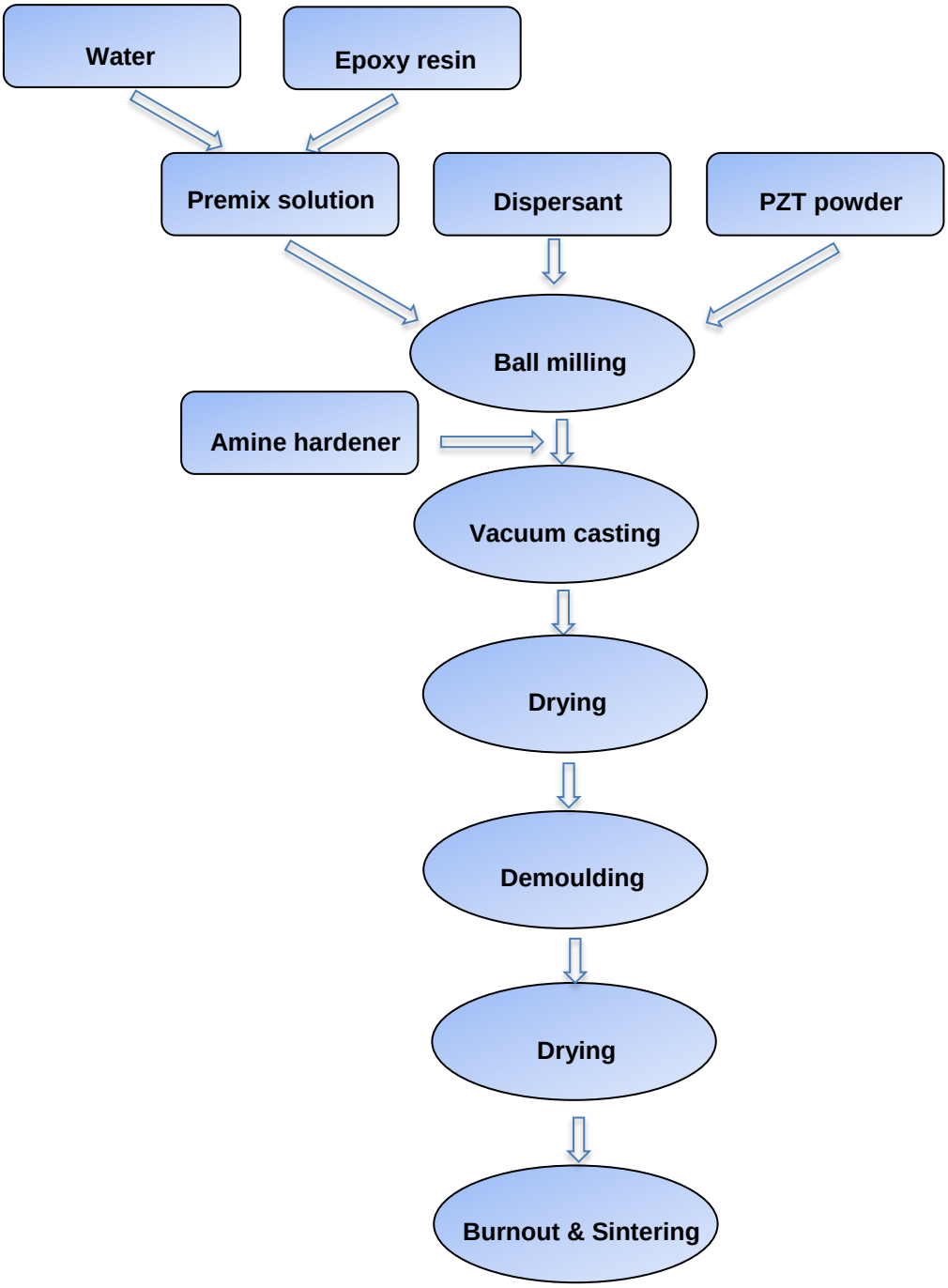

Figure 6-12 Flow chart of the gel casting process.

6.1.3 Fabrication process of 1-3 piezocomposites by gel casting

6.1.3.1 Casting and demoulding

In the fabrication of 1-3 piezocomposites, the procedures for the preparation, casting and drying of the gel casting slurry were the same as they were applied for the production of PZT bulk ceramics. Soft moulds involved had the desired negative structures of the bristle-blocks, replicated from Si masters, as described in Section 6.1.1.3. After fully filling the cavities of the moulds with the slurry, a thin glass slide with a clean and smooth surface was placed on the top of the slurry and gently pressed down. The role of the glass slide introduced at this step was to make sure that the bottom surface of the resultant PZT stock was parallel to the top surface comprising the tall and thin PZT segments. Any non-parallelism in the obtained stock base can lead to a reduction of the volume fraction of PZT in the lapped composite and even the complete loss of the PZT segments during lapping.

Demoulding of the fine-scale PZT segments from the PDMS moulds was similar to the process used to demould Si masters from the cured PDMS, but much more difficult as the surfaces of the gel cast PZT segments were much rougher compared with the Parylene-coated Si masters. The bottom surface of the dried PZT stock was initially fixed to a glass substrate using a double-sided sticky tape. The PDMS moulds were then carefully and slowly lifted up and away from the green body using tweezers.

6.1.3.2 Burnout and sintering

Burnout and sintering of gel-cast bristle-blocks was conducted using the thermal profile shown in Figure 6-11, previously applied for the bulk ceramics. Instead of being buried in lead oxide-doped ZrO_2 sands, the bristle-blocks were gently placed on

a flat bed of the sand with the segments facing upwards as shown in Figure 6-13, in order to minimise any contamination of sand on the delicate structures.

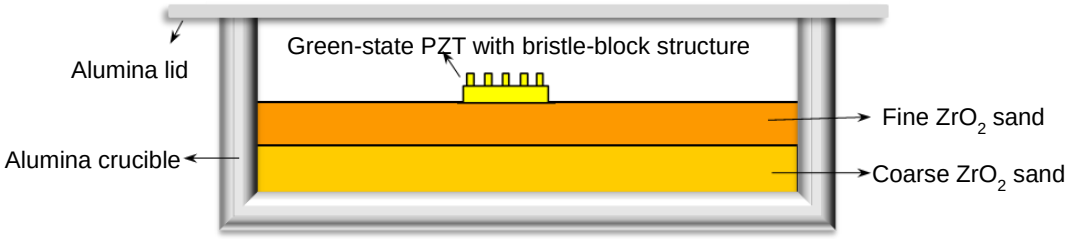

Figure 6-13 Schematic illustration of the arrangement of lead oxide doped ZrO_2 sands and the specimen in the alumina crucible for the burnout and sintering of gel cast bristle-block samples for the fabrication of 1-3 piezocomposites.

6.1.3.3 Backfilling

The sintered bristle blocks were backfilled with Epofix epoxy (Struers, UK), which was selected due to its favourable properties including low viscosity, minimal shrinkage, good mechanical properties and chemical resistance [10]. Before backfilling, the resin component of the Epofix was mixed with the hardener component at a resin to hardener weight ratio of 25:3. The sintered sample was placed in the centre of a PDMS mould with a cavity diameter of 2 cm and the mixed Epofix was slowly poured in the mould, followed by being degassed in a vacuum chamber to avoid entrapment of air in the resultant composite. After degassing, the mould was left at room temperature for 30 minutes and then transferred to a oven with the temperature increased from 40 ºC to 100 ºC at a ramp rate of 1 ºC/min. The epoxy was held at 100 ºC for 2 hours until fully cured [10] before being cooled down to room temperature.

6.1.3.4 Lapping

Precision lapping was carried out on the intermediate composite using a PM5 lapping machine (Logitech, Glasgow, UK) to achieve a flat 1-3 piezocomposite with a targeted thickness and surface finish. A suspension containing 9 µm Al_2O_3 powder and a carrier lubricant of distilled water and ethanediol was used for initial removal of excess epoxy and PZT stock base. A 3 µm Al_2O_3 powder suspension was used for further thinning of the composite until it reached a thickness of ~150 µm and then 1 µm Al_2O_3 powder suspension was finally used to lap the sample to the required thickness.

6.1.3.5 Non-contact poling

Non-contact corona poling was performed on the piezocomposites using custom assembled apparatus as shown in Figure 6-14. The high voltage required for poling in this process was obtained from corona discharges, which are a partial breakdown of air. The corona discharges are generated in an insulated chamber by applying a high voltage power supply to a copper pin. The high temperature required was provided by a hot plate, which also acted as the ground electrode. Compared with the commonly used contact poling technique, this method does not require electroding of the samples in advance and does not leave contact scratches or residues on the sample surfaces after poling. The composite was clamped using a copper plate and a glass ring to prevent curling of the composite during poling and the assembly was placed on the centre of the hot plate directly under of the copper pin. The sample was pre-heated to 110 ºC and then poled at that temperature by applying a high voltage of 30 kV for 10 min. The sample was then allowed to cool down under the set 30 kV voltage using a fan. The voltage was reduced to zero when the temperature reduced to 50 ºC.

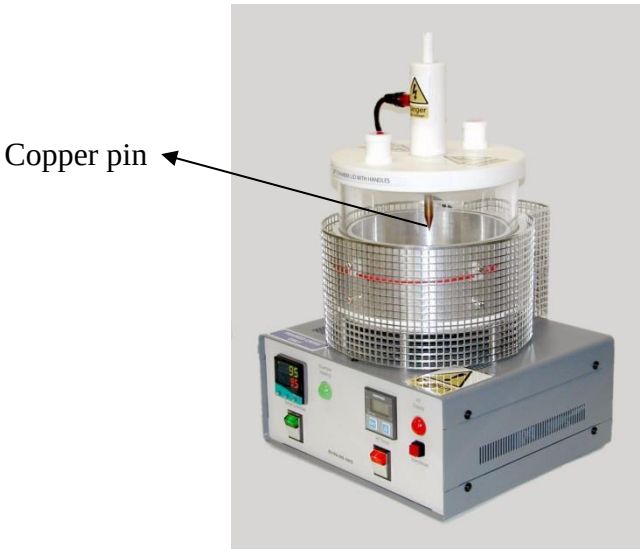

Figure 6-14 The custom assembled corona poling apparatus.

6.1.3.6 Electroding

Before electroding, an electrode mask of polycarbonate with a 2x2 mm square and a small 'tail' cut out by laser was positioned on the top of the composite, as illustrated in Figure 6-15. This ensured that the active composite area was electroded whilst avoiding shorting between the top and bottom electrodes via any pinholes in the surrounding epoxy caused by bubbles or sand that may have been included in the composite during the encapsulation stage.

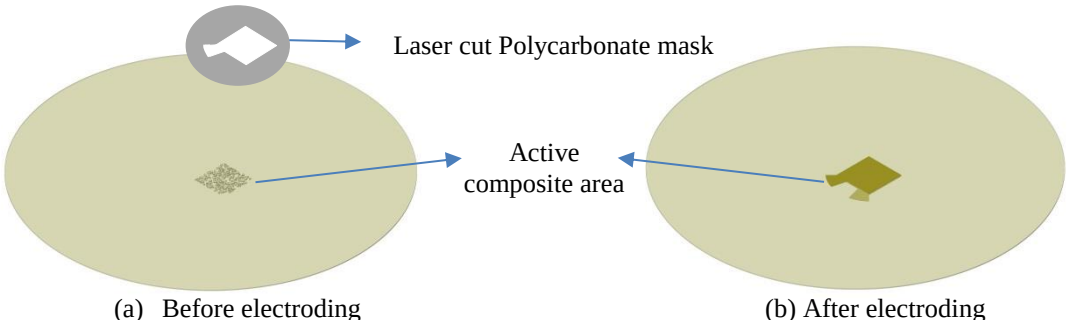

Figure 6-15 Schematic illustration of the use of a polycarbonate mask for the electroding of the piezocomposite with 2x2 mm square of active area in the centre.

Electroding was carried out using a Peltier cooled sputter coater (Emitech K575, Emitech Ltd., UK). This process involved sequentially depositing a thin layer (~10

nm) of Cr electrode at 100 mA current for two minutes, and a thicker layer (~200 nm) of Au electrode at 80 mA current for two 2 minute cycles on both sides of the samples. Cr was used to enhance the adhesion of the Au layer to PZT/epoxy composite and Au was chosen due to its well-known low resistivity [11].

6.1.3.7 Contact poling

Contact poling was employed to re-pole one of the piezocomposite samples. Poling was done in a 110 ºC oil bath by applying an electric field of 2.5 kV/mm along the thickness direction. After holding these conditions for 10 min, the voltage was then gradually reduced to zero and the sample was removed from the oil and allowed to cool down in air. The remaining poling oil on the sample surfaces was removed by dipping the samples in 2-proponol for ~30 seconds and then in distilled water for ~30 seconds.

6.1.3.8 Summary

The whole process for the fabrication of 1-3 piezocomposites with the novel random design is shown in Figure 6-16, comprising the first pattern replication from the Si master to the PDMS mould; the second replication from the negative PDMS mould to the gel cast bristle-block PZT, along with the encapsulation, lapping, poling and electroding stages necessary to achieve active piezocomposites ready for characterisation and transducer construction.

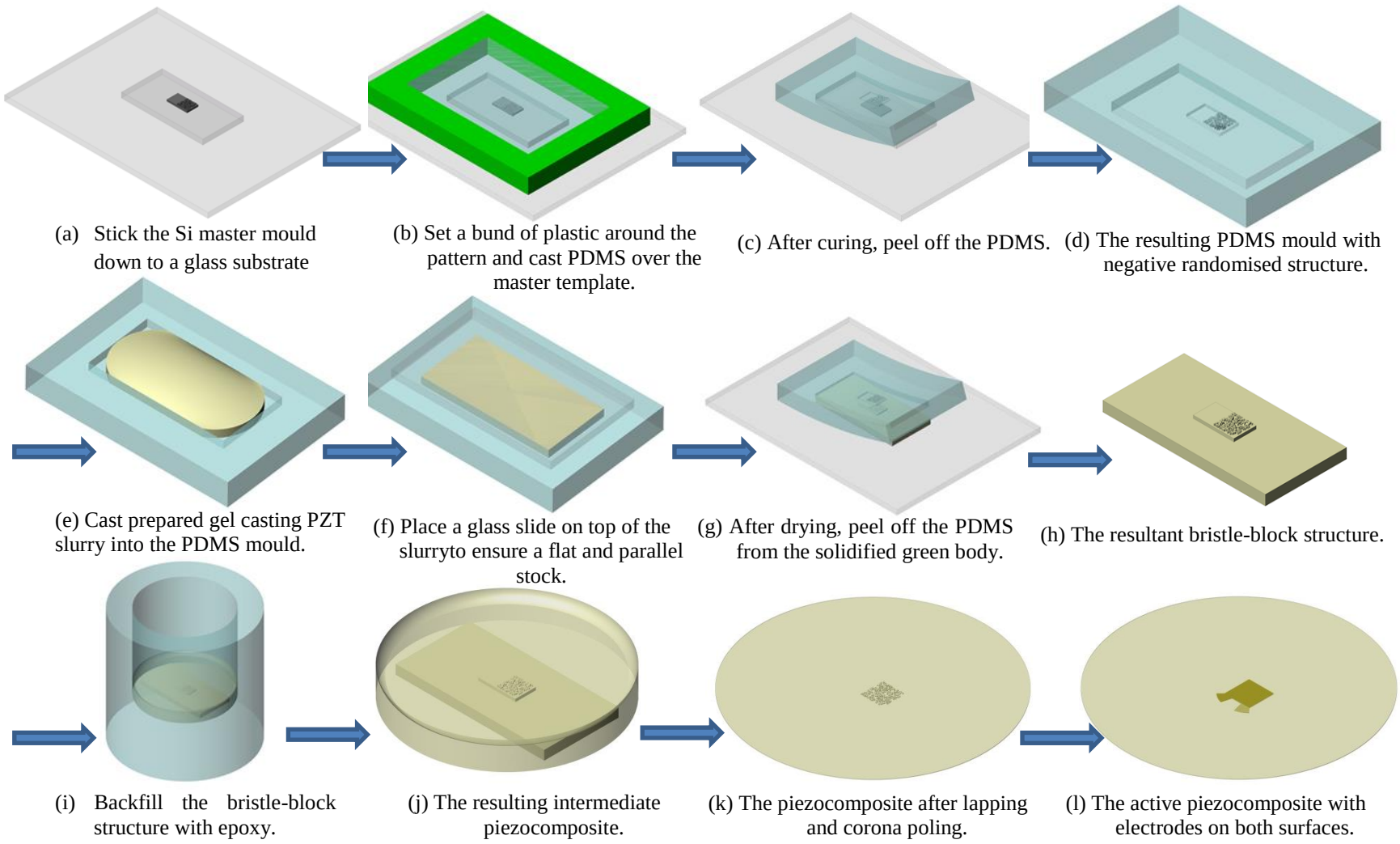

Figure 6-16 Schematic representation of the processing stages in the fabrication of the 1-3 piezocomposite.

6.2 Characterisation techniques

6.2.1 Rheological properties measurement

An AR 500 rotational rheometer (TA instruments, USA) was used to study the rheological properties of the premix solutions and the PZT suspensions. The measuring configuration adopted was a cone and plate (gap 55 μm, 40 mm, 2º). 4-6 drops of the testing material were transferred to a central position on the measuring plate for each measurement. When the final gap was attained, any excess testing fluid was carefully trimmed around the edge of the geometry.

6.2.1.1 Dynamic modulus monitoring

The elastic modulus *G'* and viscous modulus *G''* of the premix solutions and PZT suspensions during the epoxy-amine curing process was monitored by means of oscillatory shear deformation under a constant frequency of 1 Hz and a constant strain of 0.2% at various temperatures.

6.2.1.2 Viscosity measurement

A pre-shear of 10 seconds was applied to the testing fluids before each viscosity measurement. The flow behaviour of the PZT slurries with different dispersant concentrations and resin contents was characterised by measuring the viscosity under the continuous shear mode within the shear rate range of 0.1-600 s^{-1} at 25 °C. The gelation behaviour of the PZT slurries with varying resin contents was studied by monitoring the evolution of the viscosity under a constant shear of 0.1 s^{-1} at 25 °C.

6.2.2 Powder surface area measurement

The specific surface areas of the powders were measured using BET single point nitrogen adsorption (Micromeritics Area meter ASAP2010c, Norcross, USA). Two PZT powders including the as-received TRS 610C powder and the same powder after 24 hours vibro-milling have been tested.

6.2.3 Particle size analysis

The particle size of the powder was measured using a laser diffraction particle size analyser (Sympatec, Bury, UK). Before each test, a PZT suspension was prepared in a 5 ml vial, involving ~0.5 g PZT powder, ~3 g distilled water and one drop of $Na_4P_2O_7$ employed as a dispersant. After a reference measurement, a few drops of the prepared suspension were added into the integral ultrasonic bath of the analyser and sonicated for 15 s to break the soft agglomerates. During the measurement, the powder passed through a broadened beam of laser light which scatters the incident light onto a lens. By collecting the diffracted data from the lens, a particle size distribution was obtained.

6.2.4 Thermal analysis

NETZSCH simultaneous thermal analyser (STA 449C Jupiter) was used to study the influences of organic burnout on the weight loss and heat flow of the gel cast PZT samples. Thermogravimetric analysis (TGA) was used to detect the changes in weight as a function of temperature/time. Differential scanning calorimetry (DSC) measured the amount of heat absorbed or released from the sample during phase transitions. In this study, TGA/DSC was conducted in a flowing air atmosphere at a heating rate of 5 °C/min and 1°C/min respectively until 600 °C.

6.2.5 Density measurement

The densities of the green and sintered PZT plates were obtained according to Archimedes principle. The formula used for the calculation of the density ρ is given below:

$$\rho = \frac{W_d}{W_d - W_w} \qquad \textbf{Equation 6-1}$$

where W_d and W_w is the dry weight and the wet weight of the sample, respectively.

6.2.6 Linear shrinkage measurement

The linear shrinkage of the samples upon drying was obtained by measuring the diameters of the master moulds for producing the PDMS moulds and subsequent demoulded samples after complete drying, and calculated by the equation shown below:

$$L = \frac{D_M - D_d}{D_M} \times 100\% \qquad \textbf{Equation 6-2}$$

where L is the linear shrinkage, D_M is the diameter of the master mould, D_d is the diameter of the sample after drying.

6.2.7 Green strength measurement

To study the effect of resin content on the green strength, green PZT bars of 5.6 cm length, 0.9 cm width and 0.4 cm thickness were fabricated by consolidating gel casting PZT slurries with different resin concentrations in the PDMS moulds. After complete drying, the flexural strength of the PZT bars was measured by a three-point bending method using an Instron testing machine (Instron, Buckinghamshire, UK).

All the measurements used a specimen span of 50 mm and a load rate of 1 mm/min. For a rectangular bar, the flexural stress σ_f is calculated from the following equation:

$$\sigma_f = \frac{3xP_f}{2hw^2} \qquad \textbf{Equation 6-3}$$

where x is the specimen span, P_f is the fracture load during bending, h is the thickness and w is the width of the rectangular bar.

6.2.8 Impedance Analysis

An Agilent 4395A impedance analyser (Agilent Ltd, UK) with a frequency range of 10 Hz-500 MHz was used for the impedance measurements of the 1-3 piezocomposites and transducers operating at high frequencies up to 100 MHz. For each sample, impedance magnitude and phase, as well as capacitance were measured. The capacitance measurement was taken at 1 kHz (C_L) and at two times the anti-resonant frequency (C_H). The obtained parameters of each piezocomposite along with the values of the thickness, active area, and the mass were used for the calculation of piezoelectric properties based on the equations listed in Appendix I. d_{33} values of these piezocomposites were obtained by inputting the piezoelectric parameters into a one-dimensional modelling software package provided by the University of Dundee. This method for the calculation of d_{33} was previously reported by [12].

6.2.9 Laser vibrometry

The surface motions of the random piezocomposites was characterised using an ultra-high frequency (up to 1.2 GHz) laser vibrometer recently developed by Polytec Ltd. As shown in Figure 6-17(a), the whole testing system was composed of a heterodyne interferometer (UHF-120, Polytec Ltd., UK), a controller box (UHF-120, Polytec Ltd.,

UK), a signal generator (SMBV100A, Rohde & Schwarz, UK), an oscilloscope (WavePro 725Zi-A, Teledyne LeCroy, UK) and a computer.

Figure 6-17(b) schematically depicts how the components were connected. The sensor head utilised a visible laser that was focused on the point of interest on the sample surface. Precise focusing was achieved by using a video camera with an illumination device integrated in the sensor head and a sample positioning stage. The piezocomposite sample was driven by an input electrical signal from the generator. The resulting surface vibration of the sample was detected by the sensor, giving an electrical voltage signal proportional to displacement. Such information was fed directly to the oscilloscope for digitalisation, and then transferred to Vibsoft software (Polytec Ltd., UK) for analysing.

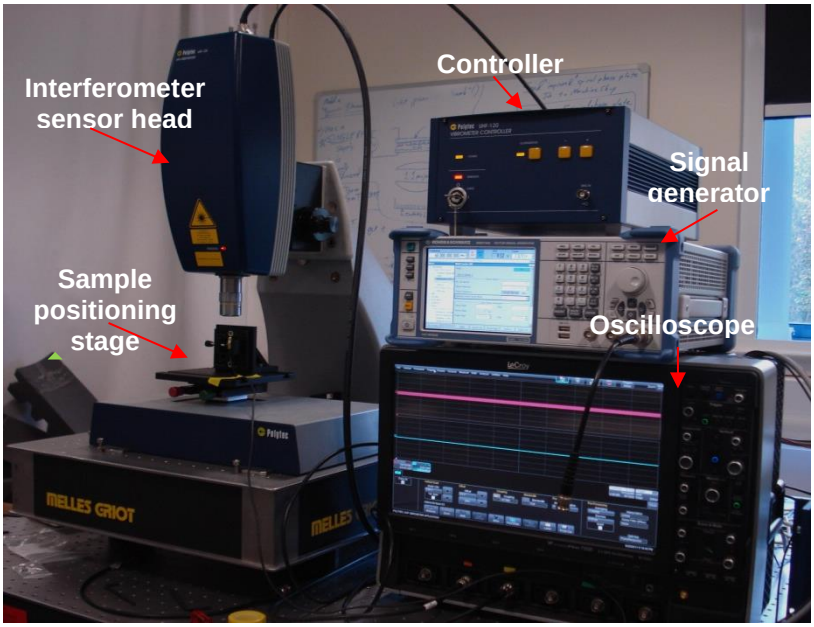

(a)

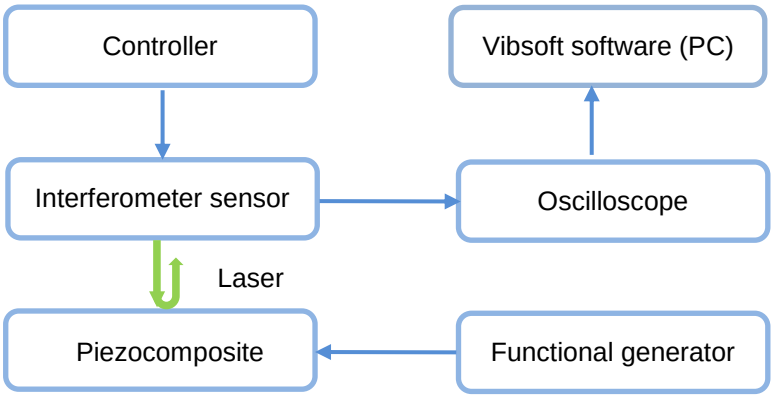

(b)

Figure 6-17 (a) Photograph of experimental set up for laser vibrometry measurements and (b) schematic diagram of the component connections.

6.2.10 Transducer scanning

A high frequency scanning system built up by the University of the Dundee was used for pulse-echo response tests, tungsten wire scanning (B-scan) and tissue imaging (B-scan) of the transducers fabricated in this work. The system consisted of a frame, a scanner, a sample holder, a pulser/receiver (DPR/500, JSR Ultrasonics, UK), an oscilloscope (HP54810A, Agilent, UK) and a computer, as shown in Figure 6-18(a).

The frame of the system was composed of an optical breadboard assembly and custom made aluminium pillars to minimize vibration in the scanner by rigidly fixing the scanning stages to the base of the frame. The stages were controlled by an intelligent two-axis driver (SHOT-602, Sigma Koki, Japan), that offered a resolution of 2 μm in the X and Y directions. The functions of the driving system were controlled by an intuitive LabVIEW interface. In each measurement, the transducer was driven by the pulser to produce an acoustic pulse into a liquid medium. The echoes reflected back from the target were amplified by the receiver and recorded by the oscilloscope. The acquired data was then sent to LabVIEW and processed by MATLAB. The component connections in this scanning system are shown in Figure 6-18(b).

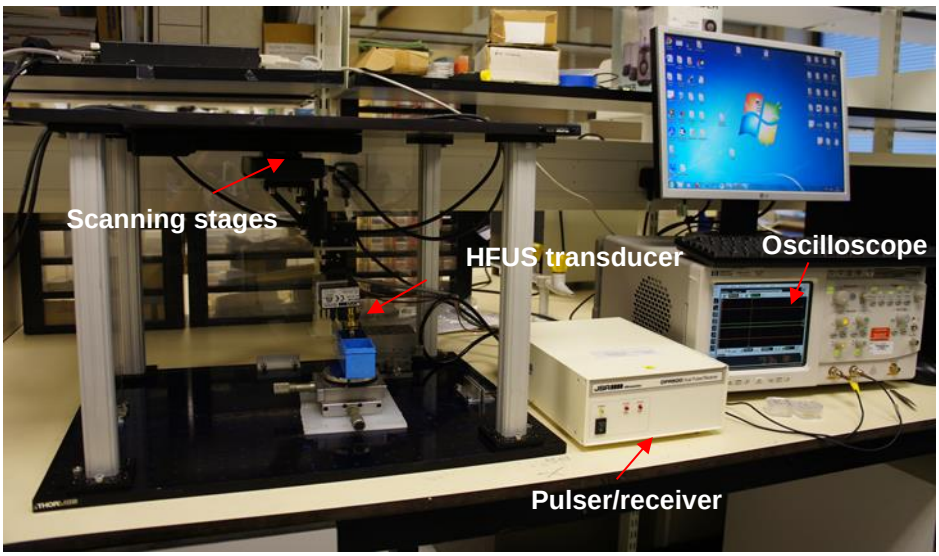

(a)

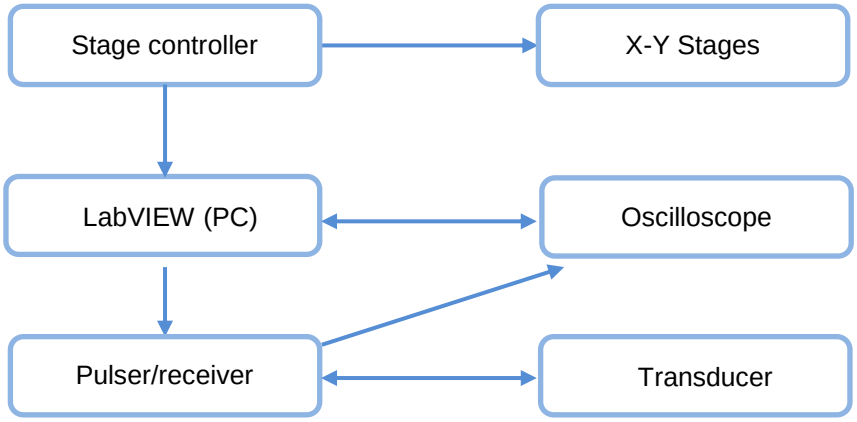

(b)

Figure 6-18 (a) Photograph of the high frequency scanning system and (b) schematic diagram of the component connections in the scanning system.

For the pulse-echo response tests, a flat, stainless steel block was employed as the echo target, submerged in water and located at the geometric focus of the transducer. The obtained pulse response in time was used to calculate axial resolutions according to Equation 2-6. The frequency spectra of the echoes were obtained by applying the Fast Fourier Transformation (FFT) after patching zeros to the time waveform through a MATLAB script (The Mathworks Ltd., Cambridge, UK). Bandwidths were then determined from the resultant frequency spectra.

In order to evaluate the resolution and the focal length of the transducer, B-scan images of a set of tungsten wires were produced. Tungsten wires were chosen because of their acoustically highly reflective characteristics. They all had a diameter of 25 μm and were positioned on a sample holder so that they were separated by 1 mm along the axial and lateral directions, and then submerged in water for the scanning tests. The distance between the transducer and the uppermost wire was adjusted to be less than the designed focal length (5 mm) and then gradually increased by an increment of 1 mm each time until that wire was shown to be out of the focal zone in the resultant image.

Tissue scanning was also conducted to test the real-time imaging capability of the transducers for medical diagnostic purposes. Two thin samples resected from a cancerous Min-type mouse bowel and a wild-type one, respectively, were employed as the imaging targets. Before scanning, the two types of tissues were pinned on to a flat surface of solidified agar and then immersed in a phosphate-buffered saline solution. The transducer for imaging was adjusted to be perpendicular to the surface of the samples and lowered down into the solution. A photograph showing the transducer and the tissues set up for the scan is presented in Figure 6-19.

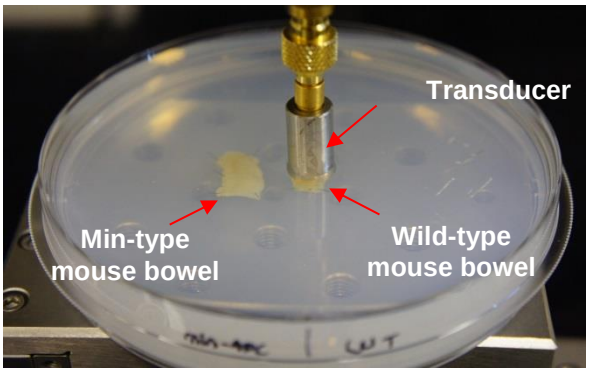

Figure 6-19 Photograph of the transducer and two mouse bowel tissue samples positioned for B-scan. The tissues were fixed on to a flat surface of agar. The transducer and the tissues were all submerged in a buffer solution during scanning.

6.2.11 Microstructure Characterisation

6.2.11.1 Scanning Electron Microscopy (SEM)

Scanning electron microscopy (SEM) including JSM 7000 (JEOL, Tokyo, Japan), JSM 6060 (Jeol, Tokyo, Japan) and XL-30 (Philips) were used to study the morphology of the samples. Most of the SEM samples were prepared by adhering the sample to an aluminium stub using a conductive carbon adhesive tape. For imaging the cross-sections of the photoresist moulds, Blu-Tack (Bostik, UK) was used to fix the samples on an aluminium stub. All the samples were gold coated at 80 mA for 2 min using a sputter coater (Emitech K575, Emitech Ltd., UK) to increase the conductivity before imaging by SEM.

6.2.11.2 Optical microscopy

Optical images of the photoresist moulds were obtained from an Olympus microscope (BH2-UMA, Olympus, UK). An optical microscope (Axioskop 2 MAT mot, Carl Zeiss, USA) was used to characterise the microstructure of the random composites. The obtained images were analysed by Image J software to calculate the ceramic volume percentage in the composites. Optical images taken during the construction of transducers were from another optical microscope (RZ, Meiji Techno microscopy, UK).

6.3 Finite element analysis

PZFlex (Weidlinger Associates Inc., Mountain View, USA) was used for the finite element analysis of the random piezocomposites. The positions of ceramic and epoxy phases in the composite was defined by importing an SEM image of the sintered randomised ceramic segments with the Importing Material Tool. Measured material

parameters of the Epofix matrix and typical properties of PZT 5H were used for modelling.

Random piezocomposites with the same pattern design (300 x 300 µm square), but different thicknesses ranging from 10 to 40 µm, were modelled for the evaluation of their performance. Figure 6-20 shows an image of the random pattern and the 40 µm thick 3D model as an example. The element size of the model was 1.887 µm, determined by the pixels of the imported image.

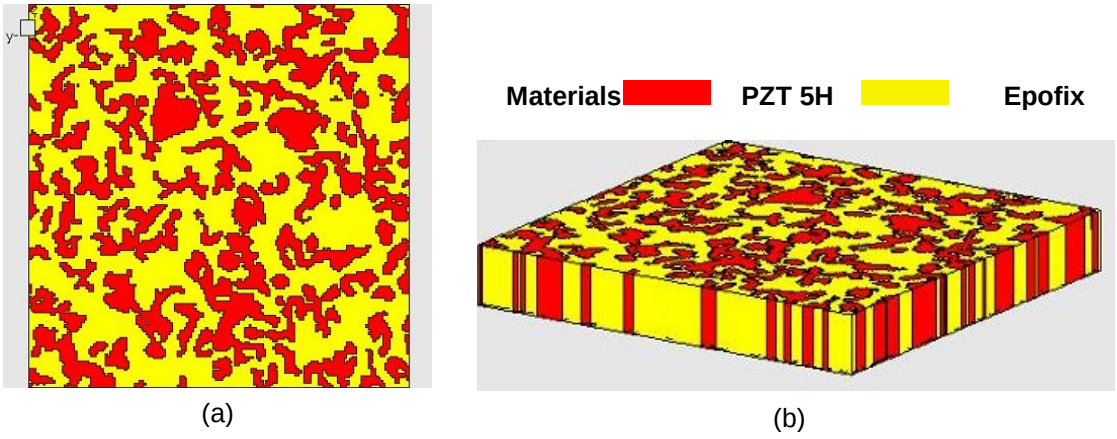

Figure 6-20 (a) 300 x 300 µm top surface of the model and (b) the 40 µm thick 3D finite element model used for finite element analysis of the random composite.

6.4 References

[1] (Last accessed 2012/04/26). *TRS piezoelectric materials datasheet*. Available: http://www.trstechnologies.com/Materials/Piezoceramics/properties.php

[2] X. Mao, *et al.*, "Rheological characterization of a gelcasting system based on epoxy resin," *Ceramics International*, vol. 35, pp. 415-420, 2009.

[3] S. M. Olhero, *et al.*, "Innovative fabrication of PZT pillar arrays by a colloidal approach," *Journal of the European Ceramic Society*, vol. 32, pp. 1067-1075, 2012.

[4] M. Janney, *et al.*, "Gelcasting," *The Handbook of Ceramic Engineering*, pp. 1-15, 1998.

[5] M. Mitchell, *et al.*, "Ceramic microreactors for on-site hydrogen production," *Journal of Catalysis*, vol. 241, pp. 235-242, 2006.

[6] X. Zhu, *et al.*, "Improvement in the strength of reticulated porous ceramics by vacuum degassing," *Materials Letters*, vol. 51, pp. 363-367, 2001.

[7] B. Su, *et al.*, "Control of the particle size and morphology of hydrothermally synthesised lead zirconate titanate powders," *Journal of materials science*, vol. 39, pp. 6439-6447, 2004.

[8] S. Cochran, *et al.*, "Net-shape ceramic processing as a route to ultrafine scale 1-3 connectivity piezoelectric ceramic-polymer composite transducers," in *Ultrasonics Symposium, 2004 IEEE*, 2004, pp. 1682-1685 Vol.3.

[9] B. Su, et al., "Embossing of 3D ceramic microstructures," *Microsystem technologies*, vol. 8, pp. 359-362, 2002.

[10] A. L. Bernassau, *et al.*, "Characterisation of an epoxy filler for piezocomposite material compatible with microfabrication processes," in *Ultrasonics Symposium, 2008. IUS 2008. IEEE*, 2008, pp. 62-65.

[11] R. A. Webster, "Passive Materials for High Frequency Piezocomposite Ultrasonic Transducers," PhD, University of Birmingham, 2009.

[12] D. MacLennan, "Fundamental Characterisation and Early Functional Testing of Micromoulded Piezocomposites " PhD, University of Strathclyde 2009.

CHAPTER 7 OPTIMISATION OF GEL CASTING PROCESS

7.1 Introduction

A variety of gel casting systems have been discussed in Chapter 3 and a novel system based on water soluble resin has been selected to produce PZT high aspect ratio micro-scale structures for the fabrication of 1-3 piezocomposites. In the search for the optimum parameters of the gel casting process, initially bulk PZT plates and bars were produced and characterised and the results are reported and discussed in this chapter, instead of applying gel casting directly to fabricate PZT micro-scale structures. A series of parameters involved in the gel casting process have been studied including hardener concentration, gelation temperature, the rheological properties of the premix solutions and the PZT slurries, burn-out of binders, resin content and its effects on the properties of the bulk green bodies and sintered ceramics.

7.2 Polymerisation process of premix solutions

7.2.1 Effect of hardener concentration

As illustrated in Section 3.5.2.4, during epoxy-amine curing, each of the epoxide rings can be opened up by each of the active hydrogens on the end of the amine hardener to produce chemical bonds between epoxy and amine. As a general rule, epoxy-amine systems are processed at 1:1 stoichiometric ratio of active amine hydrogen to epoxide groups to ensure the maximum stability of the cured products. However, in some cases, desirable properties such as higher modulus [1] can be achieved from slightly off-stoichiometric mixtures of epoxy and amine [1, 2]. For a particular application, the optimum epoxy/amine ratio can only be obtained experimentally based on the properties of the network structure developed as well as the reaction rate.

In this gel casting system, Bis(3-aminopropyl)amine hardener provides five active hydrogens which are available to crosslink with epoxide groups. Therefore, theoretically, 0.2 mol Bis(3-aminopropyl)amine which contains one equivalent weight of active hydrogen is able to thoroughly react with per equivalent weight of epoxy. For the hardener addition smaller than 0.2 mol/eq, epoxy is in excess while for the hardener addition larger than 0.2 mol/eq, amine is in excess.

Figure 7-1 shows the elastic modulus G' and viscous modulus G'' of 20 wt% premix solutions during the polymerization process with hardener additions of 0.1, 0.2, 0.4 and 0.6 mol/eq at 40 ºC as a function of time. The elastic modulus G′ in the plateau region, which reflects the strength of the formed gel, increases with the hardener content first and then decreases dramatically. Similar trends have been observed for other epoxy-amine systems [3, 4]. As expected, the highest G' value of 90590 Pa is achieved from the stoichiometric composition with the hardener addition of 0.2 mol/eq. In this case, all amine hydrogens should be linked with all epoxide groups, yielding a network of interconnected rings with high amounts of branching and crosslinking. For the lower hardener addition of 0.1 mol/eq, 50 % of epoxide groups could not be consumed and a fairly constant low G' value of 0.13 Pa suggests that no gel was formed within 1 h. For the higher addition of 0.4 mol/eq, G' values in the plateau region are slightly lower than those obtained from the stoichiometric composition, implying the production of a less cross-linked network structure. Further increasing the hardener concentration to 0.6 mol/eq significantly decreases G' values in the plateau region to around 20 Pa, indicating the formation of a viscous gel. In the two amine-rich systems, epoxide groups were not sufficient to react with all the secondary amines generated from the primary amine additions. As observed from the

epoxy-amine reactions presented in Figure 3-20, primary amine additions only produce linear molecules; crosslinking and branching do not start until secondary amines begin to be consumed by epoxide groups. According to Vanlandingham et al. [5], with an increase in excessive amines, the tendency to form linear chains increases, and the content of unreacted secondary amines increases, hence the decreased degree of crosslinking, which explains the decrease of the maximum G' values with increased hardener addition from 0.2 mol/eq to 0.6 mol/eq. The variation of the steady-state G'' values (G'' is a measure of viscous response) with the hardener addition follows the same trend. Higher amounts of cross-linking achieved at the stoichiometric composition leads to higher molecule weight, which gives rise to increased viscosity and thus larger G'' values.

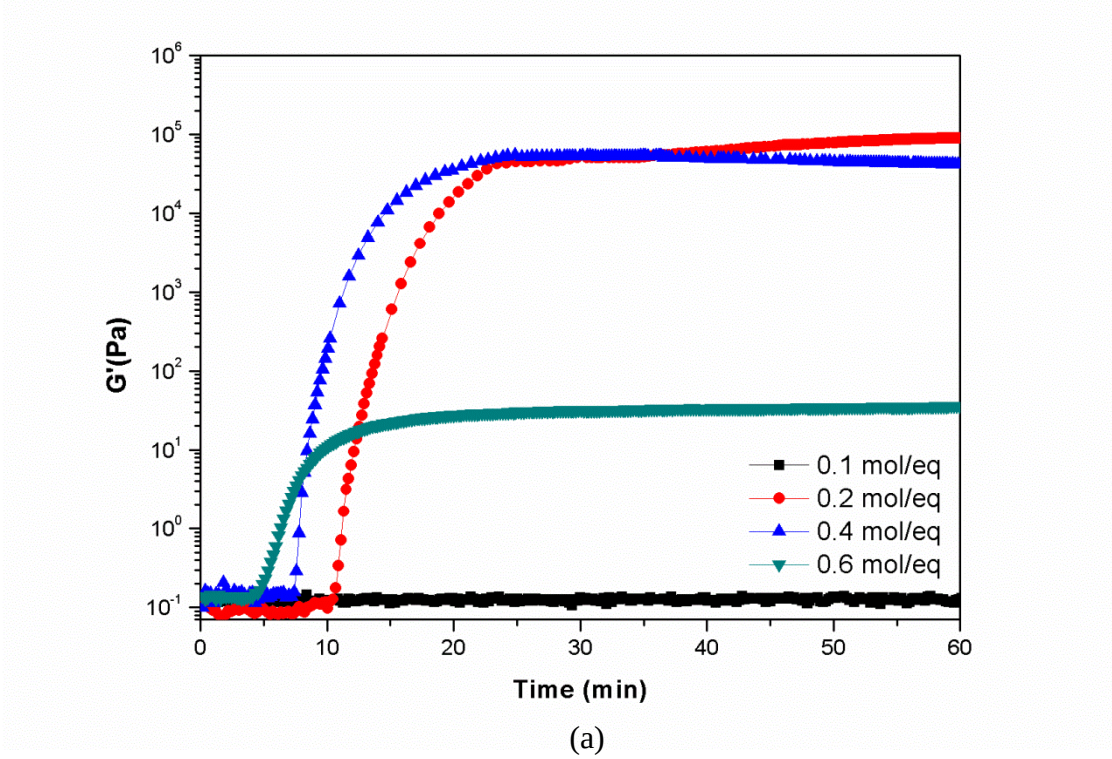

(a)

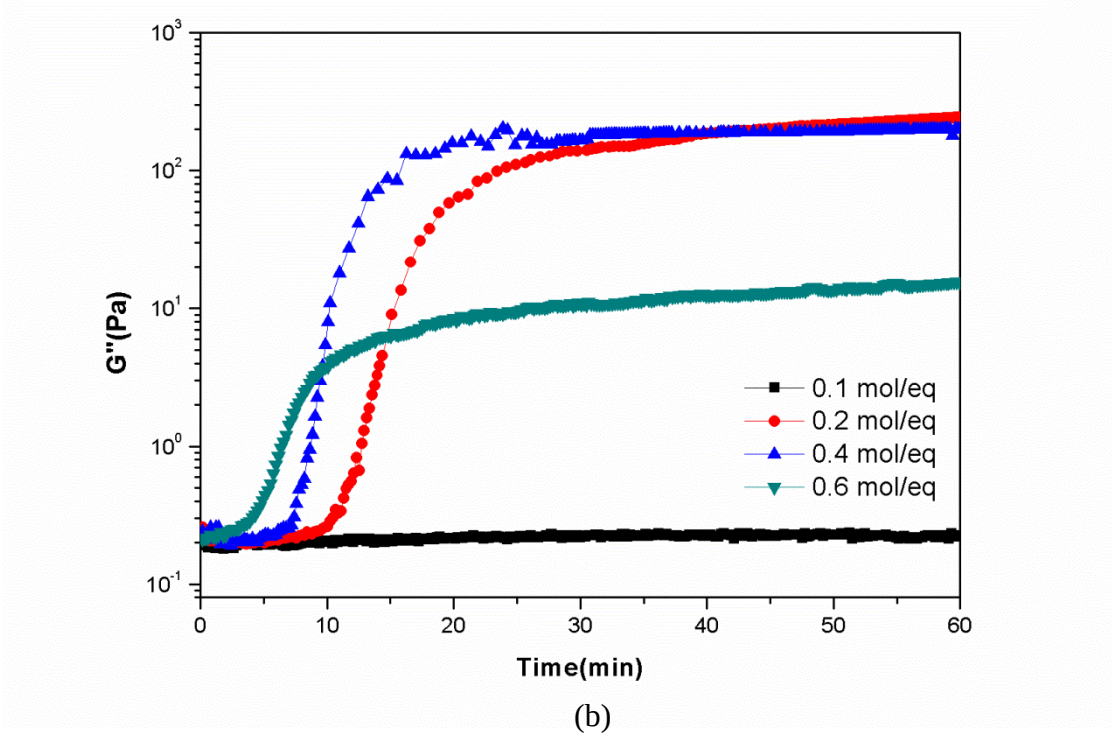

(b)

Figure 7-1 (a) Elastic modulus G′ and (b) viscous modulus G″ of 20 wt% EGDGE premix solutions cross-linked with 0.1-0.6 mol/eq hardener at 40 ºC .

The gelation time indicates the available time for mixing and casting. The most generally accepted criterion for gelation is the crossover point of the elastic modulus G' and the loss modulus G'' [6]. G' and G'' curves of 20 wt% resin premix solution cross-linked with 0.2 mol/eq hardener at 40 ºC are is presented in Figure 7-2 as a typical example. Three main phases can be distinguished from the time-sweep cuvers. Firstly, at the initial stage of the curing process, both of the moduli were low and the viscous portion G″ was larger than the elastic viscous portion G′ as the viscous properties of the liquid state dominated. The small elastic portion of the mixture possibly came from the strectching and the physical entanglements of polymer chains. Secondly, when the crosslinking reaction proceeded, the polymer network started to develop and both of the moduli increased with the increasing of molecular weight of polymer chains but G' rose much more sharply and exceeded G″. In the final phase, as the reaction came to completion, both of the moduli reached their plateau regions. Table 7-1 gives the gelation times for 20 wt% premix solutions cured with various hardener concentrations. It can clearly be seen that with increasing amine hardener concentration, the gelation time is shortened due to the increased number of activated amine hydrogens to initiate the crosslinking reaction, which is in agreement with the previous study reported in [5]. The optimum hardener addition was chosen as 0.2 mol/eq to avoid comparatively long gelation times, and viscous and fragile polymerised gel.

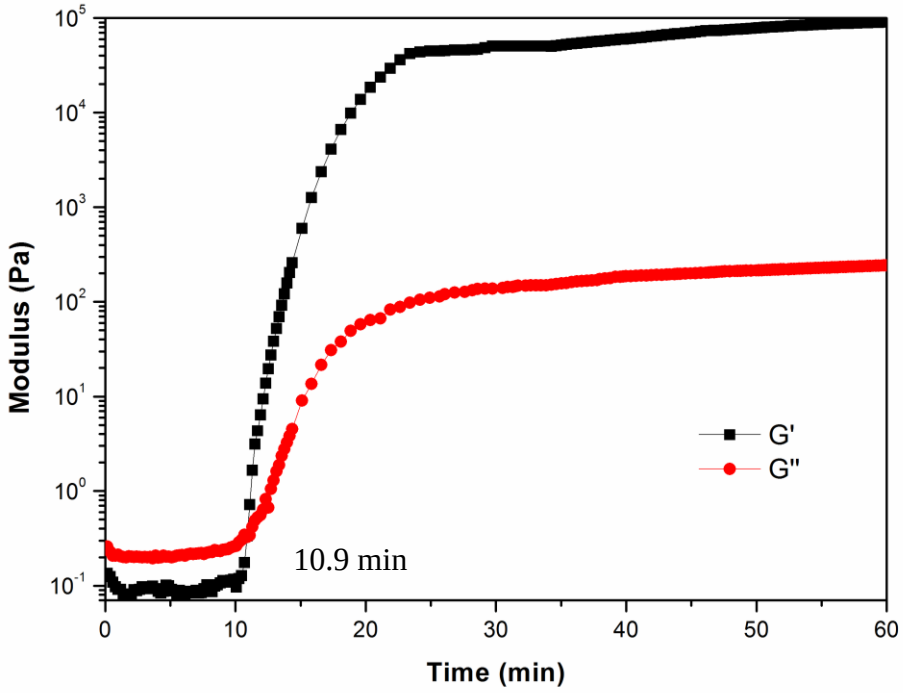

Figure 7-2 Elastic modulus G′ and viscous modulus G″ of 20 wt% EGDGE premix solution cross-linked with 0.2 mol/eq hardener at 40 ºC.

Table 7-1 Gelation time for 20 wt% EGDGE premix solution cross-linked with 0.1-0.6 mol/eq hardener at 40 ºC.

Hardener concentration (mol/eq)	0.1	0.2	0.4	0.6
Gelation time (min) at 40 ºC	>60	10.9	7.6	6.1

7.2.2 Effect of resin content

Figure 7-3 shows G' and G'' of premix solutions containing 10-40 wt% EGDGE cross-linked with 0.2 mol/eq hardener at 40 ºC as a function of time. It can be seen that G' values in the plateau region increase with the increase of the resin content in the premix solution, suggesting higher resin content leads to a stronger gel after polymerisation. A possible interpretation of this effect is related to the presence of water. During the ring-opening process, it is widely recognised that water serves only as a catalyst to accelerate the reaction and increases the mobility of polymer chains [7,

8]. The additional ring-opening polymerisation in the presence of water is presented in Figure 7-4. However, as the polymerisation reaction progresses, crosslinks and branches start to develop and water is able to diffuse into the generated polymer network by two generally accepted approaches [9], residing in the free cavity of the network in the form of free water and binding to hydrophilic functional groups such as hydroxyl or amine in the form of bound water. According to Zhou et al. [9], there are two possible types of bound water existing in the epoxy resins depending on the difference in bond complex as shown in Figure 7-5. The dominant form is type 1 with a single hydrogen bond formed between each water molecule and the polymer network. The absorbed water in the polymer network acts as a plasticizer [10] which decreases the strength of the cured epoxy. For a given amount of premix solution, as the resin content increases, the amount of water presented in the mixture and further retained in the gel decreases, resulting in a tougher network structure with higher elastic modulus.

Gelation times for the premix solutions with different resin contents are given in Table 7-2 based on the crossover points of G' and G'' as described earlier. For the 10 wt% resin content in the solution, the gelation time is 24.6 min. When the resin content rises to 20 wt%, the gelation time dramatically reduces to 10.9 min as the polymer chains were closer to each other in the premix solution with higher resin concentration. With further increases of the resin content, the gelation time is reduced and the variation in gelation time becomes smaller.

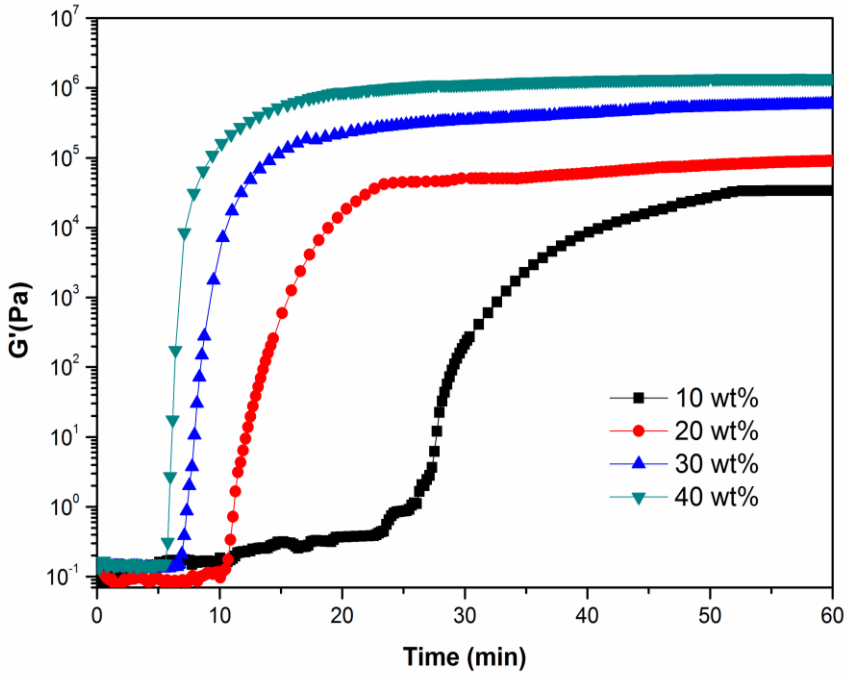

(a)

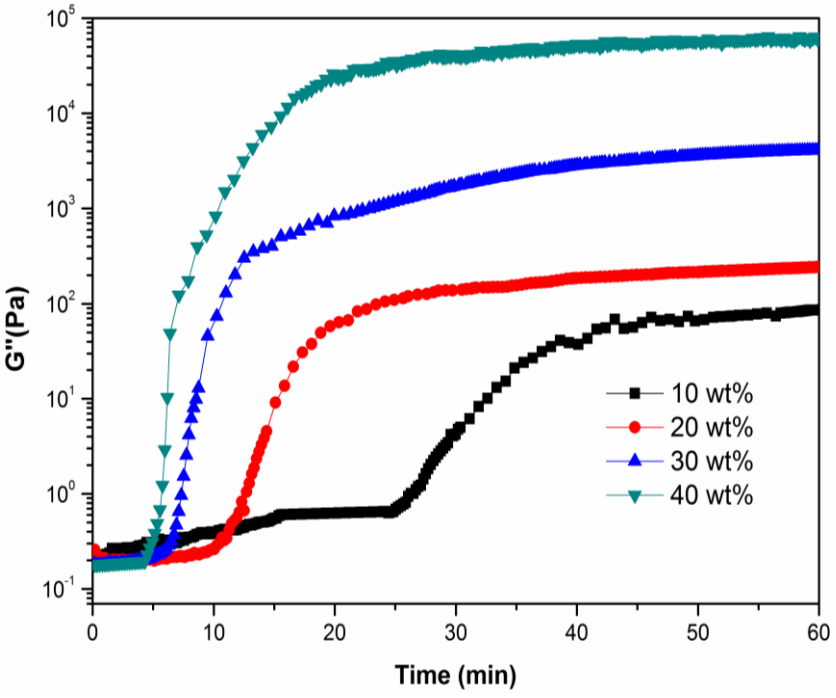

(b)

Figure 7-3 (a) Elastic modulus G′ and (b) viscous modulus G″ of premix solution containing 10-40 wt% EGDGE cross-linked with 0.2 mol/eq hardener at 40 ºC.

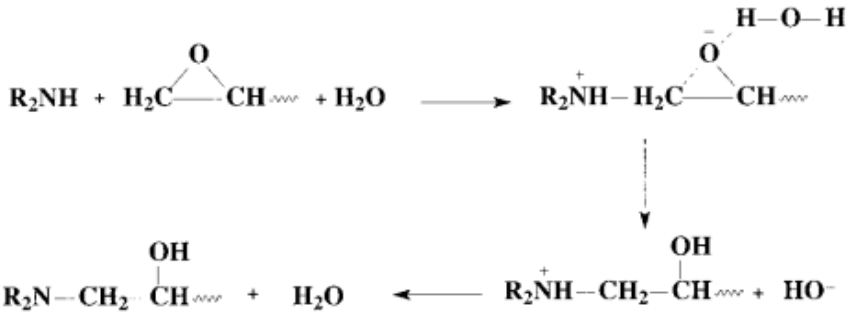

Figure 7-4 Ring opening polymerisation in the presence of water [7].

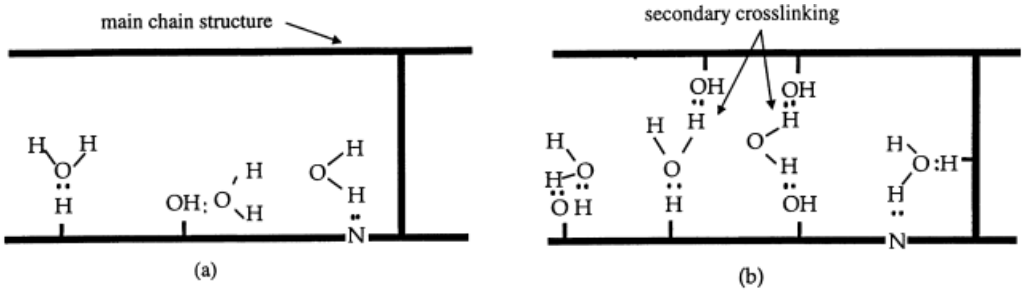

Figure 7-5 Possible bound water types in epoxy resins. (a) Type 1: A water molecule forms a single hydrogen bond with the epoxy resin network. (b) Type 2: A water molecule forms multiple hydrogen bonds with the resin network [9].

Table 7-2 Gelation time for premix solutions containing 10-40 wt% EGDGE cross-linked with 0.2 mol/eq hardener.

Resin content	10 wt%	20 wt%	30 wt%	40 wt%
Gelation time (min) at 40 °C	24.6	10.9	7.3	6.2

7.2.3 Effect of reaction temperature

According to the basic polymerisation mechanism, temperature plays a vital role in controlling the reaction rate of gel casting. Figure 7-6 shows the evolution of G' and G'' of 20 wt% premix solution cured with 0.2 mol/eq hardener at different temperatures. It can be observed that with increasing temperatures from 25 ºC to 40 ºC, the induction period of both G' and G'' is apparently shortened from more than 40 min to

around 10 min, suggesting a higher reaction temperature results in higher reaction rate for epoxy-amine curing. This is attributed to the fact that the mobility of polymer chains increases as temperature rises. It can also be observed that temperature has no obvious effect on the plateau G′ and G″ values, which indicates that no further crosslinking takes place at elevated temperatures.

The relationship between gelation time t_g and temperature may be expressed by an Arrhenius-type equation [4]:

$$t_g \propto \frac{1}{K_r} = Ae^{E_\alpha / R_g T_k} \qquad \textbf{Equation 7-1}$$

Where K_r is the reaction rate, A_a is the Arrhenius pre-exponential factor, R_g is the gas constant, E_α is the activation energy of polymerization reaction, and T_k is the absolute temperature. Figure 7-7 plotted based on the data obtained from Figure 7-6, shows a nearly linear relationship between In (t_g) and 1/ T_k as predicted. Theoretically, the slope of the fitting line is equal to E_α/R_g. By substituting the slope value, the calculated E_α value of the curing reaction between the premix solution containing 20 wt% EDGDE and 0.2 mol/eq hardener is 72.7 kJ/mol, which is a sensible value in agreement with the typical value of 50-70 kJ/mol reported for epoxy-amine curing [11].

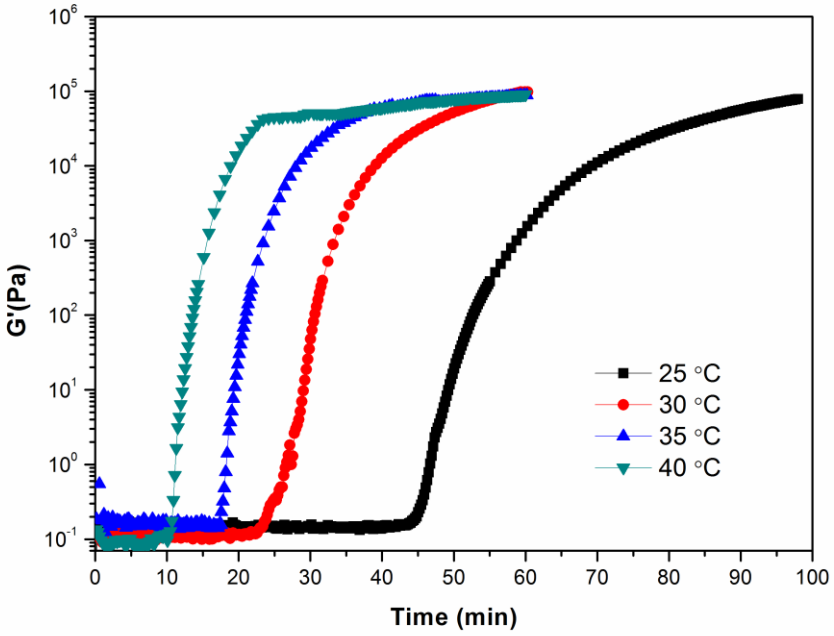

(a)

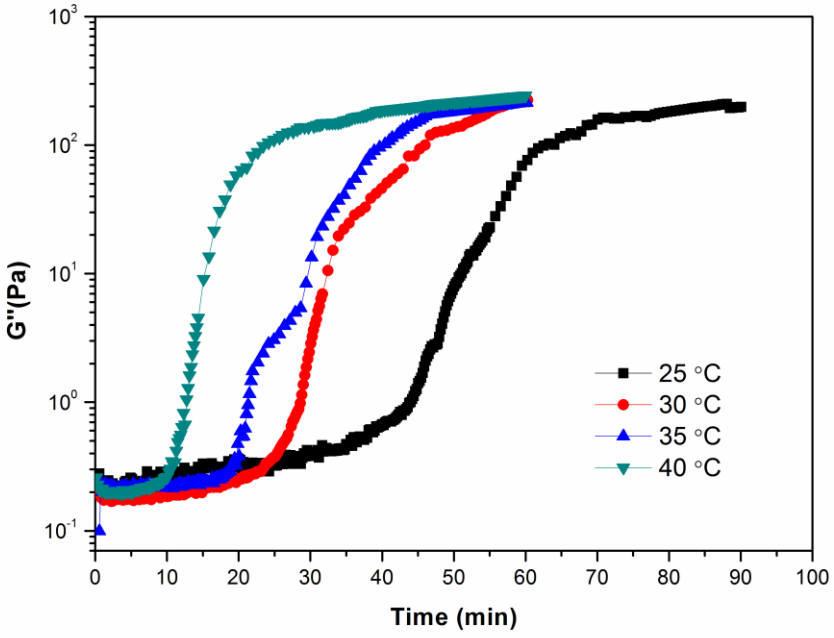

(b)

Figure 7-6 (a) Elastic modulus G′ and (b) viscous modulus G″ of 20 wt% EGDGE premix solution cured with 0.2 mol/eq hardener at various temperatures.

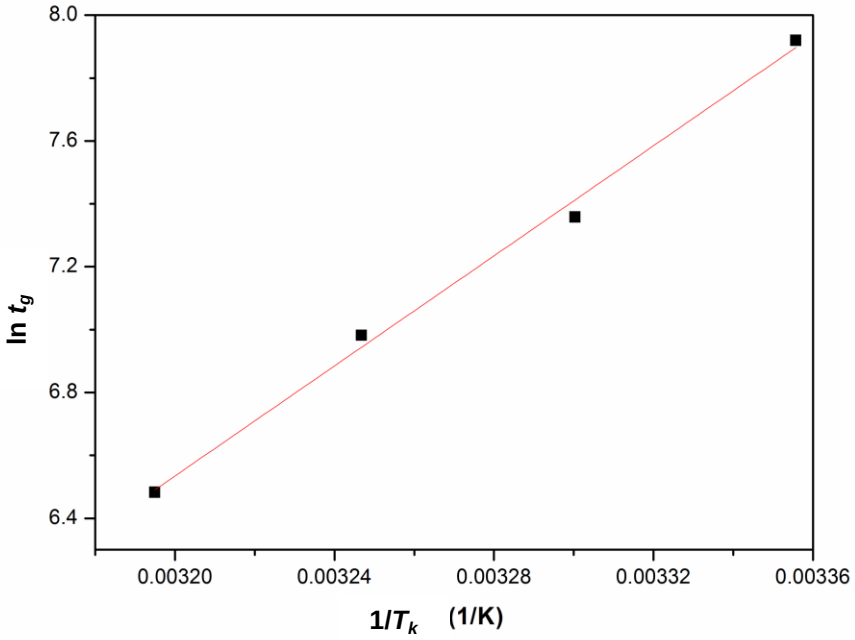

Figure 7-7 Arrhenius plot showing the relationship between gelation temperature and gelation time.

7.3 Characterisation of PZT powders

An appropriate selection of PZT particle size for this particular application depends on many factors including application, properties and processing requirements. First of all, considering that the feature sizes of the high aspect ratio micro scale structures in this study are in the range of 2-50 μm, particle size larger than 2 μm would possibly lead to incomplete mould filling in gel casting and therefore finer powder is preferred. Also, from a sintering point of view, a smaller particle size is desirable as it has a greater pore/solid interfacial surface area and higher surface energy which speeds up the sintering process and reduces the sintering temperature. However, several disadvantages can arise when using very fine piezoceramic particles in practice. On the one hand, submicron-grained PZT (sub-micrometer) has been found difficult to maintain high piezoelectric properties as the domain wall mobility was significantly constrained by the strong transgranular coupling between the grain boundaries and the

domain walls [12, 13]. On the other hand, smaller particles indicate larger surface area which makes full and stable dispersion of the powders more difficult. Taking these factors into account, a compromise has to be made for the particle size selection.

As-received commercial PZT powders TRS 610C with a particle size claimed to be 1.2 μm was initially chosen as the starting material. However, the average particle size of the powders was measured as 16.10 μm and a bimodal particle distribution can be observed in Figure 7-8, with one large peak centered at around 25 μm and the other small peak centered at about 3 μm, indicating the presence of large agglomerates. After 24 hrs of vibro-milling, the coarser particles broke down, resulting in a narrow mono-modal particle size distribution as seen in Figure 7-9 with the median particle size decreased to 1.10 μm. Finer particle size could be obtained by attrition milling of the vibro-milled powder. However, considering the problems in dealing with small particles as discussed above, it was considered not necessary.

The SEM results of as-received and vibro-milled powders, shown in Figure 7-10, are in good agreement with the particle size measurements. Agglomerates with sizes ranging from less than 5 μm to over 20 μm were observed in the as-received powders shown in Figure 7-10(a) and no large agglomerates were found in the vibro-milled powders shown in Figure 7-10(c). It can be seen in Figure 7-10(b) and Figure 7-10(d), obtained at high magnification, that the powders before and after vibro-milling both showed very similar morphology with a primary particle size around 1 μm.

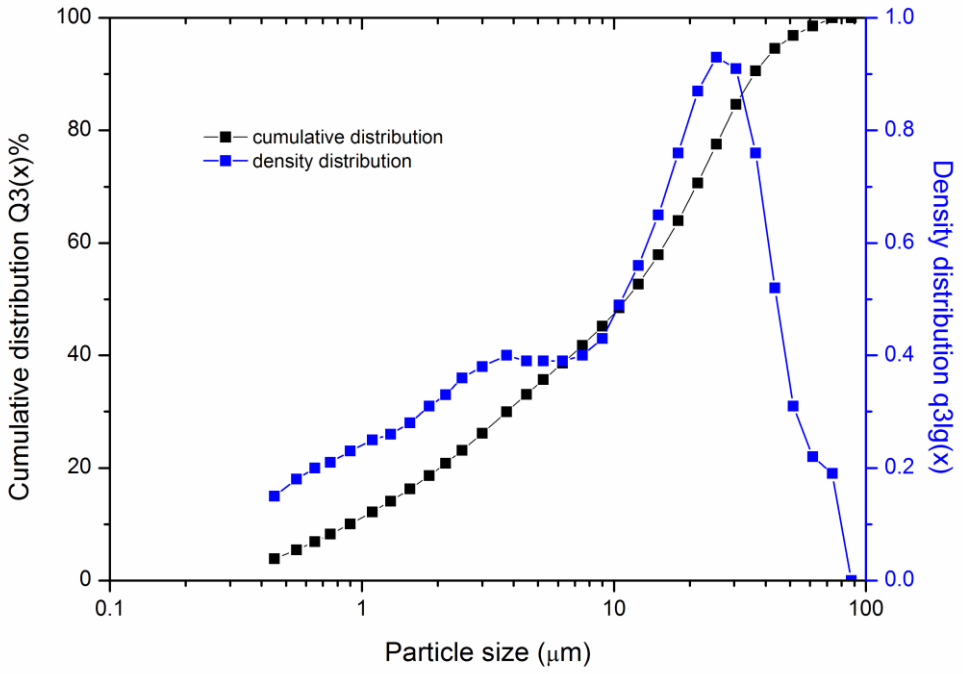

Figure 7-8 The particle size distribution of the as-received commercial TRS 610C PZT powder.

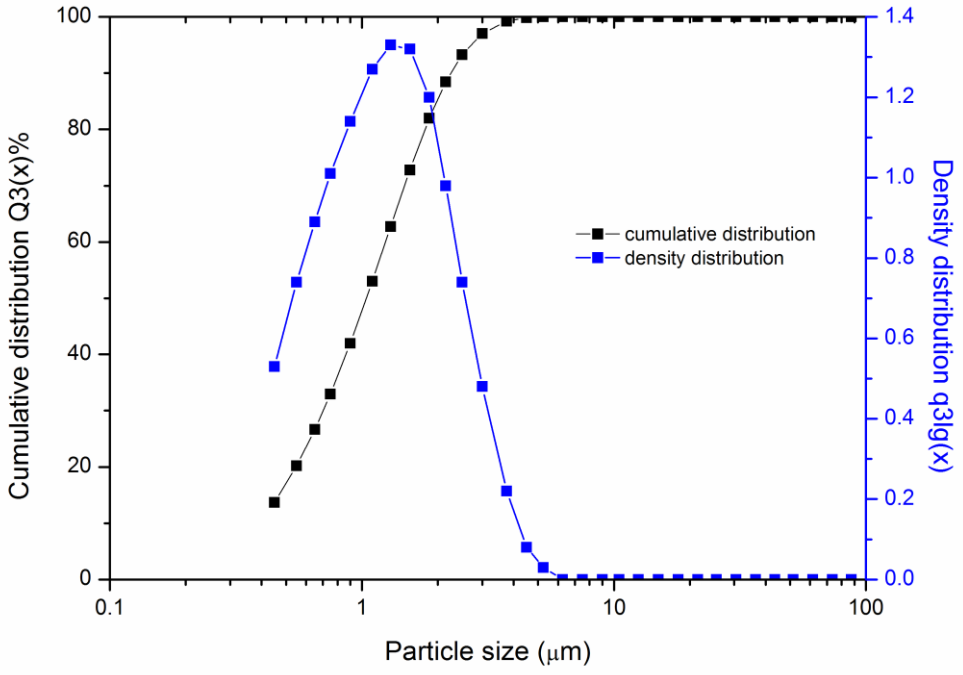

Figure 7-9 The particle size distribution of TRS 610C PZT powder after vibro-milling for 24 hrs.

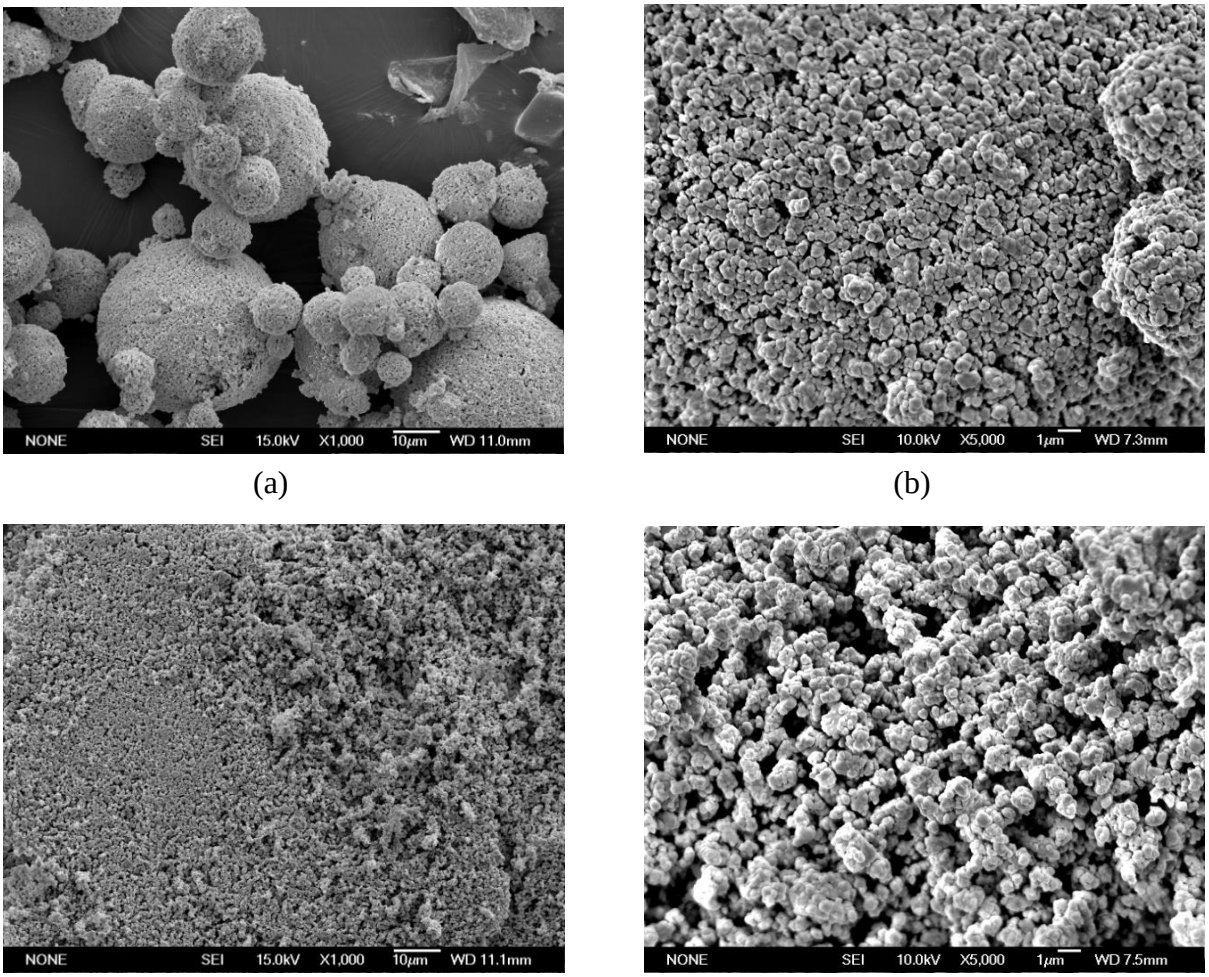

Figure 7-10 SEM images of as-received TRS 610C PZT powders: (a) low magnification (b) high magnification, and after vibro-milling for 24 hrs: (c) low magnification (d) high magnification.

The specific surface area (SSA) values of the two powders were determined by the BET method, as 1.0922 m^2/g and 1.5474 m^2/g for the as-received and vibro-milled powders respectively. The SSA results can also give an estimation of the average particle size assuming all the particles have the same spherical shape. The mean particle size is given by:

$$Mean\ particle\ size = \frac{6}{A\rho} \qquad \textbf{Equation 7-2}$$

where A is the SSA and ρ is the true density of the powders [14]. Given ρ is the theoretical density of 7.95 g/cm^3, the calculated mean particle size for the received and vibro-milled powders is 0.69 μm and 0.49 μm, respectively. As the nitrogen gas in the BET measurement was able to penetrate into the boundaries of agglomerates, at least some of them, the BET method is more reliable for determining the primary particle size than the laser diffraction sizing technique in the presence of large hard agglomerates. However, in the case of vibro-milled PZT powder, the irregular shapes of the particles and the difference between true density and theoretical density cause some inaccuracies in the above calculation, hence the variation of the average particle size predicted from the SSA and that given by the laser diffraction sizing.

Generally a narrow distribution of particle size allows homogeneous packing, leading to better control of microstructure. The existence of large agglomerates which may not be broken down in the subsequent ball-milling stage tends to cause differential densification during sintering, leading to the development of large pores. Thus vibro-milled PZT powder was chosen as the starting material for the gel casting process.

7.4 Slurry Characteristics

7.4.1 Effect of dispersant concentration on the viscosity of the slurry

It is well known that the dispersant plays a vital role in the preparation of stable and well-dispersed colloidal suspensions. Dispex A40, a solution of ammonium polyacrylate (NH_4PAA), was chosen as the dispersant in this gel casting system, as it has been successfully applied for the dispersion in a variety of aqueous suspensions incorporating PZT powders [15, 16]. NH_4PAA provides both electrostatic and steric stabilization to disperse and stabilise the particles, which is usually referred to as

electrosteric dispersion [17]. The electrostatic effect comes from the net surface charge of the particles and the charges from the dissociation of NH_4PAA in water. The steric component originates from the repulsion of the insoluble polymer chains which anchor to the surface of the particles.

The amount of the dispersant can have significant influence on the rheological properties of the slurry. Figure 7-11 illustrates the dependence of the viscosity of 45 vol% PZT suspension with 20 wt% resin content on the dispersant concentration (based on the powder dried weight basis) measured at a shear rate of 100 s^{-1}. It can be seen that at a lower concentration of 0.4 wt%, a high viscosity was observed, possibly because there was insufficient dispersant to cover all the available surface area of the particles, and that some of the particles were attracted by Van der Waals forces resulting in some aggregation. As the surface coverage of the absorbed polymer chains increased, the repulsion forces increased accordingly and eventually reached a level that was strong enough to overcome Van der Waals forces, hence leading to the initial decrease of the viscosity with increasing NH_4PAA concentration. Further addition of the dispersant over 1 wt% led to a slight increase of the viscosity, as the unabsorbed dispersant remained in solution which could then function as an electrolyte, decreasing the range and the extent of the electrostatic repulsion force [18]. The other possible reason for the increase in the viscosity at the highest level of dispersant examined might be due to the interlocking of the free ionic PAA causing the bridging of the particles. The optimum dispersant amount was determined as 1 wt% as it gave the lowest viscosity.

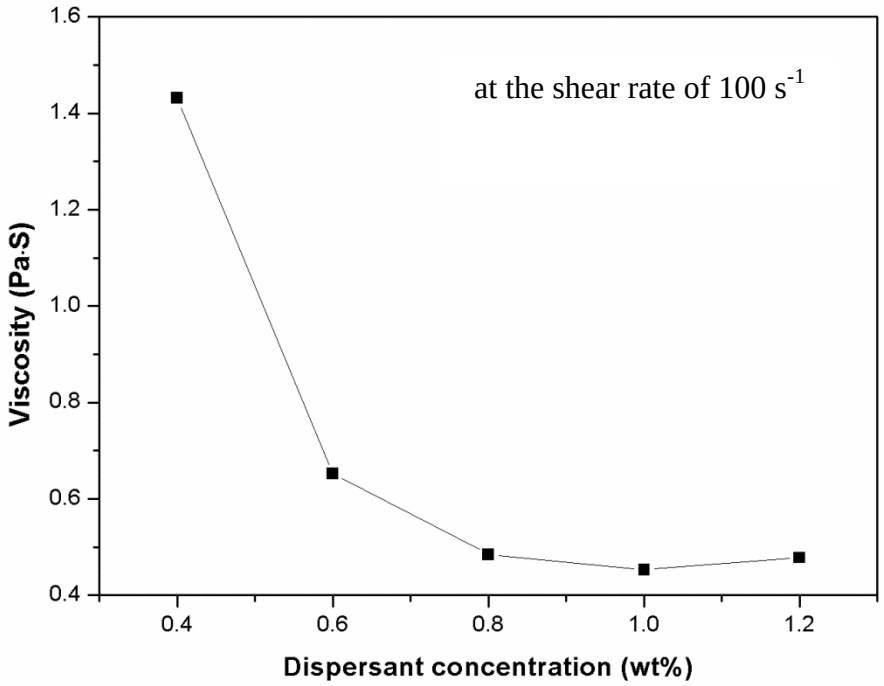

Figure 7-11 Viscosity of the PZT slurry with 45 vol% solids loading and 20 wt% resin content as a function of dispersant concentration measured at the shear rate of 100 s^{-1}.

It should be mentioned that the pH value of the slurry is of great importance to the dissociation behaviour of the NH_4PAA. Comprehensive research has been done on the dispersion of highly concentrated PZT powders using NH_4PAA over a range of pH values [16, 17, 19]. At pH<4, the polymer chains are unlikely to dissociate, resulting in poor adsorption and thus high viscosity. Under basic conditions, NH_4PAA is negatively charged and stretched due to the repulsive forces between the negatively charged segments of the polymer. According to one previous study [16], the intrinsic pH of the PZT slurries is high enough to promote the dissociation of NH_4PAA, therefore, it was considered not necessary to adjust the pH value of the suspension.

7.4.2 Effect of resin content on the viscosity of the slurry

Slurries with low viscosity as well as high solids loading are particularly desirable for gel casting. In the development of the new gel casting system reported in this work, the influence of the epoxy resin on the viscosity has been studied. Figure 7-12 shows the viscosity of 45 vol% PZT suspensions with 1 wt% Dispex A40 and resin concentrations ranging from 10-40 wt% and the viscosity of these slurries after mixing with 0.2 mol/eq hardener measured at a critical shear rate of 100 s^{-1}, which is considered close to the processing conditions in the casting and moulding stages [20].

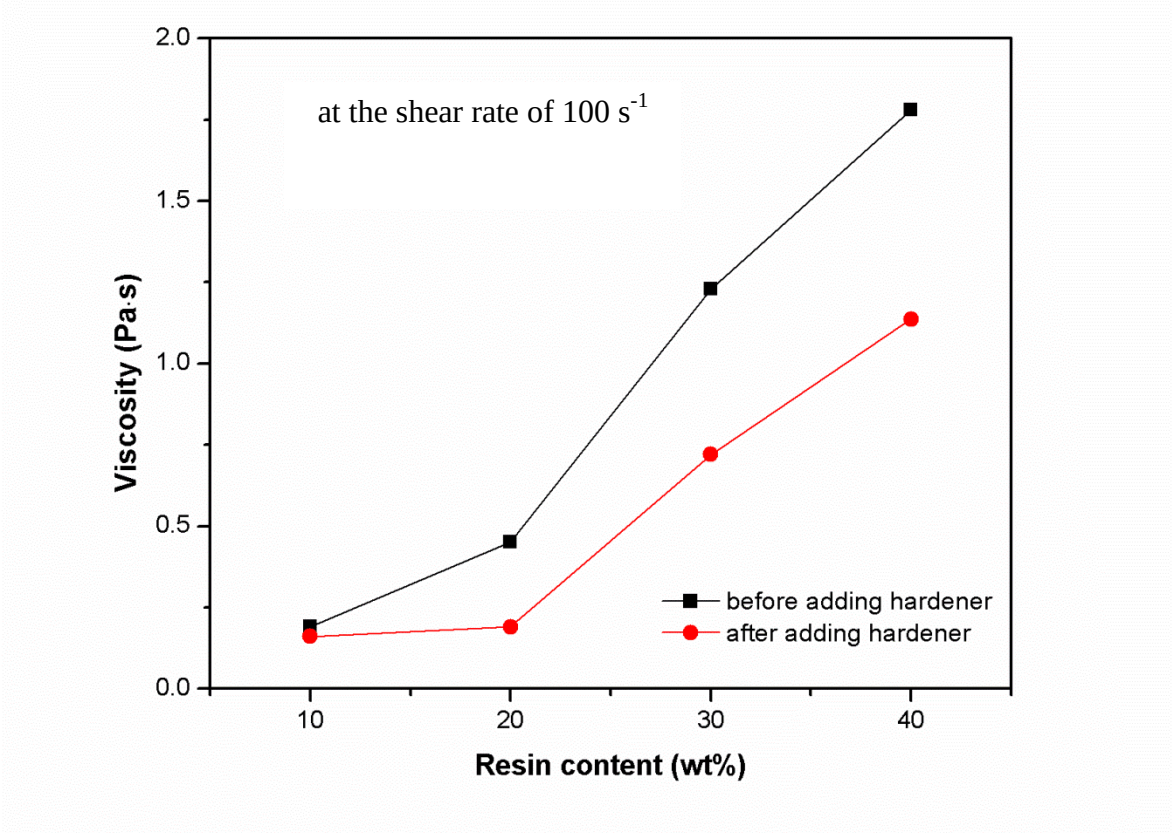

Figure 7-12 Viscosity measured at the shear rate of 100 s^{-1} of the 45 vol% PZT slurries with 1 wt% Dispex A40 and different amounts of resin ranging from 10-40 wt% before and after mixing with 0.2 mol/eq hardener.

It can be seen that before adding any hardener, the viscosity of the 45 vol% PZT slurries increased as the resin content increased. The increase of the viscosity with the increase of the resin content could be explained from three aspects. First, because the

viscosity of the resin was higher than that of the distilled water, the viscosity of the dispersing media increased with an increase of the resin content, hence the increased viscosity of the slurry. Second, the degree of the intermolecular entanglement in the solution might increase as the resin concentration increased, which in turn exerted more restrictions in the movement of individual chains. This effect could partially contribute to the increase of the viscosity. Third, the presence of the non-absorbing epoxy resin in the slurry with higher resin content probably caused the flocculation of the PZT particles. This effect is referred to as depletion flocculation, which has been indicated by a variety of theories and experimental data [21-24]. When the concentration of the non-absorbing polymer exceeds a certain critical value, the free polymer chains from the interparticle space are driven out into the bulk solution. The concentration difference between the particle-particle approaching zone and the bulk solution produces an osmotic pressure, causing the attraction of the particles i.e. flocculation. At lower resin contents, most of the resin molecules were prone to be absorbed onto the hydrated surfaces of the PZT particles according to Olhero et al. [16]. As the resin increased, more free polymers were introduced into the suspension, therefore, the degree of flocculation as well as the viscosity increased.

The flocculation of the slurries was mitigated by the dilution effect of the amine solutions, evidenced by the decrease of the viscosity after the addition of the hardener as shown in Figure 7-12. It can be observed that a sharper decrease of viscosity occurred in the slurry with higher resin content because a higher amount of hardener was added. Although the slurries with 30 wt% and 40 wt% resin exhibited relatively high viscosities of 1.23 Pa·s and 1.78 Pa·s at the shear rate of 100 s^{-1} respectively,

after mixing with the hardener, the viscosities of them decreased to a lower level, which favoured the following casting and moulding processes.

7.4.3 Effect of resin content on the gelation of the slurry

The gelation time of the slurry is a critical parameter in gel casting, as it is related to the production efficiency and more importantly defines the time available for mixing, casting and degassing. If cross-linking occurs during or before casting, it might result in incomplete filling of the mould due to the increased viscosity, as well as variations in cross-linking density within the gel [25] hence inhomogeneous properties of the gel cast ceramic. Moreover, if gelation takes place during or before degassing, the air bubbles would be trapped in the partially gelled slurry which could lead to the formation of large pores in the sintered ceramic. In the cases when the curing process is too rapid or too long, adjusting the gelation time becomes necessary, which is typically realised by controlling the reaction temperature.

The traditional way for the detection of the gel point based on the crossover point of G' and G'', was initially applied to the gel casting slurries as it had been used for the characterisation of the premix solutions (see Section 7.2). Figure 7-13 shows the evolution of G′ and G'' of the PZT slurries with 45 vol% solids loading and resin contents ranging from 10 wt% to 40 wt% in the premix solutions cross-linked with 0.2 mol/eq hardener at 25 °C. It can be observed that with the increase of the resin concentration, the time for G' to reach its plateau value reduced implying an increased reaction rate. In addition, the steady-state G' values increased indicating enhanced strength of the solidfied slurry. This is consistent with the effect of the resin content on the gelation of premix solutions as discussed in Section 7.2.2.

Based on the G' and G'' plots, the gelation time (t_g) for the slurry with 10 wt% resin in the premix solution was around 3 min and for those with 20 wt% and 30 wt% resin content, t_g was shortened to less than 1 min. Moreover, unexpectedly, when the resin content increased to 40 wt%, t_g was unable to be determined for the slurry as G' was larger than G'' throughout the gelation process. However, as noticed in practical processing, no evident gelation was detected for these slurries within 10 min, which conflicted with measured t_g values. In this case, it was reasonable to consider the suitablity of this criterion for the determination of the gel point in this slurry system despite the fact that it has been adopted for other slurry systems as reported in [16, 26].

As a typical example, Figure 7-14 presents the G' and G'' plots of the slurry containing 20 wt% resin in the premix solution. By comparing Figure 7-14 with Figure 7-2, distinct differences have been found in the viscoelastic behaviour between the slurry and the premix solution at a given resin content. First, for the premix solution, the induction periods with constant low values of G' and G'' (in the order of 0.1 Pa) are clearly seen while G' and G'' of the slurry started to sharply increase at the beginning of the measurements from higher initial values of around 10 Pa. Also, the plateau G' and G'' values are higher in the slurry than those obtained from the premix solution. These differences indicate that the incorporaton of PZT powders altered the mechanical properties of the solution as well as the polymerised gel. As solids, the suspended ceramic particles enhanced the elastic response of the suspension system when undergoing small deformation, which explains the increased initial and steady-state G′ values. Meanwhile, the addition of PZT powders also caused the increase of G″ due to the increased viscosity. Considering the effects of the particles, the crossover point of G′ and G″ cannot be ensured to accurately reflect the structural

change of the polymers thus no reliable gelation time of the slurries can be obtained by using this criterion. Similar phenomena has been reported in Alumina–Poly(vinyl alcohol) gel casting systems by Morissette et al. [27], where G' of the slurries exceeded G'' over the gelation process and the steady-state G' values were found to have nearly linear dependence on solid-filler content at volume percentages < 30%.

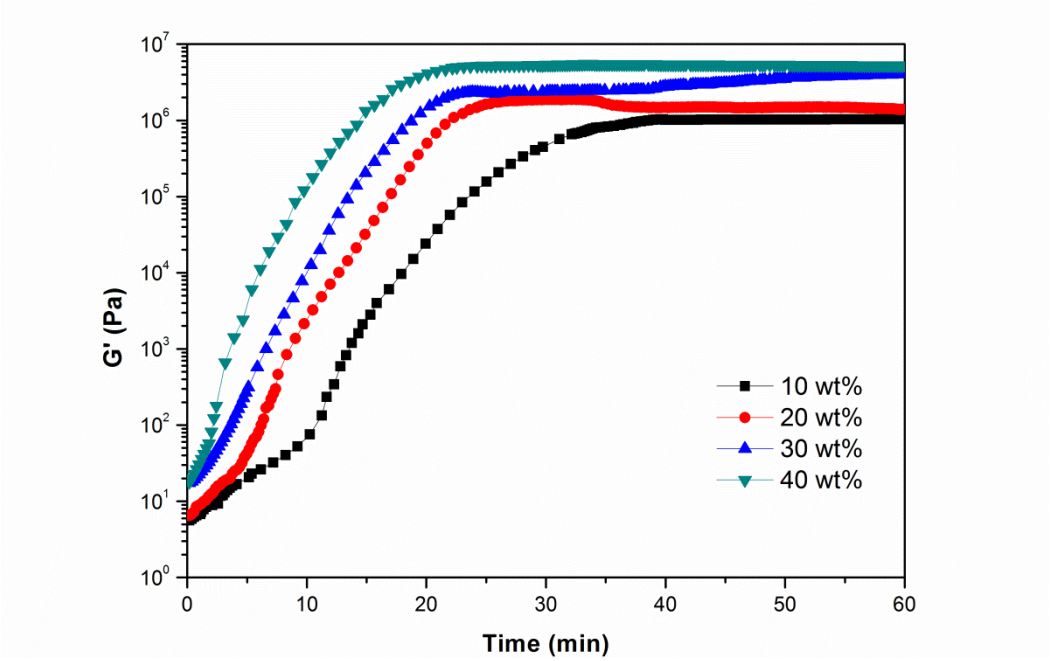

(a)

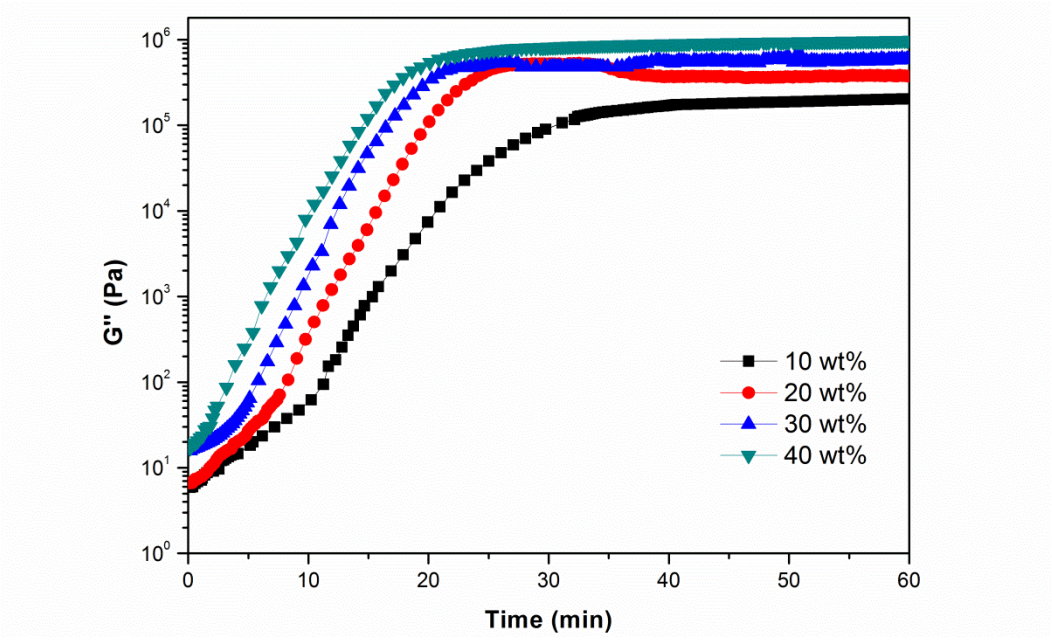

(b)

Figure 7-13 (a) Elastic modulus G′ and (b) viscous modulus G″ of PZT slurries (45 vol% solids loading) containing 10 wt%-40 wt% EGDGE in the premix solutions cross-linked with 0.2 mol/eq hardener at 25 °C.

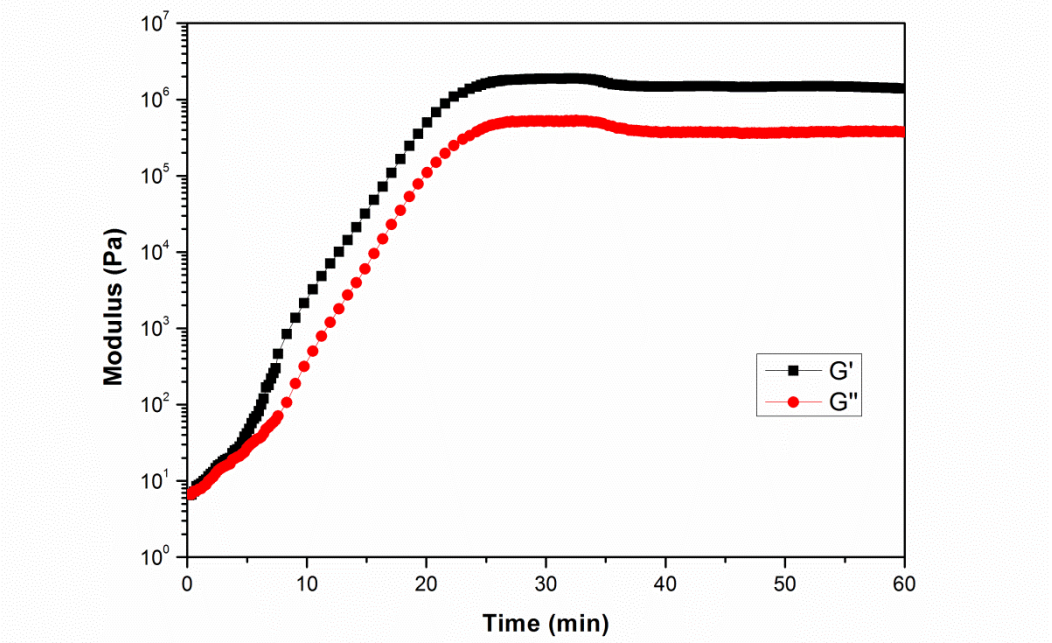

Figure 7-14 Evolution of G' and G'' for the slurry with 45 vol% solids loading and 20 wt% resin in the premix solution cross-linked with 0.2 mol/eq hardener at 25 °C.

Apart from the traditional criteria, a variety of different ways for the determination of the gelation time have been reported. For example, according to Hisieh et al. [28], the gel point was determined by extrapolating the rapidly rising values of G′ to the time axis. However, Hisieh's method would give negative time values for the slurries measured in this work, which is not meaningful. Mao et al. [29] and Dong et al. [3] used the time determined by the abrupt change of G′ for the slurries. However, as seen in Figure 7-13 (a), it is difficult to identify such changes of G′ for the slurries with higher resin contents of 30 wt% and 40 wt%.

Here, another criterion is introduced based on the classical theory that one of the attributes of the gel point is an infinite steady-shear viscosity [30]. After the addition of hardener, a constant low shear rate of 0.1 s^{-1} was applied to the the slurries containing the range of resin concentrations at 25 ºC, and their viscosity measured and plotted against time as shown in Figure 7-15. It can be observed that for all the

slurries, the viscosity remained at a constant value for a period and increased rapidly towards infinity, where the inactive period is defined as the gelation time. It should be noted that t_g determined by this way is still imprecise as an infinite viscosity is not possible to be measured, but can still provide an effective estimation of time for gelation. As shown in Figure 7-15, the gelation time reduced from around 50 min to less than 10 min as the resin content was increased from 10 wt% to 40 wt%. It is worth noticing that the gelation time of the slurry with 20 wt% resin is around 20-30 min, which is shorter than the 45 min gelation time of the premix solution containing 20 wt% resin determined from Figure 7-6. A possible interpretation to the reduced gelation time in the presence of PZT powder is related to the 'container' effect of the slurry [3] . In the slurry, the particles are closely spaced and the small gap (a few nanometers) in between is regarded as a container which holds the gel. During the gelation of the slurry, the polymer chains keep growing until the container is filled. While for the premix solution gelation, the space that the polymer chains need to fill is the rheometer gap (55 μm), which is much larger compared with the container in the slurry, hence the longer gelation time.

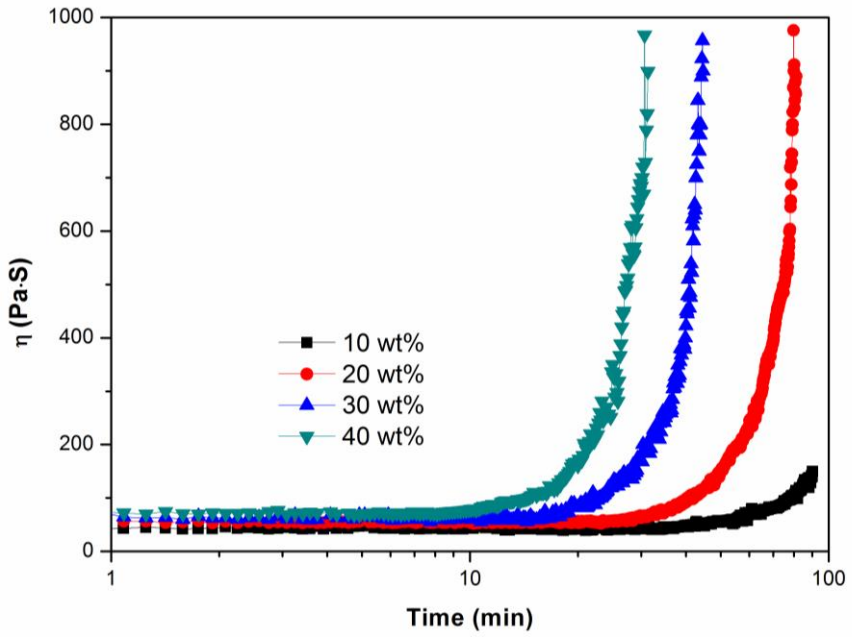

Figure 7-15 Evolution of viscosity for 45 vol% slurries with different resin contents ranging from 10 wt% to 40 wt% in the premix solutions.

7.5 Organic burnout

Prior to sintering, complete removal of organic addictives from green ceramic compacts is a critical step in the ceramic fabrication processes. It is predominantly realised by a thermal removal technique, in which key parameters such as heating rate and temperature need to be carefully considered. Gel cast PZT samples with 40 wt% resin in the premix solution and 45 vol% solids loading were used for thermal behaviour analysis. The reason to use the green compacts with the highest resin content is to maximise weight loss effects as a worst case scenario in terms of disruption to the structure. Samples were initially dried at room temperature for 1 day and then at 40 °C for 1 day, followed by further drying at 100 °C for 2 hrs. Experiments were carried out in air which is consistent with the practical burnout atmosphere. Figure 7-16 shows the simultaneous TGA (wt% loss) and DSC curves (mW/mg) conducted at 5 °C/min which is the routine heating rate in thermal analysis and 1 °C/min which is closer to equilibrium conditions.

It can be seen that at 1 °C/min, the burnout of organic additives completes at around 400 °C. At the higher heating rate, the onset of decomposition shifts to the higher temperature and no constant weight is achieved until 500 °C, which shows that the decomposition of polymer is not only related to the temperature but also the heating rate. At 1 °C/min, the sharp weight loss occurs at 200-400 °C and the major exothermal peak in DSC appears at about 400 °C, demonstrating the burnout of the epoxy resin, hardener and dispersant within a range of temperature. Several slope changes have been observed from the TGA curves in both figures, which might correspond to the breakdown of different bonds including C-C, C-O and C-N etc. It is worth noticing that at lower temperatures below 200 °C, no weight loss was observed in both figures, indicating no free water existed in the dried samples. The total weight loss for 5 °C/min heating rate is 7.32 wt% and for 1 °C/min it is 7.30 wt%, which are in close agreement with the calculated value of 7.26 wt% considering only the organic additives. This further confirmed that no free or bound water is retained in the gel cast green body after three-step drying, enabling the strength of the green compact to be fully explored without the influence of being plasticised by residual water. To ensure the complete burnout of organic components, the debinding process was conducted up to 500 °C under a slow heating rate of 1 °C/min based on these results.

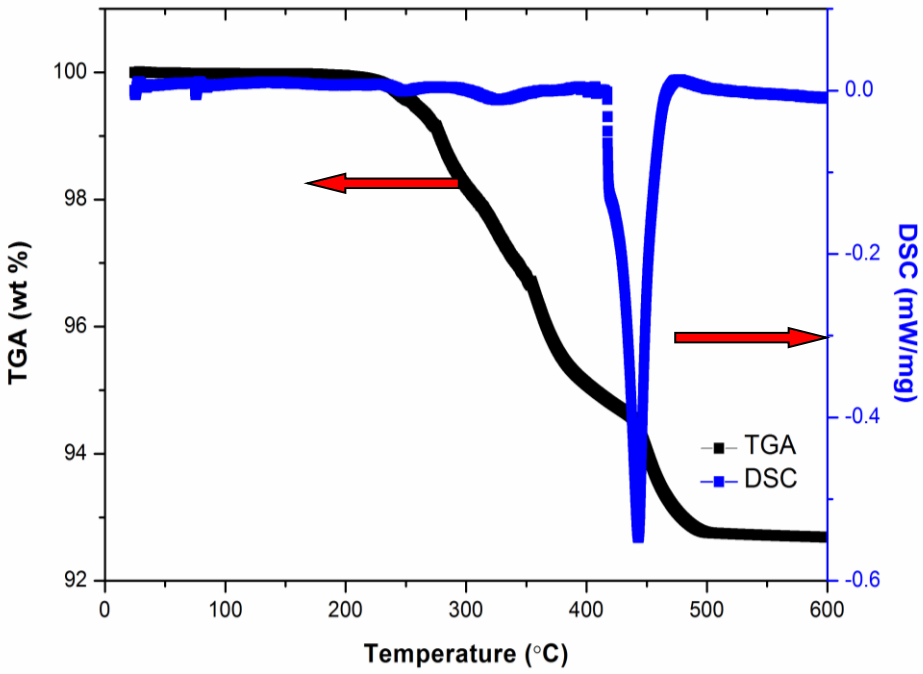

(a)

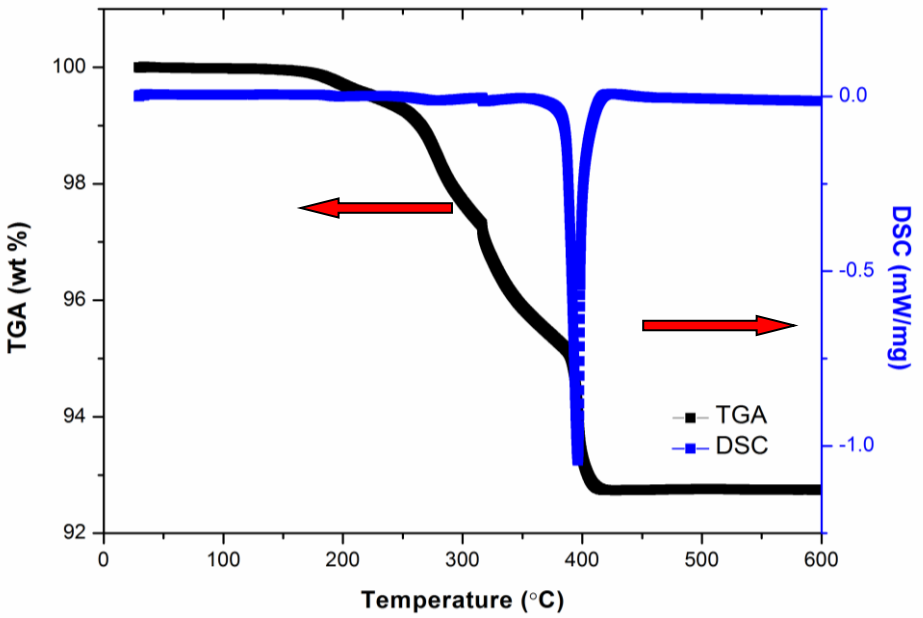

(b)

Figure 7-16 Thermal analysis of gel cast PZT green compact with 40 wt% resin in the premix solution and 45 vol% solids loading conducted at (a) 5 °C/min and (b) 1 °C/min.

7.6 Characterisation of gel cast green bodies

A typical gel cast green sample after demoulding and drying as described in Section 6.1.2 is shown in Figure 7-17 (~12 mm in diameter and ~2 mm in height). As it can be seen that, the green body has a clean and distinct outline and no visible cracks or air bubbles are presented on the surface.

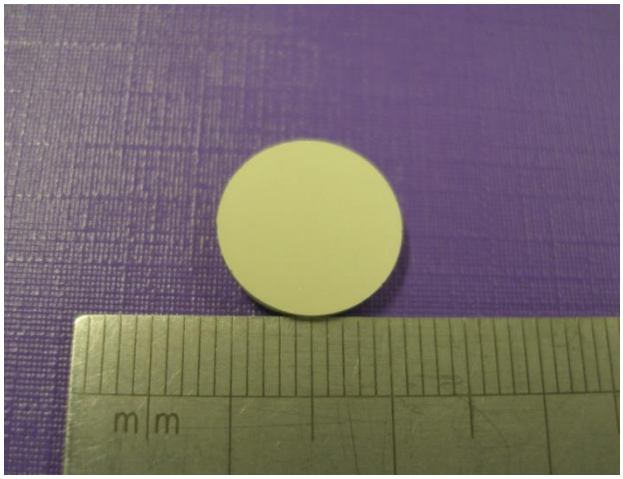

Figure 7-17 Typical green PZT plate obtained from 45 vol% solids loading PZT slurry with 20 wt% resin and 1 wt% Dispex A40 after demoulding and complete drying as described in Section 6.1.2.

Figure 7-18 shows the microstructure of the as-gelled surfaces of the gel cast green bodies obtained from 45 vol% solids loading with resin concentrations ranging from 10-40 wt%. With the increase of the resin content, a gradual decrease in pore size can be observed in the green bodies. Moreover, the presence of the polymeric film became more evident in the samples with higher resin contents, which is due to the fact that as the resin content increased, there was a higher fraction of cross-linked polymer filling in the interstitial spaces among the PZT particles.

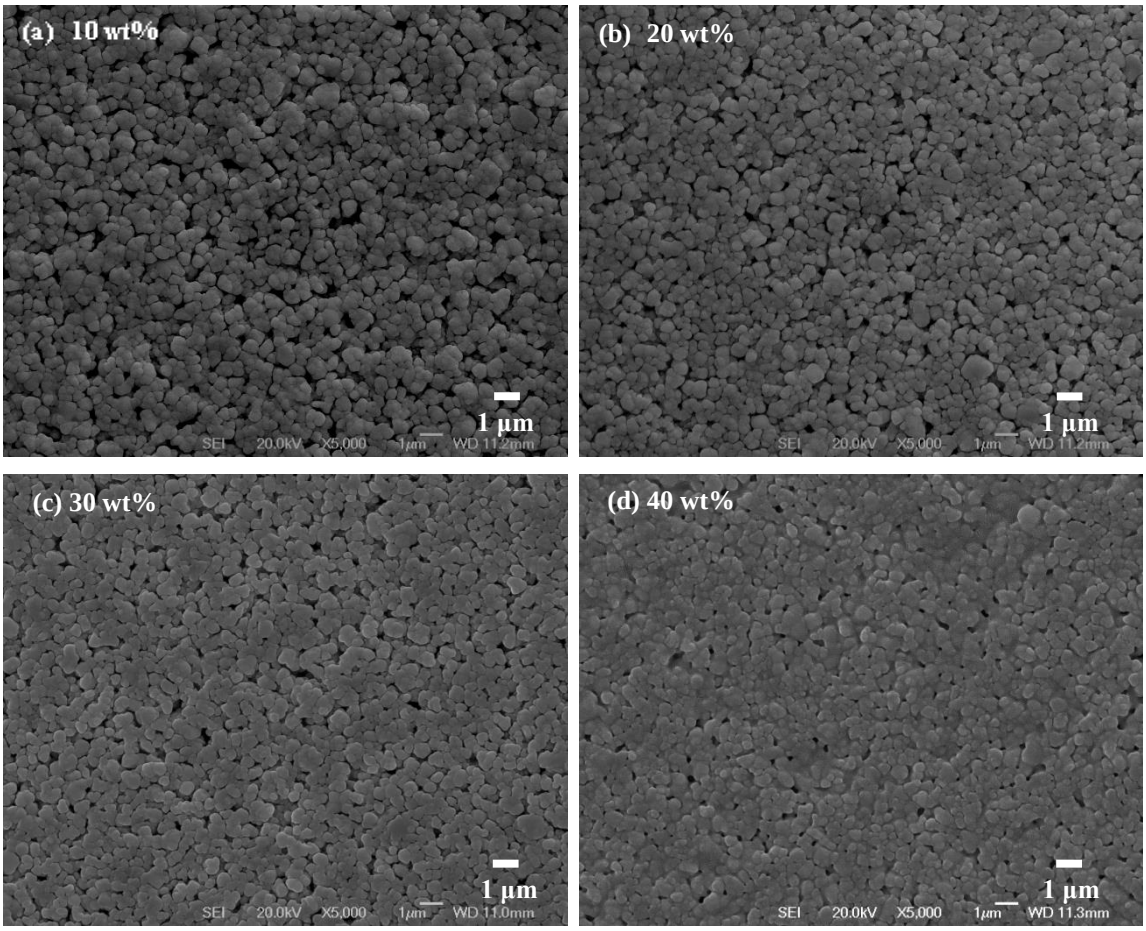

Figure 7-18 SEM images of as-gelled surfaces of the green bodies obtained from 45 vol% solids loading PZT slurries with different resin concentrations: (a) 10 wt% (b) 20 wt% (c) 30 wt% (d) 40 wt% after demoulding and complete drying.

Similar phenomena were found in the fracture surfaces of the green bodies obtained from 45 vol% solids loading PZT slurries with different resin concentrations as shown in Figure 7-19. It can be seen that in the green bodies with lower resin contents, the PZT particles were more defined while in the ones with higher resin contents, the outlines of the particles were less distinct as higher amounts of cured resin presented in the gaps. These fracture surfaces all presented relatively homogeneous microstructures, which can be attributed to the thorough mixing during the ball milling process.

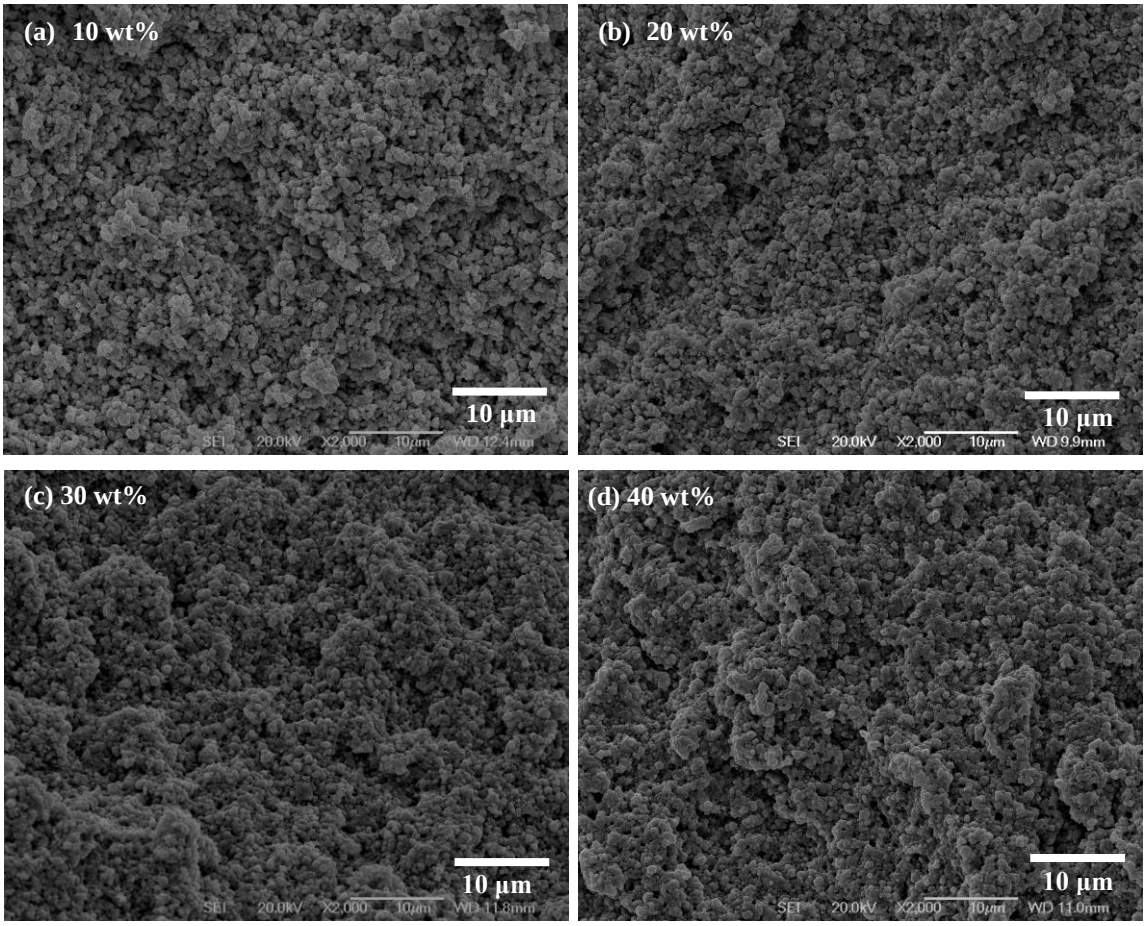

Figure 7-19 SEM images of fractured surfaces of the green bodies obtained by from 45 vol% solids loading PZT slurries with different resin concentrations: (a) 10 wt% (b) 20 wt% (c) 30 wt% (d) 40 wt% after demoulding and complete drying.

Particle packing is one of the most important physical characteristics of a green compact. Generally speaking, improved particle packing is desirable in ceramic processing as it decreases the overall shrinkage during sintering and also increases the number of material transport paths for densification thereby promoting the sintering rate [31]. From these SEM images, it is difficult to observe the effect of the resin content on the particle packing of the green bodies while the linear shrinkage data shed more light on it. As seen from Figure 7-20, with the increase of the resin content, the linear shrinkage increased, which means that the particle packing in the green bodies was enhanced, assuming the slurries with different resin contents have the

same particle packing. Before sintering, the shrinkage in this gel casting process comes from two sources: one being the consolidation shrinkage due to the contraction occurred during the cross-linking of epoxy-amine and the other being the drying shrinkage caused by the removal of water. As the gel casting slurries with higher resin contents have lower water concentrations, their linear shrinkage contributed from the evaporation of water should be smaller than that of the slurries with lower resin contents. However, the net linear shrinkage of the samples with higher resin contents was actually greater, which can be understood as follows. At lower resin contents, most of the resin molecules were attracted onto the surface of the particles according to Olhero et al. [16], causing local inhomogeneous distribution of the polymer chains. In that case, the interconnection of the polymer chains during curing might occur mainly near the surface of individual particles and the 3D network generated in this process would exert little contraction force on the neighbouring particles. At higher resin contents, the resin molecules were not only anchored to the particles but also freely filled in the interparticle spaces, providing more uniform local distribution of the polymer chains. During curing, a higher fraction of the 3D network developed in the interstitial gaps dragged the neigbouring particles together, leading to a closer mutual approach in the suspensions. Moreover, higher resin contents encouraged the formation of a finer porous network. These finer porous networks would exert a higher capillary suction pressure [16], causing possibly higher shrinkage during drying in spite of the lower water concentrations. The increased contraction among particles during curing and the increased suction pressure during drying both account for the increased overall shrinkage for the samples with higher resin contents. Detailed linear shrinkage data obtained at different processing stages would be able to prove what was the dominant factor responsible for the shrinkage. However, it was

considered out of scope in this work due to the complexity of the scenarios including the time for the slurries to be fully cured varies with the resin content and the curing stage overlaps with the drying stages etc. Similar phenomena were reported in other gel casting systems [32].

Because of the enhanced particle packing as well as the higher fraction of the polymerized resin filled in the interstitial gaps as evidenced by the SEM images, the green density of the green bodies increased with increases in the resin content as presented in Figure 7-20.

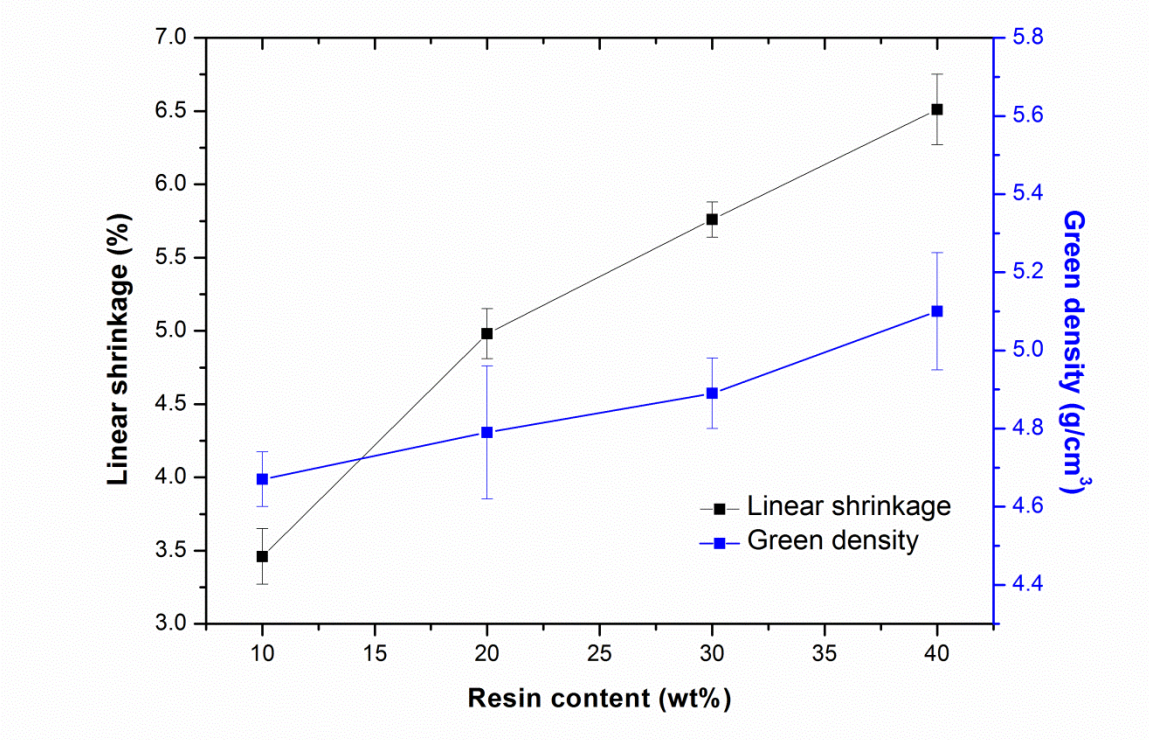

Figure 7-20 Linear shrinkage and green density of the gel cast PZT samples versus resin content at a solids loading of 45 vol%.

As expected, denser green bodies with higher resin contents also possessed higher green strength. As shown in Figure 7-21, with the resin concentration increasing from 10 wt% to 40 wt%, the green strength increased from around 6 MPa to 38 MPa. The green strength of 38 MPa achieved is enhanced compared with the values obtained

from the ceramic components fabricated by conventional gel casting systems as described in Section 3.5.2, which justifies the selection of the new epoxy-amine gel casting system. High green strength is of great importance for demoulding and handling of the ultra-fine structures required for the high frequency ultrasound application. In practice, the minimum green strength value needed for keeping the integrity of the green bodies depends on a variety of factors including the complexity of the structures, the aspect ratios of the components, demoulding techniques and operator's processing skills etc.

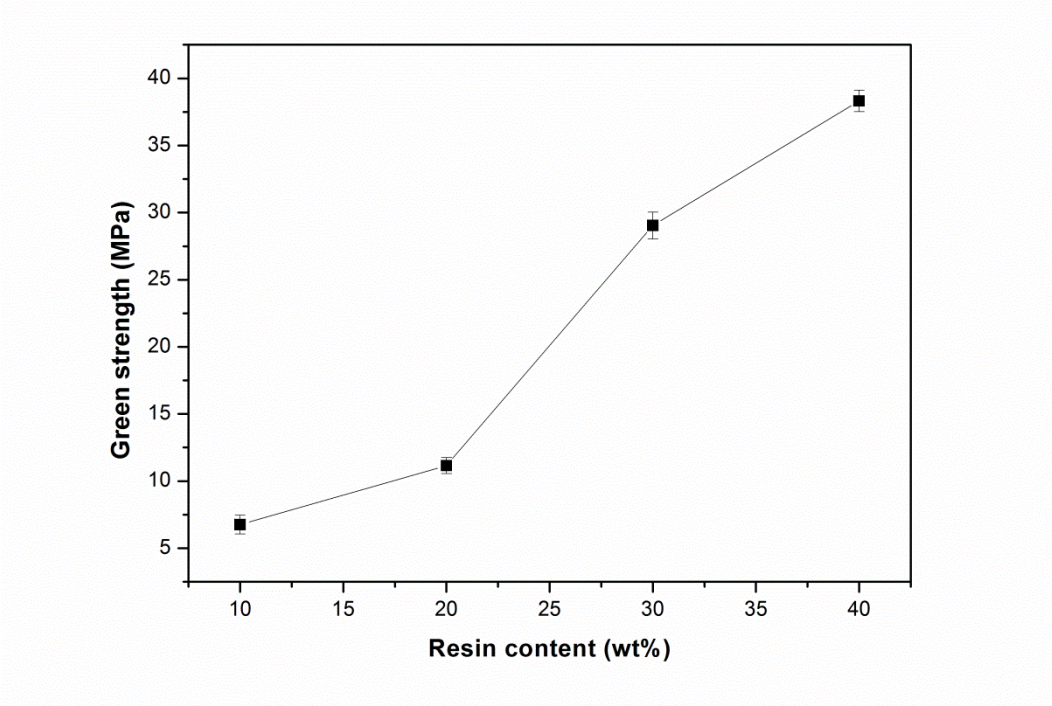

Figure 7-21 Green strength of the gel cast PZT samples versus resin content at a solids loading of 45 vol%.

7.7 Characterisation of gel cast sintered samples

Figure 7-22 shows the effect of the resin content on the sintered density of the gel cast PZT samples. It can be observed that the sintered density tended to decrease with

increases in the resin concentration, clearly indicating that high green density obtained in the green bodies with higher resin content did not translate to high sintered density.

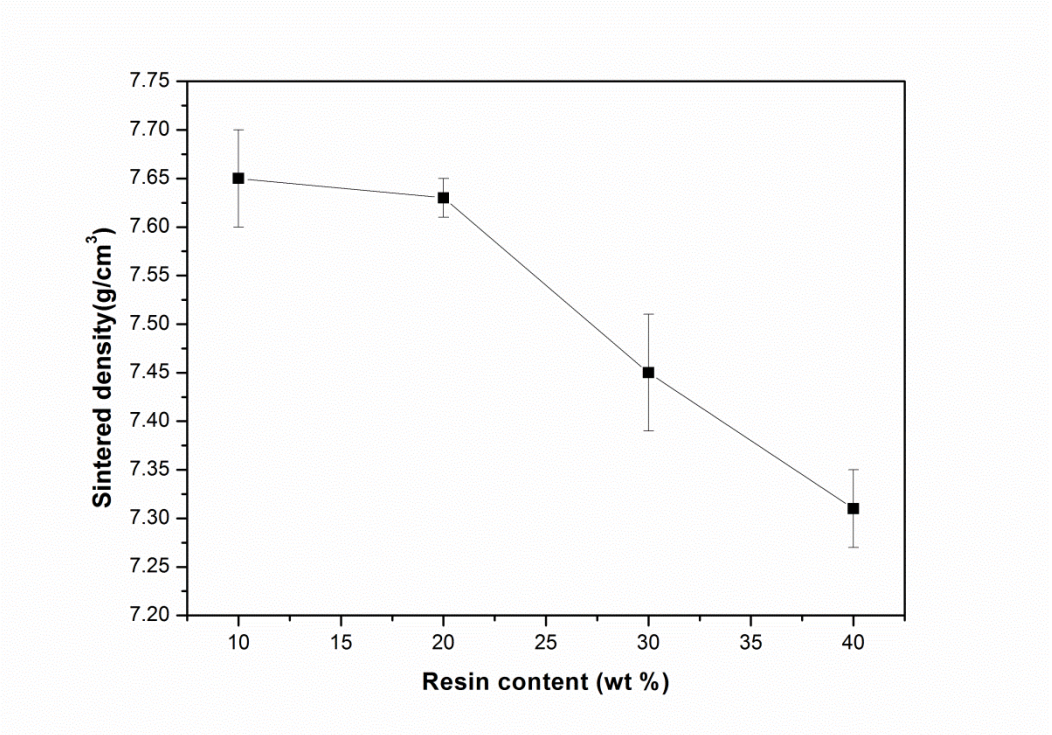

Figure 7-22 Sintered density of the gel cast PZT samples versus resin content at a solids loading of 45 vol%.

Figure 7-23 presents the SEM images of the facture surfaces of the sintered PZT samples. The samples obtained from the resin content of 10 wt% and 20 wt% show relatively dense and homogenous microstructure. With increases in the resin concentration, an increase of the porosity can be observed, which supports the decreasing trend in sintered densities shown in Figure 7-22. The results of the sintered density and microstructure suggest that the burning off of the resin might cause local disruption to the structure. The burnout process is an intricate complex process involving decomposition of organics, liquid migration, evaporation and heat transfer in the porous green compacts etc., in which the major event is related to the volume expansion from solid to gas due to pyrolysis [33]. The accumulation of the

voluminous gaseous decomposition products before flowing away through the porous media causes the buildup of the internal pressure, which depends on the gas evolution rate, gas permeability, size and specific surface area of the green body [33, 34]. In the green bodies with higher resin content, due to the larger amounts of the gaseous products as well as the lower gas permeation rate caused by the closer particle packing, such internal pressure would be increased which might then lead to the formation of defects such as cracks, blisters and expanded voids. These defects cannot be remedied in the later sintering process, resulting in increased porosity and decreased sintered density.

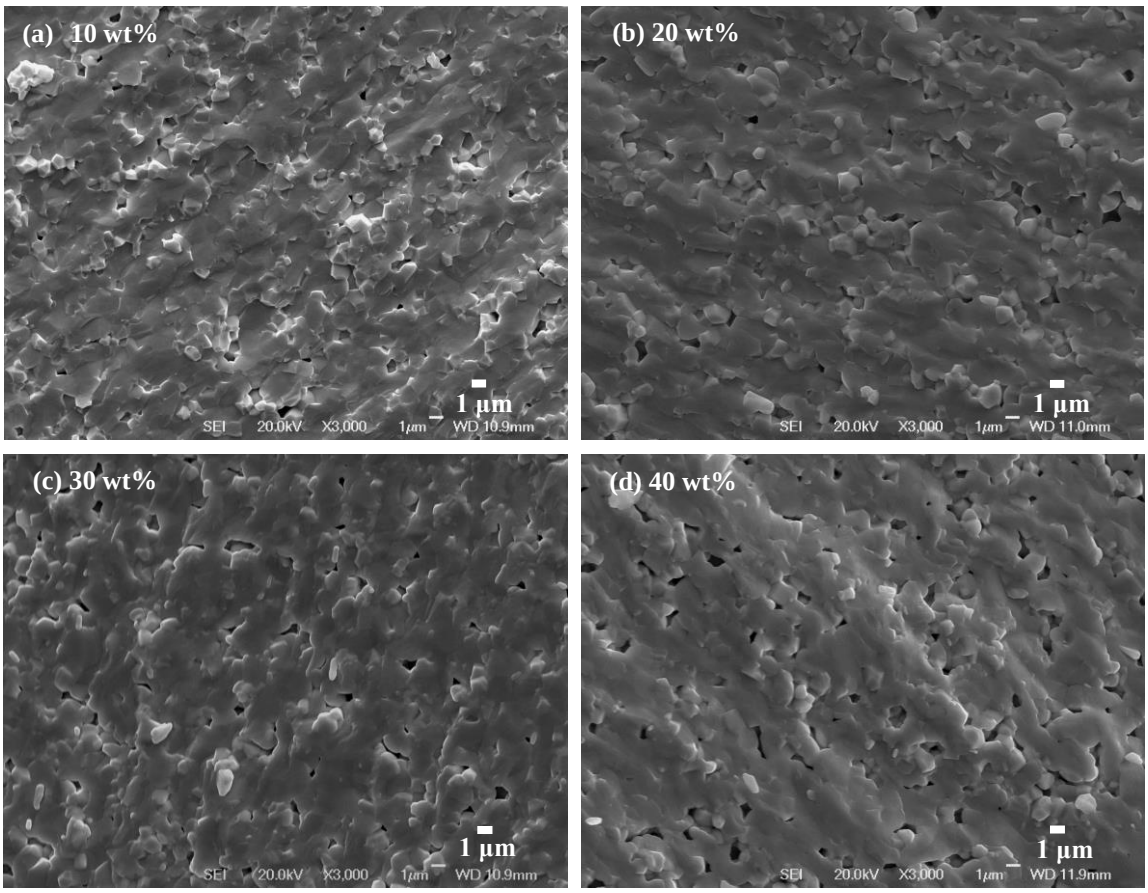

Figure 7-23 SEM images of fractured surfaces of the sintered PZT samples obtained from 45 vol% solids loading PZT slurries with different resin concentrations: (a) 10 wt% (b) 20 wt% (c) 30 wt% (d) 40 wt%.

7.8 Summary

This chapter has focused on gel casting of PZT bulk ceramic based on water soluble resin and amine hardener. The study of the gel casting process has been conducted by investigating the influences of a variety of the processing parameters on the rheological properties of premix solutions and PZT slurries as well as the physical properties of the green bodies and sintered samples. The results presented in this chapter are summarised as follows:

(1) The polymerisation process of the premix solution was greatly influenced by the hardener addition, resin content and the curing temperature. 0.2 mol/eq Bis(3-aminopropyl)amine was chosen as the optimal hardener addition as it gave the highest elastic modulus and a reasonable gelation time. With increasing resin content, the gelation time decreased and the elastic and viscous modulus of the polymerised gel increased. Increasing the curing temperature decreased the gelation time but had no obvious effect on the elastic and viscous modulus.

(2) The optimum dispersant (Dispex A40) concentration was determined as 1 wt% (based on the dried PZT powder weight) as it gave the lowest viscosity.

(3) Room temperature was used for the polymerisation of the gel casting slurries as it gave reasonable gelation times for all the slurries with various resin contents.

(4) The green bodies and sintered ceramics showed relatively homogeneous microstructures due to the thorough mixing during the ball milling process.

(5) Increasing the resin concentration in the gel casting slurry was beneficial in enhancing the green density and green strength of the gel cast component due

to improved particle packing and higher fraction of polymerised resin in the interstitial gaps; especially, green strengths as high as 38 MPa achieved in the green bodies with 45 vol% solids loading and 40 wt% resin. This is much higher than that obtained from commonly used gel casting systems and traditional colloidal processing routes, justifying the selection of the epoxy-amine system.

(6) The increase of the resin content also brought a series of undesirable consequences: (a) viscosity of the slurry increased; (b) gelation time decreased; (c) sintered density decreased. The deterioration of the properties in the sintered samples obtained from high resin contents suggested that burning off the resins caused disruption to the gel cast green bodies. For the fabrication of bulk ceramics, a compromise could be achieved at 20 wt% resin content as it gave low viscosity (<1 Pa·s), moderate gelation time (20-30 min) at room temperature, excellent sintered properties as well as the sufficient green strength (11 MPa) to keep the integrity of the structure. For the fabrication of the ultra-fine structures with high aspect ratios for HFUS applications, high green strength is of paramount importance to the demoulding process, and therefore the use of high resin content might be necessary, which is discussed in Chapter 9.

7.9 References

[1] J. R. M. d'Almeida and S. N. Monteiro, "The influence of the amount of hardener on the tensile mechanical behavior of an epoxy system," *Polymers for Advanced Technologies*, vol. 9, pp. 216-221, 1998.

[2] J. R. M. d'Almeida, *et al.*, "Ageing of the DGEBA/TETA epoxy system with off-stoichiometric compositions," *Materials Research*, vol. 6, pp. 415-420, 2003.

[3] M. Dong, *et al.*, "Gelcasting of SiC using epoxy resin as gel former," *Ceramics International,* vol. 35, pp. 1363-1366, 2009.

[4] X. Mao, *et al.*, "Rheological characterization of a gelcasting system based on epoxy resin," *Ceramics International,* vol. 35, pp. 415-420, 2009.

[5] M. R. Vanlandingham, *et al.*, "Relationships between stoichiometry, microstructure, and properties for amine-cured epoxies," *Journal of Applied Polymer Science,* vol. 71, pp. 699-712, 1999.

[6] C.-Y. M. Tung and P. J. Dynes, "Relationship between viscoelastic properties and gelation in thermosetting systems," *Journal of Applied Polymer Science,* vol. 27, pp. 569-574, 1982.

[7] L. Wu, *et al.*, "Effects of water on the curing and properties of epoxy adhesive used for bonding FRP composite sheet to concrete," *Journal of Applied Polymer Science,* vol. 92, pp. 2261-2268, 2004.

[8] G. Van Assche and B. Van Mele, "Interphase formation in model composites studied by micro-thermal analysis," *Polymer,* vol. 43, pp. 4605-4610, 2002.

[9] J. Zhou and J. P. Lucas, "Hygrothermal effects of epoxy resin. Part I: the nature of water in epoxy," *Polymer,* vol. 40, pp. 5505-5512, 1999.

[10] T. S. Ellis and F. E. Karasz, "Interaction of epoxy resins with water: the depression of glass transition temperature," *Polymer,* vol. 25, pp. 664-669, 1984.

[11] S. Vyazovkin, *et al.*, "Kinetics of Epoxy–Amine Curing Accompanied by the Formation of Liquid Crystalline Structure," *Macromolecular Rapid Communications,* vol. 24, pp. 1060-1065, 2003.

[12] W. Cao and C. A. Randall, "Grain size and domain size relations in bulk ceramic ferroelectric materials," *Journal of Physics and Chemistry of Solids,* vol. 57, pp. 1499-1505, 1996.

[13] C. A. Randall, *et al.*, "Intrinsic and Extrinsic Size Effects in Fine-Grained Morphotropic-Phase-Boundary Lead Zirconate Titanate Ceramics," *Journal of the American Ceramic Society,* vol. 81, pp. 677-688, 1998.

[14] K. Nogi, *et al.*, Eds., *Nanoparticle Technology Handbook*. 2012, p.^pp. Pages.

[15] D. Zhang, *et al.*, "Microfabrication of Three-Dimensional, Free-Standing Ceramic MEMS Components by Soft Moulding," *Advanced Engineering Materials,* vol. 5, pp. 924-927, 2003.

[16] S. M. Olhero, *et al.*, "Innovative fabrication of PZT pillar arrays by a colloidal approach," *Journal of the European Ceramic Society,* vol. 32, pp. 1067-1075, 2012.

[17] R. Suntako, *et al.*, "Effects of dispersant concentration and pH on properties of lead zirconate titanate aqueous suspension," *Ceramics International*, vol. 35, pp. 1227-1233, 2009.

[18] D. Zhang, *et al.*, "Preparation of concentrated aqueous alumina suspensions for soft-molding microfabrication," *Journal of the European Ceramic Society*, vol. 24, pp. 231-237, 2004.

[19] N. Traiphol, *et al.*, "Roles of polymeric dispersant charge density on lead zirconate titanate aqueous processing," *Ceramics International*, vol. 36, pp. 2147-2153, 2010.

[20] D. Zhang, "Fabrication of ceramic micro-components," PhD, School of Metallurgy and Materials, University of Birmingham, Birmingham, 2005.

[21] A. U. Khan, *et al.*, "Interaction of binders with dispersant stabilised alumina suspensions," *Colloids and Surfaces A: Physicochemical and Engineering Aspects*, vol. 161, pp. 243-257, 2000.

[22] Y. Mao, *et al.*, "Depletion force in colloidal systems," *Physica A: Statistical Mechanics and its Applications*, vol. 222, pp. 10-24, 1995.

[23] P. Jenkins and M. Snowden, "Depletion flocculation in colloidal dispersions," *Advances in Colloid and Interface Science*, vol. 68, pp. 57-96, 1996.

[24] Y. Otsubo, "Rheology Control of Suspensions by Soluble Polymers," *Langmuir*, vol. 11, pp. 1893-1898, 1995/06/01 1995.

[25] Z.-p. Xie, *et al.*, "Ceramic forming based on gelation principle and process of sodium alginate," *Materials Letters*, vol. 57, pp. 1635-1641, 2003.

[26] I. Ganesh, *et al.*, "Gelcasting of Magnesium Aluminate Spinel Powder," *Journal of the American Ceramic Society*, vol. 92, pp. 350-357, 2009.

[27] S. L. Morissette and J. A. Lewis, "Chemorheology of Aqueous-Based Alumina-Poly(vinyl alcohol) Gelcasting Suspensions," *Journal of the American Ceramic Society*, vol. 82, pp. 521-528, 1999.

[28] Y. L. Hsieh, *et al.*, "Gel Point of Whey and Egg Proteins Using Dynamic Rheological Data," *Journal of Food Science*, vol. 58, pp. 116-119, 1993.

[29] X. J. Mao, *et al.*, "Gelcasting of alumina using epoxy resin as a gelling agent," *Journal of the American Ceramic Society*, vol. 90, pp. 986-988, 2007.

[30] M. A. Rao, Ed., *Rheology of Fluid and Semisolid Foods*. Springe, 2007, p.^pp. Pages.

[31] R. Loehman, *Characterization of Ceramics*: Momentum Press, 2009.

[32] S. M. Olhero, *et al.*, "Synergy of polysaccharide mixtures in gelcasting of alumina," *Journal of the European Ceramic Society*, vol. 20, pp. 423-429, 2000.

[33] D.-S. Tsai, "Pressure buildup and internal stresses during binder burnout: Numerical analysis," *Aiche Journal*, vol. 37, pp. 547-554, 1991.

[34] K. Li, *Ceramic Membranes for Separation and Reaction*: John Wiley & Sons, 2007.

CHAPTER 8 MOULD FABRICATION

8.1 Introduction

Net-shape moulding based on the gel casting technique has been shown to be a promising fabrication route for the fabrication of high frequency piezocomposites. As one part of the moulding route for the slurry preparation, a novel gel casting system has been developed and presented in Chapter 7. As another significant part for the random pattern realisation, moulds with the negative structures of the desired shapes of piezoceramic segments, compatible with the gel casting process, have been fabricated and characterised and the results are reported in this chapter.

Possible moulding strategies involving various mould materials and different demoulding techniques are summarised at the beginning of this chapter, followed by detailed explanations of the development of both direct and indirect moulding routes. Effects of a range of processing parameters on the obtained patterns were investigated for the optimisation of the processes and compatible demoulding methods were considered and developed. The chapter concludes with the selection of the most appropriate moulding route for the production of desired random structures.

8.2 Overview of different moulding routes

Requirements of the mould material for this application and a series of micro-mould fabrication techniques involving different mould materials have been discussed in Chapter 4. Thick photoresists and deep etched Si have been identified as promising candidates for the mould materials. Potential moulding routes involving these two types of materials are shown in Figure 8-1. To simplify the scenario, regular-shaped cavities are used for illustration. In the direct moulding route shown in Figure 8-1(a),

a thin layer of photoresist is spin-coated and UV patterned on a silicon wafer, thus transferring a 2D pattern on a pre-designed mask to a 3D structure. The gel casting slurry is directly cast into the resulting photoresist mould, which is removed afterwards usually by chemical dissolution in a stripper solution. In the indirect moulding route shown in Figure 8-1(b) and (c), a master mould is produced first with the desired bristle-block structure which is subsequently replicated by a soft mould. The gel casting slurry is vacuum cast into the soft mould and after drying the mould is carefully peeled off leaving the green-state ceramic segments standing on the surface of a stock base. Both UV patterned photoresist polymers and etched Si can be used as master moulds. By comparison, it can be found that the direct moulding route has the merit of a shorter production cycle while the indirect moulding route has the advantage of providing recyclable soft moulds thus reducing the cost and production time in the longer term.

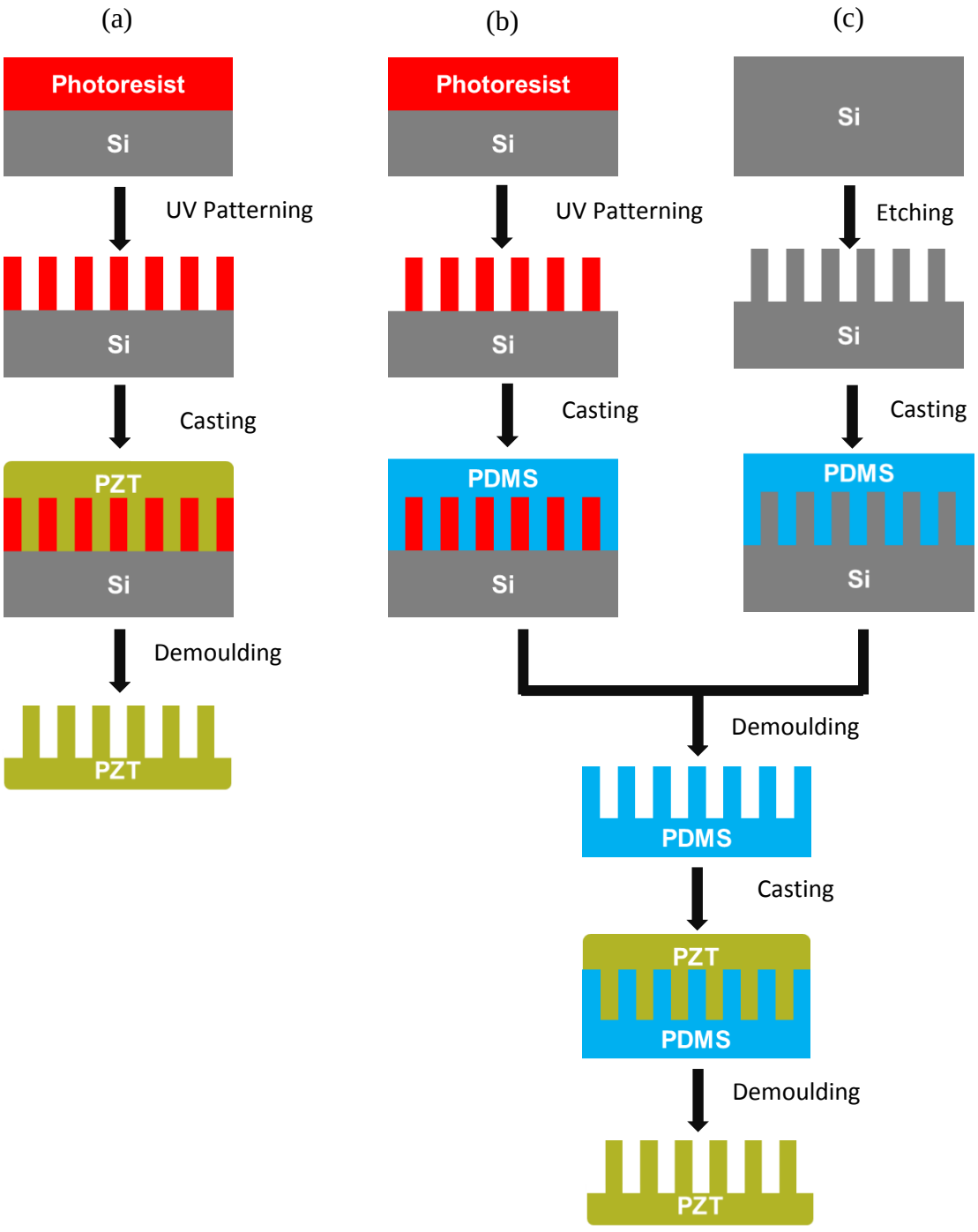

Figure 8-1 Different moulding routes for the fabrication of random moulds: (a) direct moulding based on patterning photoresist materials; (b) indirect moulding based on patterning photoresist materials; and (c) indirect moulding based on etching Si wafer.

There is a range of processing parameters involved in both the direct and indirect moulding routes, for example, the dosage of UV energy for the photoresist, and the duration of each step. In order to understand the effect of the parameters on the resulting moulds, micro-sized moulds with regularly arranged cavities of simple cross-sectional shapes such as circles, were initially targeted. Based on the knowledge and experience acquired from producing regular-shaped moulds, novel random moulds were fabricated subsequently. A series of masks with regular or random patterns were designed to be used for pattern transfer and each set contained a bright and a dark field mask with the same pattern prepared for negative and positive photoresists, respectively.

8.3 Photoresist moulds for direct moulding

As introduced in Chapter 4, photoresist polymers have been widely employed in advanced micro-fabrication applications. In this section, hard moulds for the direct moulding route were fabricated using a routinely used photolithographic process as explained in Section 6.1.1.1 and the moulds were characterised, followed by preliminary trials of green-state ceramic structures demoulded from such moulds. Several photoresists have been investigated and the results of one representative positive and negative resist are presented and discussed in detail.

8.3.1 Negative photoresist mould

8.3.1.1 Regular pattern

Compared with commonly used positive photoresists, negative-tone ones were considered more suitable for the mould fabrication required in this application mainly because they are generally thicker with better adhesion to the substrate despite their

poorer strippability as discussed in Section 4.4. AZ 125nXT is claimed by the manufacturer to be able to produce over 100 µm thick layer in a single coating and be strippable by a commercial remover [1]. AZ125nXT met many of the criteria desired for a negative photoresist mould and was chosen as a viable candidate to be investigated further. A mask shown in Figure 8-2 was first applied for patterning AZ 125nXT, having regularly arranged circles 25 µm in diameter with 10 µm spacing. The circular area was shadowed by the mask during exposure and dissolved in the subsequent development stage while the area outside of the circles was supposed to be exposed and remain in situ. To increase the understanding of the behaviour of this photoresist, the thickness of the single coating layer on the Si substrate was gradually increased and the processing parameters were correspondingly optimised aiming at through holes with precisely transferred patterns and straight sidewalls.

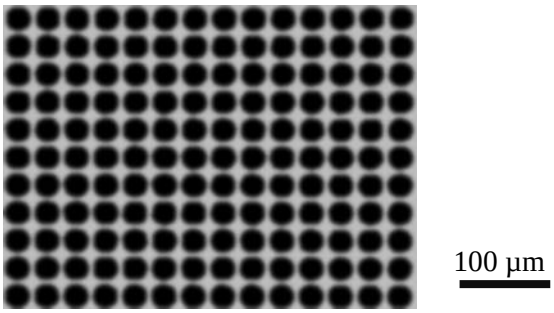

Figure 8-2 Optical image of the regular pattern on the mask for the negative photoresist mould fabrication. The circles are 25 µm in diameter with 10 µm spacing.

Table 8-1 shows the optimised parameters of each processing step during the fabrication of AZ 125nXT holes with thicknesses of 50-120 µm. They were optimised by adjusting the data provided by the supplier [1] based on the knowledge of photolithography principles discussed in Section 4.4 as well as the behaviour of the facilities employed. Thickness of the mould is ultimately decided by the rotating speed of the wafer and the time at that speed. As suggested by the supplier (see

Section 4.4.1), the spin speed at the beginning of coating was desired to be greater than that required for a certain thickness to make sure that the Si substrate was completely covered by this viscous resist. For each thickness, the initial spin speed was 200-300 rpm greater than the steady speed as shown in the table. The choice of the steady speed was demonstrated by measuring the thickness of the resist layer after soft baking and drying using a digital dial indicator (Mitutoyo, UK) mounted on a comparator stand, along with the side-viewed SEM images of the resulting moulds. The temperature required for soft baking was suggested to be 140 ºC, which was adopted for the moulds with thicknesses <100 µm. For 120 µm thicknesses, a two-step soft bake was performed to give more uniform and thorough heating, and prevent the formation of cracks and lift-off of the photoresist from the wafer surface due to rapid heating as explained in Section 4.4.2. A series of bake times have been tried and the times listed in the table are the ones giving non-sticky, crack-free surface of the resist layer. An appropriate combination of the UV exposure dosage and the development time is routinely considered as the most important factor in achieving the required geometries and dimensions, and thus the optimisation of this combination is discussed in detail in the following paragraphs.

Table 8-1 Optimised photolithography conditions for the 50 µm, 70 µm, 85 µm and 120 µm thick AZ 125nXT moulds with regularly shaped patterns.

Thickness	**Spin coating speed/ time**			**Soft bake temperature/time**		**Relaxation time**	**Exposure time**	**Relaxation time**	**Development time**
(µm)	**(rpm/s)**			**(°C/min)**		**(min)**	**(No. of stages/ min per stage)**	**(min)**	**(min)**
	Stage 1	*Stage 2*	*Stage 3*	*Stage 1*	*Stage 2*				
50	400/2	2200/2	1900/10	140/7		10	3/3,3,2	10	2.5-3
70	400/2	1200/2	1000/10	140/10		10	4/3,3,3,1	10	4-5
85	400/2	1100/2	900/12	140/12		10	5/3,3,3,3,1	10	6-7
120	400/2	1100/2	600/10	90/2	135/25	15	6/3,3,3,3,3,2	15	12-13

Note: 1. The thicknesses of the photoresist layers were determined by measuring Si wafers before coating and after coating, baking and cooling.

2. The intensity of the UV lamp was 4.58-4.88 mW/cm^2 during the experiments.

3. During exposure, a relaxation period of 2 min was introduced between stages.

When exposing a photoresist film, it is crucial to ensure the correct areas are exposed for the right amount of time. For each thickness value, a series of exposure doses and development times varying around the estimated optimum values were investigated. For discussion purposes, only results from the 120 μm thick films are presented as being representative of the behaviour of the photoresist.

Optical images of the top surface of the photoresist moulds with corresponding exposure and development times are shown in Table 8-2. It can be seen that at lower exposure times of 13 min and 15 min, the size of the holes are obviously larger than the pattern on the mask after a short development period of 3 min. This suggests that the area outside of the circles was insufficiently exposed and therefore was partially cross-linked after exposure, leading to the gradual dissolving of it in the developer. After 6 min developing, the photoresist layer exposed for 13 min lifted off the wafer surface and was washed way, and the one exposed for 15 min was partially separated from the Si wafer as the developer continued to dissolve the sidewalls of the holes until the neighbouring holes were merged into one. As the exposure time increased to 17 min, the photoresist after 3 min development time gave the desired circular features with approximately the required size. Further development slightly increased the size of the holes but no severe erosion of the exposed area (outside of the holes) was observed. For a longer exposure time of 19 min, a small portion of the photoresist inside of the holes was observed to remain after developing 3 min, showing as brighter dots in the holes in the image. Prolonging the development period to 6 min still gave little effect on the dissolution of the residues. This indicates the area inside of the holes, especially the parts at or near the surface, was partially exposed and cross-linked afterwards, which is highly possible due to the scatter and diffraction of

the UV light during the long exposure time. It must be noted that during these experiments, the intensity of the UV lamp was 4.55-4.85 mW/cm^2, which is substantially lower than the initial reading of 13.26 mW/cm^2 and commonly reported values for conventional mercury lamps [2], and therefore, an unusually long exposure time over 15 min had to be applied to give the required exposure energy of over 4000 mJ/cm^2. Using a UV lamp with a higher UV intensity would effectively reduce the exposure time and possibly prevent the shadowed parts from being exposed. Based on the discussion above, the optimum exposure time was determined to be 17 min. By imaging the cross sections of the resulting moulds, the development time was found to be not long enough to dissolve the holes all the way through until it was increased to 12 min.

Table 8-2 Top-viewed optical images of the regular AZ 125nXT moulds obtained from different exposure times (t_{exp}) and development times (t_{dev}).

t_{dev} \ t_{exp}	13 min	15 min	17 min	19 min
3 min	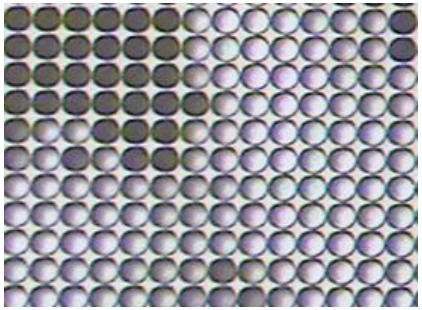	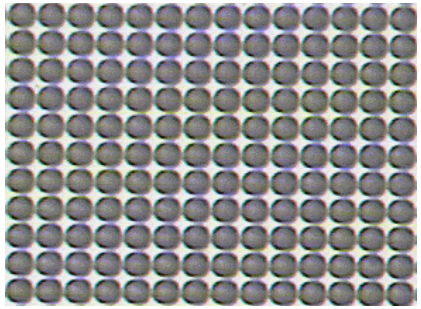	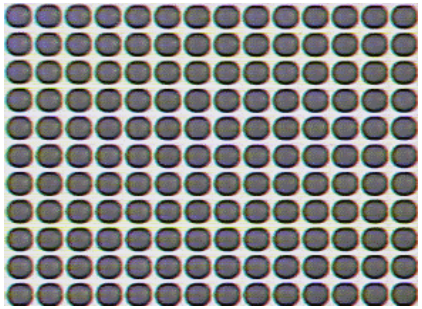	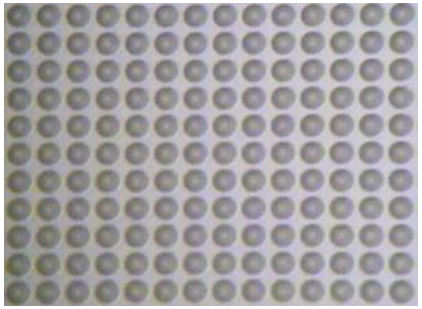
6 min	Photoresist layer lifted off from the Si wafer	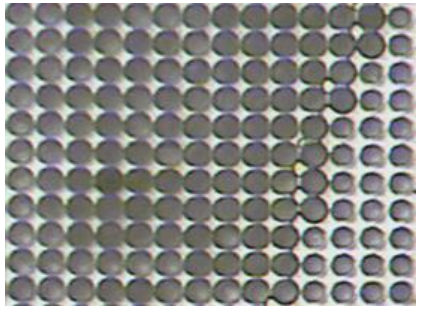	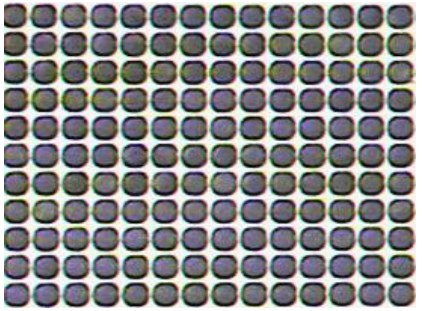	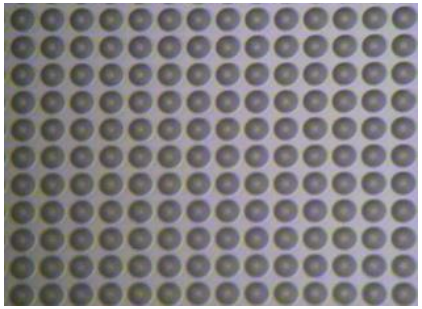 100 μm

Figure 8-3 shows SEM images of the cross-sections of moulds fabricated by using the optimised parameters listed in Table 8-1. It can be observed that parallel and through holes with thicknesses varying from 50 µm to 120 µm and aspect radios over 10 have been successfully achieved. It is worth noticing that the sidewalls of the moulds with different thicknesses are not accurately vertical to the Si substrates. This is a common issue in the fabrication of ultra-thick photoresists [3, 4]. It can be explained by considering the following processing conditions. Firstly, with thick photoresists, it is difficult and time-consuming for the base sections to receive enough UV energy to drive the crosslinking reaction. Especially, in this case as the UV lamp employed was significantly degraded and not efficient enough for exposure. The extremely long exposure time applied would increase the difference in the energy received at the top and at the base of the photoresist layer. Insufficiently exposed sections at the base would be more liable to be dissolved by the developer than those near the surface, leaving tapered sidewalls or even lifted structures. Moreover, long exposure time would introduce undesired exposure by scattering, diffraction and reflection of the UV light, which probably accounts for the variation of the sidewall profiles. Additionally, the development time applied was longer than suggested by the manufacturer in order to thoroughly remove resists inside of the arrays of fine holes, leading to the increase of the sidewall angle.

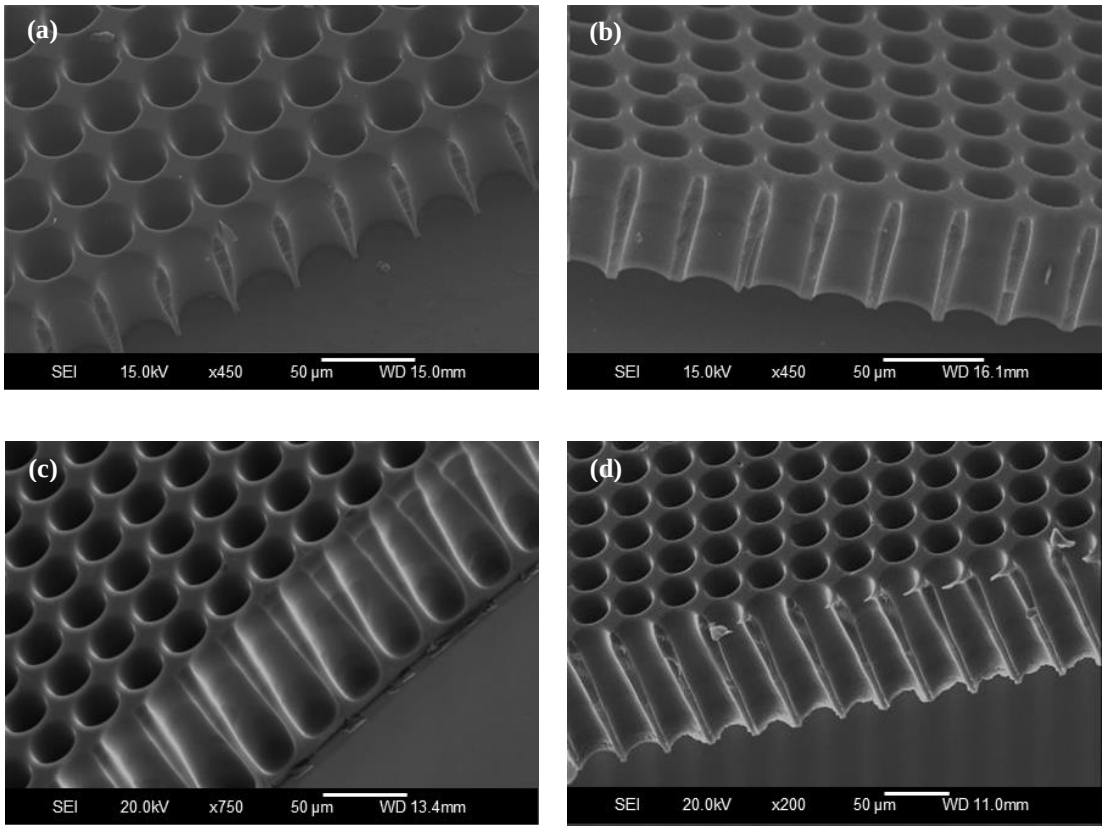

Figure 8-3 Side-viewed SEM images of AZ 125nXT moulds with regularly arranged through holes and thicknesses of (a) 50 µm (b) 70 µm (c) 85 µm and (d) 120 µm.

8.3.1.2 Random pattern

The optimised processing parameters discussed in the previous section were subsequently applied for the fabrication of the moulds with random patterns. Figure 8-4(a) shows the optical image of the mask used for exposure and the 120 µm thick random moulds using the AZ 125nXT resist. After 12 min development, the developed randomised pattern shown in Figure 8-4(b) appear to have larger feature sizes compared with the mask. As seen at higher magnification, the comparatively small features of the moulds are obviously under developed. Applying longer development times of up to 15 min still could not resolve the fine holes but enlarged the sizes of developed holes and even joined the neighbouring features as observed in Figure 8-4(d) and Figure 8-4(e). It suggests that AZ 125nXT may not be able to

provide sufficient resolution for the fabrication of random moulds with feature sizes down to a couple of micrometres.

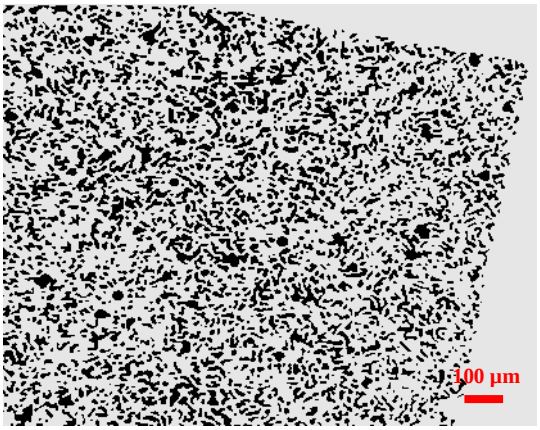

(a) Mask

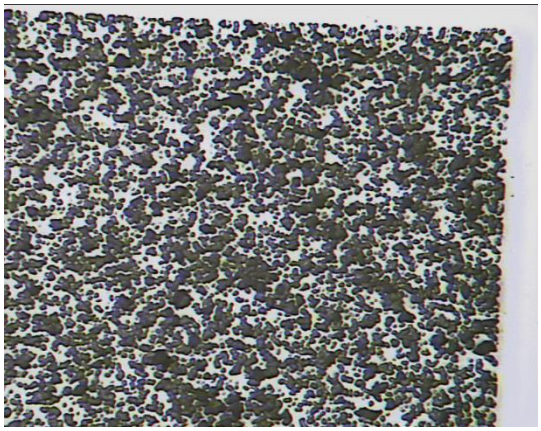

(b) After 12 min development

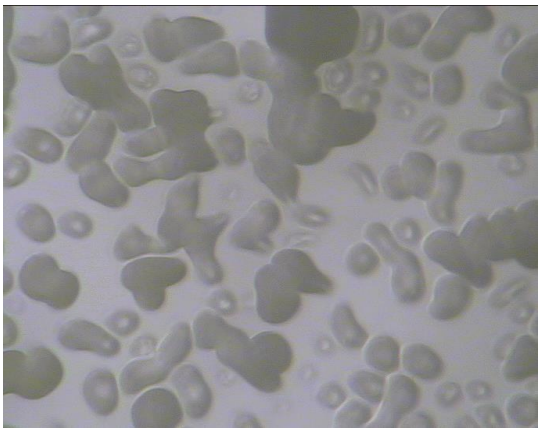

(c) After 12 min development

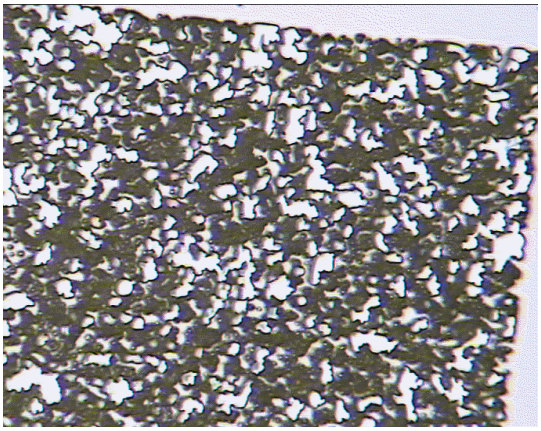

(d) After 15 min development

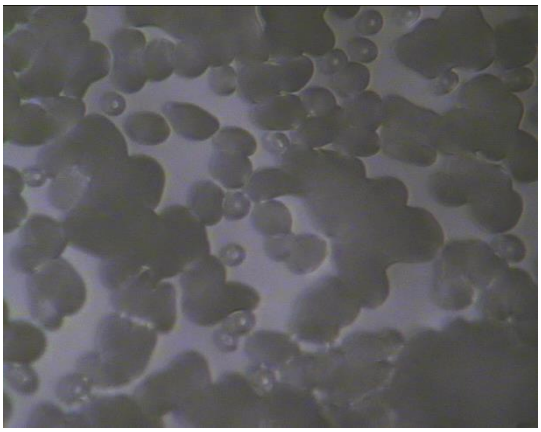

(e) After 15 min development

Figure 8-4 Top-viewed optical images of (a) the mask, (b) and (c) the AZ 125nXT random mould after 12 min development; (d) and (e) the AZ 125nXT random mould after 15 min development.

SEM images of the 120 µm thick AZ 125nXT random mould after 12 min development are shown in Figure 8-5. It can be seen from the cross-sectional view that at least some of features have been developed all the way through the photoresist layer to the silicon substrate. Thus it can be deduced that the suitability of the processing parameters greatly depends on the feature size. The optimised conditions shown in Table 8-1 may only be applicable to the features with lateral dimensions of around 25 µm. For features with much larger sizes, the development time optimised for 25 µm holes would be overwhelming, resulting in a decrease of the sidewall thickness. For features with much smaller sizes, the long exposure time caused unwanted exposure, leading to undesired crosslinking and hence under developed holes. The greater the differences in feature sizes, the more evident the phenomena would be. Considering the variations in size and shape of the random pattern as well as the possible resolution limitation of AZ 125nXT, this negative photoresist was considered not suitable for the fabrication of random moulds with feature sizes of 2-50 µm.

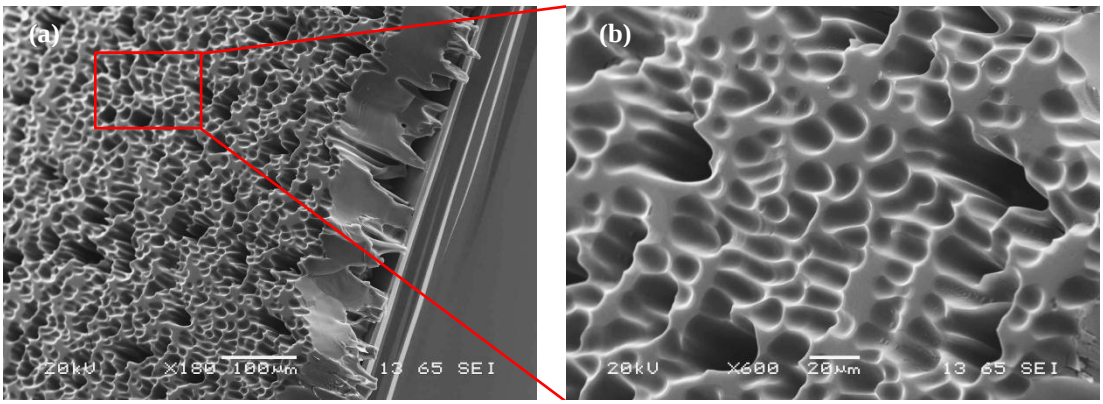

Figure 8-5 SEM images of a 120 µm thick AZ 125nXT random mould fabricated using the optimised conditions shown in Table 8-1, viewed at (a) lower magnification and (b) higher magnification.

8.3.1.3 Demoulded green-state PZT structures

Despite AZ 125nXT not meeting the requirements for random moulds, the AZ 125nXT moulds with regularly shaped features were considered acceptable for the gel casting of PZT. A 70 µm thick AZ 125nXT regular mould was cast with a gel casting slurry containing 20 wt% EGDGE (Sigma-Aldrich, Germany) (selected based on the work reported in [5] for trial tests) and subsequently degassed and dried according to the procedures described in Section 6.1.2.3. Removal of the mould was first tried using DMSO (dimethyl sulfoxide) solution (MicroChemicals GmbH, Germany) at 80ºC as suggested by the supplier. SEM images of the PZT filled mould after stripping for 12 hrs are shown in Figure 8-6. Although the Si substrate is completely separated from the green body, the photoresist is observed to be partially stripped, leaving a non-continuous polymer layer on the stock and photoresist residues between the pillar structures. Moreover, distortion of the pillars can be seen from the images, which is possibly due to the softening of the green body itself in the remover and the disturbance from the swelling of the photoresist. Additional factors might include the heat flow during stripping and the evaporation of DMSO during drying. It is also noticed that the holes are incompletely filled with gel cast materials, which is one of the drawbacks of using hard moulds for casting fine-scale structures. Due to the fact that hard moulds are not optically transparent, whether they are fully filled up during gel casting cannot be determined until they are being stripped.

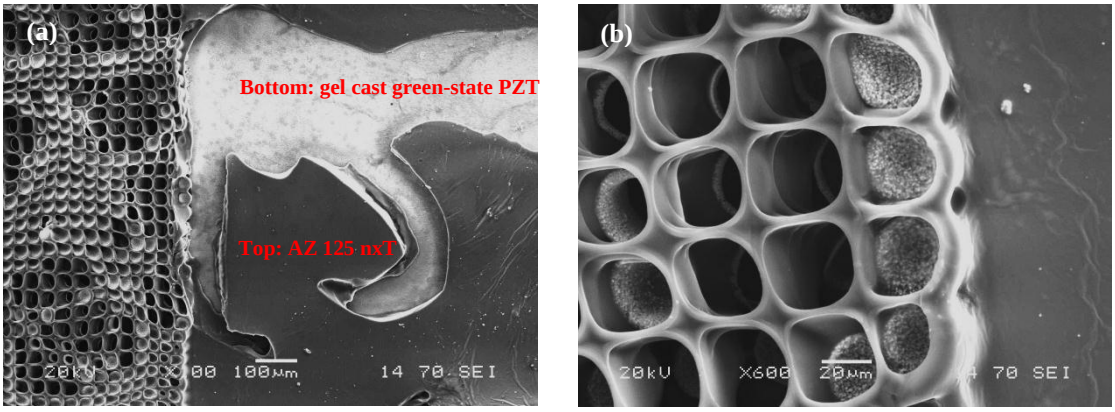

Figure 8-6 SEM images of a 70 µm thick AZ 125nXT mould filled with gel cast green-state PZT after being stripped in the DMSO solution at 80ºC for 12 hrs., viewed at (a) lower magnification and (b) higher magnification.

A more effective stripper than DMSO remover for stripping AZ 125nXT was found to be NaOH aqueous solutions. Figure 8-7 shows SEM images of the green-state PZT pillars after being demoulded from a 70 µm thick AZ 125nXT regular mould in a 4 wt% NaOH aqueous solution at room temperature for 12 hrs and dried at room temperature. Most of the mould structure has been successfully dissolved even at the base of the pillars, although traces of residue can still be seen on top and in between the pillar structures. The tilting and collapsing of the pillars was not observed during stripping but during drying, which suggests that the pillar structure is highly sensitive to capillary forces. According to Ye et al. [6] and Namatsu et al. [7], the capillary pressure P_c imposed on the pillar structure can be expressed as follows:

$$P_c = \frac{2\cos(\theta_c)\sigma}{x} \qquad \textbf{Equation 8-1}$$

where θ_c is the contact angle between liquid and the solid surface, σ is the surface tension at the liquid-solid-vapour interface, and x is the spacing or kerf between two solid structures as shown in Figure 8-8. During drying, at the liquid-gas boundary or

drying front, the amount of the liquid tends to decrease, causing a reduction of θ_c. According to Equation 8-1, the reduction of θ_c leads to an increase of the capillary pressure P_c. When P_c is increased to an amount greater than the mechanical strength of the PZT pillars, the delicate structures would start to bend. Pillars with higher aspect ratios and smaller kerfs are more desirable for HFUS applications but more likely to be susceptible to collapse. One commonly adopted solution to prevent the collapse of such structures is to introduce surfactants such as liquid CO_2 to lower the capillary forces by reducing surface tension [3, 8, 9]. Because finding an appropriate surfactant with an optimised concentration is costly and time-consuming, which was out of the scale of this project, no further experiments were carried out on the demoulding of PZT pillars from the AZ 125nXT moulds. The gel casting system developed in this work increased green strength of the green-state PZT pillars as discussed in Chapter 7 and may allow easier stripping, but time did not allow this to be investigated further.

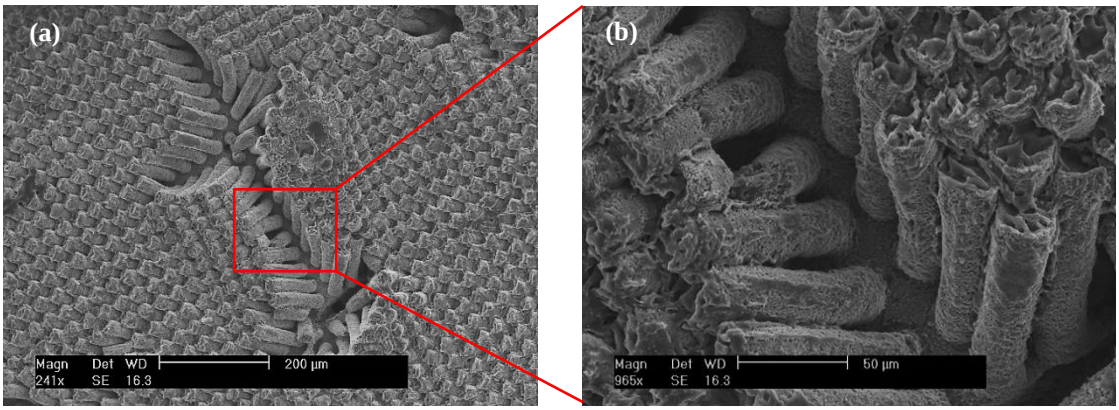

Figure 8-7 SEM images of gel-cast green-state PZT structures after being stripped from a 70 µm thick AZ 125nxT mould with regularly arranged holes in a 4 wt% NaOH aqueous solution at room temperature for 12 hrs and dried at room temperature, viewed at (a) lower magnification and (b) higher magnification.

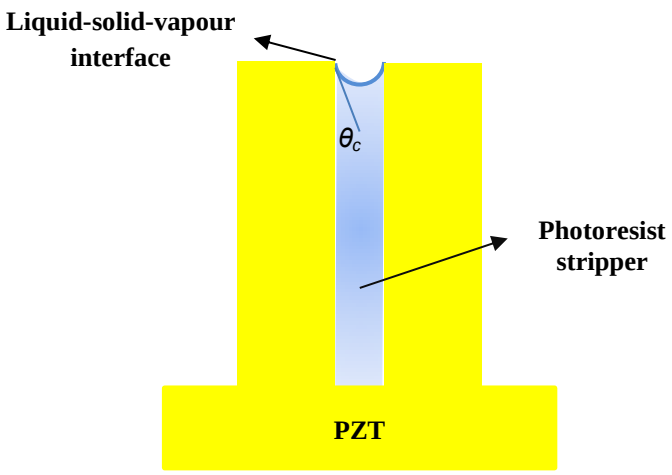

Figure 8-8 Schematic diagram of the green-state PZT bristle-block structure surrounded by the photoresist stripper when most of the photoresist mould has been dissolved.

8.3.2 Positive photoresist mould

It was shown in the previous section that the negative photoresist AZ 125nXT was not able to provide the required high resolution for patterning randomised features and also suffered from poor strippability. As an alternative, a positive photoresist was investigated. It was claimed to offer micro-scale resolutions and be more easily removed. The resulting moulds with both regular and random patterns fabricated from such photoresist, as well as the stripping tests are presented and discussed in this section.

8.3.2.1 Regular pattern

The only difference between the masks used for exposing the negative and positive photoresists was that the area desired to remain was transparent for the negative resist but dark for the positive one. The optimisation process performed on the AZ 40XT positive photoresist for the fabrication of regularly arranged holes was similar to that applied on the negative photoresist as described in Section 8.3.1.1, through which the

photolithography parameters for the moulds with different thicknesses were determined as shown in Table 8-3.

Figure 8-9 shows cross-sectional SEM images of the moulds with thicknesses of 30 and 60 µm fabricated by using the optimised parameters. It can be seen that regularly shaped and arranged through-holes have been achieved. The diameters of the holes at the top end are observed to be slightly larger and the kerfs are narrower in comparison with the mask (see Figure 8-2) and the holes made from AZ 125nXT (see Figure 8-3). This could be related to the nature of the photoresist along with the conditions of the instruments. As mentioned earlier, in order to make sure that no residues were trapped at the bottom of the holes, slightly longer development times were used than those suggested by the manufacturer, which might cause the dissolution of the unexposed parts in the developer. On the other hand, over exposure at/near the surface and insufficient exposure at/near the bottom of the photoresist layer could also explain the results.

Table 8-3 Optimised photolithography parameters for the 30 µm, 60 µm and 100 µm thick AZ 40XT regularly shaped moulds.

Thickness	**Spin coating speed/ time**			**Soft bake temperature/time**		**Relaxation time**	**Exposure time**	**Relaxation time**	**Post-exposure bake temperature/time**		**Relaxation time**	**Development time**
(µm)	**(rpm/s)**			**(°C/min)**		**(min)**	**(No. of stages/sec per stage)**	**(min)**	**(°C/sec)**		**(min)**	**(min)**
	Stage 1	*Stage 2*	*Stage 3*	*Stage 1*	*Stage 2*				*Stage 1*	*Stage 2*		
30	400/2	1750/10		126/7		10	3/25, 25, 25	10	70/30	105/90	10	2.5
60	400/2	1100/2	1000/8	126/14		10	5/30,30,30	10	70/30	105/100	10	5
100	400/2	1100/2	950/2	80/5	126/21	15	(see text)	15	70/30	105/120	15	(see text)

Note: 1. The thicknesses of the photoresist layers were obtained by measuring Si wafers before coating and after coating, baking and cooling.

2. The intensity of the UV lamp was 4.58-4.88 mW/cm^2 during the experiments.

3. During exposure, a relaxation period of 1 min was introduced between stages.

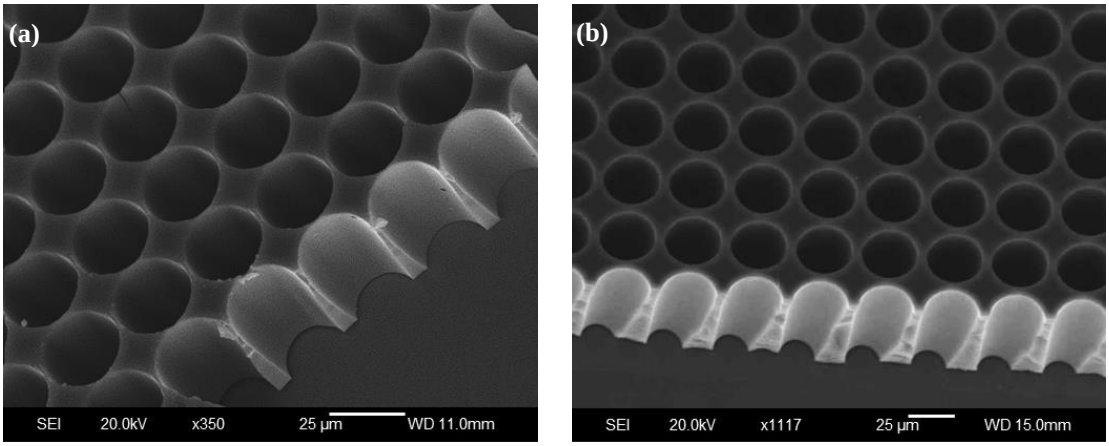

Figure 8-9 Side-viewed SEM images of AZ 40XT moulds with regularly arranged through holes and thicknesses of (a) 30 µm (b) 60 µm.

When fabricating 100 µm thick AZ 40XT moulds, an appropriate combination of the exposure and development time was found difficult to achieve. Figure 8-10 shows cross-sectional SEM images of the 100 µm thick AZ 40XT moulds fabricated using the same processing parameters except for exposure periods. With increasing the exposure time, the depth of the holes increased as expected but no through holes were obtained even after a long exposure time of 4 min and the 'erosion' of the unexposed parts appeared to be more evident. Specifically, a 4 min exposure led to partial dissolving of the sidewall in the developer, leaving holes in the wall as shown in Figure 8-10(c). The cavities are observed to be significantly tapered through the thickness of the mould, with the diameter at the top much larger than that of the bottom. These phenomena can be understood as follows. Firstly, the surface of the photoresist layer received more exposure energy than the bottom parts. The longer the exposure time in this case, the greater the difference between exposure energy absorption at the upper and deeper parts of the mould. Secondly, during the development, the top layer is immediately in contact with the developer while the bottom cannot contact the developer until the solution reaches that thickness. In addition, for thick photoresist layers, non-uniform baking

might occur. The bottom layer receives more energy during baking than the top surface, which might cause the bottom parts to be over-baked and the top to be under-baked. Over-baking degrades the photosensitivity of positive photoresists, causing the reduction of their solubility in the developer, while under-baked positive photoresists would be readily attacked by the developer in both exposed and unexposed area. In summary, the differences in the exposure energy, the length of time in contact with the developer, as well as the degree of baking between the top and bottom photoresist layers are the possible factors contributing to the 'blind' and tapered holes shown in Figure 8-10. Considering the difficulties in minimising the differences, no further optimisation was performed on the 100 μm thick AZ 40XT layers.

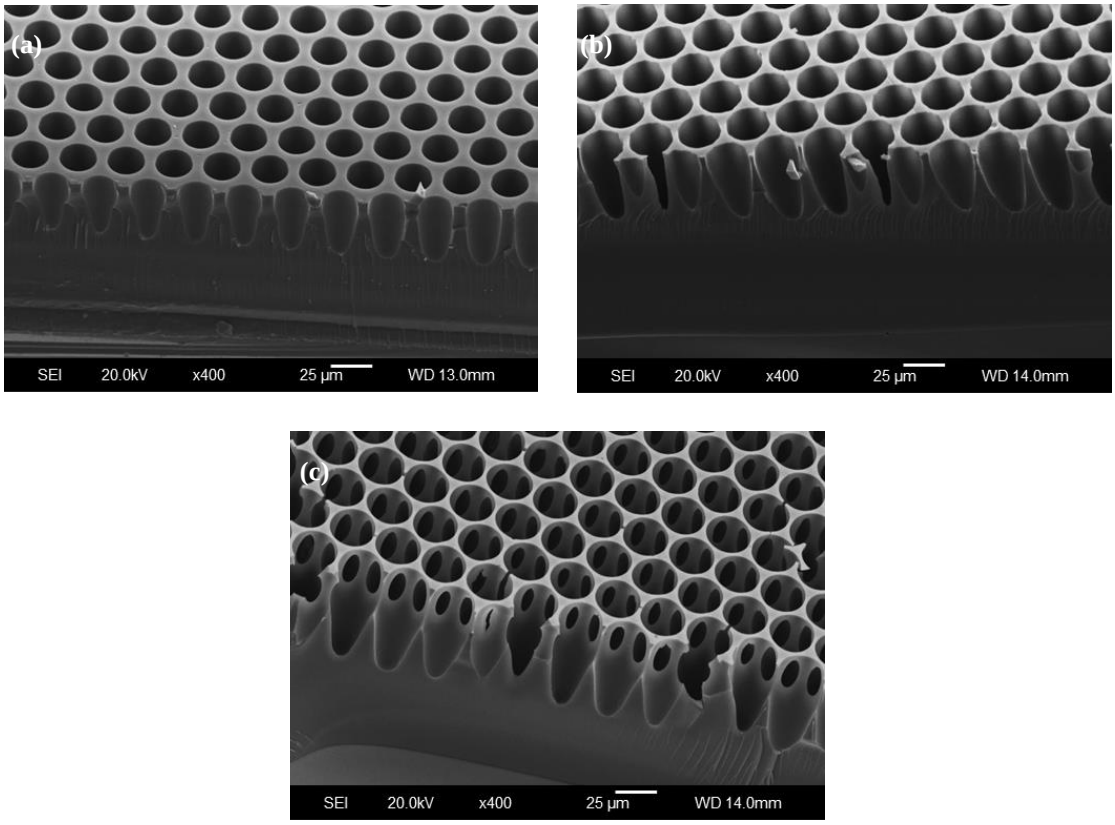

Figure 8-10 Side-viewed SEM images of 100 μm thick AZ 40XT moulds after (a) 2 min, (b) 3 min and (c) 4 min exposure and 7 min development (the other processing parameters were kept the same as listed in Table 8-3).

8.3.2.2 Random pattern

Following the fabrication and characterisation of the AZ 40XT regular moulds, the possibility for the production of moulds with a random pattern using this photoresist was explored. Figure 8-11 shows optical images of the surface of random moulds with thicknesses of 30 µm and 60 µm, fabricated using the optimised parameters shown in Table 8-3. The pattern on the mask used for exposure was the same as the one used for the fabrication of AZ 125nXT random moulds as shown Figure 8-4(a) but with the pattern area to be exposed. By comparing Figure 8-11(a) and Figure 8-4(a), it can be seen that the randomised features on the mask have been accurately transferred to the 30 µm thick AZ 40XT mould in terms of the size and shape of the features. This demonstrates the high resolution that this positive photoresist can provide, which is a key advantage over the negative photoresist for patterning micro-scale features. However, in the case of the 60 µm thick AZ 40XT random mould, some parts that were supposed to be unexposed and remain, were washed away in the developer causing the neighbouring holes to join together and giving larger features than desired, as shown in Figure 8-11(c). This is possibly because the exposure and development times used were optimised for holes that were 25 µm in diameter, but overwhelming for the relatively smaller features of the random pattern, especially for the sections near the top surface. For the thinner AZ 40XT random mould of 30 µm thick, the overall exposure and development times applied were much shorter, which exerted much less effect on the top photoresist layer and therefore the ‘erosion’ of the unexposed area was negligible.

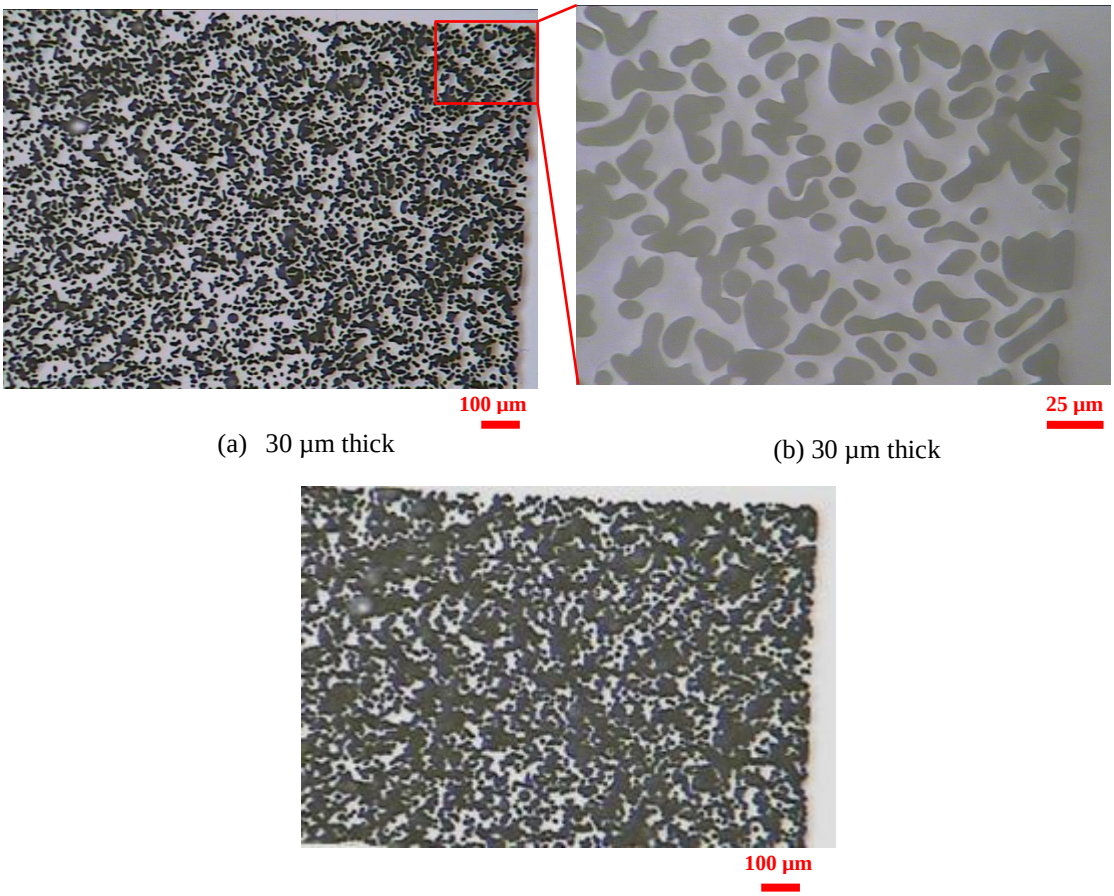

(a) 30 µm thick

(b) 30 µm thick

(c) 60 µm thick

Figure 8-11 Optical images of (a) a top view of a 30 µm thick AZ 40XT mould, (b) detailed view of (a) and (c) a top view of a 60 µm thick AZ 40XT mould, processed using the parameters shown in Table 8-3.

8.3.2.3 Demoulded green-state ceramic structures

In order to test the strippability of AZ 40XT photoresist in the presence of gel cast green-state ceramic, a 30 µm thick AZ 40XT random mould was cast with a gel casting slurry containing 20 wt% EGDGE [5] and then degassed and dried, followed by being stripped in DMSO at room temperature overnight and finally rinsed in DI water. Figure 8-12 shows SEM images of the green body with randomised ceramic structures upstanding from a stock demoulded from the AZ 40XT mould. A complete square of the PZT segments have survived the stripping process as seen in Figure 8-12(a). The volume fraction of the segments in the square can be estimated at close to the designed value by comparing the SEM image with the top view of the pattern on the mask. Even the fine

pillar structures with lateral dimensions <5 µm are standing without collapsing as shown in Figure 8-12(b). The realisation of the randomised segments with a height of approximately 30 µm in turn proves the features were fully developed all the way through the thickness of the photoresist. It is worth noting that no residue of the photoresist is observed in between the segments, demonstrating excellent strippability of AZ 40XT. However, considering the limited height of the segments, it is extremely difficult, although not impossible, for them to be further processed to a functional 1-3 composite without being destroyed in the lapping stage, and these segments were therefore not processed further.

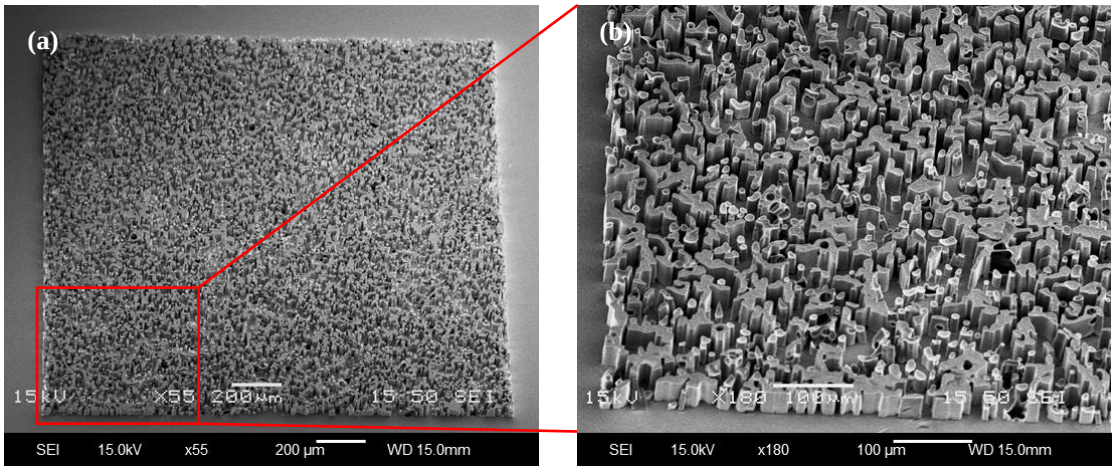

Figure 8-12 SEM images of randomly distributed green-state PZT segments demoulded from the 30 µm thick AZ 40XT mould, after being immersed in DMSO remover at room temperature overnight and rinsed in DI water.

8.3.3 Summary

Moulds with the regular and random patterns fabricated from both AZ 125nXT negative photoresist and AZ 40XT positive photoresist have been presented and discussed. The main advantages and disadvantages of these two photoresists for this application are summarised and shown in Table 8-4. It can be concluded that neither AZ 125nXT nor

AZ 40XT had satisfied all the requirements of the candidate mould material described in Section 4.1 under the limited experimental conditions. AZ 125nXT mainly suffered from low resolution and poor strippability while the primary drawback of AZ 40XT lies in the limitation of the thickness. It should be noted that these limitations can be possibly overcome when using improved or more advanced instruments and/or when a more effective and efficient developer or stripper is involved.

Table 8-4 Comparison of the main advantages and disadvantages of AZ 125nXT and AZ 40XT photoresists for the fabrication of regular and random moulds.

	Advantages	**Disadvantages**
AZ 125nXT **Negative photoresist**	1. No post-exposure bake stage required. 2. Excellent adhesion without being lifted up off the Si wafer in the developer. 3. Single coating thickness up to **120 µm** for the regular pattern.	1. Poor resolution. Not suitable for patterning random features. 2. Difficult to be stripped completely. 3. Long exposure time required (per unit thickness).
AZ 40XT **Positive photoresist**	1. Short exposure time required (per unit thickness). 2. High resolution down to 2 µm features. 3. Easily stripped in the presence of the green-state ceramic.	1. Limitation of single coating thickness. Up to **60 µm** for the regular pattern and up to **30 µm** for the random pattern. 2. Poor stability. Susceptible to temperature effects and erosion by the developer. 3. Poor adhesion to Si wafer.

8.4 Photoresist moulds for indirect moulding

In addition to being used for direct moulding, photoresists can also be patterned as the desired structures of the PZT segments and used as master moulds for indirect moulding as illustrated in Figure 8-1. For this purpose, SU 8, as one of the most commonly used negative photoresists for the fabrication of high-aspect-ratio structures with superb chemical resistance as described in Section 4.4.4, was applied in trial tests. SU 8-50 (Microchem Corporation, Newton, MA, USA), one of the SU 8 formulations, was processed according to data suggested by the supplier [10] for the target thickness of 100 µm. Considering the delicate nature of the structures, extreme caution was taken throughout the processing stages. However, the pillars obtained from the trial tests all ended up with joining together. The tilting of the pillars was observed particularly during drying rather than any other stages. Figure 8-13(a) shows a surface view of the resulting SU 8 pillars just after being developed and rinsed, still with some water covered. At that stage, the pillars were upstanding from the substrate and well separated from each other by approximately the distances desired. After drying at room temperature, the pillars on the same sample were found tilted and joined with the neighbouring ones as displayed in Figure 8-13(b). The failure of the SU 8 pillars can be explained by the factors resulted in the collapsing of the PZT pillars after being chemically demoulded from AZ 125nXT moulds as described in Section 8.3.1.3. With the help of surfactants, high-aspect-ratio (>5) pillar structures have been reported to be realised by patterning SU 8 [9, 11], but the fabrication difficulty increases with the reduction of kerf sizes as well as pillar dimensions. This aspect was not explored further in this project due to time constrains and equipment limitations.

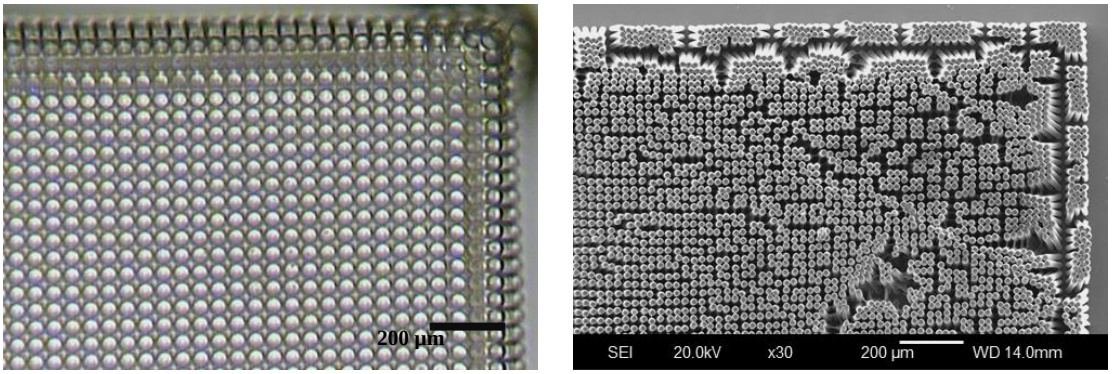

(a) **(b)**

Figure 8-13 (a) Top-viewed optical image of the 'wet' SU 8 pillars (diameter: 22 µm, height: 100 µm) just after being developed and rinsed; and (b) top-viewed SEM image of the SU 8 pillars after they were thoroughly dried at room temperature.

8.5 Si moulds for indirect moulding

In this project, the Si master moulds for soft moulding were manufactured at the University of Edinburgh using the process depicted in Section 6.1.1.2. All of the etched master moulds were conformally coated with Parylene to improve the surface finish as described in Section 4.6.

Optical images of the mask used for the deep etching process and an example of the resulting Si structures are shown in Figure 8-14. Nearly all the features on the mask have been transferred to the Si substrate. By comparing the details on the two images, it can be concluded that the deep etching technique had the ability to accurately replicate the pre-designed pattern, down to feature sizes of 2 µm and regardless of the shape of the features.

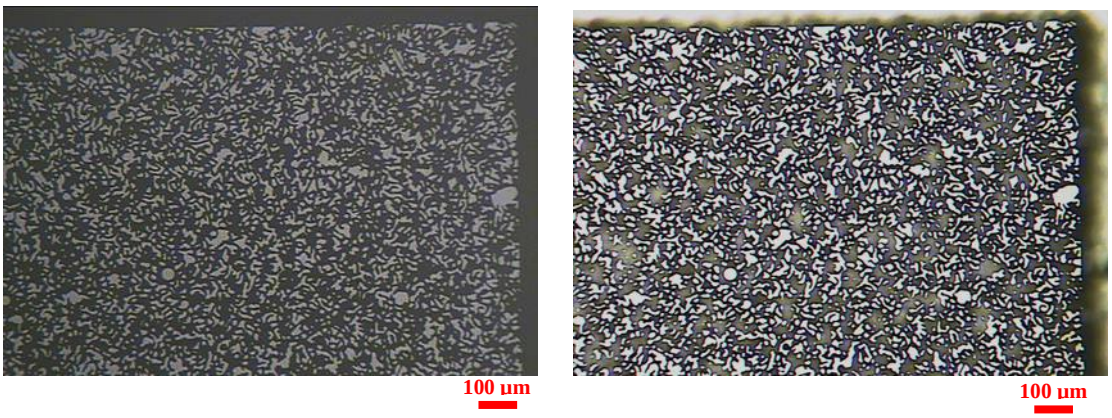

(a) (b)

Figure 8-14 Top-viewed optical images (a) the random pattern on the mask used for deep etching of Si and (b) an example of the deep etched Si structures manufactured at the University of Edinburgh.

Figure 8-15 shows the side-viewed SEM images of the resulting Si structures with heights of ~90 µm and ~170 µm, respectively. The shorter Si segments (see Figure 8-15(a)) can be observed to have high aspect ratios up to 45 and very straight sidewall angles along with a smooth surface finish, which indicates low adhesion and friction would be exerted on the structures during demoulding. Higher aspect ratios up to 85 have been achieved when increasing the etching depths to ~170 µm but 'grass-like' residues with thicknesses of ~10-20 µm are seen on the roots of the resulting Si structures. The formation of the residues could be related to the difficulty in complete removal of passivation component [12] for the segments with such heights and large aspect ratios.

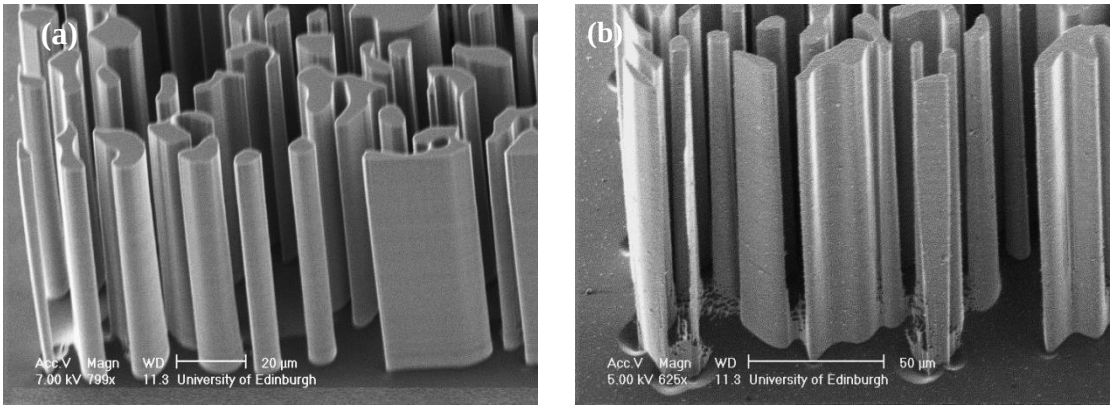

Figure 8-15 Side-viewed SEM images of the deep etched Si structures with heights of (a) ~90 µm and (b) ~170 µm provided by the University of Edinburgh.

Considering that Si master moulds with randomised segments ~170 µm in height would offer a greater chance to achieve the 1-3 piezocomposites targeted with thicknesses of 20-50 µm, they were selected to be used in the soft lithography process for the production of soft moulds as illustrated in Figure 8-1. Peeling PDMS from the Si master with very fine structures i.e. high surface area is a delicate process that requires the operator to be extremely cautious and patient. SEM images of an example of the resulting PDMS moulds are shown in Figure 8-16. Most of the random features were able to be transferred to the soft mould including small features, demonstrating the benefits of Parylene. The uneven surface of the PDMS mould (see Figure 8-16(a)) was a result of the grass-like residues mentioned previously on the bottom surfaces of Si master. Although the resultant holes vary in depth, such variations are within 20 µm in general, giving an average depth of ~150 µm as seen in Figure 8-16(b). Green-state PZT segments demoulded from these soft moulds are shown in Chapter 9, which demonstrate the success of the pattern replication from deep etched Si master moulds to PDMS soft moulds.

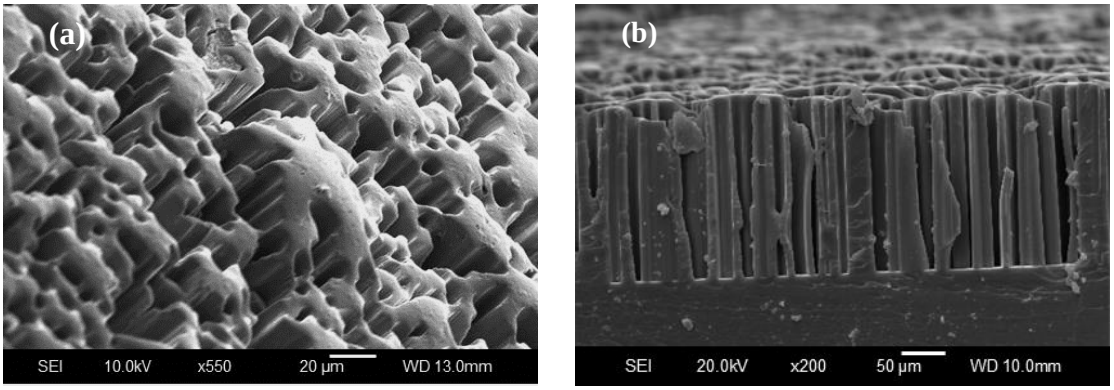

Figure 8-16 SEM images of the PDMS mould replicated from deep etched Si master mould with randomised segments ~170 µm in height: (a) top view and (b) side view. Note: the broken PDMS sections observed in (b) were caused by cutting the sample for side-view imaging.

8.6 Summary

This chapter has focused on the preparation of moulds for the gel casting process with particular emphasis on ultimately producing moulds with varying feature sizes and separations (random moulds). Two potential fabrication routes involving photoresists and Si mould materials were proposed at the beginning of the chapter, followed by detailed presentation of the moulds produced by each route. The results obtained from these mould materials and discussed in this chapter are summarised in Table 8-5.

For the direct moulding route, the possibilities for the AZ 125nXT and AZ 40XT photoresists to produce moulds with regular and random patterns as well as varying depths have been investigated along with their strippability in the presence of the gel-cast ceramics. The advantages and disadvantages of these two photoresists for this application have been summarised in Section 8.3.3. Their drawbacks shown in Tables 8-4 and 8-5 prevented their further applications to producing regular and particularly, random featured moulds.

For the other indirect moulding fabrication routes, both SU 8 photoresist and Si have been patterned for use as master moulds. SU 8 pillars obtained by photolithography

(diameter: 22 µm and height: 100 µm) were found to be difficult to keep upright during drying, which could be overcome if a suitable surfactant was identified. Deep etching of silicon substrates by the University of Edinburgh achieved very successfully, Si segments as tall as 170 µm with the desired randomised structures. The PDMS mould peeled from the Si master had kept most of the randomised features with average depths of ~150 µm.

Considering the dimensional accuracy and integrity of the pattern as well the thicknesses or depths of the resulting moulds, PDMS soft moulds replicated from the Si masters were selected for the use in the gel casting process.

Table 8-5 Summary of the results of the mould fabrication discussed in Chapter 8.

Fabrication route	**Mould Materials**	**Results and issues**		
		Regular moulds	*Random moulds*	*Demoulding*
Direct moulding	**AZ 125nXT**	Depth: 50-120 µm Diameter: 25 µm	Poor resolution	Difficult to be stripped; Gel-cast pillars collapsed during drying.
	AZ 40XT	Depth: 30-60 µm Diameter: 25 µm	High resolution down to 2 µm, but limited by the thickness (<30 µm)	Easily stripped.
Indirect moulding	**SU 8 (master)**	Pillars tilted during drying	N/A	N/A
	Si (master)	N/A	High resolution down to 2 µm and heights up to 170 µm	Most of the features survived the process of peeling PDMS from the Si masters.

8.7 References

[1] (Last accessed 2013/04/12). AZ 125nXT ultra-thick negative photoresist. Available: http://www.microchemicals.com/products/photoresists/azr_125nxt.html

[2] J.-Y. Zhang, *et al.*, "Modification of polymers with UV excimer radiation from lasers and lamps," *Journal of Adhesion Science and Technology,* vol. 8, pp. 1179-1210, 1994.

[3] M. C. Peterman, *et al.*, "Building thick photoresist structures from the bottom up," *Journal of Micromechanics and Microengineering,* vol. 13, p. 380, 2003.

[4] G. Flores, *et al.*, "Lithographic Performance in Thick Photoresist Applications," in *OCG Microlithography Seminar, Interface'93 Proceedings*, 1993, pp. 41-59.

[5] S. M. Olhero, *et al.*, "Innovative fabrication of PZT pillar arrays by a colloidal approach," *Journal of the European Ceramic Society,* vol. 32, pp. 1067-1075, 2012.

[6] Y. Jincao, *et al.*, "Prevention of Photoresist Pattern Collapse by Using Liquid Carbon Dioxide," *Industrial & Engineering Chemistry Research,* vol. 40, pp. 5858-5860, 2001/11/01 2001.

[7] H. Namatsu, *et al.*, "Dimensional limitations of silicon nanolines resulting from pattern distortion due to surface tension of rinse water," *Applied Physics Letters,* vol. 66, pp. 2655-2657, 1995.

[8] D. Goldfarb, *et al.*, "Aqueous-based photoresist drying using supercritical carbon dioxide to prevent pattern collapse," *Journal of Vacuum Science & Technology B: Microelectronics and Nanometer Structures,* vol. 18, pp. 3313-3317, 2000.

[9] N. J. Shirtcliffe, *et al.*, "The use of high aspect ratio photoresist (SU-8) for super-hydrophobic pattern prototyping," *Journal of Micromechanics and Microengineering,* vol. 14, p. 1384, 2004.

[10] (Last accessed 2013/04/12). SU 8-50 Data sheet. Available: http://microchem.com/pdf/SU8_50-100.pdf

[11] A. d. Campo and C. Greiner, "SU-8: a photoresist for high-aspect-ratio and 3D submicron lithography," *Journal of Micromechanics and Microengineering,* vol. 17, 2007.

[12] J. Bhardwaj, *et al.*, "Dry silicon etching for MEMS," in *Proc. Symp. Microstructures and Microfabricated Systems, ECS*, 1997.

CHAPTER 9 1-3 PIEZOCOMPOSITES AND HIGH FREQUENCY ULTRASOUND TRANSDUCERS INCORPORATING RANDOMISED CERAMIC SEGMENTS

9.1 Introduction

One aim of the project is to develop a cost-effective fabrication approach for the physical realisation of the random piezocomposites. The gel casting system for the ceramic fabrication has been developed as presented in Chapter 7 and the moulds with randomised patterns have been fabricated and characterised as shown in Chapter 8. In the following sections, by combining the gel casting and the soft moulding technique, randomised PZT structures and a series of 1-3 piezocomposites with a range of thicknesses were fabricated and characterised. Two high frequency transducers incorporating the random composites were subsequently constructed, tested and applied for real-time imaging.

9.2 Micro-scale randomised PZT structures

9.2.1 Green-state randomised PZT structures

As outlined in the results presented and discussed in Chapter 7, increasing the resin content in the gel casting slurry led to an increase of green strength but a decrease of sintered properties. Therefore, in this epoxy-amine gel casting system, it is desirable for the resin content to be as low as possible, whilst ensuring that the resulting green strength is sufficient for the subsequent cast structures to be demoulded.

Gel casting slurries with 45 vol% solids loading and resin concentrations varying from 10 wt% to 40 wt% were vacuum cast into the PDMS soft moulds with the negative

structure of the randomised segments of ~150 μm height. After curing and drying, the soft moulds were carefully peeled off, leaving the structures shown in Figure 9-1. It can be seen that at 10 wt% resin content, effectively none of the PZT segments were completely demoulded and most of the segments broke off or near to their bases. The remaining parts of the segments were found to be trapped in the soft moulds. With the resin content increased to 20 wt%, approximately 30% of the segments were seen to have survived the peeling process. However, tilting, collapsing and breaking of the segments was also observed, suggesting the green strength obtained was enough for some of the segments to be demoulded but insufficient for them to stay upright. At higher resin content of 30 wt%, over 50% of the segments were observed to be demoulded and standing in position, demonstrating the improvement of the green strength. As an example, to show the demoulding problems at low green strength, Figure 9-2 presents the detailed view of the structures shown in Figure 9-1(c).

On inspection, it was observed that a portion of the structures survived while the rest of them failed during the demoulding process with resin contents of 20 wt% and 30 wt%. This can be explained by taking the following three factors into account. Firstly, the resulting green strength at such resin contents was not high enough for all the components to withstand the high shear stresses produced upon demoulding. Secondly, at a given green strength or elastic modulus of the material, the stability of the demoulded structures against gravity and adhesive forces that induced buckling and collapsing varies with the size, geometry and aspect ratio [1]. Segments with higher aspect ratios were more liable to break, distort and collapse. Thirdly, peeling off the PDMS moulds was a manual process and the peeling forces exerted on the components was difficult to keep uniform and consistent. Chemical dissolving of the PDMS moulds

was an alternative way for demoulding. However, cross-linked PDMS is chemically stable and cannot be dissolved in most organic solvents. According to Lee et al. [2], dipropylamine was found to be able to completely dissolve cured PDMS but the process took 39 days. Also, this solvent may be aggressive to gel cast green bodies as it possibly interacts with epoxy resin, resulting in softening and/or distortion of the structures. In addition, during the removal and drying of the solvent, the ultrafine components with high aspect ratios are subjected to strong capillary forces which would be very likely to cause the already softened fine scale structures to become unstable and collapse. This effect has been observed in the dissolution of polycarbonate moulds in another fabrication method. This processing problem and the practicality of such a long dissolution process, lead to the exclusion of using a chemical route for the removal of PDMS moulds in this study.

When the resin content increased to 40 wt%, a 2x2 mm square of randomised structures was successfully demoulded with no obvious distortion or collapsing of the segments observed as presented in Figure 9-1(d). Compared with the demoulded structures obtained from other lower resin contents, Figure 9-1(d) shows a considerable improvement in terms of the number of the demoulded segments, which was attributed to not only the enhancement of green strength but also the increase of linear shrinkage with a resin content of 40 wt% as discussed in Section 7.6. The accurate calculation of the volume fraction of the segments based on the top-view SEM image was not possible due to the differences in contrast and brightness of individual components caused by their slightly uneven height. It can be seen that the integrity and the fraction of the PZT segments in the square is comparable with that of the random structures obtained in the Si master moulds as shown in Figure 8-14, demonstrating the capability of this

fabrication approach in combining gel casting and a soft moulding technique in pattern replication.

Figure 9-3 presents two high magnification images of the structure shown in Figure 9-1(d). It can be seen that the green-state PZT segments exhibited dense, smooth and homogeneous surface morphology with no obvious defects or cracks. The segments with irregular shapes, well-defined edges, very sharp angles as well as ultrafine feature sizes were precisely replicated from the PDMS moulds and remained intact and complete. This proves the manufacturing flexibility of this fabrication approach in producing micro-ceramics with different shapes and dimensions, which overcomes the limitation of other techniques for producing fine-scale ceramic structures. Figure 9-4(a) shows the overall side view of the 'bristle-block' structure consisting of green-state micro-ceramics with very straight sidewalls upstanding from the PZT block. Figure 9-4(b) presents the dense and uniform microstructure of the lateral side of the green-state segments and also shows the approximate aspect ratios of the structures. Given that the finest feature size of the segment is less than 2 μm and the height of the structures is around 140 μm (~6.5% drying shrinkage), a large height-to-width aspect ratio up over 70 has been achieved, which is much higher than that of the PZT pillars made by other fabrication methods [3-5] as discussed in Section 3.4, demonstrating the high strength of the gel-cast green body.

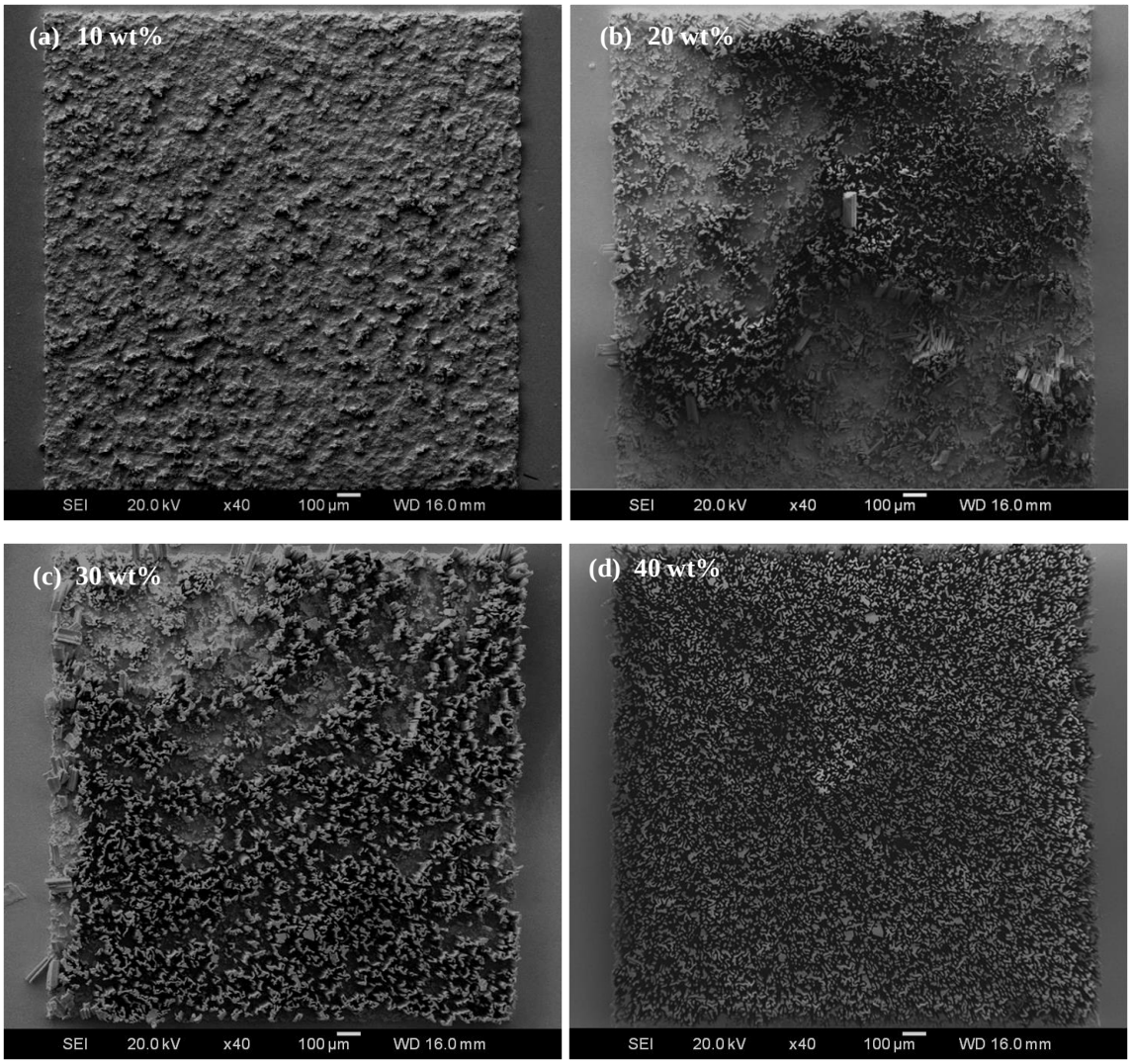

Figure 9-1 Top-viewed SEM micrographs of 2x2 mm squares of demoulded randomised PZT structures consolidated from gel casting slurries with 45 vol% solids loading and various resin contents: (a) 10 wt%; (b) 20 wt%; (c) 30 wt%; (d) 40 wt%.

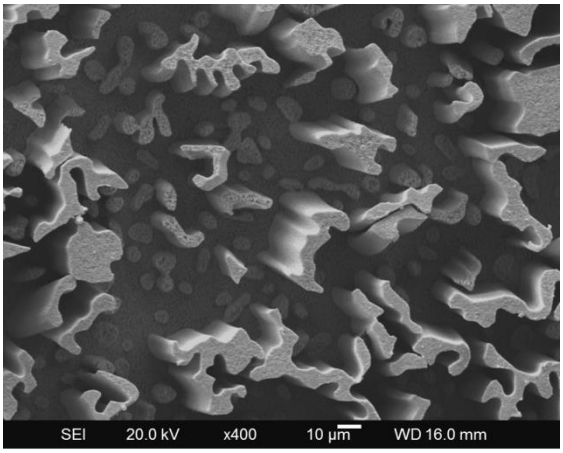

Figure 9-2 SEM micrograph showing a detailed view of the structures presented in Figure 9-1 (c).

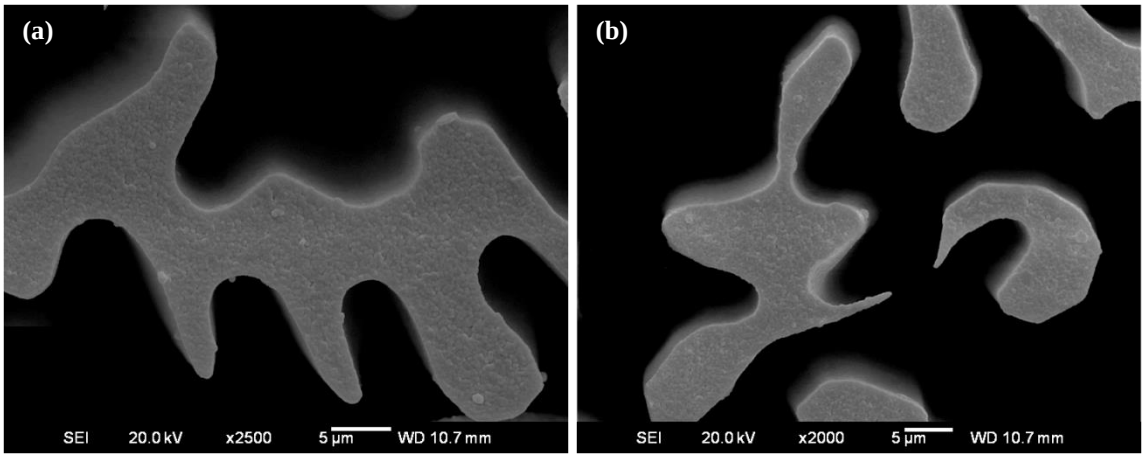

Figure 9-3 Top-viewed SEM micrographs of the structures consolidated from the gel casting slurry with 45 vol% solids loading and 40 wt% resin content after drying and demoulding.

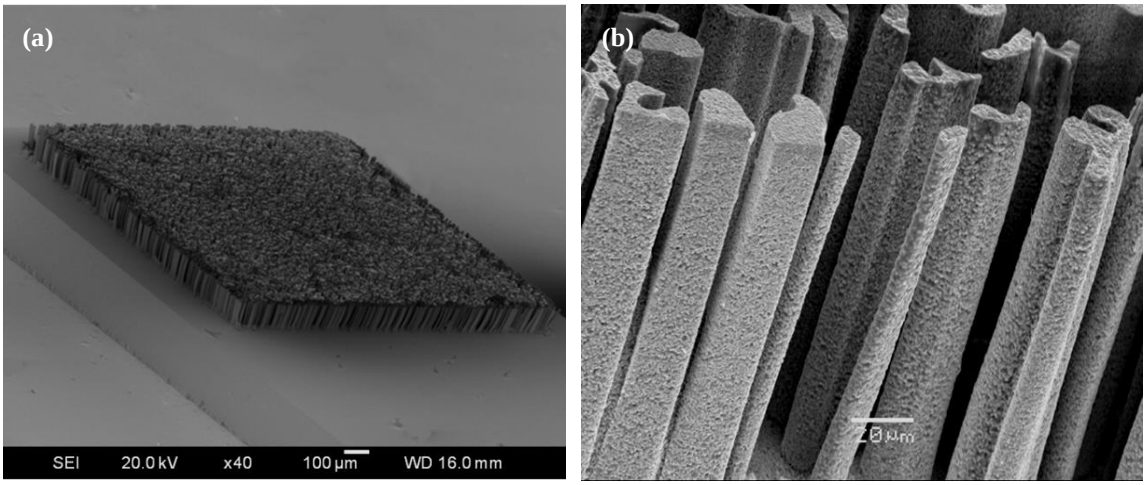

Figure 9-4 SEM micrographs of (a) overall and (b) detailed side view of the randomised PZT segments consolidated from the gel casting slurry with 45 vol% solids loading and 40 wt% resin content after drying and demoulding.

Shaping and forming of the ultra-fine PZT random structures initially was of paramount importance for the fabrication of 1-3 piezocomposites. Although as mentioned, decreasing the resin content was beneficial in avoiding disruption of the structures during the burnout process thereby achieving high sintered densities, a relatively high resin content of 40 wt% was chosen for the following work as random PZT segments could not be successfully demoulded at lower resin contents of 10 wt%, 20 wt% and 30 wt%.

9.2.2 Sintered randomised PZT structures

In order to make a quantitative comparison of any distortion occurring during sintering, a corner of a 'bristle-block' sample was imaged before and after sintering as shown in Figure 9-5(a) and (b), respectively. By comparing Figure 9-5(a) and 9-5(b), it can be found that after sintering, the size of the segments and the distances in between decreased and most of the segments survived with no apparent disruption of the structures. Only a few segments were observed to have tilted or collapsed as marked in red circles. The collapsed segments would be removed during the following lapping process. The tilted segments, which had partly joined together, were considered not to influence the overall performance of the resulting piezocomposite as they could be regarded as one component with no overall effect on the random characteristic of the structure. From the length of the collapsed segment in the right hand corner of the image, the height of the sintered structures can be estimated as ~110 μm, giving the linear sintering shrinkage in the thickness direction of ~20%.

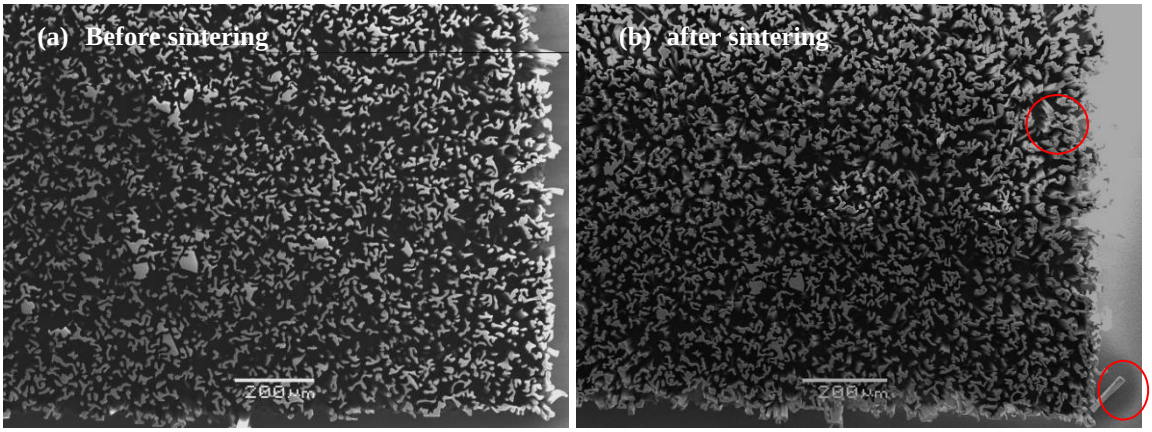

Figure 9-5 SEM micrograph of top view of the randomised PZT segments (a) before sintering and (b) after sintering.

The surface morphology of the randomised PZT segments after sintering is shown in Figure 9-6. By comparing Figure 9-6(a) with Figure 9-3(a), it can be seen that the sintered segment remained complete and kept the shape characteristics of its green state including smooth surface, sharp angles and distinct outlines. The average grain size determined from Figure 9-6(a) is around 1.5-2 μm, which is comparable with that of the PZT pillars fabricated by VPP and sintered at 1150 ℃ [6].

Although all the samples were fabricated from the slurries with 45 vol% solids loading and 40 wt% resin content, the bulk samples after sintering presented relatively high porosity as illustrated in Section 7.7, while the sintered segments shown below exhibited dense and homogeneous microstructures with few pores and no obvious defects. This is mainly attributed to the difference of the surface area that the random segments and the bulk samples possess. During the burnout process, higher surface area of the segments means more diffusion paths, which alleviated the build-up of the internal gas, hence reducing the internal stress and local disruption. Furthermore, as observed during processing, fewer air bubbles were trapped in the small structures while some air

bubbles remained in the stock. Improved de-airing is also responsible for the denser microstructure shown in Figure 9-6.

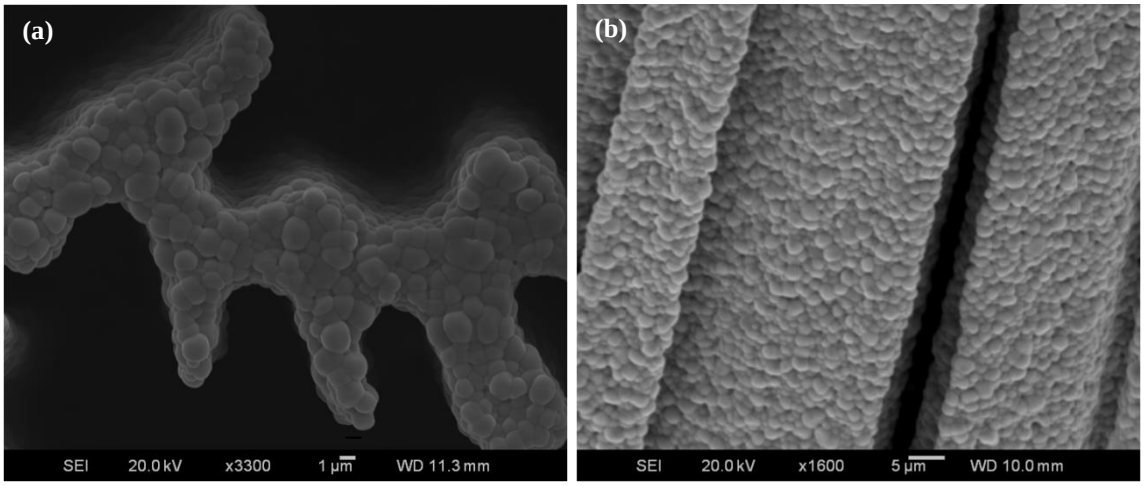

Figure 9-6 SEM micrographs of surface morphology of (a) the top surface of a PZT segment and (b) the lateral side of PZT segments.

9.3 1-3 piezocomposites

9.3.1 Microstructure of 1-3 piezocomposites

As described in Section 6.1.3, after sintering the 'bristle-block' structures were backfilled with epoxy. The ceramic stock and excess epoxy was then removed in the subsequent lapping stage to achieve the required thickness and surface finish. In this work, a series of 1-3 composites were prepared for the fabrication of single element transducers which also demonstrated the repeatability of this fabrication approach.

Figure 9-7 shows the optical images of the surface of a typical random composite. During sintering, the micro-ceramics underwent approximately 20 % shrinkage, leaving a 1.6 x 1.6 mm square of active material as shown in Figure 9-7(a). It can be seen that there were a few segments missing on the left side of the square, which could be a consequence of the non-uniform peeling force during demoulding. Most of the ceramic segments survived the sintering, back-filling and lapping stages, allowing the composite

to keep a comparatively high ceramic volume percentage of 35.4%. Figure 9-7(b) presents a detailed image of a section of the composite. Large segments with feature sizes up to 50 μm and pillars finer than 2 μm, able to be seen as small spots in the image, are clearly visible. A randomised distribution of the ceramic shapes, feature sizes, distances in between, as well as aspect ratios, has been achieved in the composite demonstrating an accurate replication of the Si master mould.

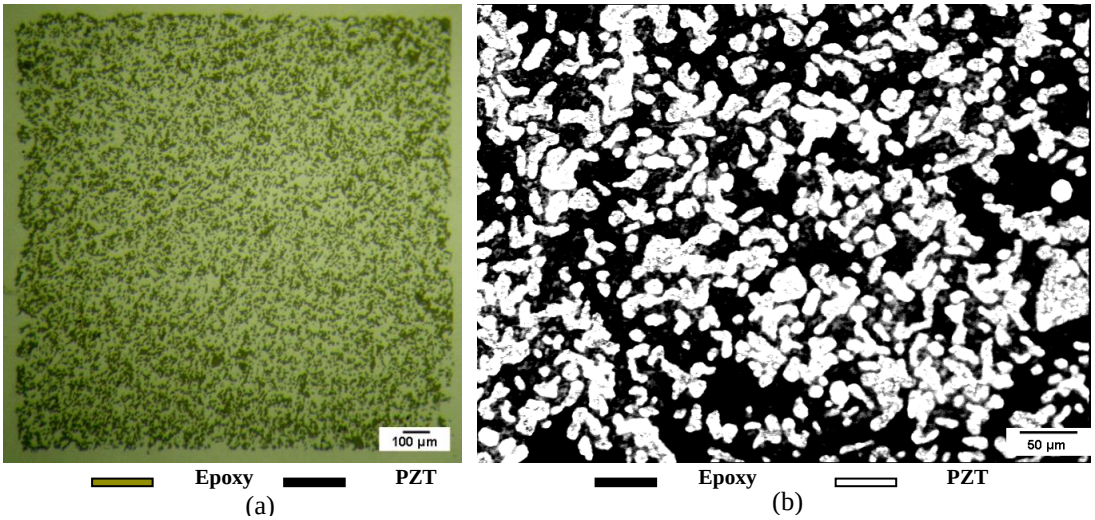

Figure 9-7 Optical images of a random composite with ceramic volume percentage of 35.4%: (a) overview and (b) details.

9.3.2 Impedance analysis of 1-3 piezocomposites

As described above, a series of random composites have been fabricated utilising Si master moulds with the same pattern and then lapped to different thicknesses. The electrical impedance spectra of the novel composites were measured and are shown in Figure 9-8. It can be seen that in the very broad frequency range of 100 kHz to 150 MHz, only one peak, corresponding to the thickness resonance, is found for each of the impedance and phase curves. This proves that any spurious modes within the random composites were effectively suppressed by the random distribution of the ceramic geometries and dimensions, and that the resonance in thickness was the only coherent mode, which confirms the previous modelling results on random composites [7] as

described earlier in Section 3.3.3. Meanwhile, it is interesting to notice that there were distinct differences presented in the impedance spectra for the composites with various thicknesses. For Random 1 and 2, with thicknesses of 52.5 μm and 40.5 μm, respectively, the changes of the impedance and phase magnitude at resonant frequencies are as expected, referring to the sharp peaks presented in Figure 9-8. As the thickness of the composites decreased, resonant frequencies were pushed to higher values as expected according to Equation 3-18, but the resonances were observed to be broader, corresponding to the attenuated peaks. This phenomenon was not found in the piezocomposites with periodic pillar structures [8]. This broad resonance characteristic might be caused by the variation of local thickness mode velocity over the samples due to the variation of local ceramic volume fraction. When the thickness of the composite is uniform but the propagating speed varies, the resulting resonant frequency would vary from place to place, spreading out and diminishing the impedance features corresponding to resonance.

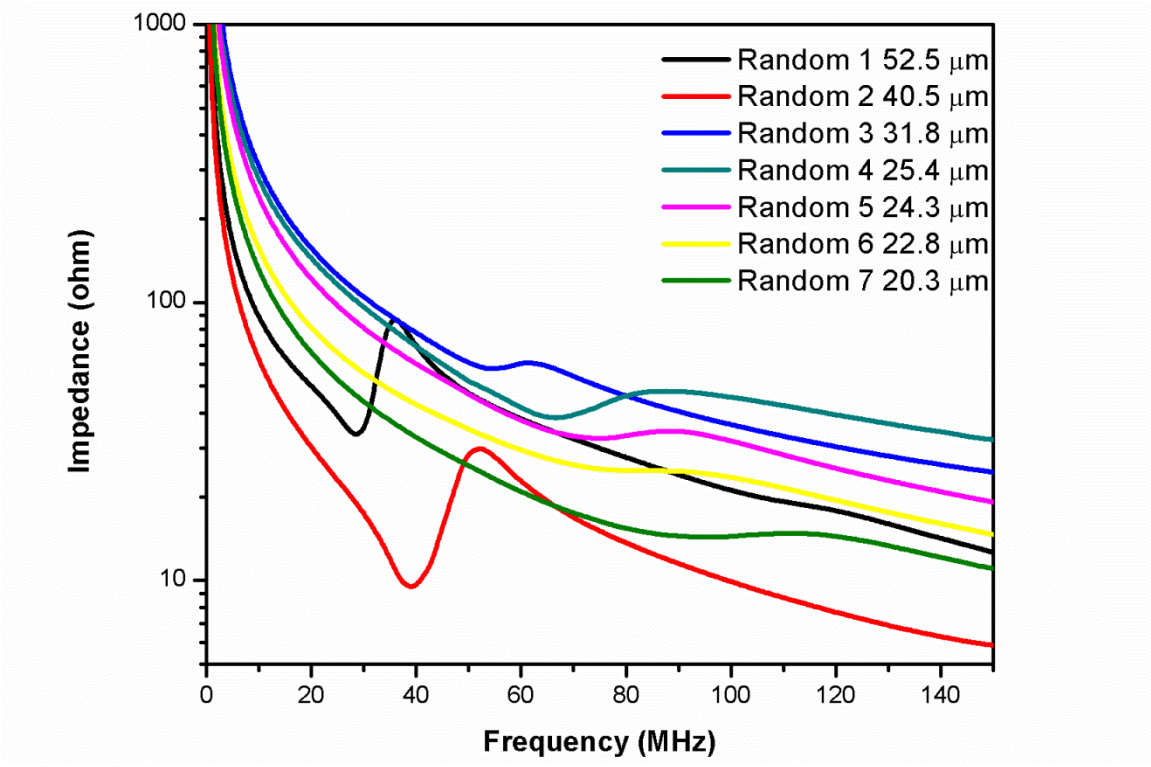

(a)

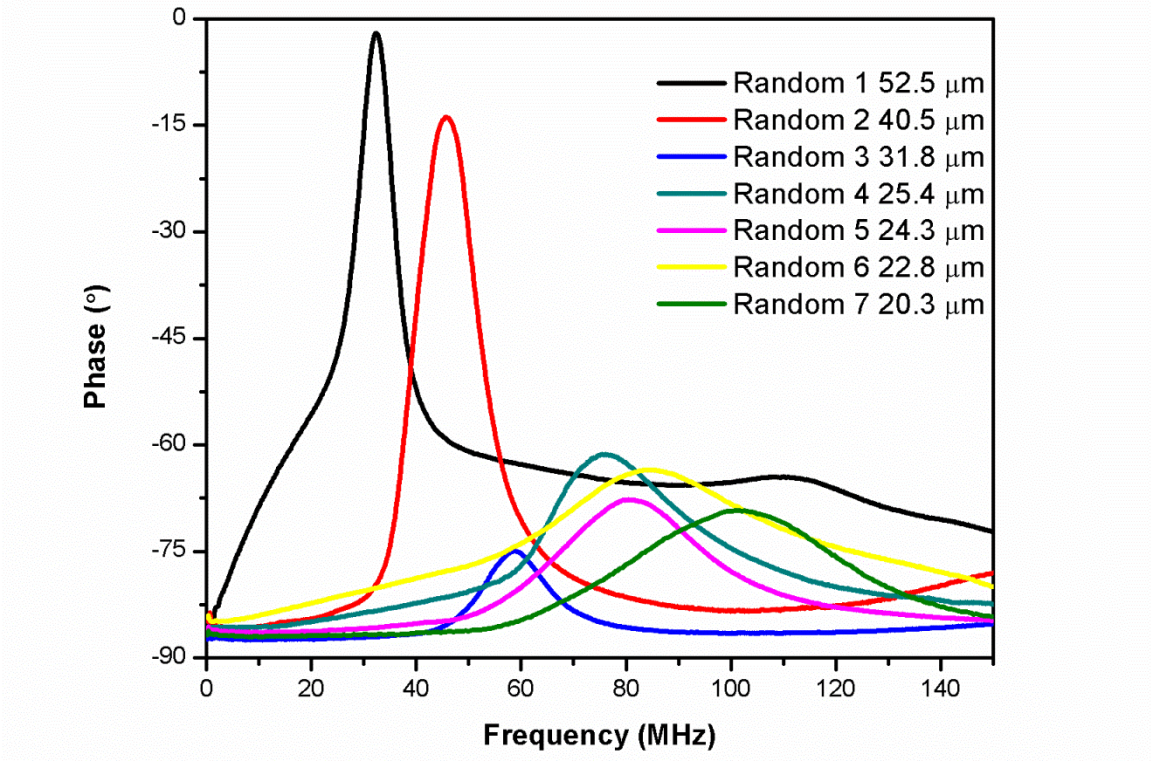

(b)

Figure 9-8 Impedance (a) and phase (b) magnitude diagrams measured from the random composites with thicknesses ranging from 52.5 μm to 20.3 μm.

The basic information of the seven random composites including their thicknesses h, ceramic volume percentages V_c, resonant frequencies f_r and anti-resonant frequencies f_a are summarised in Table 9-1. The ceramic volume percentages of the group, except for Random 5, are all approximately 30% or over which are in good agreement with the designed value of 40%. It must be pointed out that the relatively low V_c of Random 5 was due to a processing error rather than inherent defects in the fabrication approach. It demonstrates the reproducibility of the gel casting technique for the fabrication of piezocomposites with random pattern. Considering the broad characteristics of their thickness resonances, for the composites thinner than 31.8 μm, their resonance frequencies presented were obtained by averaging 9 values at each corresponding impedance peak or valley. Predicted from the given resonant and anti-resonant frequencies, the operating frequency of them is ranging from around 30 MHz to over 100 MHz varying with thickness. It suggests that, without the disturbance of spurious modes, the innovative random composites which have a high tolerance of ceramic dimensions and geometries, can be produced flexibly to satisfy the requirements of different frequencies.

Table 9-1 Summary of the random composites.

Sample	h (μm)	V_c (%)	f_r (MHz)	f_a (MHz)
Random 1	52.5	35.4	28.39	36.08
Random 2	40.5	34.1	39.07	52.00
Random 3	31.8	30.3	54.25	61.37
Random 4	25.4	33.5	66.58	86.60
Random 5	24.3	21.3	74.96	88.17
Random 6	22.8	32.6	75.43	93.60
Random 7	20.3	29.7	96.48	110.96

Note: h, V_c, f_r and f_a stands for thickness, ceramic volume percentage, resonant frequency and anti-resonant frequency, respectively.

9.3.3 Functional performance of 1-3 piezocomposites

In this section, a series of key parameters of the random composites derived from electrical impedance data are presented including the thickness coupling coefficient k_t, the piezoelectric coefficient d_{33}, the relative permittivity at constant strain ε_r^S, and the acoustic impedance Z_a. For the purpose of assessing their effective functional properties, two composites with regular periodic patterns fabricated by the VPP route [8] were introduced as references. The physical characteristics of the two VPP samples are listed in Table 9-2 [8]. VPP 1 and VPP 2 were made with a latest-generation process, representing the properties of the VPP piezocomposites presently in production [9].

Table 9-2 Physical characteristics of VPP 1 and VPP 2.

	VPP 1	**VPP 2**
Dimensions (mm)	1.8 x 1.8	1.81 x 1.67
Thickness (μm)	20	53
Piezoelectric Material	PZT 5H (TRS 600FG)	PZT 5H (TRS 600FG)
Polymer	RX771	Epofix
Volume Fraction	0.5	0.46
Pillar shape	Hexagonal	Circular
Pillar Size (μm) /Aspect ratio	20 / 1	30 / 1.8
Operational Frequency (MHz)	91.3	35.9

Figure 9-9 shows the thickness coupling coefficient k_t of the gel-cast random composites and the VPP regular composites. For the random composites, k_t values are all over 0.5, representing good energy transduction efficiency. Especially, relatively high k_t values lying between 0.6-0.7 are observed for four of them. While in comparison VPP 1 and VPP 2 with higher volume fractions have lower k_t values of 0.48 and 0.51, respectively. According to the supplier, the piezoelectric properties of TRS 600FG used for the VPP piezocomposites are similar to those of TRS 610C. Therefore, it is reasonable to deduce

that the enhanced k_t values obtained in the random composites are mainly attributed to the novel design of randomised geometry and distribution of the piezoelectric segments. They are much higher than figures varying between 0.1 and 0.2 reported for PVDF [10, 11] and higher than k_t values reported for single crystals (see Table 3-2), suggesting the potential advantage of employing the random composites for HFUS applications.

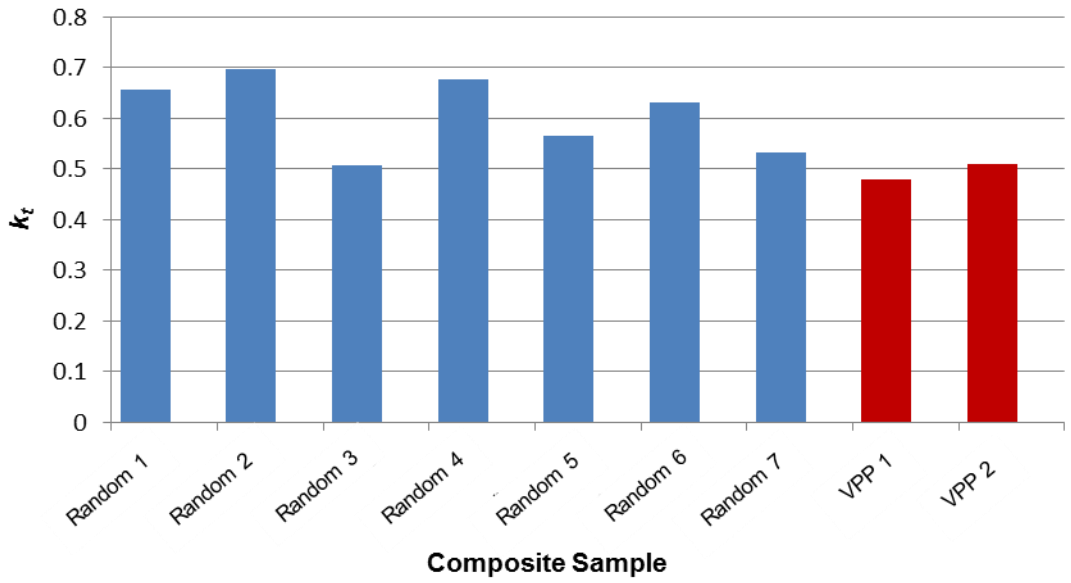

Figure 9-9 Thickness coupling coefficient k_t of the random composites and two VPP regular composites.

It was noticed that the k_t of the Random 3 composite was lower than the other random composites. This is possibly due to the fact that the corona poling process applied was not optimised for these novel composites. With the aim of further exploring its potential piezoelectric properties, a contact poling process routinely used to pole bulk samples in this research group was tried on the Random 3 composite as described in Section 6.1.3.7. However, wrinkling of the sample and damaging of the electrodes was found after repoling, suggesting the present contact poling setup was not suitable for these thin composites and special jigs for clamping composite samples were needed. Due to the irreversible damage to Random 3, no further characterisation was carried out. The

Random 2 composite with the highest k_t value was used for the fabrication of a single element transducer at the University of Dundee before measuring its capacitance. Therefore, the other parameters of the Random 3 and Random 2 composites were not presented in the following paragraphs.

Figure 9-10 shows the longitudinal piezoelectric coefficient d_{33} for all the composites. These figures are much lower than that of bulk PZT samples but still much higher than PVDF. It is interesting to notice that the Random 1 composite with 52.5 μm thickness has a satisfying d_{33} value as expected from piezocomposite material, which is even higher than the two VPP composites while Random 4-7 composites thinner than 30 μm have substantially low $d_{33.}$ Varying d_{33} of Random 4-7 composites approximately corresponds to volume fraction. However, for the two VPP samples, despite the difference in thickness, the d_{33} values of them are very similar. This indicates that either the measurements of Random 4-7 composites were inaccurate because of their unusually high resonance frequencies or this is the nature of the innovative random composite that d_{33} decreases with the decrease of the thickness. One possible explanation of this observation is as follows. As the thickness decreases, the aspect ratio of individual segment reduces. For the ones with comparatively large lateral feature size (30-50 μm), when the thickness decreases to a level that is smaller than the width, i.e. aspect ratio <1, the vibration of these segments along the thickness direction is significantly restrained, resulting in local decreased d_{33}. Given the same volume fraction, the thinner the random composite, the more evident this phenomenon would be. In order to experimentally verify the relationship between the thickness and the piezoelectric properties, more samples with varying thickness but fixed volume fraction are needed.

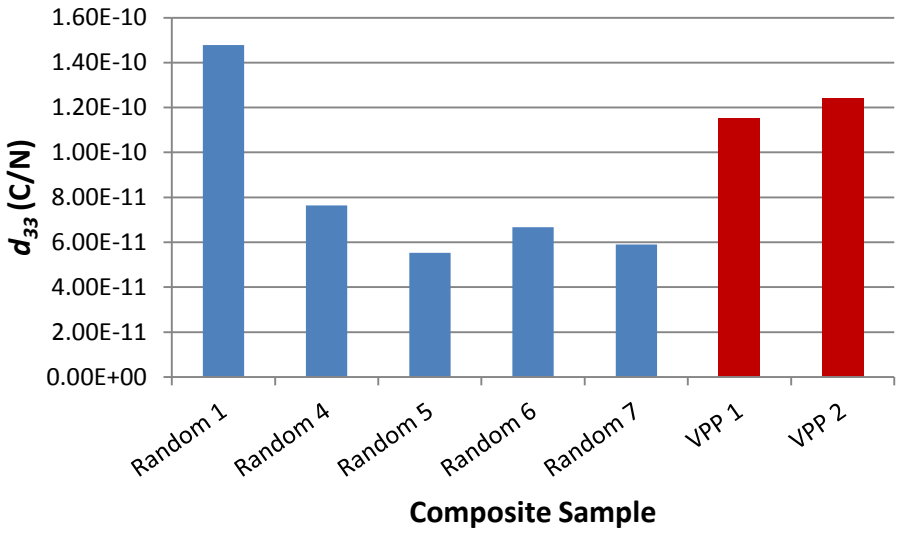

Figure 9-10 Longitudinal piezoelectric coefficient d_{33} of the random composites and two VPP regular composites.

The relative permittivity of the random composites at constant strain as presented in Figure 9-11 is also linked to the thickness. Similar to what has been found from the d_{33} data, Random 1 has a relatively high ε_r^S figure of 291, but the ε_r^S values of Random 4-7 are less than 100. Especially, Random 5 with the smallest PZT volume percentage of 21 vol% among all the samples has the lowest ε_r^S. Again, in comparison, VPP 1 and VPP 2 with similar ceramic volume percentages but different thicknesses have close ε_r^S values. ε_r^S of Random 1 is lower than that of the VPP samples, which is reasonable considering the fact that the ceramic volume fraction of Random 1 is lower than that of the VPP samples. It is worth noticing that although the ε_r^S values of Random 4-7 composites are lower than that of Random 1 and VPP samples shown here, they are still higher than that of PVDF, for which ε_r^S=5 (see Table 3-2), and $LiNbO_3$, for which ε_r^S=39 [9].

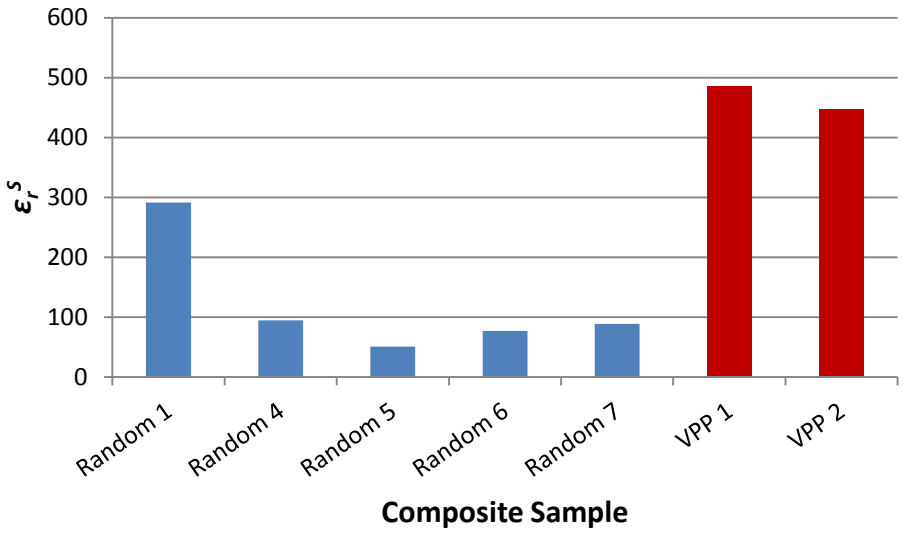

Figure 9-11 Relative permittivity at constant strain ε_r^S of the random composites and two VPP regular composites.

Acoustic impedance Z_a for each of the composites is shown in Figure 9-12. These values appear to be generally in line with the ceramic volume fraction, although Z_a of Random 1 was expected to be slightly higher. Z_a is a product of the material density ρ and the velocity of sound v in the medium as illustrated in Equation 2-3. As the sound travels much faster in the piezoceramic phase than in the polymer matrix, a higher volume fraction of ceramic leads to an increase of v in the composite. A higher volume fraction of ceramic also contributes to higher ρ for the composite. Therefore, Z_a increases with the increase of the volume fraction of the piezoceramic, regardless the geometry and distribution of the ceramic segments. Z_a values of these composites are higher than that of PVDF, but significantly lower than that of typical single crystal materials (see Table 3-2).

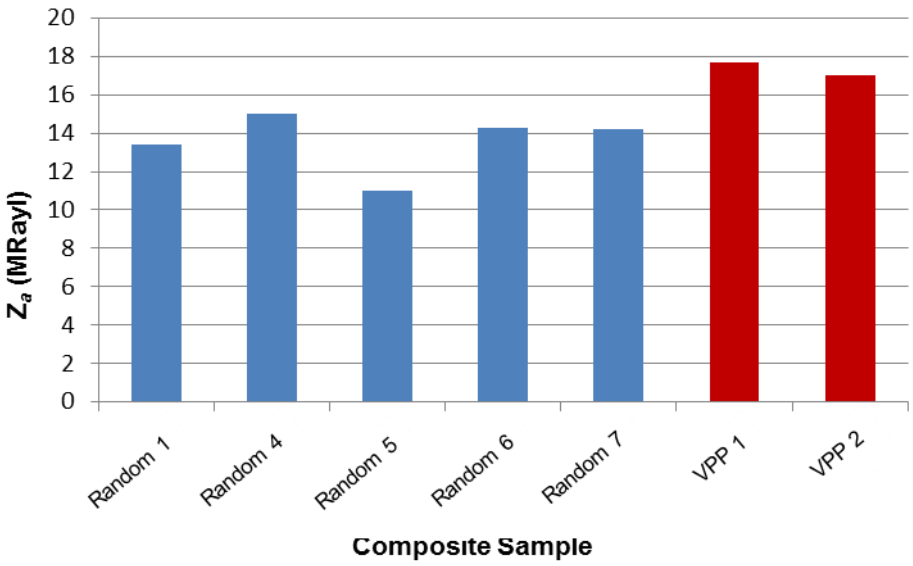

Figure 9-12 Acoustic impedance Z_a of the random composites and two VPP regular composites.

9.3.4 Laser vibrometry of 1-3 piezocomposites

A newly developed ultra-high frequency laser vibrometer, capable of measuring very small amplitudes down to picometer level, was used to characterise the surface motion of the random piezocomposites. Detailed working principle of it as well as the experimental setup is presented in Section 6.2.9. Due to the limited availability of the vibrometer; it was on loan to the University of Dundee for a week, only Random 1 (52.5 µm) and Random 4 (25.4 µm) were chosen as representatives to be tested and only preliminary measurements were accessible.

A sweep signal, denoting a sine signal whose frequency is slowly altered over a particular range of interest was used to excite the composites. The resulting vibration displacement of a randomly chosen single point with diameter <2 µm on the composites was collected simultaneously. The voltage magnitude of the excitation signal and the corresponding displacement magnitude of the vibration for Random 1 and Random 4 are presented in Figure 9-13 and Figure 9-14, respectively.

The selected frequency range is 25-35 MHz (resolution = 7.8 kHz) for Random 1 and 50-100 MHz (resolution=31.3 kHz) for Random 4, chosen according to the measured f_r and f_a as shown in Table 9-1. For Random 1, the highest vibration displacement of 30.6 pm was obtained at 29.38 MHz, which is in between its f_r and f_a as expected. Compared with the clear and distinctive displacement response of Random 1 at the resonance frequencies, Random 4 had displacement magnitudes above 100 pm over a range of frequency (60-65 MHz) near its f_r instead of one particular frequency. This further identifies the broad resonance nature of the thin random composites as described in Section 9.3.2, and also proves that this characteristic is strongly related to the composite thickness.

It is worth noticing that Random 4 has a higher signal to noise ratio than Random 1 by comparing Figure 9-13(b) and Figure 9-14(b), suggesting Random 4 probably had a better surface finish which encouraged the reflection of the incident laser. Though it was aimed to calculate d_{33} values of the composites from the vibration displacement data, the strength of the reflected signal greatly depended on the surface condition, varying from point to point, hence quantitative analysis of d_{33} was difficult to ascertain by using this method.

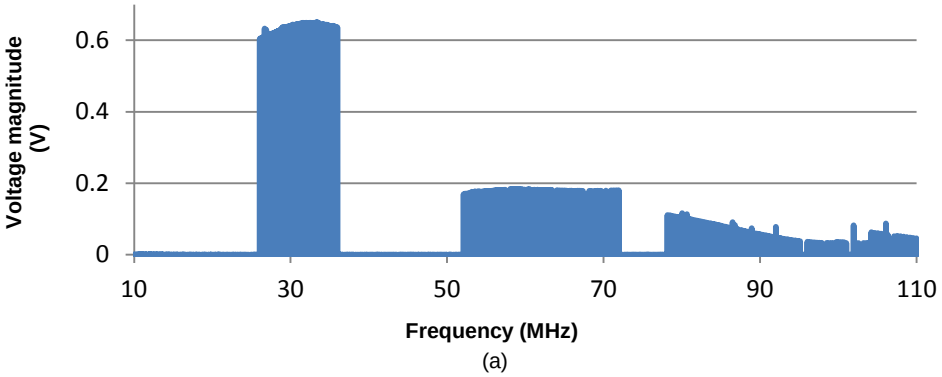

(a)

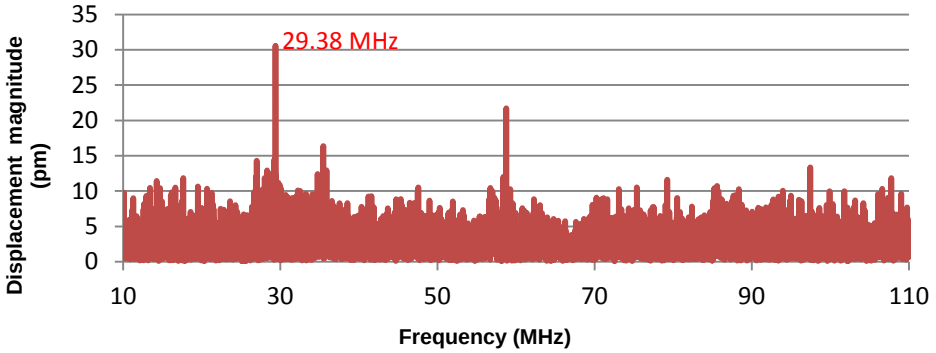

(b)

Figure 9-13 (a) Excitation signal and (b) vibration displacement of Random 1 against frequency.

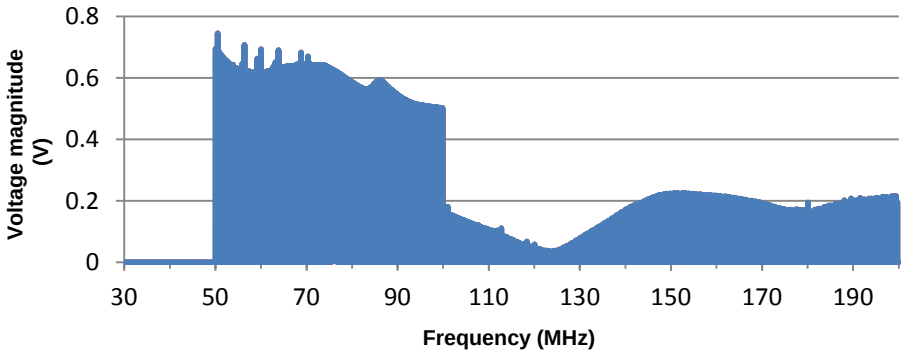

(a)

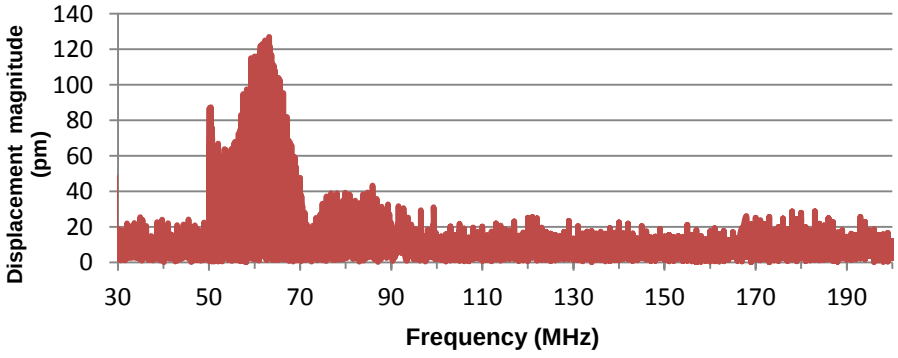

(b)

Figure 9-14 (a) Excitation signal and (b) vibration displacement of Random 4 against frequency.

9.3.5 Finite element analysis of 1-3 piezocomposites

To increase the understanding of the performance of the random composite, finite element modelling work has been carried out using PZFlex software as described in Section 6.3. An SEM image of sintered randomised structures (see Figure 9-5(b)) was imported to PZFlex to define the composite pattern. Preliminary results on the modelling work are shown and discussed below.

Figure 9-15 shows the impedance and phase diagrams of modelled piezocomposites with thicknesses of 10, 20, 30 and 40 μm, respectively. These curves are not as smooth as those from the experimental measurements shown in Figure 9-8. The slight fluctuations observed may be related to the fact that the finite element size (1.887 μm) is coarser than some of the obtained PZT grain sizes (see Figure 9-6). Nevertheless, it still can be determined that the evident peaks in these impedance curves all correspond to the resonances in the thicknesses of the composites, which agrees with the experimental results. More importantly, the thickness dependence on the composite performance can also be observed in these curves from modelling. With decreasing the composite thickness, the impedance peak becomes broader and the change in phase becomes smaller, indicating a reduction in the composite activity. In particular, the 10 μm thick composite behaves significantly differently from the others. It now can be deduced that such thickness dependence found in the experimental results was not caused by the errors in processing or measurements but most likely due to the novel random design itself. These results also indicate there would be an upper operational frequency limit of the random composite.

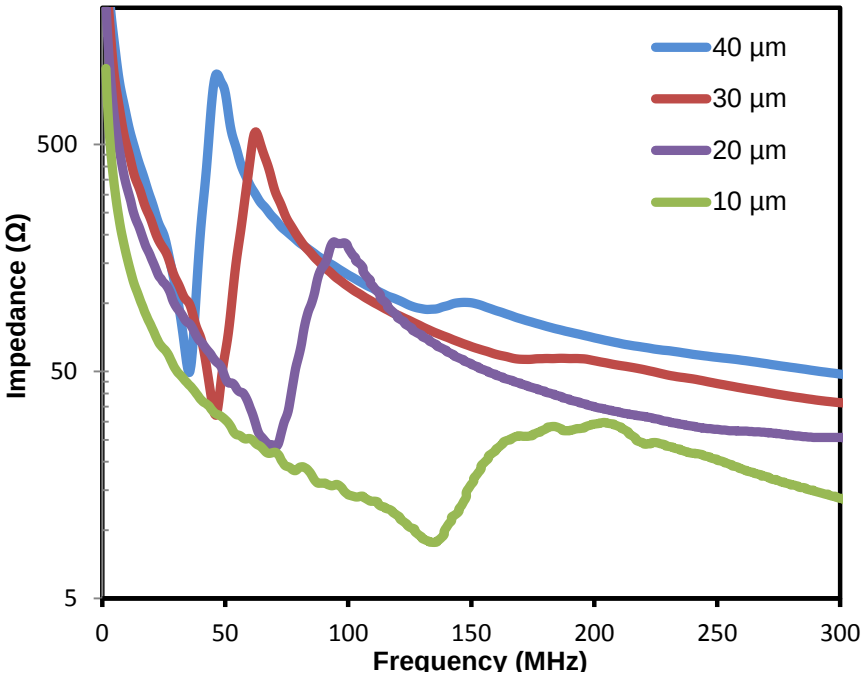

(a)

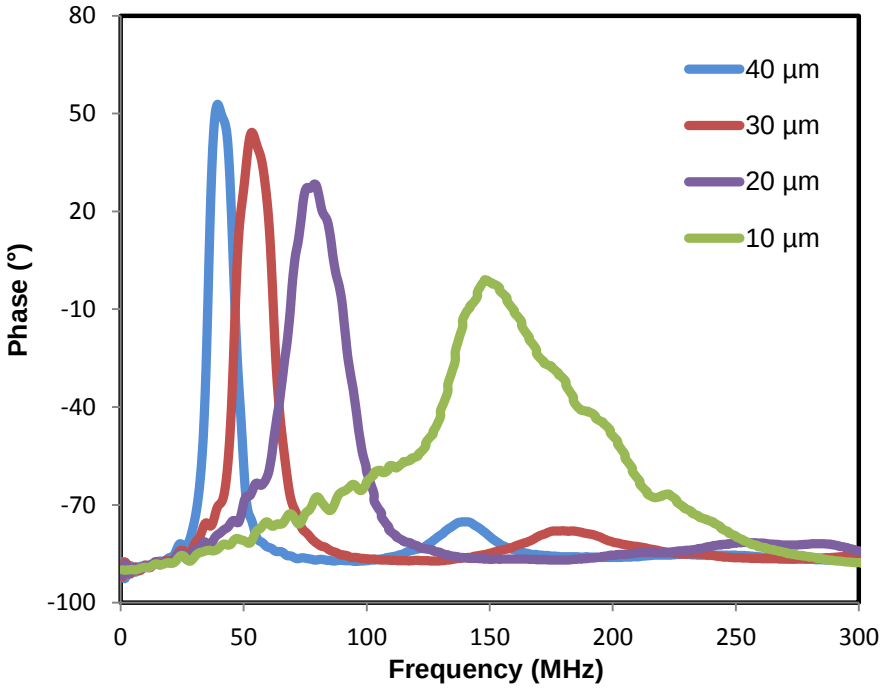

(b)

Figure 9-15 Impedance (a) and phase (b) magnitude diagrams from the modelled random composites with thicknesses ranging from 10 µm to 40 µm.

It should be noted that these impedance and phase curves are not perfectly matched with the measured data. This is mainly because of the differences between the models and real composites in damping conditions as well as material properties. Further work is needed to adjust these parameters used for modelling to match with experiment.

9.4 High frequency transducers

9.4.1 Transducer construction

In the previous work, a 45 MHz focussed single element transducer, was fabricated utilising a VPP regular piezocomposite by AFM Ltd. For the purpose of comparison, the Random 1 composite operating at around 30 MHz, close to that of the AFM transducer, was chosen to be further processed for the transducer fabrication. Also, in order to demonstrate the capability and suitability of the random composites for ultra-high frequency ultrasound imaging applications, the Random 4 composite, operating at around 70 MHz, and higher than that of routinely fabricated piezocomposite transducers was also assembled into a transducer. The two transducers incorporating the Random 1 and 4 composites are referred to as the Random 1 transducer and the Random 4 transducer, respectively, in the following paragraphs.

The fabrication procedures of the focussed transducers as illustrated in Figure 9-16 were developed by AFM ltd. The advantages of this construction route compared with other fabrication methods based on a modified SMA connector [10, 12] were discussed and reported by R.A.Webster [13]. The fabrication process started with the preparation of two PDMS moulds. One was for maintaining the central position and the desired curvature of composites whilst setting in wax (see Figure 9-16(c)) replicated from a metal/PTFE mount master (see Figure 9-16(a)). The other soft mould was for casting

tungsten epoxy insert as well as supporting the attached wire to the composites replicated from a brass former master with two steel pins (see Figure 9-16(d)).

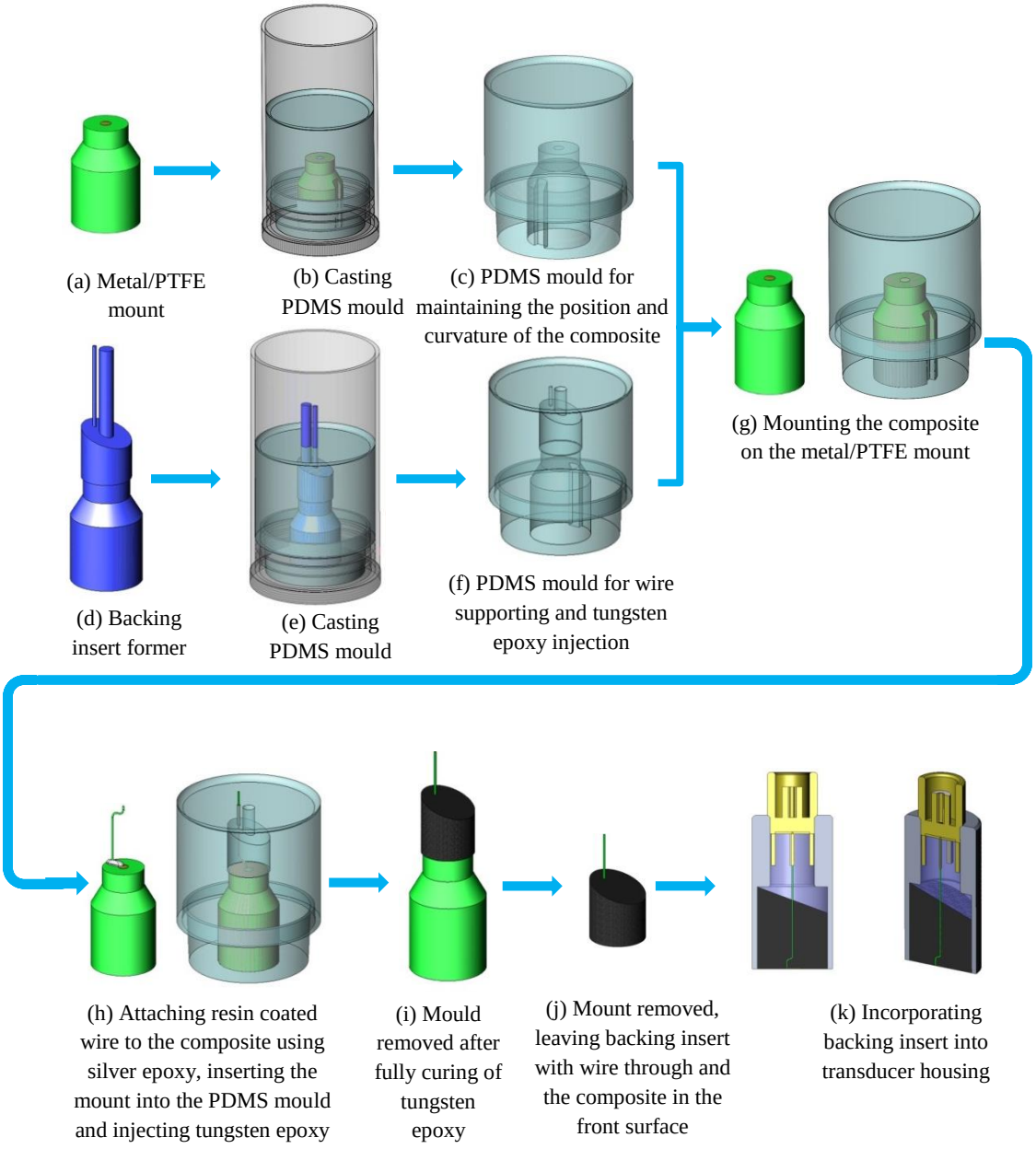

Figure 9-16 Illustration of the fabrication process of the transducers (adapted from [13]).

In this method, focussing of the transducer was achieved by curving the active composite. To fit the size of the curved metal tip on the metal/PTFE mount used for curving, the composites were laser cut into circles with diameter ~ 1.5 mm. As shown in

Figure 9-17, the marked red circle area is the part cut from Random 1 and subsequently curved for the transducer assembly. It can be seen that although there are a few scratches on the two ‘tails’ of Random 1 resulting from repeatedly being in contact with pins during measurements, the actual composite area is free of obvious defects and the electrode is continuous.

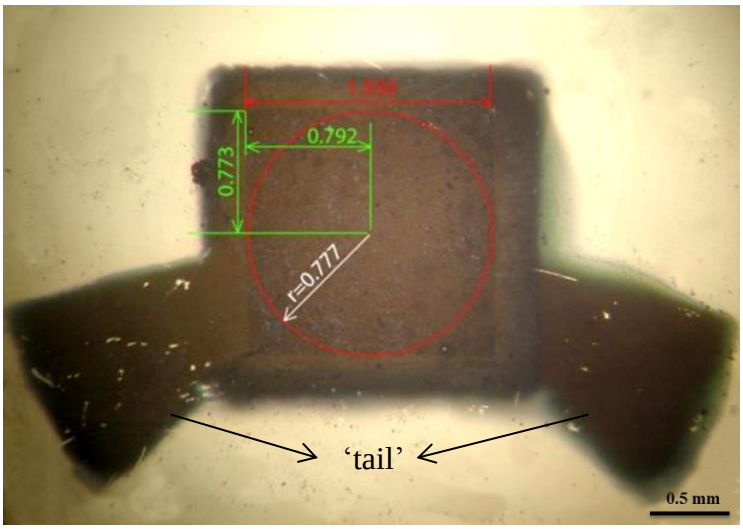

Figure 9-17 Gold electroded Random 1 composite. The red circle marked area is the part cut by laser for the transducer fabrication.

The curving stage illustrated in Figure 9-16(g) involved carefully placing and positioning the laser cut circular composite on the wax covered metal tip. The prepared soft mould positioner (see Figure 9-16(c)) was then gently slipped over the mount to exert a small amount of force thereby uniformly spreading the wax layer and facilitating curving the composite. However, it was observed that both the Random 1 and Random 4 composites had cracked after removing the positioner. The optical image of the Random 1 composite mounted on the metal tip with a central crack is shown in Figure 9-18 as an example. In previous work, a series of PVDF samples and VPP piezocomposites and were curved using the same process and very few of them cracked. The cracking of the two random composites indicates that their formability was poorer than that of polymers

and the regular composites, which may be the consequence of the random design. Compared with the elastic polymer matrix and the embedded fine segments, the relatively large ceramic structures with lateral dimensions of tens of micrometres would be more difficult to accommodate the deformation during curving, leading to the formation of local tensile stress. When curved, the central part of the composite suffered from the greatest amount of deformation and the local tensile stress became large enough to induce a crack. Although the existence of the crack would probably degrade the properties of the resultant transducer somehow, the majority of the electrode was seen to be continuous and therefore the whole composite was deemed to be functioning. In order to prevent any potential short circuit, the cracks on the two composites were cautiously filled with epoxy.

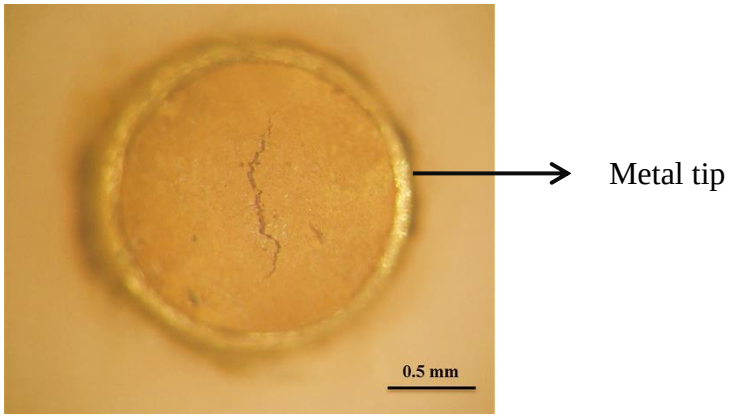

Figure 9-18 Curved Random 1 composite on top of the metal tip showing a central crack.

In order to avoid cracking in the random piezocomposites when being incorporated into focussed transducers, a number of alternative approaches could be investigated. Firstly, the way of focusing could be changed by adding a curved lens on to a planar composite as described in Section 2.4.1. A second approach could be to improve the formability of the random composites by, for example, selectively reducing the feature sizes of the ceramic segments or designing a more compliant random structure.

After mounting the composite, wiring was then performed to achieve the electrical connection as non-conducting tungsten epoxy was used as backing. As shown in Figure 9-19, a 125 µm resin coated copper wire was connected onto the outer region of the composite using a tiny amount of silver epoxy (186-3616, RS, UK). This is a tricky step requiring the operator's skill to keep the silver epoxy bulb as small as possible whilst ensuring that there is sufficient adhesion between the wire and the composite to keep the joint from breaking in the subsequent stage of casting the backing layer.

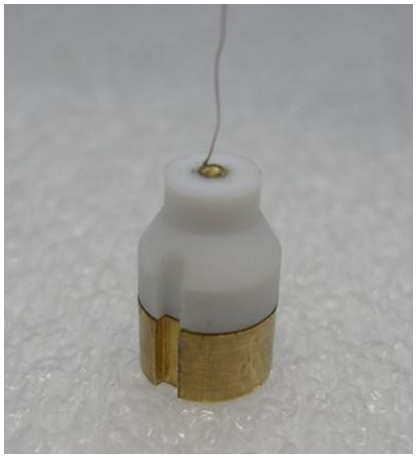

Figure 9-19 Photo of wired Random 1 composite on top of the meal/PTFE mount.

The fabricated PDMS mould for casting tungsten epoxy in place (Figure 9-16(f)) was then carefully slipped over the mount and the wire fed into the smaller hole with ~0.5 mm in diameter of the soft mould, as illustrated in Figure 9-16(h). The tungsten epoxy backing material was produced by mixing CY1301/HY1300 (Araldite, UK) and tungsten powder (Alpha Aesar, APS 1-5 micron 99.9%) at the volume fraction ratio of 7:3. According to Webster [13], if the volume percentage of tungsten filler is above 30 %, the mixture would be too viscous to be degassed and cast properly. The degassed mixture was then injected into the mould via the other hole with ~2 mm in diameter.

Any observed air bubbles were removed by using a syringe through the walls of the mould.

After setting at room temperature for 24 hrs, the whole assembly was transferred into a 40 ºC oven to soften the wax. The mount was slowly pulled out from the soft mould, allowing the composite to stay on the backing. The tungsten epoxy insert was then removed from the mould and fitted into a customised transducer housing as shown in Figure 9-16(k). The wire attached on the composite was soldered to the centre pin of the connector fitted at one end of the housing. The ground electrode was sputtered on the composite after careful cleaning of its surface. Figure 9-20 shows a photo of completed Random 1 transducer as an example.

Figure 9-20 Photo of Random 1 focussed single element transducer.

9.4.2 Transducer properties

9.4.2.1 Electrical impedance

Figure 9-21 shows the electrical impedance spectra measured from the Random 1, AFM and Random 4 transducers. Despite the presence of cracks in the random composites as mentioned above, the electrical impedance spectra of the completed transducers demonstrate that they are still active as a whole. As expected, the resonant frequencies

of the Random 1 and Random 4 transducers are around 30 MHz and 70 MHz, respectively.

It can be seen from Figure 9-21(b) that the AFM transducer has a lateral mode present at around 75 MHz, which is not very close to its operating frequency and therefore may allow operation over a reasonable bandwidth. In another VPP composite transducer with operating frequency of 36 MHz, as reported by MacLennan [8], the lateral resonance even became the dominant mode because it was found that the backing may preferentially damp the thickness mode resonance. In comparison, for the transducers incorporating the random composites only thickness mode resonances are observed in the broad frequency range of 10-150 MHz, showing their advantage in preventing the interference of any spurious modes. The third harmonic thickness resonance was observed for the AFM transducer at ~110 MHz and for the random 1 transducer at ~100 MHz.

The impedance spectra of the Random 1 and 4 transducers appear similar to those of the incorporated composites, as shown in Figure 9-8 but with apparently damped resonance peaks due to the effect of the backing. It should be noted that increase of the phase value at higher frequencies was observed for all three transducers. For the Random 1 and AFM transducers, this was visible below 150 MHz; for the Random 4 transducer, this occurred >150 MHz. It is thought that this is due to a calibration effect.

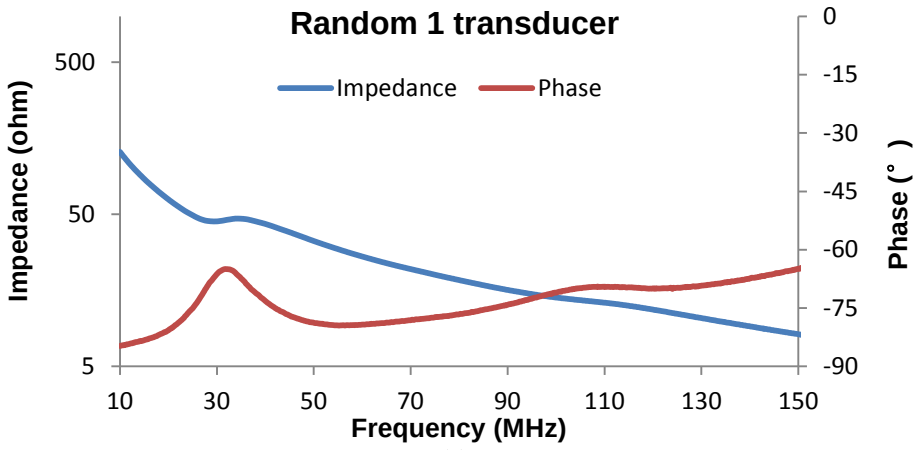

(a)

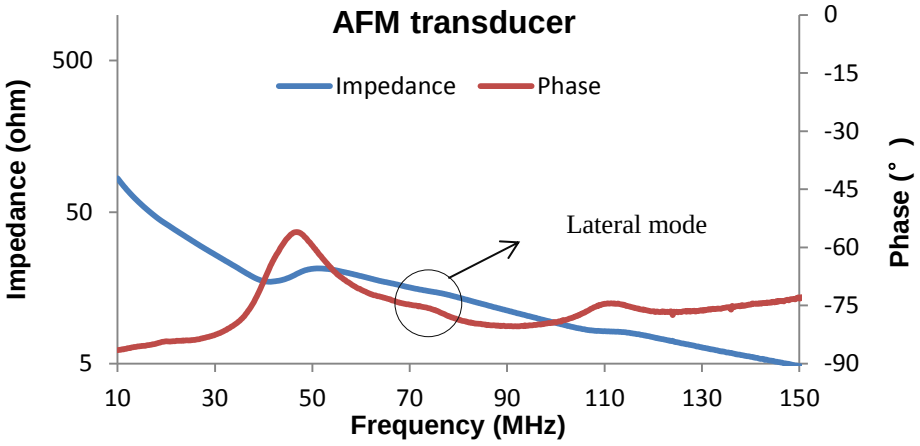

(b)

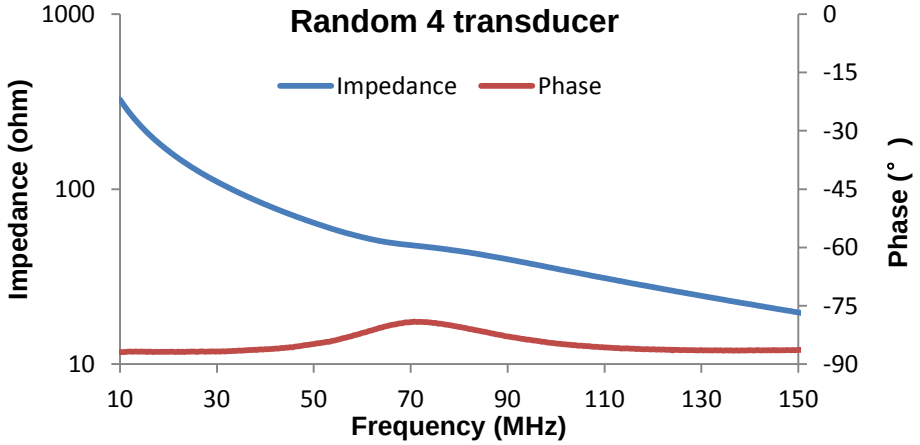

(c)

Figure 9-21 Electrical impedance and phase measured from transducers (a) Random 1, (b) AFM and (c) Random 4.

9.4.2.2 Pulse-echo response

As illustrated in Section 6.2.10, the pulse-echo responses of the transducers were tested by using a stainless steel as the echo target. Figure 9-22 and Figure 9-23 show the pulse-echo measurement results for the Random 1 and 4 transducers, respectively. The characteristics of the two transducers including pulse length, axial resolution and bandwidth obtained from the pulse-echo measurements are outlined in Table 9-3 and Table 9-4, respectively.

As exhibited in the frequency domain representation of the pulse-echo data, the centre frequency is 34.1 MHz for the Random 1 transducer and 73.0 MHz for the Random 4 transducer, which is in agreement with the impedance data shown in Figure 9-21. However, it can be observed from the pulse responses in time (see Figure 9-22(a) and Figure 9-23(a)) that both of the transducers suffer from unusual amplitude decay. This is responsible for the null values at ~20 MHz for the Random 1 transducer and at ~ 60 MHz for the Random 4 transducer in the frequency domain (see Figure 9-22(b) and Figure 9-23(b)). In consequence, the measured bandwidth is somewhat lower than expected. For example, the -6 dB bandwidth for the Random 1 transducer is 13 MHz, which is smaller than the value of 29 MHz reported for a VPP composite transducer operating at 36 MHz [8]. This may relate to the novel randomised design, to the transducer backing material, to the cracks on the composites or to misalignment of the reflecting target. Further modelling work is expected to shed more light on the functional performance of these novel random composites and to increase understanding of the experimental characterisation results.

-6 dB axial resolutions is 69.3 μm for the Random 1 transducer, which is higher than the figures of ~80 μm of VPP composite transducers operating at around 30 MHz reported

by MacLennan [8]. Although the pulse response of the Random 4 transducer contains more cycles than normal values of 2-3 [14], the -6 dB pulse length is quite short and the resulting axial resolution of 30.9 μm is reasonably good for a 70 MHz transducer.

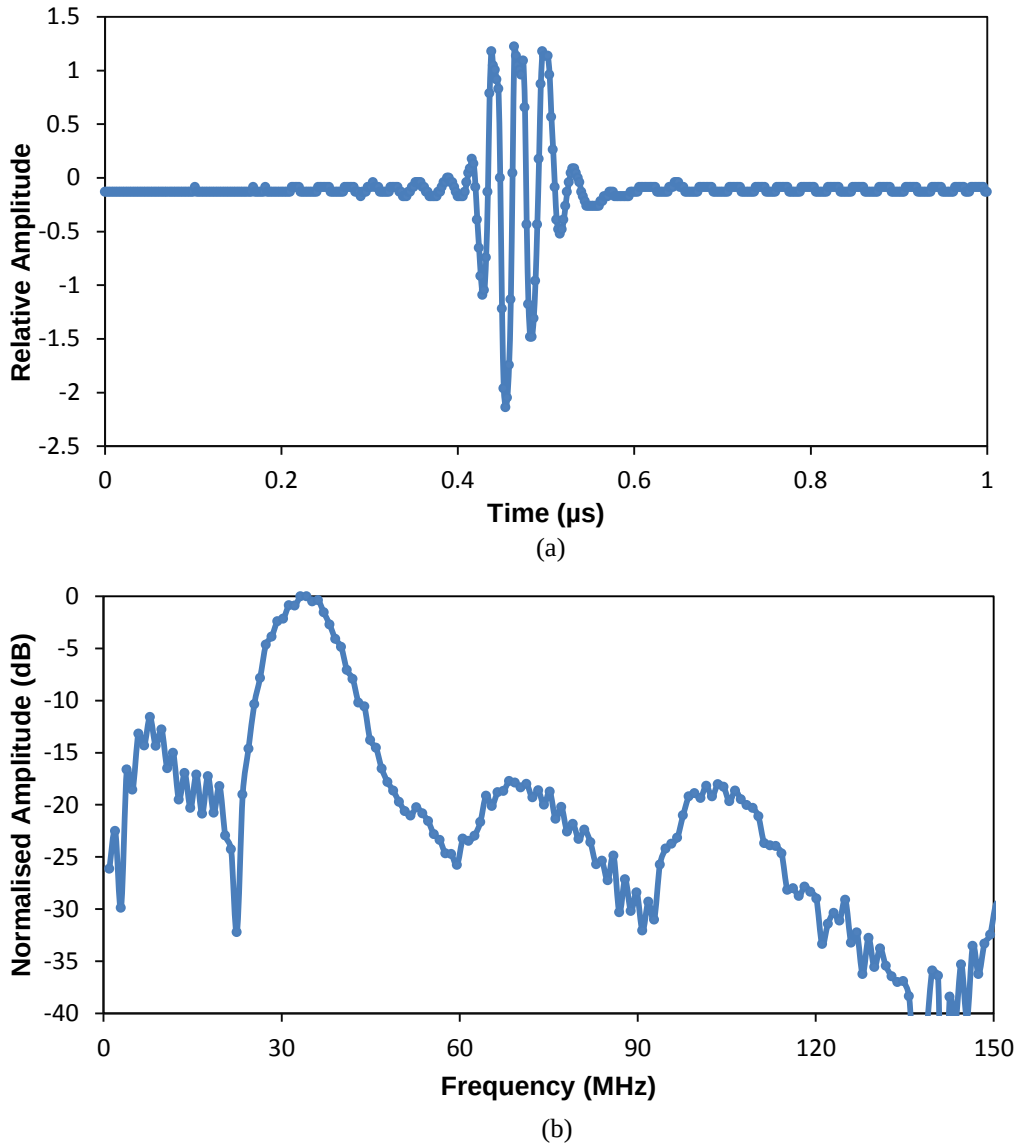

Figure 9-22 Pulse-echo measurement from the Random 1 transducer at focus in (a) time and (b) frequency domain.

Table 9-3 Parameters of the Random 1 transducer obtained from the pulse-echo measurement.

Parameter / Threshold	Pulse Length (μs)	Axial Resolution (μm)	Bandwidth (MHz) / (%)
-3 dB	0.068	52.4	9 / 26%
-6 dB	0.090	69.3	13 / 38%

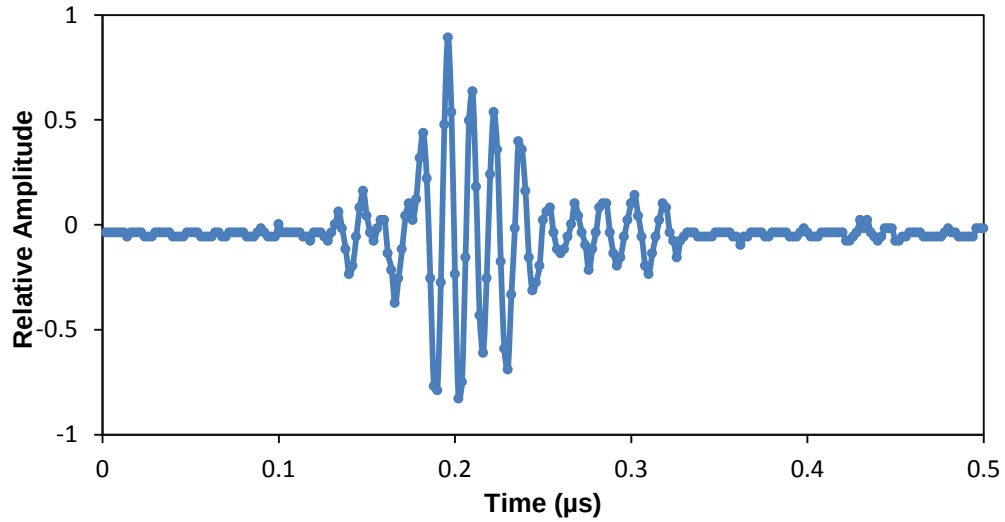

(a)

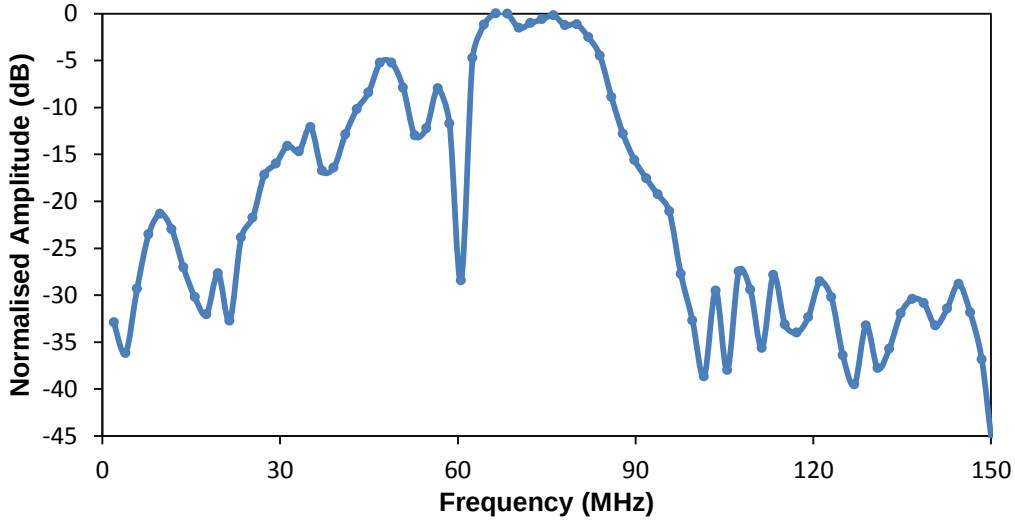

(b)

Figure 9-23 Pulse-echo measurement from the Random 4 transducer at focus in (a) time and (b) frequency domain.

Table 9-4 Parameters of the Random 4 transducer obtained from the pulse-echo measurement.

Parameter / Threshold	Pulse Length (μs)	Axial Resolution (μm)	Bandwidth (MHz) / (%)
-3 dB	0.014	10.8	20 / 27%
-6 dB	0.040	30.9	23 / 31%

9.4.2.3 Tungsten wire scan

As described in Section 6.2.10, a set of tungsten wires with step size of 1 mm were scanned by the two transducers. B-scan images of these wires produced by the Random 1 and Random 4 transducers are presented in Figure 9-24(a) and 9-24(b), respectively. It can be seen from Figure 9-24(a) that the Random 1 transducer functioned as expected, capable of imaging the fine wires with diameters of 25 μm at varying distances from the transducer. With increasing the axial distance, the lateral length of the tungsten wire shown in the image decreases first and then increases, reaching the smallest value at the distance of ~4-5 mm. This reflects the presence of three distinct regions in the beam profile of the focused transducer as introduced in Section 2.4.2.1, and more importantly verifies the focal length of the Random 1 transducer to be ~4-5 mm, which is pretty close to the designed value of 5 mm. By substituting focal length=4.5 mm into Equation 2-7, the lateral resolution of the transducer is calculated to be 149 μm.

As observed in Figure 9-24(b), the wire images generated by the Random 4 transducer are fainter in general than those from the Random 1 transducer. Moreover, wires located at an axial distance over 3 mm from the transducer cannot be clearly seen in the images. This is however not surprising considering that the 70 MHz piezocomposite itself was not as active as the 30 MHz one and the presence of the cracks in the composite.

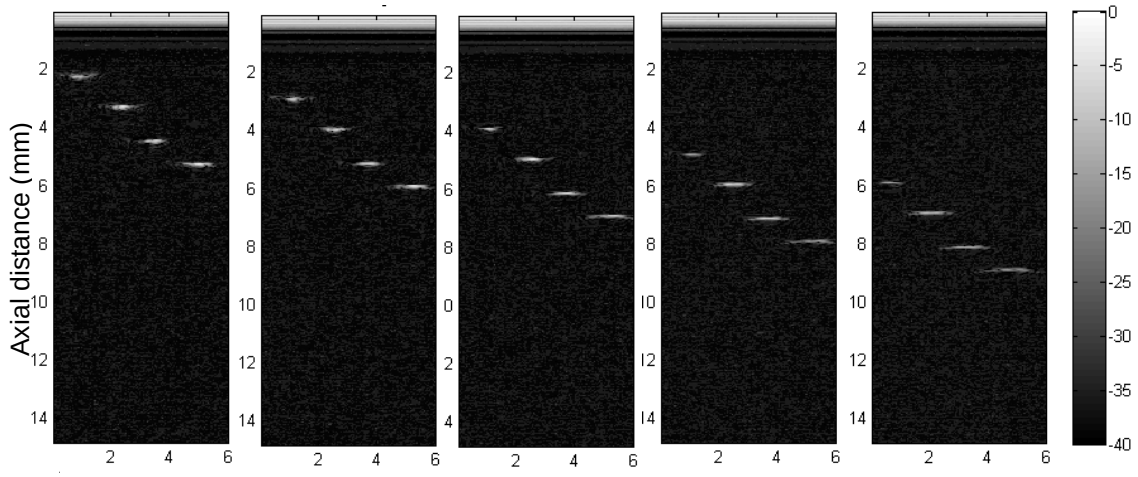

(a)

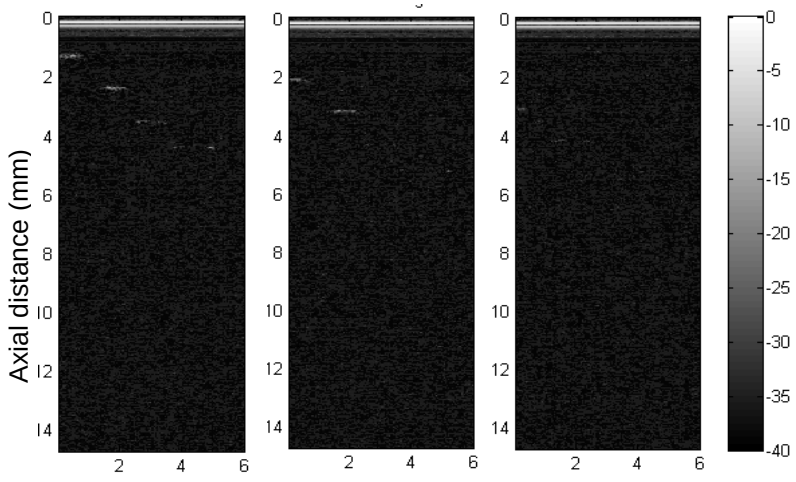

(b)

Figure 9-24 B-scan images of four 25 µm wires at a series of different distances from the transducer produced by (a) the Random 1 transducer and (b) the Random 4 transducer. The four wires were separated by 1 mm in both axial and lateral directions. The topmost wire was at axial distances of 2 mm, 3 mm, 4 mm, 5 mm and 6 mm, respectively from left to right in (a), and at axial distances of 1 mm, 2 mm and 3 mm from left to right in (b).

9.4.2.4 Tissue imaging

Figure 9-25 shows a B-scan image of two thin tissue samples resected from a cancerous Min-type mouse bowel and a wild-type one, produced using the Random 1 transducer. This image has good resolution and low noise. It clearly shows the features of the two mouse bowel tissues as marked in the figure, with the cancerous one having an adenomatous polyp on its surface while the wild-type sample having a normal mucosal layer.

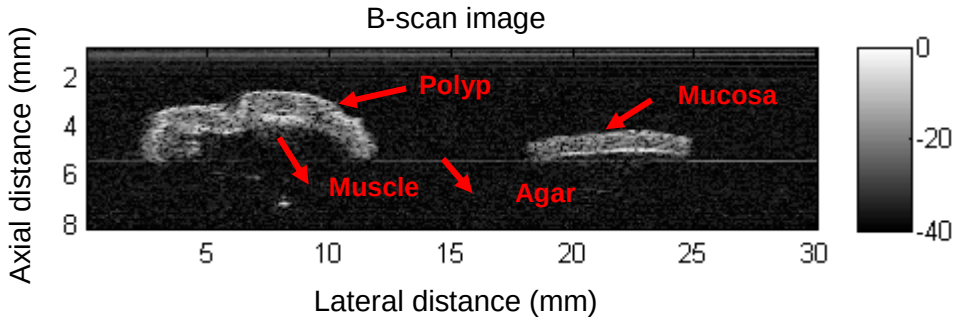

Figure 9-25 B-scan image of a cancerous (left) and a wild-type (right) mouse bowel tissues generated by the Random 1 transducer.

9.5 Summary

Randomised ceramic segments with feature sizes ranging from 2-50 μm and aspect ratios up to 70 have been successfully demoulded from micro-sized PDMS moulds, benefited from the high strength of the gel cast green body. A relatively high resin content of 40 wt% was proved to be necessary to be used for the preparation of the gel casting slurry in order to provide the sufficient green strength for demoulding. Though 40 wt% resin content led to a decrease of sintered density in bulk samples, the resultant sintered ceramic segments showed homogenous and dense microstructure which is probably owing to the high surface area of the fine structures.

A series of random piezocomposites with ceramic volume percentages close to the designed value of 40% and thicknesses ranging from ~20-50 μm have been fabricated using the developed micro-moulding technique based on the same pattern design. The impedance measurements of the composites showed that spurious modes were effectively suppressed and only the thickness resonance was presented, which confirmed previously reported modelling results [7]. All of the random composites have k_t values over 0.5, higher than generally reported values, representing high energy conversion efficiency. The 52.5 μm thick random composite was proven to have better overall

functional performance (higher k_t and d_{33}, lower Z_a, though lower ε_r^S) than two VPP regular composites reported by MacLennan [8], while the thinner random composites had considerably lower values of d_{33} and ε_r^S than the VPP composites. Such thickness-dependence of the random composite properties was also indicated by the results from laser vibrometry tests and finite element modelling.

Two focused ultrasound transducers were constructed using the random composites as active elements. Though the composites cracked during curving, the impedance and pulse-echo measurements demonstrated the functionality of the transducers operating at 30 and 70 MHz, respectively. The 30 MHz transducer was proven to have a -6 dB axial resolution of 69 μm and a lateral resolution of 149 μm. It has been demonstrated to be capable of producing B-scan images of 25 μm tungsten wires and mouse bowel tissues with high resolution and low noises. In comparison, the imaging capability of the 70 MHz transducer was poor and limited by the axial distance, which may relate to the decreased functional properties of the thin random composite or processing errors occurred during the transducer construction.

9.6 References

[1] D. Chandra and S. Yang, "Stability of High-Aspect-Ratio Micropillar Arrays against Adhesive and Capillary Forces," *Accounts of Chemical Research,* vol. 43, pp. 1080-1091, 2010/08/17 2010.

[2] J. N. Lee, *et al.*, "Solvent Compatibility of Poly(dimethylsiloxane)-Based Microfluidic Devices," *Analytical Chemistry,* vol. 75, pp. 6544-6554, 2003/12/01 2003.

[3] A. Abrar, *et al.*, "1–3 connectivity piezoelectric ceramic–polymer composite transducers made with viscous polymer processing for high frequency ultrasound," *Ultrasonics,* vol. 42, pp. 479-484, 2004.

[4] S. Cochran, *et al.*, "Net-shape ceramic processing as a route to ultrafine scale 1-3 connectivity piezoelectric ceramic-polymer composite transducers," in *Ultrasonics Symposium, 2004 IEEE*, 2004, pp. 1682-1685 Vol.3.

[5] S. Wang, *et al.*, "Fabrication of Lead Zirconate Titanate Microrods for 1–3 Piezocomposites Using Hot Isostatic Pressing with Silicon Molds," *Journal of the American Ceramic Society*, vol. 82, pp. 213-215, 1999.

[6] Z. Dou, "Fabrication of Ceramic Micro-components," PhD, University of Birmingham, 2005.

[7] C. E. M. Demore, *et al.*, "1-3 piezocomposite design optimised for high frequency kerfless transducer arrays," in *Ultrasonics Symposium (IUS), 2009 IEEE International*, 2009, pp. 1-4.

[8] D. MacLennan, "Fundamental Characterisation and Early Functional Testing of Micromoulded Piezocomposites " PhD, University of Strathclyde, 2009.

[9] D. MacLennan, *et al.*, "Fundamental performance characterisation of high frequency piezocomposites made with net-shape viscous polymer processing for medical ultrasound transducers," in *Ultrasonics Symposium, 2008. IUS 2008. IEEE*, 2008, pp. 58-61.

[10] D. MacLennan, *et al.*, "Properties and Application-Oriented Performance of High Frequency Piezocomposite Ultrasonic Transducers," in *Ultrasonics Symposium, 2007. IEEE*, 2007, pp. 100-103.

[11] M. D. Sherar and F. S. Foster, "The design and fabrication of high frequency poly(vinylidene fluoride) transducers," *Ultrasonic Imaging*, vol. 11, pp. 75-94, 1989.

[12] J. M. Cannata, *et al.*, "Fabrication of high frequency (25-75 MHz) single element ultrasonic transducers," in *Ultrasonics Symposium, 1999. Proceedings. 1999 IEEE*, 1999, pp. 1099-1103 vol.2.

[13] R. A. Webster, "Passive Materials for High Frequency Piezocomposite Ultrasonic Transducers," PhD, University of Birmingham, 2009.

[14] T.A.Whittingham, "Transducers and beam forming in medical ultrasonic imaging," *Insight-Non-Destructive Testing and Condition Monitoring*, vol. 41, pp. 8-12, 1999.

CHAPTER 10 CONCLUSIONS AND FUTURE WORK

10.1 Summary and Conclusions

An innovative random 1-3 piezocomposite design employing a distribution of shapes and sizes of the ceramic segments has shown particular advantages for high frequency ultrasound applications in comparison with conventionally used regular designs. In this thesis, for the first time, random piezocomposites have been physically realised based on the development of a novel micro-moulding approach that combines the knowledge of novel ceramic processing and micro fabrication. The work presented here is also the first time that the whole process from raw materials to working high frequency ultrasound transducers incorporating such a random design has been considered and demonstrated. All the aims and objectives defined in Chapter 5 have been achieved.

The gel casting system based on the curing of water-soluble epoxy and amine hardener was adopted for the preparation of the PZT slurry. The epoxy-amine polymerisation process was studied with varying hardener additions, resin contents and curing temperatures. 0.2 mol/eq bis(3-aminopropyl)amine was selected as the optimal hardener addition and room temperature was chosen as the reaction temperature. Increasing the resin content was found to increase the strength of the formed epoxy gel, which led to investigations into the influence of the resin content on the properties of the aqueous slurry, the solidified green bulk samples and subsequently the sintered PZT. Although increased resin content resulted in undesirable increased viscosity, decreased gelation time, and inferior properties of sintered ceramics, it led to an improvement in green strength, which was of paramount significance for the demoulding process in the micro-moulding approach. A maximum green strength of 38 MPa was achieved in the green bodies consolidated from the slurry with 45 vol% solids loading and 40 wt% resin,

which was much higher than that achieved from traditionally used colloidal processing routes and conventional gel casting systems.

In parallel with the optimisation of the ceramic processing, mould fabrication techniques for indirect and direct moulding strategies have also been developed. For direct hard moulding, the feasibilities of AZ 125nXT negative photoresist and AZ 40XT positive photoresist to be used as lost moulds were investigated. For indirect soft moulding, SU 8 and Si were proposed to be used as master moulds. AZ 125nXT was capable of producing regular-shaped holes with diameters of 25 μm and depths up to 120 μm. However, this negative photoresist suffered from low resolution and poor strippability and thus was not suitable for random mould fabrication. The capability of AZ 40XT for producing randomised features down to 2 μm was demonstrated. However, the achievable thickness of this positive photoresist was limited to 40 μm. The preliminary work on patterning SU 8 by UV lithography showed that the high-aspect-ratio pillar structures obtained were tilted or collapsed during drying. Deep etching of Si demonstrated the capacity to produce the desired randomised segments as tall as 170 μm, the structures of which were successfully transferred to PDMS soft moulds. Given the fact that the deep etching of Si technique gave the most satisfactory results in terms of the integrity and aspect ratios of the random structures, an indirect soft moulding strategy was selected, using etched Si structures as the masters and the PDMS moulds replicated from the Si masters for slurry casting.

Randomised ceramic structures with lateral feature sizes of 2 - 50 μm and high aspect ratios, up to 70, were successfully achieved by combining PZT slurry with 45 vol% solids loading and 40 wt% resin along with the soft moulding technique, demonstrating the high green strength of the gel-cast green bodies and the viability of the fabrication

technique. Impedance spectra of the resultant piecomposites with similar ceramic distributions and volume fractions but different thicknesses showed that no spurious resonance modes were evident over a broad frequency range, which agreed with the previously reported modelling results. The performance of these piezocomposites was assessed by experimental characterisation and the preliminary modelling work and the results indicated that decreasing composite thickness might constrain the vibrations of ceramic segments along the thickness direction.

Impedance measurements and pulse-echo responses demonstrated the functionality of complete transducers operating at ~30 and 70 MHz. B-scan images obtained by scanning wires and mouse tissues using the 30 MHz transducer showed good resolution and low noises, demonstrating that the randomised composite can be adopted for high frequency ultrasound imaging applications. The imaging capability of the 70 MHz transducer was not as good as expected, which might be related to the non-optimised transducer fabrication process or the thickness dependence of the random composite properties.

These results demonstrate that randomised 1-3 piezocomposites with a high tolerance of overall geometry can be produced for HFUS applications. In fact, considering the capability and versatility of the established micro-moulding approach, it could be adapted for any piezocomposite design at the micro-scale and extended to a range of other applications that require complex-shaped, ultra-fine scale and high-aspect-ratio ceramic micro-components.

10.2 Suggestions for future work

The results presented in this thesis can be regarded as the first step towards the development of novel transducers incorporating random piezocomposites. Several issues encountered during the course of the work require further investigations to push forward the technological development for HFUS applications.

Future optimisation on the gel casting system should be focussed on reducing the viscosity of the slurry, improving the physical and functional properties of sintered ceramics whilst maintaining the high strength of green bodies. Increasing the understanding of the interactions among the ceramic particles, epoxy and dispersant molecules in the colloidal suspensions should be addressed for fundamental improvements of the gel casting system. The investigations into the rheological properties should be combined with the study of the demoulding process, such that critical solids loading and resin content can be determined. Other choices of epoxy-amine combinations, dispersants and solvent media can also be considered.

The reproducibility and controllability of the demoulding process requires further improvement. From the material point of view, in additional to the improvement of ceramic green strength, surface treatments of the PDMS moulds could also aid the demoulding process, which is therefore worthwhile being investigated. On the processing side, the current peeling off process is not ideal as the manual operation is time-consuming and highly dependent on the experience and skills of the operator. An automated mechanical device for demoulding would be especially desirable for taking this laboratory-developed manufacturing approach into an industry environment. To accurately mimic the motions of human fingers may be somewhat difficult, but it may

be possible to achieve a similar peeling action by applying vacuum on the PDMS mould at suitable angles.

The properties of these novel random composites have not been fully understood. Further work on modelling is expected to shed more light on the functional performance of these composites and to increase understanding of the experimental characterisation results. Investigations should be focused on creating 3D models with various random patterns, volume fractions and dimensions and analysing the impedance spectra and surface vibrations output from the models. The parameters used for modelling such as the physical and piezoelectric properties of the ceramic phase and damping conditions should be further adjusted to match with experiment.

It is possible that the properties of these random composites have not been fully explored as the poling process was not optimised for these composites. Optimisation of the non-contact poling conditions such as the distance between the copper pin, the sample, poling voltage, temperature, and duration should be carried out.

For optimisation of the single-element transducer fabrication, cracking in the random composites during curving should be avoided. Possible solutions have been raised in Chapter 9 including changing the focusing method and improving the formability of the composite itself.

These random composites can also be adopted for the construction of ultrasound array transducers to allow electronic steering and dynamic focusing as introduced in Section 2.4. Recently, Bernassau et al. developed a photolithographic process to precisely pattern fine-scale electrodes on piezocomposites for high frequency arrays. Figure 10-1 shows photographs of a 30 MHz linear array made with a regular piezocomposite

fabricated by the VPP route, as a typical example. Such a process has also been demonstrated for patterning a 50 MHz phase array and a 100 MHz linear array [1, 2]. By defining fine electrodes on the surface of the high frequency random composites using this photolithographic process, it would be possible to achieve high frequency arrays operating up to 100 MHz without the interference of undesirable spurious resonance modes. Investigations into the surface preparation of the random piezocomposites for photolithography should be carried out in order to achieve good electrode adhesion and definition.

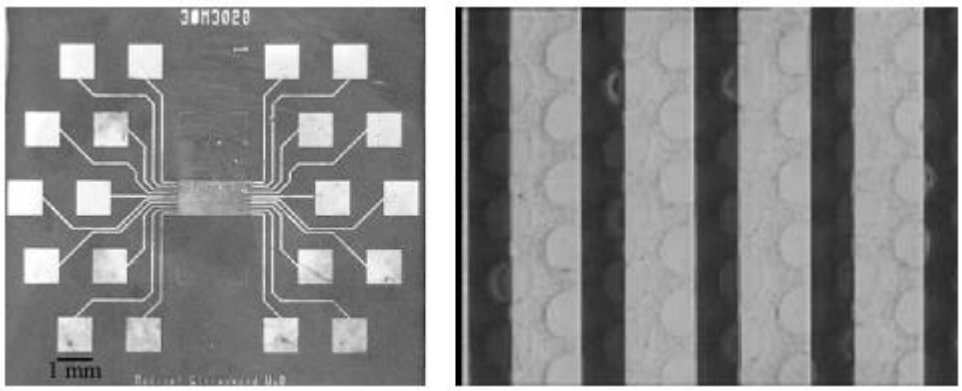

(a) (b)

Figure 10-1 (a) Photograph of the sample coupon for a 30 MHz linear array and (b) optical image of the electrode patterned on top a regular piezocomposite fabricated by the VPP process [1].

10.3 References

[1] A. Bernassau, *et al.*, "Progress towards wafer-scale fabrication of ultrasound arrays for real-time high-resolution biomedical imaging," *Sensor Review,* vol. 29, pp. 333-338, 2009.

[2] A. Bernassau, *et al.*, "Microfabrication of electrode patterns for high-frequency ultrasound transducer arrays," *IEEE transactions on ultrasonics, ferroelectrics, and frequency control,* vol. 59, pp. 1820-1829, 2012.

Appendix I: Determination of material properties from impedance and capacitance

Table I-1 Relationships between the material parameters of piezoelectric materials and the electrical impedance and capacitance.

Parameter	Measurements required	Formula used
V	h, f_a	$v = 2 f_a h$
Z_a	h, f_a, ρ	$Z_a = 2\rho f_a h$
k_t	f_a, f_r	$k_t = \sqrt{\frac{\frac{\pi f_r}{2 f_a}}{\tan\left(\frac{\pi f_r}{2 f_a}\right)}}$
ε^T	A, C_L, h	$\varepsilon^T = \frac{C_L h}{A}$
ε^S	A, C_H, h	$\varepsilon^S = \frac{C_H h}{A}$
c_{33}^D	h, f_a, ρ ,	$c_{33}^D = \rho(2 f_a h)^2$
c_{33}^E	h, f_a, f_r, ρ	$c_{33}^E = \rho(2 f_a h)^2 \left(1 - \left(\frac{\frac{\pi f_r}{2 f_a}}{\tan\left(\frac{\pi f_r}{2 f_a}\right)}\right)\right)$
e_{33}	h, f_a, f_r, ρ, C_H. A	$e_{33} = \sqrt{\left(\frac{\frac{\pi f_r}{2 f_a}}{\tan\left(\frac{\pi f_r}{2 f_a}\right)}\right)} \rho(2 f_a h)^2 \frac{C_H h}{A}$

Appendix II: Calculations of the effective properties of 1-3 piezocomposites based on a physical model

The equations used for calculating the effective electromechanical coupling factor and the effective acoustic impedance of the piezocomposite made from TRS 610 ceramic and Epofix resin discussed in Section 3.3.1 are shown below, based on a physical model reported by Smith et al [1].

In the following equations, the elastic and dielectric constants of the piezoceramic are distinguished from those of the polymer matrix by the subscript *E* and *S*.

The effective elastic constant at constant electric field $\overline{c_{33}^{E}}$ is given by:

$$\overline{c_{33}^{E}} = V_c\left[c_{33}^{E} - \frac{2V_p(c_{13}^{E} - c_{12})^2}{V_c(c_{11}+c_{12})+V_p(c_{11}^{E}+c_{12}^{E})}\right] + V_p c_{11} \qquad \textbf{Equation II-1}$$

The effective piezoelectric stress constant $\overline{e_{33}}$ is given by:

$$\overline{e_{33}} = V_c\left[e_{33} - \frac{2V_p e_{31}(c_{13}^{E} - c_{12})}{V_c(c_{11}+c_{12})+V_p(c_{11}^{E}+c_{12}^{E})}\right] \qquad \textbf{Equation II-2}$$

The effective static dielectric constant $\overline{\varepsilon_{33}^{S}}$ is given by:

$$\overline{\varepsilon_{33}^{S}} = V_c\left[\varepsilon_{33}^{S} + \frac{2V_p(e_{31})^2}{V_c(c_{11}+c_{12})+V_p(c_{11}^{E}+c_{12}^{E})}\right] + V_p\varepsilon_{11} \qquad \textbf{Equation II-3}$$

The effective elastic constant at constant electric displacement $\overline{c_{33}^{D}}$ is given by:

$$\overline{c_{33}^{D}} = \overline{c_{33}^{E}} + \frac{(\overline{e_{33}})^2}{\overline{\varepsilon_{33}^{S}}} \qquad \textbf{Equation II-4}$$

The thickness coupling coefficient of a thin piezocomposite plate is given by:

$$\overline{k_t} = \sqrt{\frac{(\overline{e_{33}})^2}{\overline{c_{33}^D \varepsilon_{33}^S}}}$$

Equation II- 5

The specific acoustic impedance is given by:

$$\overline{Z} = \sqrt{\overline{c_{33}^D}\,\overline{\rho}}$$

Equation II-6

where the average density of piezocomposite material $\overline{\rho}$ is related to the density of the piezoceramic ρ_c and the density of the polymer matrix ρ_p by:

$$\overline{\rho} = V_c \rho_c + V_p \rho_p$$

Equation II-7

Table II-1 Relative parameters of TRS 610 piezoceramic and Epofix polymer used for the calculations of the effective properties of the piezocomposite [2, 3].

	ρ_c	c_{33}^E	c_{13}^E	c_{11}^E	c_{12}^E	$\varepsilon_{33}^s / \varepsilon_0$	e_{33}	e_{31}
	g/cm^3	**10^{10} N/m^2**	**10^{10} N/m^2**	**10^{10} N/m^2**	**10^{10} N/m^2**		**C/m^2**	**C/m^2**
TRS 610	**7950**	**12.0**	**8.5**	**12.3**	**7.4**	**1250**	**25**	**-8.3**

	ρ_p	c_{11}	c_{12}	$\varepsilon_{11} / \varepsilon_0$
	g/cm^3	**10^{10} N/m^2**	**10^{10} N/m^2**	
Epofix	**1120**	**0.78**	**0.46**	**4.8**

References:

[1] W. A. Smith and B. A. Auld, "Modeling 1-3 composite piezoelectrics: thickness-mode oscillations," *Ultrasonics, Ferroelectrics and Frequency Control, IEEE Transactions on*, vol. 38, pp. 40-47, 1991.

[2] (Last accessed 2012/04/26). *TRS piezoelectric materials datasheet*. Available: http://www.trstechnologies.com/Materials/Piezoceramics/properties.php

[3] Unpublished work.

Appendix III: Random piezocomposite pattern design

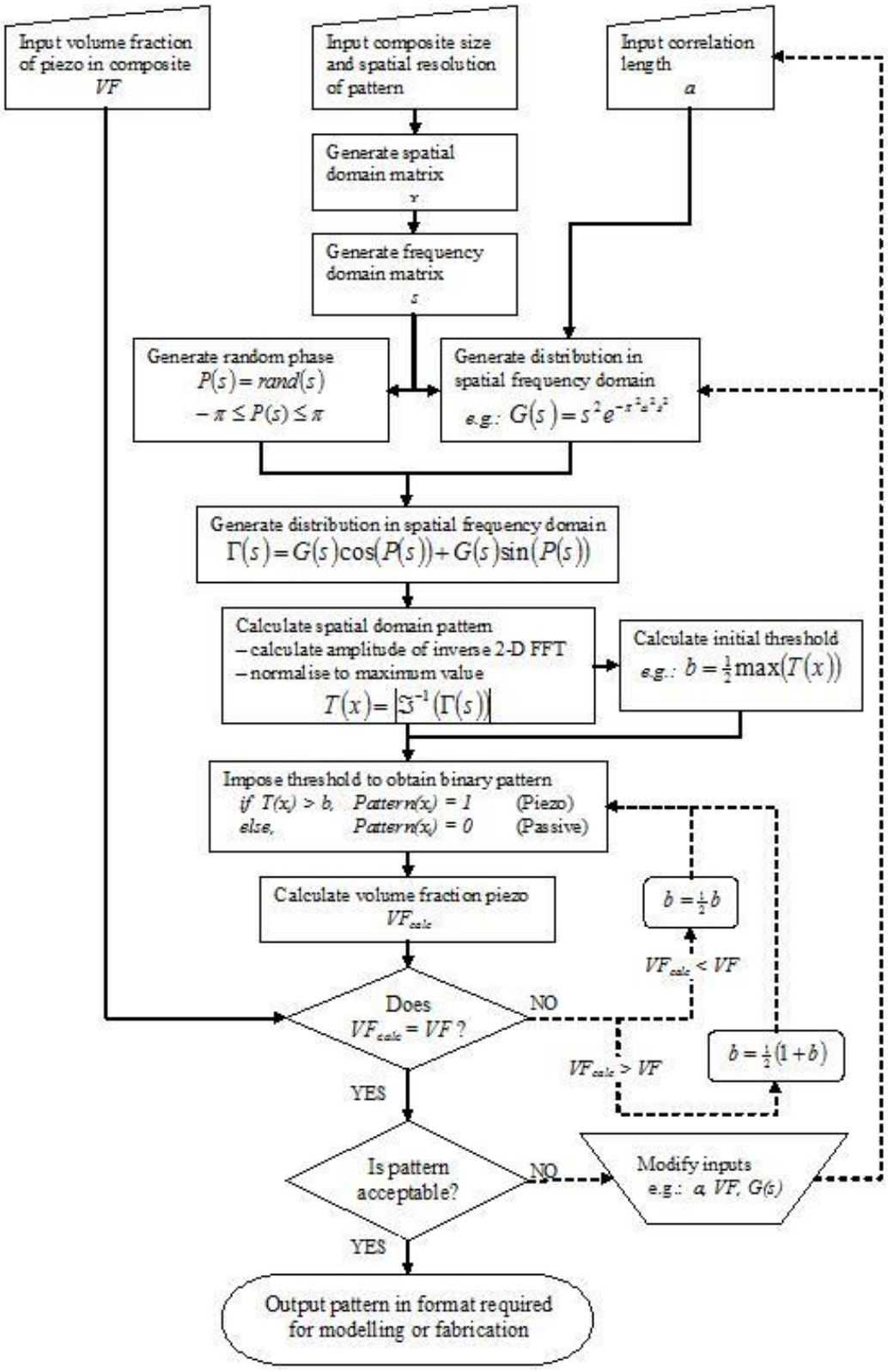

Figure III-1 Flow chart of the random piezocomposite pattern design process (unpublished work). Note: s=0: 1/max(x): 1/Δx, where x is the dimension of the composite and Δx is the required resolution.

Appendix IV Publications

Gang Liu, ***Yun Jiang***, Tim W Button, Low Temperature Sintering and Dielectric Properties of $BaTiO_3$ Ceramics Incorporating Nano-Sized Powders, Ferroelectrics, 421:1-10, 2011.

Yun Jiang, Christine E. M. Démoré, Carl Meggs, Camelia Dunare, Tom Stevenson, Jeff Bamber, Sandy Cochran, Tim W Button, Micro-moulded Randomised Piezocomposites for High Frequency Ultrasound Imaging, IEEE Ultrasonics Symposium 2012 (accepted).